A probabilistic multiscale methodology to predict the fatigue life of porous alloys from tomographic images

Abhishek Palchoudhary

PSL
UNIVERSITÉ PARIS

THÈSE DE DOCTORAT

DE L'UNIVERSITÉ PSL

Préparée à l'École Nationale Supérieure de Mines de Paris

A probabilistic multiscale methodology to predict the fatigue life of porous alloys from tomographic images

Une méthodologie probabiliste multi-échelle pour prédire la durée de vie en fatigue des alliages poreux à partir d'images tomographiques

Soutenue par

Abhishek PALCHOUDHARY

Le 19 Décembre 2024

École doctorale n°621

Ingénierie des Systèmes, Matériaux, Mécanique, Énergétique - ISMME

Spécialité

Mécanique

Préparée au

Centre des matériaux,
Mines Paris, Université PSL

Composition du jury :

Cédric DOUDARD Professeur, ENSTA Bretagne	*Président du jury* *Rapporteur*
Étienne PESSARD Professeur, ENSAM	*Rapporteur*
Rodrigue DESMORAT Professeur, ENS Paris Saclay	*Examinateur*
Lionel MARCIN Ingénieur de recherche, Safran Aircraft Engines	*Examinateur*
Pascale KANOUTÉ Ingénieur de recherche, ONERA	*Examinateur*
Cristian OVALLE Chargé de recherche, Mines Paris, PSL	*Examinateur*
Vincent MAUREL Directeur de recherche, Mines Paris, PSL	*Examinateur*
Pierre KERFRIDEN Professeur, Mines Paris, PSL	*Directeur de thèse*

MINES PARIS | PSL

Acknowledgements

As my PhD journey comes to an end, I would like to express my gratitude to several individuals who have supported me during this intense, sometimes chaotic, but ultimately enriching chapter of my life.

I am particularly grateful to my thesis supervisors, each of whom has contributed uniquely to my experience. Pierre, your investment in my PhD has been remarkable. You have consistently proposed new and innovative ideas, tirelessly enhancing my papers and scientific presentations, and addressing my queries even during your holiday. Our discussions have opened my eyes to the possibilities within this field, as your suggestions are always well-developed and strategically sound. Vincent, from the beginning of my journey as an intern to my PhD, you have helped me step back from the technical intricacies and see the broader context of my work. The memories of our musical collaborations and shared moments at conferences will always hold a special place in my heart. Cristian, your unwavering support and encouragement throughout my PhD has been invaluable. Conversations with you have always lifted my spirits, and your guidance and scientific mentoring have been invaluable. I would like to thank all three of you for granting me the freedom to explore, make mistakes (sometimes spectacular ones!), and pursue unconventional ideas that sometimes led to exciting breakthroughs. This autonomy has been pivotal in shaping both my research and my growth as a critical thinker.

I would also like to extend my gratitude to the engineers and technicians at the SESAMES platform: Youssef Atik, Stéphanie Dang, Matthieu Ramboudon, Jean-Christophe Teissedre, Yann Auriac, Abdennour Meddour, and Régis Clément, for always being available to assist with my experimental needs. Your patience, expertise, and creative problem-solving have saved more experiments than I can count (and possibly my sanity too). Without your help, my stress levels would undoubtedly have been much higher. From the SiSDev platform, I extend my thanks to Basile, Djamel, and Jean-Michel for resolving my numerical and software issues with efficiency and good humour. I am also grateful to Anne-Françoise for facilitating structured meetings where I could openly discuss the challenges and emotions of my PhD journey. Pierre Arnaud, though our interactions during my PhD were limited, I remain grateful for your assistance with numerical tools during my internship, which laid the groundwork for some of my later work. To Damien Texier, even though I stopped working with ultrathin specimens and branched out into more of a numerical field, I am grateful to have stayed in contact and for our discussions when you travelled to Paris.

To my interns, Simone and Jean-Paul, thank you for your curiosity, dedication, and patience. Supervising you was a rewarding experience that taught me as much as I hope it taught you. Your contributions and willingness to learn made our time together both productive and enjoyable.

To my fellow PhD students and colleagues, your camaraderie has made this journey all the more memorable. To Abderrahman (Abdou), Nicolas Léost, and Lili, your advice and support in my early days were invaluable. Abdou and Nicolas, you taught me to navigate the complexities of experimental setups and inspired me to pass on this knowledge to others. To Guilherme, thank you for our wonderful musical sessions and heartfelt conversations, which provided much-needed respite from the rigours of research. To Aubin, for our funk music collaborations and shared laughs; to Rawad, Maryse, Daniella, Saïd, Nicolas, Clémence, Mikel, Amina, Nadjib, Florian, Elodie and Amélia, for the unforgettable moments we shared, either at conferences, in bars, during the *match aller-retour* with Lucien, or around a cup of coffee; and to Arjun, for our friendly debates on approaches to predict the lifetime of material with defects — thank you all for your friendship and intellectual stimulation. To Mathias, Aubin, Camille, and many others with whom I shared engaging discussions over lunch, and of course, a shout-out to the legendary Cémantix challenges with Matthiew, Juliette, Gaultier, and many others. To all of you, and to everyone whom I may have inadvertently omitted — thank you for these shared moments.

Finally, I wish to express my gratitude to my family. To my father and sister in India, your unwavering support has been my anchor throughout this journey. To my late mother, I hope I have made you proud. And to Eva, my partner, thank you for your patience, understanding, and love over the past five years. Your belief in me has been a driving force: I could never have reached this milestone without you.

This PhD has been a rather rewarding journey filled with discovery, growth, and collaboration. It has had its challenges, but with the support of all of you, it has become an achievement I will always cherish. Like a recipe in the works, it had its moments of being over-salted, occasionally burnt, but ultimately it turned out pretty tasty (or at least edible). Thank you from the bottom of my heart.

Résumé

Cette étude vise à établir une méthodologie permettant de prendre en compte la variabilité du comportement en fatigue à grand nombre de cycles (HCF) des alliages, en modélisant explicitement les pores à l'échelle méso (défauts géométriques) présents dans le matériau. Bien qu'il existe des stratégies numériques pour prédire la durée de vie en HCF à partir de simulations haute résolution des réseaux de pores, plusieurs défis subsistent. Premièrement, la prédiction de la durée de vie en fatigue devient difficile lorsque les réseaux de pores exacts présents dans le matériau sont inconnus. Deuxièmement, les coûts de calcul des simulations non-linéaires par éléments finis (EF) au niveau des défauts sont élevés, car un grand nombre de degrés de liberté est nécessaire pour représenter précisément le réseau de pores dans le matériau. Enfin, l'identification des modèles de fatigue exige de nombreuses données d'essais de fatigue, longues à obtenir.

Nous développons une méthodologie multi-échelle pour intégrer les effets des défauts sur la durée de vie en HCF. À l'échelle microscopique, la variabilité de la durée de vie est traitée via des modèles probabilistes, sans modélisation explicite des défauts. À l'échelle mésoscopique, des maillages EF haute résolution sont créés à partir d'images tomographiques, afin de rendre compte des effets conjugués de la morphologie, des interactions entre pores, ainsi que des effets de surface. Un échantillonneur statistique est utilisé pour générer différentes configurations et estimer la distribution de la durée de vie en fatigue en fonction des distributions de pores. Ainsi, une nouvelle méthode pour calibrer les modèles probabilistes tenant compte de cette incertitude liée aux pores est proposée. Cette approche permet de fournir des estimations de durée de vie en HCF fonction des deux échelles analysées, tout en réduisant le nombre de données nécessaires à l'identification robuste d'un tel modèle. De plus, afin de réduire les coûts de calcul de la méthode multi-échelle, nous développons un nouvel algorithme local de correction plastique de type Neuber pour approximer le comportement plastique à partir de calculs élastiques. Nous démontrons l'efficacité de notre méthode pour diverses structures poreuses, sous des conditions de plasticité confinée et de chargement proportionnel.

Dans la dernière partie de cette thèse, nous explorons l'usage des données d'auto-échauffement pour réduire les données de calibration, comme suggéré par Doudard et al., 2004. Une augmentation de température est observée autour des pores, liée à la conductivité thermique des alliages testés. Nous proposons une méthode d'identification qui renforce la robustesse du modèle face aux mesures thermiques bruitées. Le critère de ce modèle est ensuite étendu pour inclure la plasticité, permettant son application aux matériaux poreux.

Mots clés : Durée de vie en fatigue, Pores, Tomographie X, Elements Finis, Machine Learning

Abstract

This thesis focuses on the development of methodology to account for variability in high-cycle fatigue (HCF) behaviour of alloys, by explicitly modelling the meso-scale pores (geometric defects) present in the material. Although numerical frameworks exist to predict the HCF lifetime using high-resolution simulations of pore networks, several challenges remain. Firstly, predicting fatigue lifetime becomes difficult when the exact pore networks present in the material are unknown. Secondly, the computational costs of non-linear finite element (FE) simulations at the pore level are high, as a large number of degrees of freedom are needed to accurately represent the pore networks within the material. Lastly, calibrating fatigue models requires a substantial amount of fatigue testing data, which is time-consuming to obtain.

We develop a multi-scale methodology to account for defect effects on HCF lifetime. At the micro-scale, variability in lifetime is treated by using probabilistic lifetime models, without explicit defect modelling. At the meso-scale, high-resolution FE meshes are generated based on tomographic images, accounting for the combined effects of pore morphology, inter-pore interactions, and pore-surface interactions. A statistical sampler is leveraged to generate different configurations to estimate the distribution of fatigue lifetime of the material as a function of pore distributions. Based on this, we propose a novel method to calibrate the probabilistic lifetime models in the event of uncertainty related to pore distribution. Thus, our proposed method provides HCF lifetime estimates integrating defect populations at two scales, and reduces the amount of data required to calibrate the models for alloys with different levels of porosity. Furthermore, in order to reduce the computational costs associated to the multi-scale method, we develop a new local Neuber-type plastic correction algorithm to approximate elasto-plastic behaviour from elastic computations. We demonstrate the effectiveness of our method for a range of porous materials, under conditions of confined plasticity and proportional loading.

In the last part of the thesis, we investigate the potential of using self-heating data to further reduce the data required to calibrate the fatigue model, as proposed by Doudard et al., 2004. A temperature rise from self-heating, driven by dissipative mechanisms due to defects, is observed. Temperature localisation around pores is governed by the thermal conductivity of alloys tested. We propose a new identification method for the aforementioned model, improving its robustness in the event of noisy temperature measurements. The criterion of this model is then extended to include plasticity, enabling its application to porous materials.

Keywords : Fatigue Lifetime, Pores, X-Ray Tomography, Finite Elements, Machine Learning

Contents

List of figures

List of Tables

Introduction

Defects are present across multiple scales in the majority of metallic components. One such type of defect is pores (see Figure 1(a)), which are voids at the meso-scale of the component, typically ranging in size from tens to hundreds of micrometres. Pores typically arise as a result of the manufacturing processes employed in the production of the material. Casting processes, for instance, can produce pores, some of which form due to the metal shrinking as it solidifies [Buffière et al., 2001, Le et al., 2018]. Similarly, additive manufacturing processes may result in pores due to incomplete fusion of the metal powder [Gong et al., 2014]. At the microscopic level, other defects are present, such as grain boundaries, heterogeneous grain orientations, precipitates, and similar features [Wang et al., 2001, Le et al., 2018, Wang et al., 2023]. Defects at both of these scales are at the origin of the degradation of metallic components when subjected to repeated cyclic loading, even when the applied stress remains below the macroscopic yield stress of the material. [Wang et al., 2001, Morel et al., 2015, Le et al., 2018, Wang et al., 2023]. This phenomenon is commonly referred to as high-cycle fatigue (HCF).

The variability of defects at both of these scales from one component to another — despite identical overall geometries — causes scatter observed in fatigue lifetimes (see Figure 1(b)). For the prediction of lifetime variability in structures with meso-scale pores, simplified approaches are available, which typically model the porous material as a homogenised substance with equivalent fatigue properties, eliminating the need to describe individual pores directly [Ezanno et al., 2010, ASTM, 2015]. However, the applicability of such models relies on fatigue data from components made of a specific porous material and cannot be transferred to components with the same base material but different pore characteristics.

Imaging techniques allow for detection of meso-scale pores with progressively improving resolution, and it is now possible to obtain tomographic scans of these pores relatively quickly. Furthermore, digital pipelines now exist that can integrate high-resolution information about these pores when predicting fatigue lifetimes [Le et al., 2018, Matpadi Raghavendra et al., 2024]. However, two principal challenges exist for such approaches: (a) a tomographic scanner is necessary to scan the component in question for the digital pipeline to be employed, and (b) the use of these image-based models is impeded by the substantial computation time required, unless a representative volume element exists and can be identified [Chen et al., 2023]. The simulation time associated with a high-resolution numerical model can extend to several days, owing to the large number of degrees of freedom, the non-linear behaviour of the material, and the

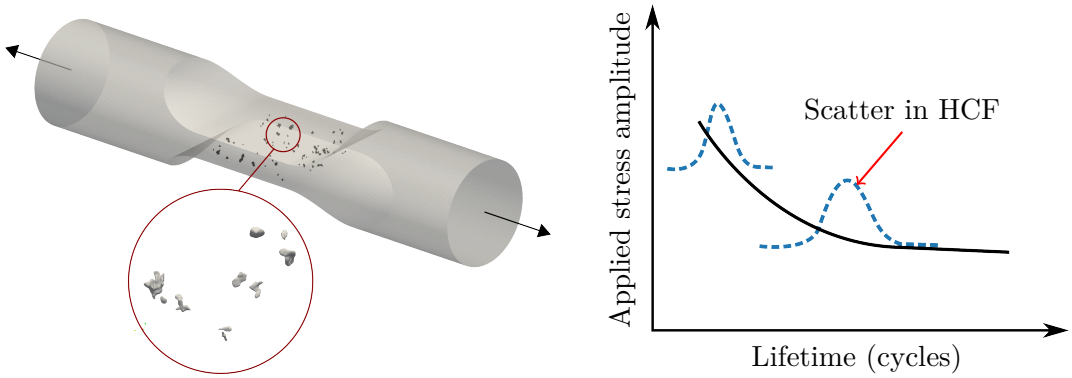

(a) Pores (a kind of meso-scale defect) in a laboratory specimen

(b) Variability in lifetime due to material defects

Figure 1: Variability in high-cycle fatigue lifetime due to the presence of material defects

prolonged time analyses required to capture transient behaviour. Consequently, solutions are required that can: (a) provide a lifetime estimate for a component constructed from this porous material without necessitating its exact pore distribution using tomographic imaging, and (b) offer a method to expedite computations at the resolution of the tomographic images, thereby facilitating the faster utilisation of digital pipelines.

To address the first challenge, a class of approaches exists that employs statistical methods to account for uncertainty in fatigue lifetime due to meso-scale pores. These methods necessitate a priori knowledge of the pore distribution likely to be present in the structure, which can be obtained from a small representative computed tomography (CT) scan of the porous material. This data serves as the input to the fatigue model, which, by sampling various potential pore configurations, computes a probability of failure for a given structure without needing precise knowledge of its pore distribution. Some of these approaches do not explicitly model the pore distribution; rather, they employ point processes to generate simplified pore distributions, with each point being assigned a random pore size based on the material's pore size distribution [El Khoukhi et al., 2019, Romano et al., 2019]. HCF lifetime predictions are then made using a Kitagawa-Takahashi (KT) diagram, which establishes a relationship between the fatigue limit and the size of the pores. As the probability of finding a large defect increases with the considered volume, the approach by [El Khoukhi et al., 2019] permits to take into account the size effect. A similar method based on this separation of scales is developed by [Shirani and Härkegård, 2012]. The approach by [Romano et al., 2019] allows incorporation of stress gradients in components with complex geometries, by a subdivision of the geometry into finite volume elements, computation of a failure probability in each element by usage of the point process in conjunction with the KT diagram, followed by weakest link scaling for the full component. All these approaches assume that only pores are at the origin of fatigue failure, and that a single killer pore is responsible for fatigue failure, and do not take into account pore morphology, interactions between pores, or pore-surface interactions. Furthermore, obtaining the KT diagram is a lengthy experimental process.

Another class of approaches avoids a separation of scales and instead employs finite ele-

ment analysis to explicitly model meso-scale pores, aiming to quantify the uncertainty in fatigue lifetime resulting from the statistical variability of these pores. The advantage of such approaches is the ability to account for pore-surface and inter-pore interactions, as well as the potential to be more representative of the actual pore morphology, all of which have been proven to have an effect on fatigue life [Billaudeau et al., 2004, Guerchais et al., 2017, Matpadi Raghavendra et al., 2024]. Existing approaches in this class typically simplify the representation of pore geometries to spheres [Lacourt, 2019], either neglecting inter-pore interactions [Bercelli et al., 2021] or restricting the FE model to two-dimensional geometries [Talemi, 2020, Hou et al., 2024]. With the exception of the work by [Lacourt, 2019] and [Hou et al., 2024], these methods generally neglect the local non-linearity in material behaviour that may arise from high stress concentrations induced by the pores.

The second challenge, namely the computational costs associated with high-resolution simulations for lifetime predictions, can be addressed in several ways. One possibility is plastic correction methods, like Neuber [Neuber, 1961] and Glinka methods [Molski and Glinka, 1981], which are heuristics that relate the stresses and strains in an elasto-plastic body to those in a geometrically similar elastic body undergoing similar loading conditions. Advancements in these methods over the years have enabled the rapid recovery of multi-axial loading states at critical points. There is a general consensus that the Neuber method tends to overestimate stresses at notches, whereas the Glinka method is more likely to underestimate them [Desmorat, 2002, McDonald and Socie, 2011, Thumann et al., 2024]. However, although the applicability of these methods has been demonstrated for points exhibiting confined plasticity [Herbland, 2009], the relevance of these methods for approximating plasticity in high-resolution simulations at the pore level is not addressed in the literature. Another category of approaches are cycle jump techniques, introduced by [Savalle and Culié, 1978, Lesne and Savalle, 1989]. These methods enable extrapolation to later stages of cyclic loading, reducing the number of computed cycles. By expressing internal variables as functions of cycle count, the method updates these variables based on a few previously computed cycles, bypassing intermediate cycles. This approach is particularly useful for materials with long stabilization processes or those exhibiting ratcheting behaviour, and have widely been adopted by the fatigue community [Sai, 1993, Van Paepegem et al., 2001, Cheng et al., 2022]. Yet another class of approaches uses reduced order modelling (ROM), where the solution to a given boundary value problem is found in a lower dimensional space and a reduced integration domain [Ryckelynck et al., 2015]. These methods have successfully been applied, to accelerate elasto-plastic computations on specimens with meso-scale pores of varying sizes and shapes, with low error margins [Lacourt, 2019].

Finally, a third challenge in high-cycle fatigue arises from the necessity of a large number of specimens to identify the scatter in lifetime attributed to variability at the micro-structural level. In this regard, a specialized approach is to use self-heating experiments — resulting from energy dissipation during cyclic loading — to inform the source of scatter in fatigue lifetime [Doudard et al., 2004]. This is one approach that allows for a reduction in the number of experiments required across various fatigue loading scenarios [Doudard et al., 2005, Ezanno et al., 2013, Bercelli et al., 2021]. In this context, the robustness

and applicability of such approaches for materials containing defects require further investigation.

The objective of this PhD is to tackle the aforementioned three critical challenges in fatigue lifetime prediction: (a) the prediction of the lifetime of a porous specimen where the precise pore geometries and locations are unknown, but a representative volume of the same porous material is available; (b) the prohibitive computational costs associated with elasto-plastic material behaviour and prolonged time analyses in the context of volumes containing pore networks; and (c) the substantial amount of fatigue data required for the calibration of lifetime models. Numerical developments will be undertaken to propose a new methodology for predicting the lifetime of specimens in the presence of micro-scale defects and meso-scale pores, with the latter explicitly modelled using the FE method. Unlike similar existing methods [Lacourt, 2019], the real pore geometries will be modelled. The proposed multi-scale methodology allows for computation of the probabilistic lifetime of a porous specimen based on a weakest link assumption which has so far only been used for notched components [Liu et al., 2020, Li et al., 2022]. A novel method is proposed for identification of the lifetime model in the case of uncertainty in the pore distributions in the specimen. The computations required for evaluating the lifetime distribution of a porous specimen will be accelerated through the development of a new Neuber-type plastic correction algorithm, which integrates Chaboche-type plasticity laws [Chaboche, 1989], and is shown to well approximate plasticity on networks of realistic pores as long as the plasticity remains confined. Furthermore, the developed algorithm is proved to be well-suited for further acceleration through simple machine learning frameworks, which is useful particularly for long-term analyses that are often necessary for obtaining fatigue lifetime criteria. Altogether, the methodology proposed addresses the third challenge by providing a foundation for reducing the amount of fatigue data required to calibrate a lifetime model, by considering the same base material behaviour for different porosity levels. Finally, a self-heating-based approach [Doudard et al., 2004] will be employed to investigate the possibility of further reduction in fatigue data necessary for calibrating a suitable lifetime model, with the perspective to expand such a model to account for porosity. The following paragraphs outline the methodology adopted.

- *Chapter One* begins with a concise literature review that encompasses the essential elements required to understand the subsequent chapters. This review includes the impact of pore characteristics on fatigue life [Billaudeau et al., 2004, Guerchais et al., 2017, Le et al., 2018, Serrano-Munoz et al., 2018, Matpadi Raghavendra et al., 2024]. Following this, existing statistical approaches for incorporating porosity into lifetime models at varying levels of computational complexity are discussed, including approaches that use a separation of scales [Ezanno et al., 2010, El Khoukhi et al., 2019, Romano et al., 2019], and those that use explicit modelling of the pores via the FE method [Lacourt, 2019, Bercelli et al., 2021, Hou et al., 2024]. Following this, a brief presentation of two methods for accelerating computations of structures subjected to non-linear material behaviour is given, including Neuber-type plastic correction methods [Neuber, 1961, Molski and Glinka, 1981, Desmorat, 2002] and cycle jump methods

[Savalle and Culié, 1978, Sai, 1993, Cheng et al., 2022]. Following this introductory chapter, the dissertation is organised into two major parts:

Part 1: Numerical pipeline for fatigue lifetime predictions of specimens with porosity

- *Chapter two* is an adapted version of an article in preparation, titled "A multi-scale probabilistic methodology to predict high-cycle fatigue lifetime for alloys with process-induced pores" [Palchoudhary et al., 2024a]. The chapter will deal with the development of a multi-scale method coupled with a probabilistic lifetime model to take into account the influence of porosity on the fatigue lifetime. A multi-axial strain-life criteria is chosen for the lifetime model [Karolczuk and Macha, 2005, ASTM, 2015], which will account for the scatter in lifetime of the base, pore-free material. The meso-scale pores will be explicitly modelled in the specimen using the FE method. The probabilistic lifetime of a porous specimen will be determined by a weakest link hypothesis [Zok, 2017] at the level of its finite elements. The chapter will propose a statistical method to address the question of obtaining an estimate for lifetime without access to the exact pore distribution in the specimen. The method consists of scanning a different, small volume made from the same porous material as the specimen, to gather statistical information about the pores likely contributing to the fatigue failure. This statistical data will serve as the input to the fatigue model, which, by considering various potential pore positions and characteristics, will compute a probability of failure for a given specimen without needing precise knowledge of its pore distribution. The method will be validated on two cast aluminium alloys with different levels of porosity for which fatigue lifetime data [Le et al., 2018] and a tomographic scan of a small volume are available.

  Furthermore, the identification of lifetime models, when pores are explicitly modelled, is typically based on lifetime data from the base material, which is pore-free [Lacourt, 2019, Bercelli et al., 2021, Hou et al., 2024]. Some techniques identify the lifetime model on porous data in the case where the exact distribution of pores is known for each specimen tested for fatigue failure [Matpadi Raghavendra et al., 2024]. In this chapter, a novel method will be introduced to identify the lifetime model directly from porous lifetime data. This procedure shares similarity to the method used for identifying the weakest link Weibull model on experimental data of notched components in [Liu et al., 2020]. Our innovation lies in the identification of the lifetime model for porous specimens, specifically addressing the case of uncertainty in the pore distribution that led to failure.

  Finally, certain properties of the model, including the optimization behavior, complexity, size effect, interaction effects between pores and the geometry of the structure, etc. will be tested. The chapter ends with a section which will investigate the possibility of using a naive homogenization approach to replace the multi-scale approach and thus bypass the need for explicit representation of pores.

- *Chapter three* is an adapted version of an accepted article titled "A plastic correction algorithm for full-field elasto-plastic finite element simulations : critical assessment of pre-

dictive capabilities and improvement by machine learning" [Palchoudhary et al., 2024b]. The chapter will be dedicated to numerical developments on a method for acceleration of non-linear finite element computations. To this end, a Neuber-type plastic correction algorithm enabled by point-wise proportional rules will be proposed that can rapidly post-process elasto-statics simulations to approximate the full-field elasto-plastic response of structures subjected to proportional loading. As far as we are aware, existing pieces of work concentrate specifically on the development of Neuber-type plastic correction methods for the prediction of multiaxial stress and strain states at notch tips [Buczynski and Glinka, 2003, Ince and Glinka, 2013, Moftakhar et al., 1994, Desmorat, 2002, McDonald and Socie, 2011]. One specific piece of work by Desmorat et al. [Desmorat, 2002] suggests using locally proportional evolutions together with Neuber-type rules to predict the evolution of elasto-plastic fields. Yet, detailed analysis of the accuracy of the suggested methodology away from notches and free boundaries, or derivations of general-purpose algorithms to integrate the resulting plastic correction equations numerically, i.e. under arbitrary (proportional) load histories, were not found in the literature. Our proposed algorithm will use a modified Neuber's rule that operates on the deviatoric part of stress and strain tensors, extended for fatigue loading via a change of peaks method. The Neuber heuristic will be coupled with a point-wise proportionality rule that reduces the tensorial elasto-plasticity laws to a set of equations operating on scalar representations of stresses and strains. The solution to this system of equations will be found by a fully implicit time integration algorithm, following which the approximated tensorial elasto-plastic solution is recovered. The accuracy of this plastic corrector will be tested on a variety of structures, including a notched structure, a specimen with spherical pores and another with realistic pores modelled based on tomography imaging.

Furthermore, 1D meta-models will be proposed that accelerate the plastic correction algorithm even further, for any quantity of interest, by sampling the output of the plastic corrector for a relatively small number of von Mises stresses, training the meta-model and using it at almost no cost in place of the time integration algorithm, which is an added novelty. The chapter ends with a section which will demonstrate the ability of deep learning to correct the plastic corrector's accuracy, on a subset of specimens with spherical pores. In addition, a novel demonstration will show why using the plastic corrector as an input to a deep learning based approach can be beneficial over inputs of lesser mechanical context, i.e. pure elasticity computations.

Part 2: Self-heating for the detection of pores and proposed numerical developments towards rapid lifetime estimation in for alloys with defects

- *Chapter four* will concentrate on a brief experimental campaign for characterization of self heating in the cast aluminium alloys presented in Chapter two. As a second objective, another alloy with low thermal conductivity (an additively manufactured superalloy) with controlled pore configurations is tested to determine whether self-heating can be used to detect pores, and what the limits of the this detection method are.

- *Chapter five* will use some of the self-heating experiments previously conducted in the fourth chapter in order to identify a probabilistic lifetime model, in the absence of porosity. Specifically, this is the stochastic micro-inclusion model [Doudard et al., 2004] with a criteria on accumulated plasticity [Desmorat et al., 2007, Ezanno et al., 2013] developing below the yield limit. This model was originally developed for specimens containing a homogeneous stress distribution in their gauge section, and, by construction, uses self-heating information for parameter identification. A maximum likelihood estimate is proposed for parameter identification, and the relative benefits over previous methods [Doudard et al., 2005] are outlined. In an attempt to use the micro-inclusion model in the presence of porosity, the multi-scale method introduced in the second chapter is adopted. The lifetime model is first coupled with the multi-scale method, for use on porous specimens whose exact distribution is unknown. Following this, an extension to the model is proposed to take into account to treat loading cases beyond the yield limit of the material (where the micro-inclusion model no longer rests valid). The proposed extended model is a mixture model with a transition between the criteria of the micro-inclusion model and a new criteria based on von Mises plasticity laws. The new model is validated on the same material as in the second chapter. The chapter concludes with a discussion and perspectives related to identifying the proposed model on self-heating data of porous material.

Chapter 1

Literature review

Résumé

Ce chapitre propose une brève revue de la littérature sur la fatigue à grand nombre de cycles dans les alliages métalliques, en se concentrant particulièrement sur l'effet des défauts, notamment la porosité à l'échelle mésoscopique. La détection des pores est abordée en explorant des techniques telles que la tomographie et la thermographie infrarouge. L'influence des défauts aux deux échelles, c'est-à-dire micro et mésoscopique, sur la durée de vie en fatigue est discutée. Ensuite, les approches statistiques existantes pour la modélisation de la durée de vie en fatigue, notamment celles qui intègrent la porosité dans des modèles, sont examinées. La discussion se concentre sur les méthodes exploitant une séparation d'échelles ainsi que celles reposant sur la modélisation explicite des pores via la méthode des éléments finis. Enfin, les méthodes d'accélération des calculs pour les simulations de comportement non linéaire des matériaux, dont les corrections plastiques de type Neuber et les techniques de saut de cycle, sont présentées. Cette revue prépare le terrain pour les développements numériques détaillés dans les chapitres suivants.

1 Introduction

This chapter provides a concise introduction to the key literature and theoretical elements underpinning the manuscript, aiming to highlight the originality of the thesis. It is divided into three sections. The first section offers a brief survey of high-cycle fatigue behaviour in alloys with material defects [Wang et al., 2001, Le et al., 2018, Wang et al., 2023], focusing on meso-scale defects, particularly porosity [Buffière et al., 2001, Le et al., 2018, Serrano-Munoz et al., 2018, El Khoukhi et al., 2022, Matpadi Raghavendra et al., 2024]. The methods used for pore detection in this thesis, namely computed tomography and infrared thermography, are also explained.

The second section discusses lifetime models for materials with defects and how meso-scale porosity is incorporated into lifetime predictions. Various methods of differing complexity are examined. First, the weakest link approach [Zok, 2017] is introduced, including typical calibration procedures. Next, the advantages and limitations of methods involving a separation of scales to account for material defects are explored [Desmorat, 2002, Ezanno et al., 2013, El Khoukhi et al., 2019, Romano et al., 2019]. Following this, some approaches that explicitly model porosity and consider its effect on lifetime are reviewed, with an emphasis on methods employing statistical analysis to quantify the uncertainty in lifetime due to variations in pore distribution [Lacourt, 2019, Bercelli et al., 2021, Hou et al., 2024]. The calibration of lifetime models in these approaches is discussed. Lastly, the self-heating-based approach to lifetime model calibration is considered [Doudard et al., 2004, Ezanno et al., 2013], focusing on current calibration practices and the performance of these models when porosity is explicitly included [Bercelli et al., 2021].

The third section addresses methods for accelerating the computation of elasto-plastic solutions used in lifetime predictions, improving the efficiency of the prediction process. Neuber-type plastic correction methods [Neuber, 1961, Molski and Glinka, 1981, Desmorat, 2002, McDonald and Socie, 2011] are covered, as they are central to the contributions of Chapter 3. Cycle jump methods [Savalle and Culié, 1978, Lesne and Savalle, 1989, Sai, 1993, Cheng et al., 2022] are also included, as they enable faster computations during long transient phases with minimal error.

2 Defects in metal alloys: detection and effect on high-cycle fatigue

While defects in metal alloys occur at both the micro and meso-scale (as outlined in the introduction), the subsequent chapters will focus explicitly on the physics of meso-scale pores. Although this section briefly addresses the influence of overall material defects on the high-cycle fatigue lifetime of alloys, the emphasis will be on meso-scale porosity. First, the methods used in this thesis for detecting porosity will be discussed. Following this, the impact of pore characteristics—such as size, morphology, proximity to the surface, and clustering—on fatigue life will be examined.

2.1 Detection of porosity

The two methods used in this PhD for the detection of pores will be described in this section.

2.1.1 Computed tomography

Tomography is a non-destructive technique that involves capturing multiple projected images of an object from various angles. The object to be imaged is placed between a X-ray emitting source and a detector. The detector captures the intensity of the waves after they pass through the object. Each projection provides a 2D view of the object, with variations in intensity corresponding to differences in the material's density or composition within the object. By applying reconstruction algorithms to these images, a three-dimensional image of the object, which can be viewed from any angle or sectioned at any plane, is created. This facilitates the identification of defects in the analyzed material. The resolution of the resulting images and the time required for data acquisition are influenced by both the inspection method used and the size and density of the scanned part. The resolution of tomographs can vary from the order of nanometers to several hundred micrometers [Tkachuk et al., 2007, Vásárhelyi et al., 2020]. Tomography provides detailed information about pores, including their precise location within the part, as well as their size and shape. Several studies have benefited from this technique in order to characterize pore density, sizes, locations and shapes in a wide range of metal alloys [Taud et al., 2005, Dezecot et al., 2016, Le, 2016, Matpadi Raghavendra et al., 2024].

2.1.2 Infrared thermography

While active infrared thermography has been successfully used to localise pores [D'Accardi et al., 2021], this PhD focuses on using infrared thermography based on the principle of self-heating, i.e., measuring temperature under cyclic mechanical loading applied to the structure. Any stress concentrator in the structure leads to localized plasticity and increased dissipation, which is conducted to the surface. The temperature on the material's surface is measured by an infrared camera. Depending on the signal-to-noise ratio—affected by factors such as pore location, presence of cracks, dissipation extent, and the material's conduction and convection properties—pores may potentially be localised using this method.

Successful applications include the detection of surface and sub-surface cracks [Leost et al., 2023, Bercelli, 2021], yet its use for pore detection remains underexplored in the literature. One study reports no localisation or average temperature difference on the surface due to a large internal pore in aluminium alloys [Messager, 2020]. Another study examines self-heating behaviour in a titanium alloy with varying porosity levels (0.001-1% volumetric fraction) and concludes that the difference in average temperature rise between porosity grades is negligible [Brot et al., 2024].

2.2 Effect of defects at two scales

The effect of material defects at two scales, i.e. micro-scale heterogeneity and meso-scale pores, will now be discussed.

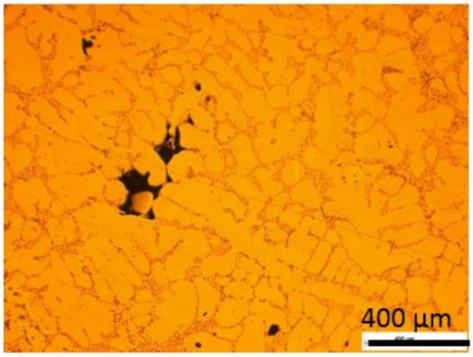

(a) Porous Al-Si alloy (Cast)

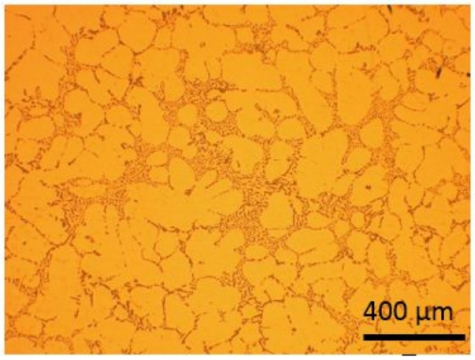

(b) Non-porous Al-Si alloy (Cast + HIP)

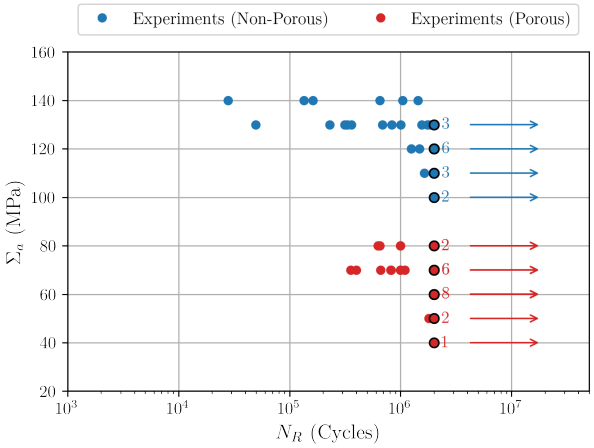

(c) High cycle fatigue lifetimes

Figure 1.1: Microstructural features governing high-cycle fatigue lifetime: effect of micro scale heterogeneity and meso scale pores [Le, 2016]

2.2.1 Micro-scale defects

Heterogeneity at the microscopic scale affects lifetime [Morel et al., 2015, Le, 2016], and this effect becomes significant when meso-scale pores are small, i.e., comparable to grain size [Bracquart et al., 2018]. In such cases, the microstructure of the base material governs the fatigue lifetime of the structure. Key factors at this micro-scale include variations in grain size, orientation, and the presence of precipitates or oxides, whose size, morphology, and distribution may vary [Wang et al., 2001, Wang et al., 2023]. An example of microstructural heterogeneity in a cast Al-Si alloy is shown in 1.1(b), with corresponding lifetimes under tension-compression loading in 1.1(c). In non-porous alloys, where pores are closed by hot isostatic pressing, fatigue failure under tension-compression is mainly due to micro-plastic activity, such as persistent slip bands from which critical cracks originate [Le et al., 2016]. The absence of large pores leads to an increased fatigue limit. However, a significant scatter in lifetimes is observed, attributed to variability in microstructure across different specimens.

2.2.2 Meso-scale pores

The local stress level at the pore surface can be significantly higher than the macroscopic stress applied [Tijani et al., 2013, Le, 2016]. Studies have demonstrated a clear correlation between specific pore characteristics and the high-cycle fatigue lifetime of specimens or structures. An example of the microstructure of a porous cast Al-Si alloy is shown in 1.1(a), with the resulting lifetimes under tension-compression cyclic loading depicted in 1.1(c). Under these conditions of tension-compression fatigue loading, porous Al-Si alloys are known to fail due to crack formation from a surface-breaking pore, interactions between sub-surface pores and the surface of the specimen, or the coalescence of cracks originating from multiple pores [Le et al., 2016, El Khoukhi et al., 2022].

The presence of large porosity is associated with a shorter fatigue lifespan [Buffière et al., 2001, Yi et al., 2007, Koutiri, 2011], as are pores located closer to the surface of the structure [Le et al., 2018, El Khoukhi et al., 2019, Nadot, 2022]. Defects of similar size but differing morphology do not influence fatigue life equally. Synchrotron in-situ fatigue testing by [Serrano-Munoz et al., 2018] has shown that tortuous defects, due to their higher stress concentration factor, tend to induce earlier crack initiation compared to spherical defects of the same size. The orientation of porosity also plays a role, with more tortuous defects aligned perpendicularly to the loading direction negatively impacting fatigue life [Wicke et al., 2016, Qian et al., 2016]. Additionally, the presence of pore clusters, which facilitate interaction among pores, further reduces the fatigue lifetime [El Khoukhi et al., 2021b, Matpadi Raghavendra et al., 2024].

2.3 Conclusions

In this section, we emphasised the role of microstructural features in the variability in the HCF lifetime of metal alloys. A distinction was drawn between micro-scale heterogeneities and meso-scale pores. Pore characteristics, including pore size, morphology, presence of clusters,

and distance to the surface, were shown to affect fatigue lifetime. Additionally, we highlighted the potential to capture porosity data through tomographic scans, which provided either high-resolution morphological detail or information on density and clustering at lower resolutions. In the methodology that will be proposed in Chapter 2, high-resolution tomographic images will be used to predict the lifetime of porous alloys. Lastly, the use of infrared thermography for detecting pores via the self-heating method—an area relatively underexplored in the literature—will form the basis of Chapter 4.

3 Statistical approaches to high-cycle lifetime modelling in the presence of material defects

As outlined in the previous section, defects at micro and meso scales can provoke fatigue failure at the macro scale, i.e., that of the structure. The effect of micro-scale defects can be accounted for using a hypothesis of separation of scales, which will be presented in this section. At the meso scale, the defects responsible for failure are pores, for which two approaches can be employed: a similar separation of scales or the explicit modelling of pore distributions. This section aims to discuss some of the main approaches within these categories, with a focus on statistical methods in the latter case.

Additionally, we note that the focus will be on methodologies for modelling the high-cycle fatigue (HCF) lifetime of structures that adopt a decoupled approach concerning material behaviour. In these methods, the structure is analysed under the assumption that damage does not affect its behaviour.

3.1 Weakest link Weibull approach

We will first explain the concept of weakest link scaling [Zok, 2017]. The survival probability of a solid with volume V is the product of survival probabilities of each volume element $* \in \mathcal{E}$ where $\mathcal{E}$ is the set of elements within the solid. This is written as:

$$S = \prod_{* \in \mathcal{E}} S^*(\sigma) \tag{1.1}$$

which, when taking logarithms, becomes

$$\ln S = \sum_{* \in \mathcal{E}} \ln S^*(\sigma) \tag{1.2}$$

for the particular case that the stress is uniform throughout the body:

$$\ln S = N \ln S^*(\sigma) \tag{1.3}$$

where N is the number of elements in the volume. $N = V/V_0$ if each element has volume V_0. The failure probability $F = 1 - S$ becomes:

$$F = 1 - \{\exp(\ln S^*(\sigma))\}^{V/V_0} \tag{1.4}$$

The expression for the survival probabilities of the constituent elements $\ln S^*(\sigma)$ is independent of weakest link theory.

The weakest link Weibull model arises from the choice of $\ln S^*(\sigma)$ that results in a Weibull distribution for the failure of the solid. Weibull suggested that $\ln S^*(\sigma)$ could be taken as a two-parameter power law, on the basis that the function made physical sense, i.e. $S^*(\sigma) = 1$ when $\sigma = 0$ and $S^*(\sigma) \to 0$ when $\sigma \to \infty$ [Weibull, 1951]:

$$\ln S^*(\sigma) = -\left(\frac{\sigma}{\sigma_0}\right)^m \tag{1.5}$$

This can be expressed as a failure probability $F^* = 1 - S^*$:

$$F^* = 1 - \exp - \left(\frac{\sigma}{\sigma_0}\right)^m \tag{1.6}$$

The combination of equation (1.2) for the weakest link with the equation (1.5) of the power law gives the failure probability of the solid, in the case of non-uniform stress in the body:

$$F = 1 - \exp\left(\sum_{*\in\mathcal{E}} -\left(\frac{\sigma}{\sigma_0}\right)^m\right) \tag{1.7}$$

Similarly, the combination of equation (1.4) for the weakest link with the equation (1.5) of the power law of Weibull gives the failure probability of the solid, in the case of uniform stress in the body:

$$F = 1 - \left\{\exp - \left(\frac{\sigma}{\sigma_0}\right)^m\right\}^{V/V_0} \tag{1.8}$$

Equations (1.7) and (1.8) represent the weakest link Weibull models for non-uniform and uniform stress in the body, respectively. Instead of stress, other mechanical quantities can be employed to describe failure probabilities, such as damage [Liu et al., 2020, Li et al., 2022]. A lifetime model that establishes the number of cycles N as a function of stress or other mechanical quantities is necessary to convert the failure probability $F(\sigma)$ to $F(N)$ through a transformation of variables. The weakest link scaling has been extensively used to obtain the probability of failure of notched components, utilising the finite element method (FEM) to obtain the non-homogeneous stress distribution by considering piece-wise constant stress in each finite element [Qvale and Härkegård, 2017, Li et al., 2022].

Furthermore, as the weakest-link model is sensitive to Weibull parameters, robust identification procedures are necessary. One specific paper by [Liu et al., 2020] employs Bayesian calibration while using the finite element method to calculate the summation term in equation (1.7). The procedure is detailed in Figure 1.2. Here, the lifetime model is limited to the low-cycle

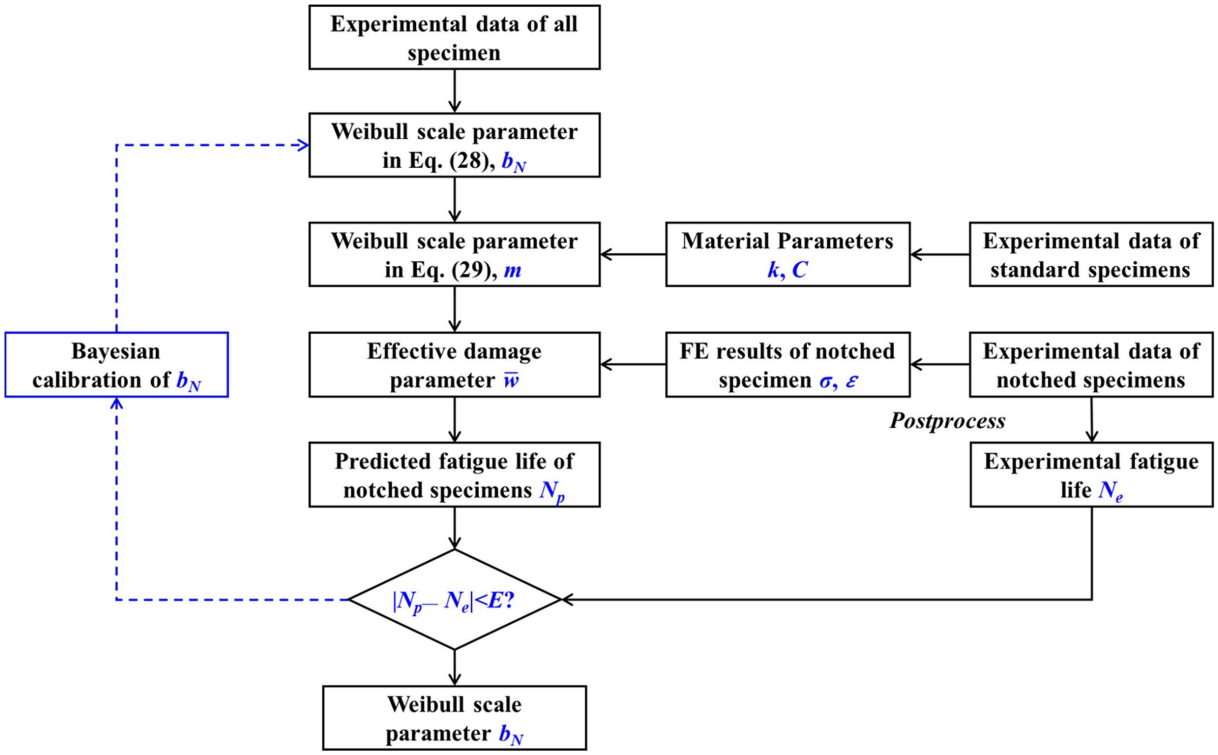

Figure 1.2: Bayesian method to calibrate the shape parameter (denoted here as b_N) of a weakest link Weibull lifetime model on smooth and notched specimens, with the optimization using 3D stress-strain fields of notched specimens obtained by FE [Liu et al., 2020]

fatigue (LCF) regime:

$$(w^*)^k N^* = C \tag{1.9}$$

In this equation, instead of stress, damage is calculated using the Smith-Watson-Topper criteria [Smith et al., 1970], which is based on the total strain range and maximum equivalent stress, where $w^* = \Delta\varepsilon^* \sigma^{\max *}$ in each element $*$. The effective damage parameter $\bar{w}$ is then computed by summation over the elements $* \in \mathcal{E}$. The weakest link Weibull model for the failure probability of a non-smooth specimen, expressed as the number of cycles to failure N, is given by:

$$F(N) = 1 - \exp\left(-\left(\frac{N}{C/\bar{w}^k}\right)^{b_N}\right) \tag{1.10}$$

The lifetime model parameters k and C are pre-identified on specimens with uniform stress, and these parameters are not optimised during the Bayesian procedure. Thus, a shortcoming of this procedure is that the calibration of the lifetime model parameters k and C was not conducted jointly on both smooth and notched (non-smooth) specimens.

We observe an interesting benefit related to the lifetime model used here: even if k and C were included in the optimisation process, the summed effective damage parameter $\bar{w}$, being independent of the lifetime parameters k and C, would not need to be re-computed during the optimisation process. Chapter 2 will demonstrate that this decoupling of the lifetime computation and the summation over elements cannot always be achieved (for example, in the case

of the more general strain-life model that models low-cycle fatigue (LCF) and high-cycle fatigue (HCF)), resulting in a significant increase in optimisation time due to the necessity of recomputing the sum over elements for a new set of test parameters at every iteration.

While the optimisation procedure for the weakest link Weibull lifetime model presented here is designed to work with 3D fields of given geometries (notched specimens), no literature has been found that utilises the weakest link scaling to identify the lifetime of porous specimens, where the pores are explicitly modelled using the finite element (FE) method. When the internal pore geometries and locations are known for every porous specimen cycled to failure, a similar procedure to [Liu et al., 2020] could be employed, where, instead of notched specimens, one could use FE equivalents of each porous specimen. However, when the internal pore geometries and locations in the porous specimens are unknown, alternative methods are required. In Chapter 2, we will address these cases with our new proposal.

3.2 Statistical methods involving a separation of scales

A deterministic two-scale model was developed by [Lemaitre et al., 1999] to explain HCF behaviour. The authors consider that at the meso-scale, the behaviour is elastic, and the material's yield stress, σ_y, is not reached in HCF. At the micro-scale, defects are present and treated as weak inclusions embedded in the material (see Figure 1.3(a)). Their behaviour is elasto-plastic, coupled with damage, and their yield stress is denoted as $\sigma_y^{(s)}$. The scale transition from meso-scale to micro-scale, governed by a modified Eshelby-Kröner localisation law, connects the micro-stresses and strains to the meso-scale stresses and strains:

$$\underline{\underline{\sigma}}^{(s)} = \underline{\underline{\sigma}} - aE\underline{\underline{\varepsilon}}^{(s)p} \tag{1.11}$$

where a is a function of the Poisson ratio and is derived from Eshelby's analysis of a spherical inclusion. With certain assumptions (no coupling between damage and elasticity, proportional loading, etc.), the damage rate at the micro-scale is expressed in terms of elastic variables at the meso-scale. Based on a critical value of damage, closed-form expressions for the fatigue lifetime are obtained.

The stochastic micro-inclusion model [Doudard et al., 2004, Doudard et al., 2005] employs the concept of separation of scales proposed by [Lemaitre et al., 1999] and renders the lifetime probabilistic. It assumes that the fatigue lifetime of a homogeneously loaded specimen, as observed at the macro scale, is governed by an underlying stochastic damage process at the micro-scale. A Poisson process is assumed for the appearance of micro-inclusions in a volume that follow a kinematic hardening law beyond their yield stresses. The intensity of their appearance is a power law of the applied stress amplitude (see Figure 1.3(b)), and the weakest link hypothesis is used to describe rupture, resulting in a Weibull distribution of the yield stress of the weakest inclusion, i.e. $\Sigma_\infty \sim \mathcal{W}(\lambda, m)$, where m is the Weibull shape parameter controlling the spread of the distribution. Several fatigue lifetime criteria exist, based on a critical value of either the dissipated energy at a site or the cumulative plastic strain at a site, which is considered to govern the fatigue lifetime N_R in a given volume [Doudard et al., 2004, Desmorat et al., 2007,

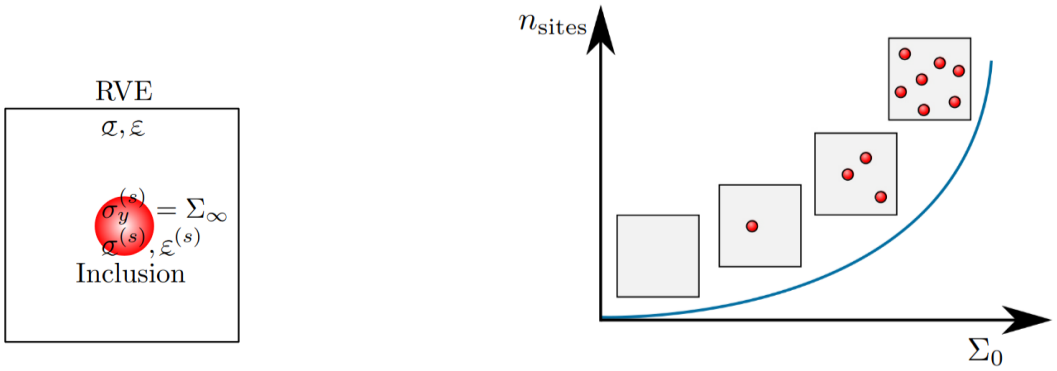

(a) RVE for material's HCF behavior, with a spherical weak inclusion

(b) Point Poisson Process for the number of active sites as a power law of cyclic loading amplitude Σ_0 (image inspired from [Doudard et al., 2005, Bercelli et al., 2021])

Figure 1.3: Principle of the probabilistic two-scale micro-inclusion model for HCF modelling [Doudard et al., 2004, Doudard et al., 2005]

Ezanno et al., 2013]. For example, if the dissipation due to a linear kinematic hardening law is considered [Doudard et al., 2004], the expression for N_R becomes:

$$N_R = \frac{A}{\Sigma_\infty \langle \Sigma_0 - \Sigma_\infty \rangle} \tag{1.12}$$

As Σ_∞ follows a Weibull distribution, N_R, obtained using a transformation of variables, is also probabilistic. An example of the probabilistic curve is shown in Figure 1.4. The parameters of the lifetime model can be identified purely through the analysis of fatigue experiments or through a combination of self-heating and a reduced number of fatigue experiments (see section 3.4 for more details or Chapter 5 for a numerical example).

The approach has been applied to a cast copper-aluminium alloy with small pores (mean size

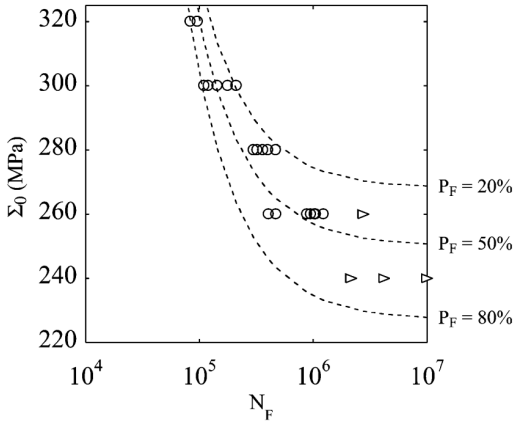

Figure 1.4: Probabilistic lifetime model for the prediction of HCF behavior of a healthy material, developed in [Doudard et al., 2004]

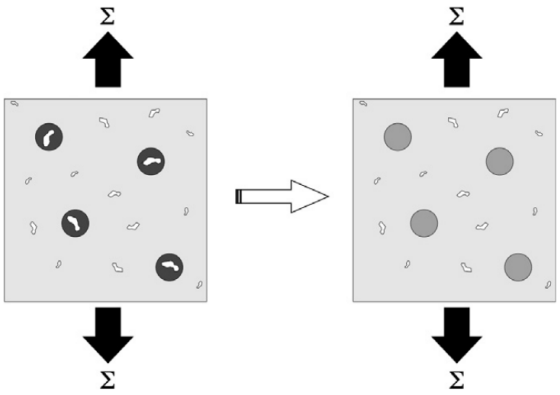

Figure 1.5: Elasto-plastic sites to represent plasticity around a certain number of casting defects under an external loading [Ezanno et al., 2013]

around 15 μm) [Ezanno et al., 2013]. The pores resulting from the casting process are considered indirectly by assuming that an elasto-plastic inclusion serves as a homogenised representation of a pore with a surrounding elasto-plastic zone (see Figure 1.5). A kinematic and isotropic hardening law is employed for the elasto-plastic inclusion, based on macroscopic material behaviour. Parameters are introduced to incorporate the effects of mean stress and hydrostatic pressure. A critical value of accumulated plastic strain is considered for failure, leading to a slightly different expression for N_{R}. However, this approach simplifies the analysis of pores by treating the porous material as a homogenised substance with equivalent fatigue properties, thus avoiding the direct description of individual pores. Such a model is not transferable to structures containing a different pore population, i.e. those made of alloys with the same base material but differing pore characteristics (sizes, density, etc.). Furthermore, for certain materials with large isolated pores, the method of assimilating pores to active elasto-plastic inclusions is not feasible [Bercelli et al., 2021].

We will now, in some detail, show the most recent approach by [Bercelli et al., 2021], which re-uses ideas from [Doudard et al., 2005, Ezanno et al., 2013]. Here, the two-scale probabilistic micro-inclusion model operating on a separation of scales is used to describe the fatigue behaviour of healthy samples, and the effect of pores is taken into account by explicit modelling of the pore populations (this part will be discussed in section 3.3). The model is briefly described here. For a given volume V experiencing equivalent stress amplitude Σ_0^{eq} (note that this is different from the uniaxial stress amplitude Σ_0, as multi-axiality is taken into account), it is assumed that the probability of having k active microplastic sites, which are seen as elasto-plastic inclusions, is modelled by a random variable X, and follows a Poisson process with intensity Λ [Doudard et al., 2005]:

$$\mathrm{Prob}(X = k) = \frac{\Lambda^k}{k!} \exp(-\Lambda) \tag{1.13}$$

where the intensity of the Poisson process Λ is assumed to be a power law of the equivalent stress

Σ_0^{eq} experienced by volume V and the mean hydrostatic pressure p_{m} [Ezanno et al., 2013]:

$$\Lambda = \frac{V}{V_0}\left(\frac{\Sigma_0^{\mathrm{eq}}}{S_0 - \alpha^{\mathrm{eq}} p_{\mathrm{m}}}\right)^m \tag{1.14}$$

where m, $V_0 S_0^m$, and α^{eq} are parameters of the model that govern the relation between the intensity of the process and the stress. A weakest link approach is used, i.e. failure of one site leads to the failure of the volume, which leads to a Weibull distribution for the weakest site, i.e. $\Sigma_\infty \sim \mathcal{W}\left(\lambda = \left(\frac{V_0(S_0 - \alpha^{\mathrm{eq}} p_{\mathrm{m}})^m}{V}\right)^{1/m}, m\right)$.

To express this density in terms of the number of cycles to failure N_R, a criterion [Ezanno et al., 2013] that considers crack initiation and rupture to be governed by a critical value of accumulated plastic strain in the micro-inclusions [Desmorat et al., 2007] is taken. The fatigue lifetime is considered to be finite if the weakest inclusion has a yield stress less than the equivalent stress amplitude Σ_0^{eq} experienced by the loaded volume, and infinite otherwise. Owing to the probabilistic nature of the appearance of the weakest inclusion, the fatigue lifetime is also probabilistic and is modelled as a random variable.

$$N_{\mathrm{R}} = \begin{cases} \frac{A}{(\Sigma_0^{\mathrm{eq}} - \Sigma_\infty)^2}, & \text{if } \Sigma_\infty < \Sigma_0^{\mathrm{eq}} \\ +\infty, & \text{if } \Sigma_\infty \geq \Sigma_0^{\mathrm{eq}} \end{cases} \tag{1.15}$$

Again, this model can be identified purely on fatigue experiments, or on fatigue and self-heating experiments. Refer to section 3.4 for the identification process proposed by the authors involving self-heating.

In [El Khoukhi et al., 2019], the authors propose an approach incorporating fractographic analysis of critical pores. The experimental campaign employs the staircase method to build a fatigue lifetime database from a set of specimens. Fracture surface analysis is conducted on each specimen to determine the thickness of a 'Fatigue Active Volume (FAV)' and the size of the critical defect. A Kitagawa-Takahashi diagram is created to relate fatigue strength—interpolated from experimental loading—to critical defect size.

Pore fields are generated N times in the FAV using a Poisson point process, with sizes based on CT scan analysis. The critical defect is defined as the largest defect within the FAV, and the distribution of critical defects due to N generations is derived accordingly. The Kitagawa-Takahashi diagram is used to obtain the fatigue strength distribution from the critical defect size distribution.

The model accounts for size effects, with larger specimens having a higher likelihood of containing larger defects. However, this trend stabilises, indicating the presence of a representative volume element (RVE). However, this approach assumes only pores are responsible for fatigue failure. Furthermore, the approach also requires lengthy fractography analysis to establish the Kitagawa-Takahashi diagram, and provides the fatigue strength distribution only. On the other hand, the approach remains sensitive to certain characteristics of pore populations important to fatigue lifetime: the size and density of pores, but not the morphology. Also, it assumes that a singular critical defect is responsible for fatigue failure, and thus neglects interaction between

pores, and surface-pore interaction effects.

The authors in [Romano et al., 2019] model the component (with elastic behaviour) using the FE method, without pores. A Poisson process is used to generate pore centres in 2D or 3D within a volume element. The sizes of these pores (square root of the area of the pores) are assigned using a Monte Carlo simulation, derived from reference tomography data. The volume of each element, along with the stress at the pore centres (at the element's centre), is obtained from the FE analysis without pores. For each volume element, a critical pore size a_{cr} is determined using the Kitagawa-Takahashi diagram, using the stress obtained from the FE analysis without pores.

The pore generation process allows for the creation of a pore size distribution, from which a 'maximum' pore size is calculated using extreme value statistics. If the extreme pore size value of the generated pore distribution exceeds a_{cr}, the volume element is deemed to fail; otherwise, it survives. The component's failure is determined using a weakest-link approach, where the failure of any individual volume element leads to the failure of the entire component. The process is shown in Figure 1.6. This approach, however, does not account for the interaction between pores and pore-surface interaction, and, as acknowledged by the authors, fails to obtain an accurate lifetime distribution in the event of a cluster of pores.

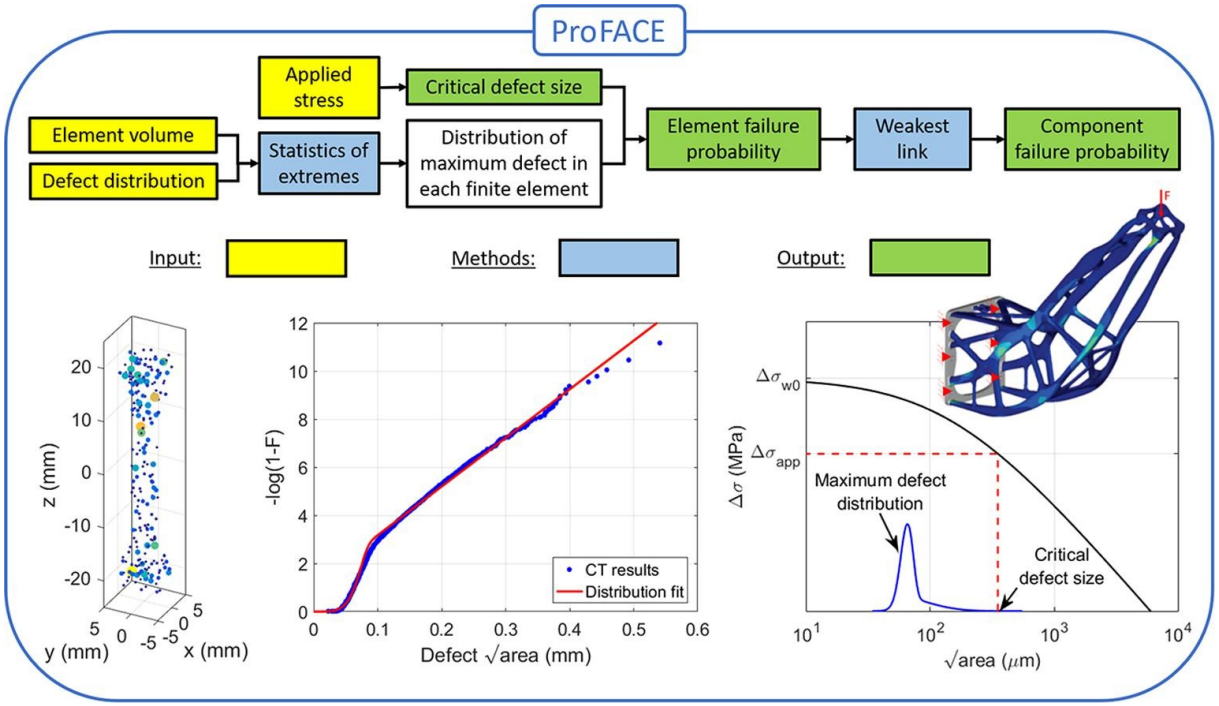

Figure 1.6: A statistical approach to take porosity into account using a separation of scales, for lifetime prediction [Romano et al., 2019]

3.3 Statistical methods involving explicit representation of pores

Certain approaches explicitly represent the geometry of the pores in the structure, and use a criterion to predict the fatigue lifetime. These could be either deterministic or probabilistic ap-

proaches. The explicit representation of the pores requires special attention for the choice of lifetime criterion, as the local loading state in the structure in the vicinity of pores could induce plasticity even if the global loading is in the elastic regime. Complex loading conditions and multiaxiality effects on fatigue lifetimes are usually taken into account via criteria selected according to application (form of cyclic loading, regime and proportionality of loading, presence of plasticity [Coffin, 1954, Maurel et al., 2009, Lacourt, 2019], presence of mean stresses [Morrow, 1968, Smith et al., 1970], multiaxiality [Papadopoulos, 1993, B., 1956, Dang-Van et al., 1982] etc). On the other hand, applying these criteria to the maximally stressed point (singularity) in the specimen usually requires an impractical level of mesh refinement to correctly resolve the stresses, and generally under-estimate the lifetime [Lacourt, 2019]. This is why non-local methods from the theory of critical distances (TCD) are employed [Taylor, 1999, Adib and Pluvinage, 2003]. Some of these approaches introduce a length scale to average the criterion values around the critical points, thus reducing the under-estimation of lifetime. These approaches also have the advantage of bypassing the requirement for a sufficiently refined mesh to resolve the criterion.

Statistical approaches involving explicit representation of pores are inherently difficult tasks, as the number of degrees of freedom rapidly increases with the number of simulations performed. Furthermore, in this case, a method for generating physically accurate pore distributions in the structure is required. This can be achieved either by using defect size and density information [Hou et al., 2024], drawing from a library of pre-imaged defects [Lacourt, 2019], or by employing methods that combine clustering measures and machine learning [Matpadi Raghavendra et al., 2023]. Through this statistical study, configurations of pores that result in low lifetime can be identified in advance, and uncertainty in lifetime due to varying pore distributions can be taken into account. This section will present a few state-of-the-art approaches in this category and detail the processes used for identifying the lifetime model.

In the approach by [Hou et al., 2024], FE models containing random porosity were generated to examine the impact of surface roughness and arbitrary distributions of subsurface porosities on stress concentration and fatigue response in as-built additive manufacturing (AM) parts. Elasto-plastic material behaviour was considered. The lifetime model is based on continuum damage mechanics (CDM), which provides the lifetime as a function of the effective stress amplitude σ_{eff}:

$$N_{\text{R}} = \frac{1}{(1+m)} \left[\frac{\sigma_r}{\Delta\sigma_{\text{eff}}} \right]^m \tag{1.16}$$

where the effective stress amplitude is computed using an area method from a tailored theory of critical distances (TCD):

$$\Delta\sigma_{\text{eff}} = \frac{2}{\pi L^2} \int_0^{\pi} \int_0^{L} \Delta\sigma_1(r,\theta) r \, dr \, d\theta \tag{1.17}$$

where L is a critical distance from the notch, computed based on linear-elastic theory of critical distances (TCD), and is a function of the threshold stress intensity factor and the range of fatigue strength. From each finite element (FE) simulation, a scalar $\Delta\sigma_{\text{eff}}$ can be extracted. The calibration of the lifetime model parameters σ_r and m is conducted using a simple 0D power law fitting on the experimental data points of machined specimens, i.e. those without

surface roughness and significant subsurface porosity, which can therefore be considered healthy (see the experimental data and dotted red line in the S-N graph in Figure 1.7).

Using such an approach, the authors are able to examine the conditions that lead to an improvement or decrease in the lifetime caused by notch-porosity interactions. In Figure 1.7(b), the lifetime results of 200 finite element (FE) simulations across several stress levels, for each of the three different notch geometries, are plotted in the Wöhler curve, which allows for the construction of an accurate uncertainty interval for the failure of the part. Certain simulations are highlighted, corresponding to the over- or underestimation of the lifetime compared to a porosity-free case. The improvement in lifetime is attributed to the presence of compressive stresses, which reduce the effective stress in the TCD region.

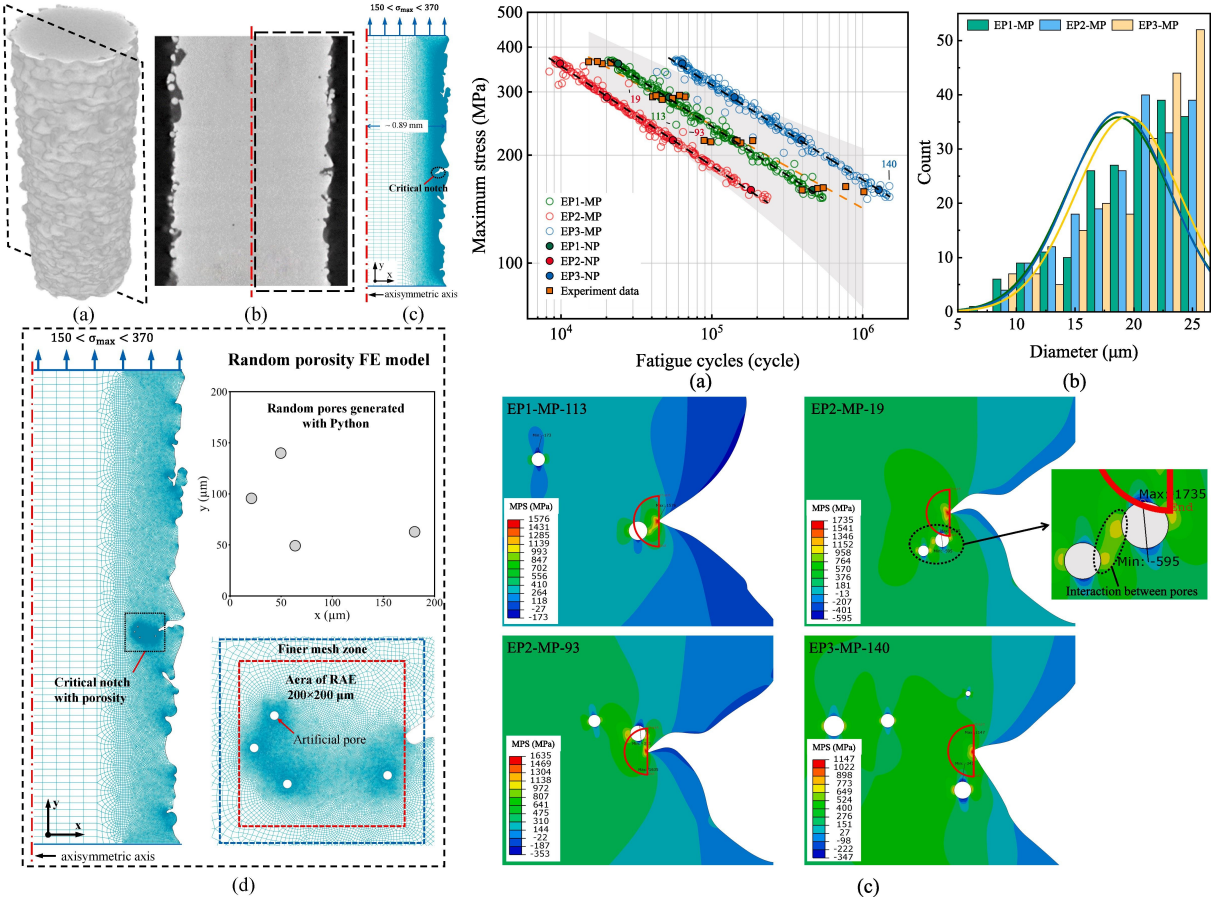

(a) Image-based generation of finite element meshes one of three notches induced by surface roughness, with random subsurface porosity

(b) Top: Lifetime uncertainty due to variability in surface roughness induced notches (3 notches) and variability in subsurface porosity (200 pore configurations per notch). Bottom: simulation images showing the cases that result in low lifetime (due to pore-notch interaction in TCD) or high lifetime (due to lowering of effective stress in TCD)

Figure 1.7: Random subsurface porosity modelling using surface profiles from X-ray tomography in a Ti6Al4V part manufactured with the powder bed fusion process [Hou et al., 2024]

A similar approach by [Lacourt, 2019] explicitly models the pores, this time in 3D geometries. The lifetime model is a type of strain-life model, originally proposed by [Manson, 1953,

Coffin, 1954] for symmetrical uni-axial tests controlled in deformation [ASTM, 2015]:

$$\frac{\Delta\varepsilon}{2} = g(N_{\mathrm{R}}) = A(N_{\mathrm{R}})^{-\alpha} + B(N_{\mathrm{R}})^{-\beta} + C \tag{1.18}$$

where A and α correspond to the parameters of the low-cycle fatigue (LCF) line, B and β correspond to the parameters of the high-cycle fatigue (HCF) line and C controls the fatigue limit. The criterion of equation (1.18) is modified to a Smith Watson Topper type criterion [Smith et al., 1970]:

$$Q_{\mathrm{eff}} = \sqrt{E\frac{\Delta\varepsilon}{2}\frac{\Delta\sigma}{2}}\, f_\sigma\left(\frac{\Delta\sigma}{2}, \sigma_m\right) \tag{1.19}$$

where f_σ is a parameterized function to take into account the effects of mean stress on the lifetime [Dowling, 2003], and is determined by data of several sets of experiments conducted at different mean stresses. This criterion is extended to multi-axial loading states, by applying it to the stress $\underset{\sim}{\sigma}$ and strain $\underset{\sim}{\varepsilon}$ tensors, where the amplitudes (e.g. $\Delta\varepsilon$) correspond to the radii of the hyperspheres (in six dimensions) circumscribed around the tensor trajectories throughout the stabilized cycle. The lifetime model and the material behavior is first calibrated on the base material without pores.

When pores are present, a volumetric non-local method is used to compute the average of a quantity of interest Q at a point x_0 using its neighbourhood. This average $\hat{Q}$ is used for the computation of the criterion (Q here denotes the stress and strain tensors):

$$\hat{Q}(x_0) = \frac{1}{\int_\Omega \phi(x_0, x)\, d\Omega} \int_\Omega Q(x)\phi(x_0, x)\, d\Omega \tag{1.20}$$

where $\varphi(x_0, x)$ is a kernel centred at x_0, involving the characteristic length l, taken as:

$$\phi(x_0, x) = \begin{cases} 1 & \text{if } \|x_0 - x\| \leq l \\ 0 & \text{otherwise} \end{cases} \tag{1.21}$$

The characteristic length is determined from an experiment on a specimen with 44 controlled holes of a given size typical for pores. The number and length of cracks originating from these holes are recorded by periodically interrupting the experiment. The specimen's lifetime is defined as the number of cycles required for a percentage of the cracks to reach a critical length of $a_c = 200$ μm. A simplified version of the specimen with holes is simulated, and the lifetime is computed by varying the characteristic length l in equation (1.21). The characteristic length that yields the closest lifetime to the experimental result is selected. Figure 1.8(a) shows the effective stress field $\hat{\sigma}_{\mathrm{eff}}$ after the averaging operation with the identified l.

The maximum value of the criterion in the vicinity of each pore is extracted within a sphere centred on the pore, with a radius twice that of the pore itself. This value is then used to calculate the local lifetime associated with each pore (see Figure 1.8(b)). By representing the lifetime of each pore in the pore size vs normalised distance-to-surface plane (see Figure 1.8(c)), the authors note certain interesting tendencies:

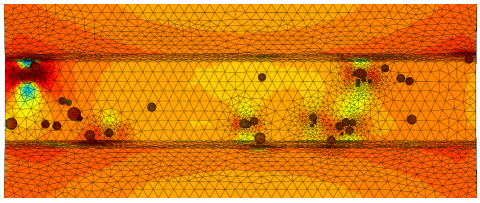

(a) $\hat{\sigma}_{\text{eff}}$ after averaging operation on stress field with a characteristic length l

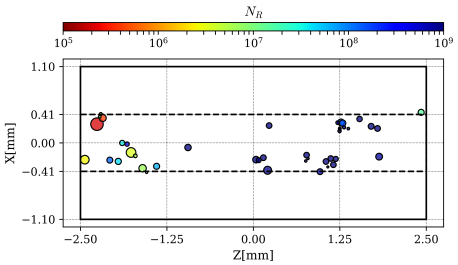

(b) Lifetime computed for each pore using the maximum strain-life criterion after the averaging operation

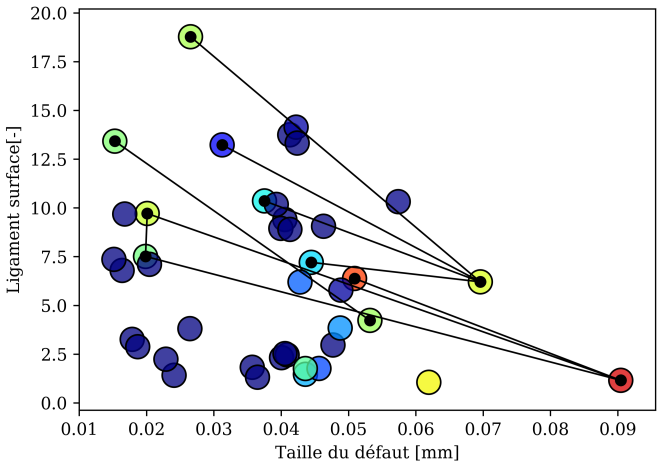

(c) Representation of pores in the pore size (x) vs normalised distance-to-surface (y) plane. The colour scheme is the same as Figure 1.8(b). Neighbouring relationships (black lines) are shown for defects with small lifetimes. The material ligament between two defects connected by a black line has a length shorter than the sum of their radii.

Figure 1.8: Illustration based on [Lacourt, 2019]

1. Certain small pores have a shorter lifetime due to being in the interaction zone of a larger pore

2. For a given normalized distance of the pore to the surface, a smaller lifetime is found for bigger pores

3. For a given pore size, a smaller ligament between the pore and the surface leads to smaller lifetimes.

A statistical study was carried out, where lifetime computations were done with random populations of spherical pores (a total of 10 simulations). The resulting lifetimes are overestimated (see Figure 1.9). In all cases, a smaller fatigue life is explained either by the size of the defect, its proximity to a free surface, or its proximity to another defect.

If any material point presents ratcheting behavior, i.e. no stabilization of the hysteresis loops, the strain-life criterion can wrongly overestimate the fatigue lifetime. The authors thus implement a method which evaluates progressive deformation due to k cycles:

$$\varepsilon_{\text{prog}} = \sum_{k=1}^{M} \delta\varepsilon_{22}^{p}(k) \tag{1.22}$$

where $\delta\varepsilon_{22}^{p}(k)$ is the plastic strain increment at the k^{th} cycle corresponding to the direction of the traction loading, described by a decreasing exponential function. This progressive deformation is compared to a user-defined maximal value $\varepsilon_{\max}$ at which the material is considered to fail. The final lifetime is taken as a minimum between the two computed lifetimes, i.e. the strain-life

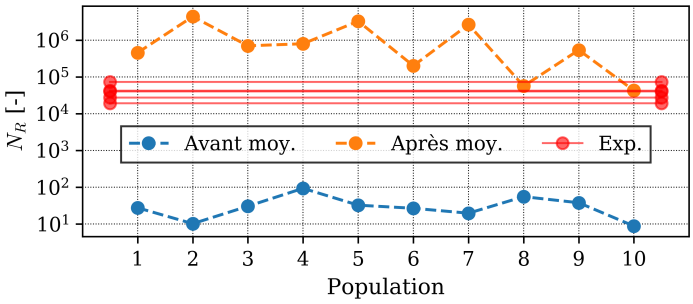

Figure 1.9: Lifetime computed for a specimen with 10 different pore populations (orange: after the averaging operation, blue: before the averaging operation). The experimental data for porous specimens is represented in red.

criterion on non-local quantities, and the lifetime due to ratcheting.

In the approach presented in [Bercelli et al., 2021], the lifetime scatter of healthy material was taken into account by a separation of scales (refer to section 3.2). The authors model the effect of pores on lifetime uncertainty by explicit representation of the pores. Numerical porous sampled are generated on which FE simulations are carried out, which are used along with the previously identified probabilistic micro-inclusion model operating on a separation of scales to obtain individual Wöhler curves. These are combined to get a general trend. Σ_0^{eq} becomes the nominal loading, and inputs to the model change in the porous case:

$$\Sigma_\infty \sim \mathcal{W}\left(\lambda = \left(\frac{V_0(S_0 - \alpha^{\text{eq}} K_t p_{\text{m}})^m}{K_t^m V_{\text{eff}}}\right)^{1/m}, m\right) \tag{1.23}$$

where K_t is the stress concentration factor due to a pore, and V_{eff} is the volume with a homogeneous stress $K_t\Sigma_0^{\text{eq}}$, which has the same probability of failure as the porous structure. This is computed as:

$$V_{\text{eff}} = V^{\text{hom}} \frac{1}{K_t^m} + V_{\text{eff}}^{\text{zoom}} \tag{1.24}$$

where V^{hom} is the part of the volume of the porous structure where stress is homogeneous, and $V_{\text{eff}}^{\text{zoom}}$ is the part of the volume around the pore where there is a stress gradient, which needs FEA computation to identify. The knowledge of stress state in the structure allows for computation of its lifetime distribution via equation 1.15. The authors explain that V_{eff} is different for each pore, i.e. a smaller pore with high k_t may not have a significant impact on fatigue lifetime due to a low $V_{\text{eff}}^{\text{zoom}}$ and therefore lower V_{eff}.

A number of elasto-static finite element computations with a single spherical pore, at select values of pore size D and pore distance to surface d_e are computed, and corresponding K_t and V_{eff} are computed. D is drawn from a beta distribution that is fitted from tomographic imaging of pores, and is bounded. For any other combination of D and d_e, the values of K_t and V_{rm} are able to be interpolated based on the computed database. K_t and V_{rm} together give the criticality of the pore in the structure, and are sufficient for evaluating the lifetime probability. The effect of multiple pores is taken into account by considering them as independent sources

of stress concentrations, and thus computing a combined V_{eff} from all the pores, and taking the maximum value of K_t over all the considered pores. This, of course, assumes no interaction between pores. Furthermore, the morphology of the pores is considered spherical, while the actual pore population has varying values of sphericity. This assumption is useful for limiting FEA computation time.

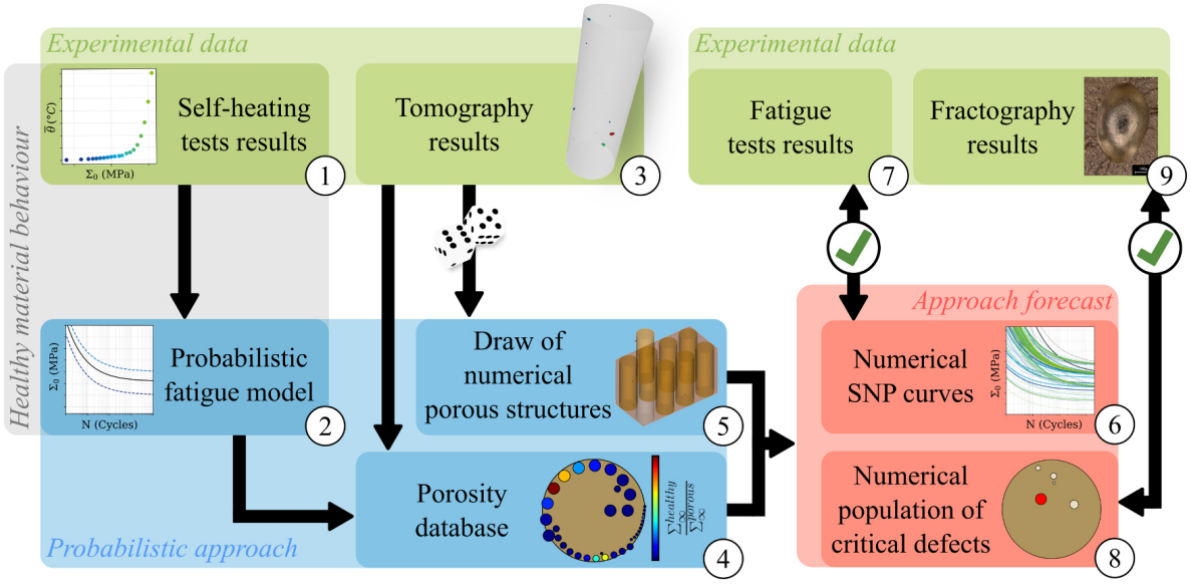

(a) Overview of the approach

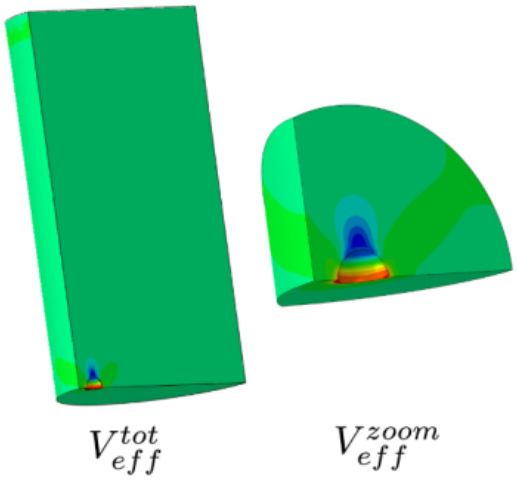

(b) $V_{\text{eff}}^{\text{zoom}}$ and k_t determined for a pore by FEA

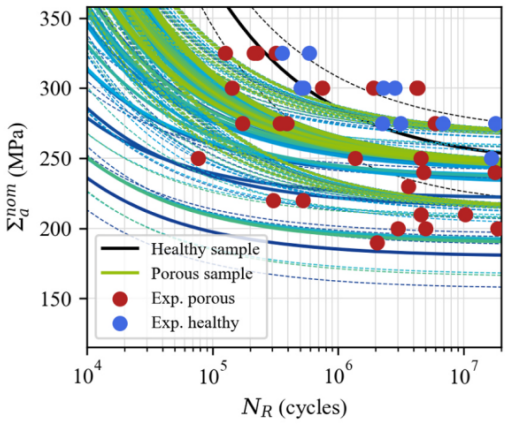

(c) Scatter in lifetime due to varying number of pores, pore sizes, and distance to surface, for a fixed value of pore density and maximum pore size

Figure 1.10: The approach developed by [Bercelli et al., 2021], that uses a seperation of scales approach (see section 3.2) to model the scatter in lifetime of healthy material, and explicit modelling of pores by FEA to characterize their effect

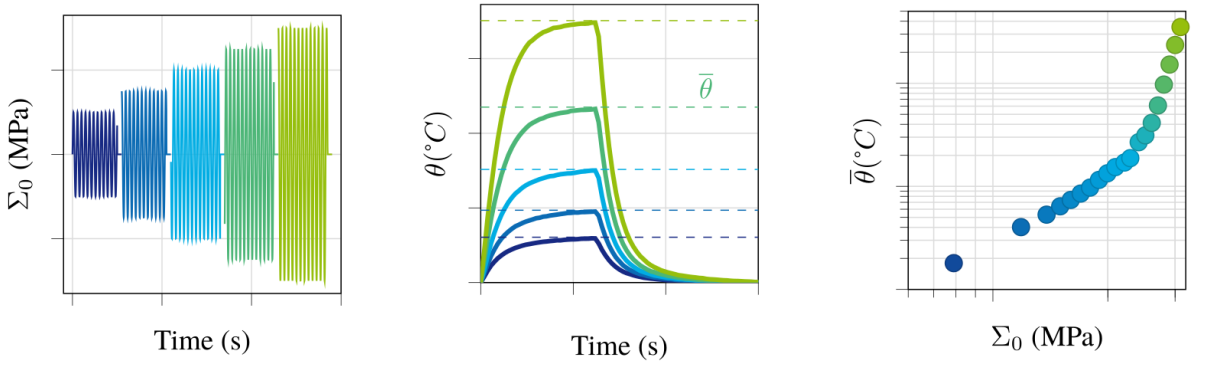

(a) Successive loading sequences with progressively higher Σ_0

(b) Temperature rise θ due to cyclic loading, with steady-state temperature rise denoted by $\bar{\theta}$

(c) $\bar{\theta}$ as a function of Σ_0, here showing the presence of two self-heating regimes

Figure 1.11: Illustration of the self-heating test protocol, taken from [Bercelli et al., 2021]

3.4 Self-heating for fatigue model identification

The phenomenon of rise in temperature within the material during cyclic loading is known as self-heating. The rise in temperature is due to energy dissipation due to degradation of the material. Several authors have shown, in the case of a strong change in the regime of intrinsic dissipation, a quantitative connection between self-heating and the fatigue limit can be made [Luong, 1995, La Rosa and Risitano, 2000, Wei et al., 2024].

The probabilistic model for the high-cycle fatigue lifetime based on a separation of scales [Doudard et al., 2004, Doudard et al., 2005], presented in section 3.2, can be partially identified on self-heating experiments. Specifically, certain parameters of the model, notably the one controlling the spread of scatter, can be calibrated using these experiments. This reduces the number of fatigue experiments needed for model calibration to approximately 10-15, in addition to self-heating experiments conducted on a single specimen. The process consists of identifying the fatigue limit Σ_∞ and Stromeyer law coefficient A on the Wöhler curve, and the Weibull parameter m controlling the dispersion on self-heating curves.

The general process of identification consists of obtaining a curve that relates temperature variation to the applied loading. The temperature variation $\theta(t) = T(t) - T_0$ of the specimen due to uniaxial cyclic loading with amplitude Σ_0 is obtained, where T_0 is the initial temperature before cyclic loading. Next, the steady-state temperature variation $\bar{\theta}$ is obtained typically after a few thousand cycles. This process is repeated for progressively higher Σ_0 (see figure 1.11. By relating the RVE dissipation due to the elasto-plastic micro-inclusions under cyclic loading to the steady-state self-heating temperature rise, the parameters of the model can be found. For [Doudard et al., 2005], this is a relation of the form $\bar{\theta} = f(\Sigma_0; m, h, V_0 S_0^m)$, where the function f is a power law, and h is a hardening parameter of the elasto-plastic sites. The parameters m and h are identified from the slope and intercept of the second regime of self-heating in the $\log(\bar{\theta})$ - $\log(\Sigma_0)$ graph. $V_0 S_0^m$ and the lifetime parameter A are identified by analysis of a few experiments in the Wöhler curve. A demonstration of this identification procedure will be

shown in more detail on a numerical example in Chapter 5, where the relative benefits of a new identification procedure proposed in this thesis will be examined.

For the identification of the model by [Bercelli et al., 2021] presented in sections 3.2 and 3.3, the $\bar{\theta}$ vs Σ_0 curve is obtained in the same fashion as previously described. This time, the relation between the steady-state self-heating temperature rise and the RVE dissipation is of the form $\bar{\theta} = f(\Sigma_0; m, K, h, V_0 S_0^m, \alpha^{\text{eq}})$, where the parameter K is an additional hardening parameter related to the matrix around the elasto-plastic sites, to be identified on the first regime of self-heating. The parameter α^{eq}, introduced by [Ezanno et al., 2013] to take into account the effect of varying stress ratios, is identified on multiple self-heating tests at different stress ratios. Similar to previous approaches [Doudard et al., 2005, Ezanno et al., 2013], the value of m is identified from the slope of the second regime of self-heating in the $\log(\bar{\theta})$ - $\log(\Sigma_0)$ graph. This time, $V_0 S_0^m$ is identified by imposing V_0 equal to the volume of the self-heating sample's gauge section and from the intercept of the second regime of the self-heating curve, thus not requiring analysis of the Wöhler curve. Similar to [Ezanno et al., 2013], A is identified by carrying the self-heating specimen to failure on the last highest value of Σ_0. It is worth noting that this approach, unlike the one by [Doudard et al., 2005], requires only one specimen for the identification of the lifetime model of healthy material. Nevertheless, a few more experiments at high Σ_0 will improve the confidence in estimation of the parameter A.

3.5 Conclusions

This section presented several approaches for high-cycle lifetime modelling in the presence of defects. In the presence of porosity, the approaches can be classified into two main types, i.e. those using a separation of scales and those explicitly representing pores. Approaches using a separation of scales, while being relatively fast to use, cannot account for a number of effects, including stress fields generated by pore-pore or pore surface interaction. In the second category (explicit representation of pores), most of the approaches occupy an intermediate position in terms of both complexity and fidelity in describing pore characteristics. These approaches assume a degree of randomness in the pore distribution in order to model the uncertainty in lifetime. This approach is required when the exact pore distribution is unknown.

However, identification of lifetime models when pores are explicitly modelled is usually done on the lifetime data of the base material, which is pore-free [Lacourt, 2019, Bercelli et al., 2021, Hou et al., 2024]. Chapter 2 will introduce a method of identifying the lifetime model directly on porous lifetime data, using a 3D procedure. The procedure is similar to the procedure for identifying the weakest link Weibull model on experimental data of notched components in [Liu et al., 2020], but has not been proposed yet for porous structures with uncertainty in pore distribution.

4 Methods for accelerated computation of lifetime criteria in the presence of non-linear material behavior

Computation of the behavior of structures under cyclic behavior is time-consuming, especially when non-linearity in material behavior is present. Coupled with the fact that fatigue criteria are generally computed on stabilised cycles, a method of acceleration of the computation time is useful. When the lifetime models need entire fields of this criteria, for example the approaches that involve explicit modelling of the pores presented in the previous section 3.3, it becomes almost a necessity. A large number of methods are available for this, however, we will focus on Neuber-type plastic correction methods that post-process the elasto-plastic results from an elastic solution, as this will elaborate the novelty of the contributions in Chapter 3 of this thesis. Cycle jump methods will also be presented for their particular usefulness for acceleration of the computation of long transitory material behavior.

4.1 Neuber-type plastic correction methods

Several types of plastic correction methodologies have been developed in the past to post-process the elasto-plastic response of structures from elastic finite element solutions. One family of methods uses homogenization theory, which consists in viewing the plastic zone as an inclusion in an elastic matrix and deriving local constraints to simulate the evolution of plastic quantities at the notch tip under load, starting from an elastic finite element solution [Herbland, 2009, Chouman et al., 2014, Levieil et al., 2019]. Another family of methods relies on the use of Neuber-type rules [Neuber, 1961, Herbland, 2009]. These rules are heuristics that relate the stresses and strains in an elasto-plastic body to those in a geometrically similar elastic body undergoing similar loading conditions. The section will focus on the development of Neuber-type rules.

The original Neuber rule was developed for a uni-axial stress state at a notch subjected to monotonic loading [Neuber, 1961]. Figure 1.12 illustrates the Neuber rule. An elasto-plastic body subjected to nominal loading Σ_a undergoes stress and deformation σ, ε. The approximate solution using the Neuber rule is denoted as $\hat{\sigma}, \hat{\varepsilon}$. An elastic computation is done on a body of the same geometry and subjected to the same loading, giving $\sigma^{\#}, \varepsilon^{\#}$. This permits the recovery of $\hat{\sigma}, \hat{\varepsilon}$ using the following rule:

$$\hat{\sigma}\hat{\varepsilon} = \sigma^{\#}\varepsilon^{\#} \tag{1.25}$$

in conjunction with a non-linear material behavior $\sigma = f(\varepsilon)$. The above equation of a hyperbola (1.25) implies that the area of the rectangle obtained by using the point $\hat{\sigma}, \hat{\varepsilon}$ is equal to the area using the point $\sigma^{\#}, \varepsilon^{\#}$, and that both these points are on this hyperbola.

Two extensions of this rule were proposed for cyclic loading. The first one [Topper et al., 1967] uses stress-strain amplitudes in equation (1.25) and uses the material's cyclic loading curve [Lee et al., 2011, Ladinek et al., 2018], and the other one [Chaudonneret and Culié, 1985] proposes a change of peaks method, which has the advantage of being able to take into account the presence of non-zero mean stresses in the nominal loading.

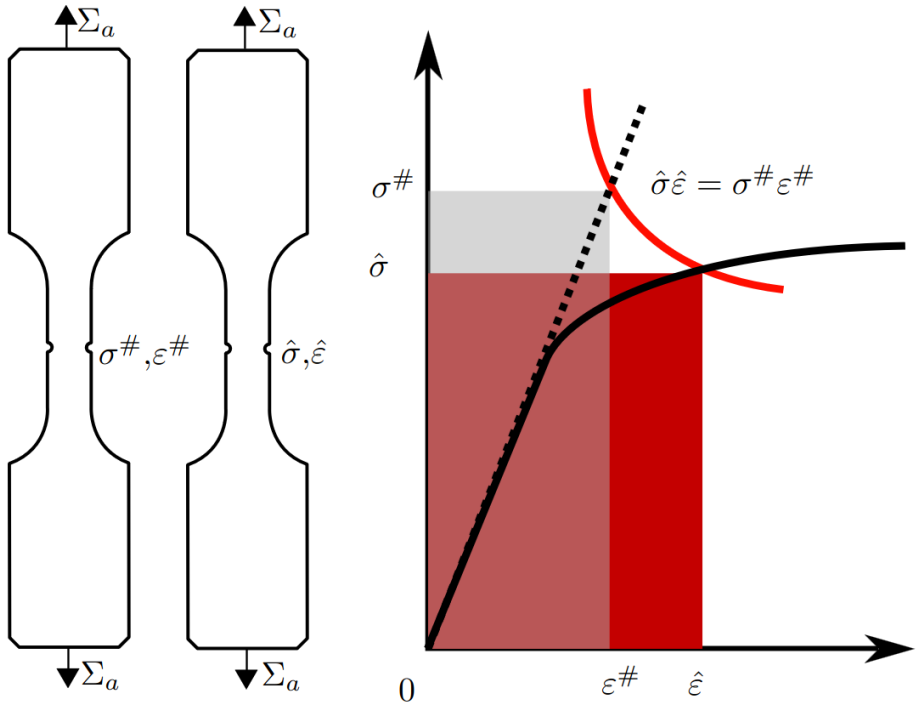

Figure 1.12: For uni-axial stress-strain states: an elastic computation (left), the approximated elasto-plastic computation (centre) using the Neuber rule (right)

This latter method re-applies the Neuber rule at every peak of cyclic loading, by performing a change of origin. Further details about this method will be given in Chapter 3.

Other Neuber-type methods like the Equivalent Strain Energy Density (ESED) approach [Molski and Glinka, 1981]) have been proposed, which make use of the area under the stress strain curves instead of the rectangular area. These rules have been generalized to multi-axial loading states at notch tips. In the multi-axial case, some sort of additional heuristic on the evolution of the stress or strain is needed to obtain a closed set of equations permitting the recovery of the approximated elasto-plastic solution. Another type of plastic correction method, using a modification of the radial return method considering effective parameters in lieu of initial elastic tensor, has been proposed in [Antoni, 2019], with full-field comparisons on structures showing good performance for a variety of multi-axial boundary value problems, even when the plasticity is non-confined.

One sub-family of Neuber-type methods for multi-axiality is based upon independently employing Neuber-type rules for every scalar component of the stress and strain tensors [Buczynski and Glinka, 2003, Ince and Glinka, 2013]. The other sub-family of Neuber-type approaches reduces the complexity of the previous approach by employing variations of proportional evolution rules for the stress tensor, strain tensor, or for a combination of stress and strain [Hoffmann and Seeger, 1985, Moftakhar et al., 1994, Desmorat, 2002, Ye et al., 2008, McDonald and Socie, 2011]. These existing pieces of work concentrate specifically on the development of Neuber-type plastic correction methods for the prediction of multi-axial stress and strain states at notch tips. All of these approaches report over-estimation of the elasto-plastic

solution when using the Neuber rule, and under-estimation when using the ESED rule. One specific piece of work by Desmorat et al. [Desmorat, 2002] suggests using locally proportional evolutions together with Neuber-type rules to predict the evolution of elasto-plastic fields. In this approach, an assumption of local proportional evolution is introduced, wherein a given local elasto-plastic quantity is constrained to evolve in the same direction as the respective local elastic quantity. For example, at any point in the structure, the stress tensor remains proportional to a time-independent tensor:

$$\underset{\sim}{\sigma}(t) = s(t)\bar{\underset{\sim}{\sigma}}^{\#} \tag{1.26}$$

However, despite the generality of the approach, the accuracy is tested only on a two-dimensional mesh of a notched structure, and reports over-estimation of the Neuber method in that case (see Figure 1.13). This kind of local proportionality rule will be implemented along with a multi-axial Neuber rule in Chapter 3, with the accuracy tested on full 3D structures with pores of various types.

4.2 Cycle jump methods

Cycle jump methods, originally proposed by [Savalle and Culié, 1978, Lesne and Savalle, 1989] allow access to the later stages of cyclic loading through extrapolation, thereby reducing the number of computed cycles. By expressing internal variables as a function of the cycle count, these variables are updated with values corresponding to a later cycle, without the need to compute all intermediate cycles. This update is based on a sequence of a few previously computed cycles. Thus, the method is useful if the stabilisation process of the cycles is long, or if the material presents ratcheting behavior. The procedure [Sai, 1993] is detailed in the subsequent paragraphs.

Let $\underline{Y}(N)$ represent the evolution of a vector of internal variables $\underline{Y} = [\underset{\sim}{\alpha}, \underset{\sim}{\varepsilon}, p]$ as a function of the number of cycles N and $\underline{y}(t)$ represent this evolution as a function of time t. Let $\mathcal{T}$ be the period of a cycle. τ is one particular instant in this cycle, i.e. $0 \leq \tau \leq \mathcal{T}$. Thus $\underline{Y}(N)$ is obtained as:

$$\underline{Y}(N) = \underline{y}((N-1)\mathcal{T} + \tau) \tag{1.27}$$

Now, a second order Taylor expansion of $\underline{Y}(N)$ is used to express the evolution of the internal variables as a function of the cycles:

$$Y(N + \Delta N) \approx \underline{Y}(N) + \underline{Y}'(N)\Delta N + \underline{Y}''(N)\frac{\Delta N^2}{2} \tag{1.28}$$

In order to obtain the first and second derivatives of $\underline{Y}(N)$, we assume that for three cycles M, N and K ($M<N<K$) the vector of internal variables $\underline{Y}(M)$,$\underline{Y}(N)$ and $\underline{Y}(K)$ is available. Thus:

$$\underline{Y}'(N) = \frac{\underline{Y}(K) - \underline{Y}(N)}{K - N} \tag{1.29}$$

with

$$N = M + \Delta N \tag{1.30}$$

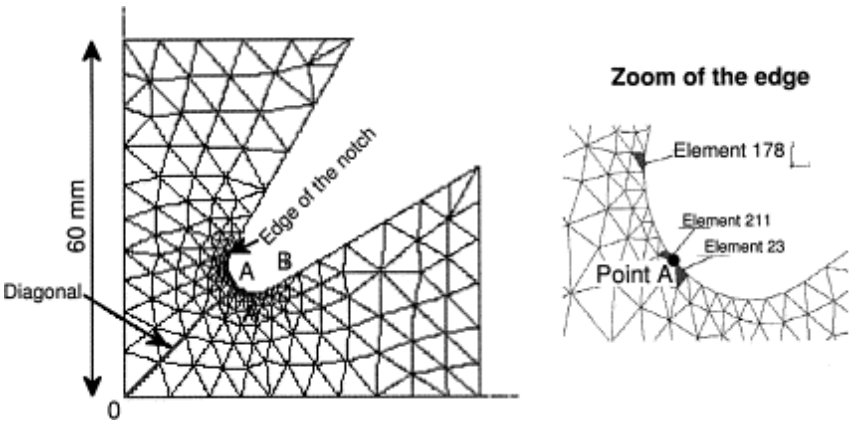

(a) Notched test geometry

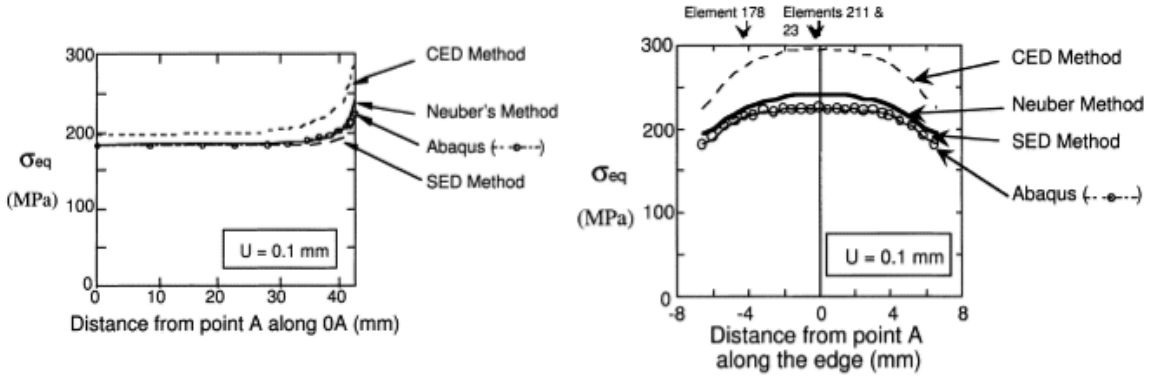

(b) Performance when applied displacement leads to confined plasticity

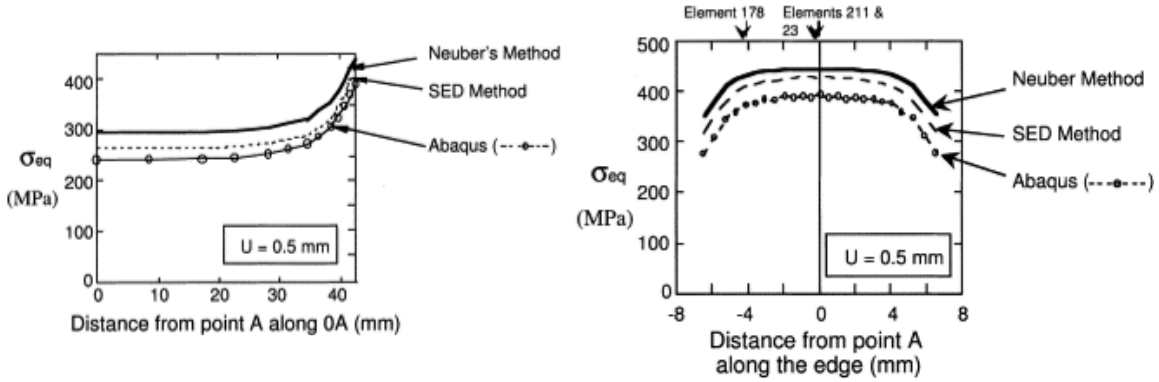

(c) Performance when applied displacement leads to plastic deformation of full area

Figure 1.13: Performance of Neuber and SED method in a notch, for monotonic loading [Desmorat, 2002]

The second derivative is expressed as:

$$\underline{Y}''(N) = \frac{2}{(N-M)^2}\left[\underline{Y}(M) - \underline{Y}(N) + (N-M)\underline{Y}'(N)\right] \tag{1.31}$$

ΔN is determined by supposing that the second order derivative $\underline{Y}''(N)$ is negligible compared to the first order derivative $\underline{Y}'(N)$, for all the components:

$$\frac{1}{2}\underline{Y}''(N)(N-M)^2 \ll \underline{Y}'(N)(N-M) \tag{1.32}$$

From equation (1.30) and the previous inequality (1.32):

$$\Delta N \ll \frac{2\underline{Y}'(N)}{\underline{Y}''(N)} \tag{1.33}$$

To satisfy this condition, a user-defined precision factor η is introduced:

$$\Delta N_i = \frac{2\eta\underline{Y}_i'(N)}{\underline{Y}_i''(N)} \tag{1.34}$$

where each internal variable of the vector Y, denoted as Y_i, will give rise to different ΔN_i (one for scalar components and six for tensorial components). The smallest ΔN_i is chosen.

Following the definition of the boundary value problem, the cycle jump method is applied as follows. The user chooses the particular instant of time in the cycle τ at which a cycle jump sequence is to be initiated (this is generally chosen in the elastic domain for stability). The value of η is usually fixed as 0.01, which is sufficient for acceptable results. A few cycles (3-5) are computed, then ΔN is computed for all the internal variables using equation (1.34) and the smallest value for applying the cycle jump is chosen. The internal variables are computed for $N + \Delta N$ using (1.28), and the number of cycles is updated. The process is repeated k times, until the end of the desired number of cycles. A schematic for the procedure is shown in Figure 1.14.

Similar implementations of the cycle jump method exist, some of which make use of only the first order derivative $\underline{Y}'(N)$ for the update of variables after the jump [Sai, 1993, Mukhopadhyay et al., 2018] or both the first and second order derivatives [Sai, 1993, Van Paepegem et al., 2001]. The selection of ΔN for the jump is either user-defined as a fixed value or increasing sequence [Van Paepegem et al., 2001, Cheng et al., 2022], or adaptative based on a user-defined precision criteria [Sai, 1993, Van Paepegem et al., 2001, Cheng et al., 2022, Caradec et al., 2023].

The number of cycles jumped, in the case of multiple integration points, e.g. a structure, can either be computed for one particular element and then used for the cycle jump for the whole structure [Sai, 1993] or taken as the minimum ΔN^* of all elements $* \in \mathcal{E}$ where $\mathcal{E}$ is the set of elements comprising the structure [Cheng et al., 2022]:

$$\Delta N = \min_{*\in\mathcal{E}}\{\Delta N^*\} \tag{1.35}$$

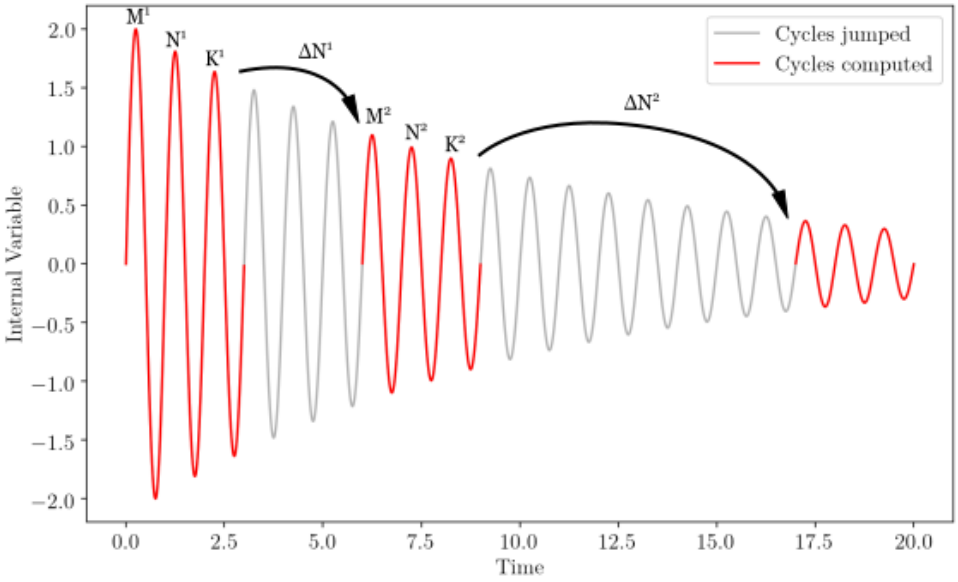

Figure 1.14: Schematic of the cycle jump procedure for an internal variable, with the number of cycles jumped ΔN^k for the k^{th} step based on the cycles M^k, N^k and K^k

which may result in low values of ΔN due to some integration points in the computational domain evolving rapidly. To overcome this issue, an approach using the relative frequency of integration points for all ΔN was proposed [Van Paepegem et al., 2001], allowing access to the cumulative relative frequency function of ΔN. Following this, a small percentile of the cumulative relative frequency distribution of all ΔN is taken, with the cost of added extrapolation errors.

4.3 Conclusions

In the vast number of methods available for accelerating finite element computations, we have covered plastic correction methods and cycle jump methods. Cycle jump methods will not be considered further, as will be shown later; the material under study stabilises quickly and does not exhibit ratcheting behaviour in the presence of pores when the global applied stress corresponds to the high cycle fatigue (HCF) loading regime. In plastic correction methods, we have discussed Neuber-type methods, which have thus far been developed for notches and tend to overestimate the lifetime. We found no discussion on the performance of this rule for porous structures with arbitrary geometries of pores in the loading regime where plasticity remains confined. This motivates the developments of Chapter 3, where a new Neuber-type plastic correction algorithm will be proposed.

Part 1:

Numerical pipeline for fatigue lifetime predictions of specimens with porosity

Chapter 2

A multi-scale probabilistic methodology to predict high-cycle fatigue lifetime for alloys with process-induced pores

Résumé

Ce chapitre présente une méthodologie multi-échelle pour intégrer les effets des défauts sur la durée de vie en HCF. À l'échelle microscopique, la variabilité de la durée de vie est traitée via des modèles probabilistes, sans modélisation explicite des défauts. À l'échelle mésoscopique, des maillages EF haute résolution sont créés à partir d'images tomographiques, afin de rendre compte des effets conjugués de la morphologie, des interactions entre pores, ainsi que des effets de surface. Un échantillonneur statistique est utilisé pour générer différentes configurations et estimer la distribution de la durée de vie en fatigue en fonction des distributions de pores. Ainsi, une nouvelle méthode pour calibrer les modèles probabilistes tenant compte de cette incertitude liée aux pores est proposée. Cette approche permet de fournir des estimations de durée de vie en HCF fonction des deux échelles analysées, tout en réduisant le nombre de données nécessaires à l'identification robuste d'un tel modèle. La validation de cette méthode repose sur des données expérimentales de fatigue obtenues pour des alliages d'aluminium à différents niveaux de porosité. Des investigations numériques de la méthodologie seront présentées, incluant le processus d'optimisation, la convergence de la solution, et sa capacité à prendre en compte l'effet de taille. Ce chapitre testera également les limites d'une approche de homogénéisation naïve, dans l'objectif de réduire le coût de l'approche multi-échelle qui repose sur la description explicite des pores.

1 Introduction

The preceding chapter presented a literature review that served to introduce the key elements necessary for an understanding of the characterisation of lifetime in a structure containing porosity. This chapter is an adaptation of the article titled 'A multi-scale probabilistic methodology to predict high-cycle fatigue lifetime for alloys with process-induced pores' written during the PhD program [Palchoudhary et al., 2024a]. The chapter proposes a multi-scale methodology that accounts for uncertainty in fatigue lifetime of structures due to uncertainty in entities at two scales: the meso-scale pores and the micro-scale heterogeneity. A local strain-life model, as proposed by Manson [Manson, 1953], is selected for computing the lifetime resulting from plasticity caused by micro-scale heterogeneity, including factors such as varying grain orientation and the presence of precipitates. The physics of this heterogeneity are not explicitly modelled. The variability at this scale is accounted for by making the criterion of the strain-life model probabilistic. Moreover, the criterion has been carefully selected to address the existence of two fatigue regimes (dependent on the loading) that are commonly observed in experiments [ASTM, 2015], and to accommodate multiaxial stress-strain states [Brown and Miller, 1973, Fatemi and Socie, 1988, Karolczuk and Macha, 2005]. The meso-scale pores are explicitly modelled via a finite element method, and a elasto-plastic material behaviour is adopted in order to address the presence of plasticity in the vicinity of the pores.

The probabilistic lifetime of this porous structure is determined by a weakest link hypothesis [Zok, 2017, Liu et al., 2020, Li et al., 2022], on the finite elements that comprise the structure. In the event of uncertainty regarding the meso-scale pore distribution, the overall lifetime of the structure is addressed by introducing statistical variability into the pore distribution within the structure. In other words, a degree of randomness is assumed in the pore distribution due to the unavailability of precise prior information on the pore states in the structure that lead to fatigue failure. The model operates under the assumption that the precise pore distribution responsible for a particular fatigue lifetime data point is unknown. Instead, a computed tomography (CT) scan of a different volume, made from the same porous material as the structure, is obtained to gather statistical information regarding the pores that are likely to be contributing to the observed failure of the structure. This statistical data serves as the input to the proposed lifetime model, which, by considering various potential pore positions and characteristics, computes a lifetime probability for a given structure without the need for precise knowledge of its pore distribution. This approach allows for the uncertainty in lifetime due to all possible pore distributions to be taken into account, including the effect of interactions between pores and between pores and the geometry of the specimen.

The proposed approach, when compared with the literature, occupies intermediate position in terms of complexity and fidelity in describing pore characteristics. A simplified approach treats the porous material as a homogenised substance with equivalent fatigue properties, thereby avoiding the necessity to directly describe individual pores [Ezanno et al., 2010]. Such a model requires extensive fatigue data on the porous material in order to identify it, and is not transferable to structures containing the same base material but differing pore characteristics. Other,

more recent approaches rely on the availability of the exact pore distribution in order to predict the fatigue lifetime of the structure [Le et al., 2018, Matpadi Raghavendra et al., 2024]. However, this may not be suitable for all scenarios, as CT scans of a structure are expensive to obtain and analyse. Another category of approaches employ statistical methods to consider all possible pore distributions in a structure when making lifetime predictions [El Khoukhi et al., 2019, Romano et al., 2019], in conjunction with the Kitagawa Takahashi (KT) diagram. These approaches assume that a single killer pore is responsible for fatigue failure, and do not take into account pore morphology or interactions between pores. Furthermore, obtaining the KT diagram is a lengthy experimental process. Finally, other proposals exist that quantify uncertainty in fatigue lifetime due to statistical variability in meso-scale pores by employing finite element analysis to represent the pores. These approaches typically simplify the representation of pore geometries to spheres or ellipses [Lacourt, 2019, Shirani and Härkegård, 2012], either neglecting inter-pore interactions [Bercelli et al., 2021] or restricting the method to two-dimensional structures [Talemi, 2020, Hou et al., 2024]. The method proposed in this chapter will make use of the finite element method to incorporate the actual three-dimensional geometries of the pores and typical inter-pore spacing.

Probabilistic lifetime models based on the weakest link approach for non-smooth geometries are identified through iterative optimisation in one of two methods. One approach employs an effective criterion within an equivalent volume to address non-homogeneous stress distributions, thereby reducing the optimisation to a 0D space [Muñiz-Calvente et al., 2015]. Other authors employ full-field mechanical information in the optimisation process. For instance, the stress is utilised when the loading remains elastic throughout [Lanning et al., 2003], while the strain energy is employed in the event of plasticity [Li et al., 2022]. However, the majority of weakest link approaches are concerned with notched structures [Lanning et al., 2003, Karolczuk and Palin-Luc, 2013, Liu et al., 2020, Li et al., 2022]. The identification of a lifetime model based on the weakest link approach for a porous structure modelled with the finite element method, where the exact pore distribution is unknown, has yet to be addressed in the literature and will be discussed in this chapter.

This chapter is divided into six sections. Section two presents a data set pertaining to a material with two levels of porosity, which will be used for further developments. Section three presents the lifetime model and the multi-scale methodology for obtaining the lifetime of porous structures. Section four is dedicated to maximum likelihood methods for identifying the parameters of the lifetime model on experimental fatigue data sets, including a proposal for dealing with structures with unknown pore distributions. Section five presents the results of calibration for the previously presented high-cycle fatigue data set, while detailing the process of the convergence of the solution and the optimisation behaviour, and also presents an analysis of the fatigue model complexity. Section six is dedicated to numerical investigations of additional natural properties of the model, including its capacity to account for the size effect, and interactions between pores and specimen geometry. This section also tests the limits of a naive homogenisation approach with the objective of reducing the cost of utilising the multi-scale approach, which involves explicit pore descriptions. The chapter concludes with an overview of the findings and

elements of discussion.

2 Experimental data

Although the proposed methodology is relatively general by design, the developments are dedicated to the case of a specific porous material for which the following data is available: (i) the number of cycles to failure in the high cycle fatigue (HCF) regime for a relatively large number of traction specimens, and (ii) tomographic data to characterise the distribution and morphology of the pores. This dataset is described below.

Composition, grades and manufacturing process

An Al-Si7Mg0.3 alloy is considered (i.e. 7% silicon, 0.3% magnesium and balance aluminium in weight %). Alloy 'B' is produced using the lost foam casting process, followed by a heat treatment, and contains shrinkage and gas pores. The second alloy, designated 'C', is produced using the same lost foam casting process as the alloy 'B', followed by hot isostatic pressing (HIP) at a temperature of 500°C and a pressure of 1000 bars. This results in a virtually porosity-free alloy, which is then subjected to the same heat treatment as the alloy 'B'. The alloy 'C' is therefore referred to as the non-porous alloy.

The manufacturing process yields slabs of these materials, and specimens for subsequent characterisation (including fatigue tests and CT scans) were obtained from the centre of these slabs, in order to avoid edge effects during casting and thus ensure the accuracy of the microstructure of the materials. Further details on the manufacturing process can be found in the work of other authors [Le, 2016].

Microstructure and tension-compression fatigue failure mechanisms

The microstructures and characteristics of pores in these alloys have been previously investigated by other researchers [Le et al., 2016, El Khoukhi et al., 2019, El Khoukhi et al., 2022]. The base material found in the two grades 'B' and 'C', have very similar microstructural characteristics. These include similar values of dendrite and secondary dendrite arm spacing, similar sizes of silicon precipitates, and comparable grain sizes [Le, 2016].

The porous alloy 'B' has a volumetric fraction of pores of approximately 0.28%, exhibiting a distribution of varying pore shapes and sizes. The maximum equivalent pore size, defined by the square root of the area observed by optical microscopy scans, reaches up to 300 μm. In the case of the non-porous alloy 'C', the presence of very small pores (with the maximum effective size < 50 μm) has been observed.

In conditions of tension-compression fatigue loading, the porous alloy 'B' is known to fail due to high stress concentration factors in the vicinity of pores. This often occurs as a result of a crack forming from a surface-breaking pore, from the interaction between sub-surface pores and the surface of the specimen, or from the coalescence of cracks originating from several pores

[Le et al., 2016, El Khoukhi et al., 2022]. The primary cause of tension-compression fatigue failure in the non-porous alloy 'C' is micro-plastic activity, namely the formation of persistent slip bands from which critical cracks originate [Le et al., 2016].

Tension-compression fatigue experiments without prior tomography

A limited data set comprising 32 fatigue experiments for the non-porous alloy and 34 fatigue experiments for the porous alloy is available [Le et al., 2016]. These experiments were conducted in the HCF regime, under symmetric tension-compression conditions with zero mean stress ($R = -1$) at a frequency of 100 Hz. The applied stress range on these specimens ($\Delta\Sigma$) is always within the elastic regime and is defined as the difference between the maximum and minimum applied load in a cycle. The applied stress amplitude is defined as half the applied stress range, expressed as follows: $\Sigma_a = \frac{\Delta\Sigma}{2}$.

The geometry of the specimens used is shown in Fig. 2.1 (a) and the results are recalled in a applied stress amplitude (Σ_a) - lifetime (N_R) plot in Fig. 2.1 (b). The tomographies of the specimens used for fatigue experiments are not available. As the specimens were cut from a bigger slab, the pores in these specimens are volumetric pores created due to the manufacturing process. For all experiments, a maximum limit on the number of loading cycles was set at 2×10^6 cycles. The specimens which did not break (termed run-outs) were counted and reported at the $N_R = 2 \times 10^6$ mark with an arrow to the right to indicate potential failure for a larger number of cycles (Figure 2.1(b)).

Computed tomography of a volume with pores

A computed tomography (CT) scan of a $12 \times 13 \times 3\,\mathrm{mm}^3$ region of a planar specimen, made using the same porous material as the cylindrical specimens used for fatigue experiments, was carried out in order to get information on the pore characteristics likely to have caused fatigue failure. The specimen and CT scan was provided by Stellantis. The planar specimen was cut from a larger slab, as was the case with the cylindrical specimens employed in fatigue testing. Thus, the pores in the planar specimen are also volumetric pores resulting from the manufacturing process. The resolution of the tomograph was $\sim 11\,\mu$m. The tomographic volume of interest was $424 \times 1211 \times 1000$ voxels with 16-bit unsigned images. Segmentation of the pores was carried out using a threshold value in grey-level contrast levels, resulting in a binary 3D image of the pores. A surface mesh was generated using Avizo, employing smoothing to remove artefacts. The resulting surface mesh, illustrated in Fig. 2.2 is used in subsequent sections.

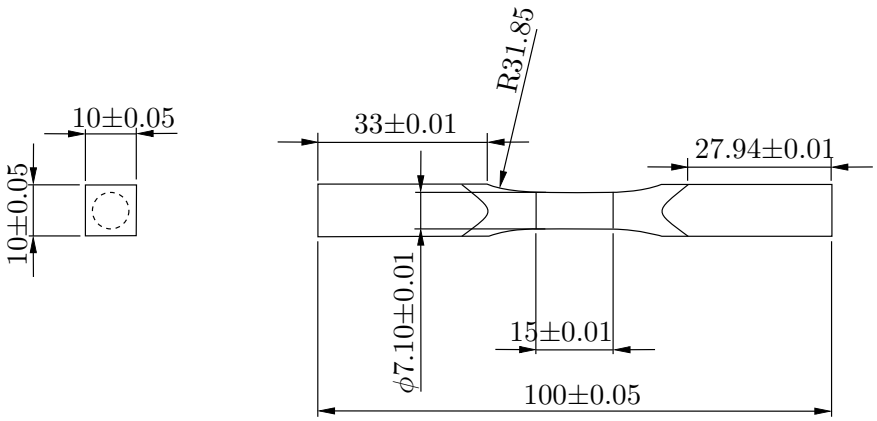

(a)

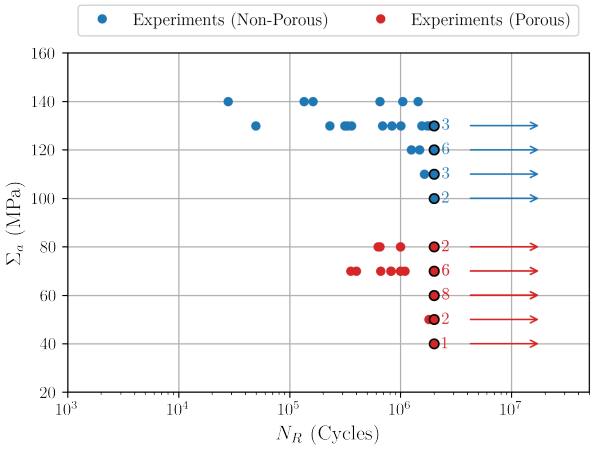

(b)

Figure 2.1: (a) Geometry of specimens (with values in mm) used for fatigue experiments (from the authors in [Le et al., 2015]) (b) Fatigue experiments reported using these specimens (from the authors in [Le et al., 2015]), with the applied stress amplitude Σ_a as a function of the number of cycles to failure N_R. The run-outs (at $N_R = 2 \times 10^6$ cycles) are all counted and reported with a number and arrow to indicate possible failure for a larger number of cycles

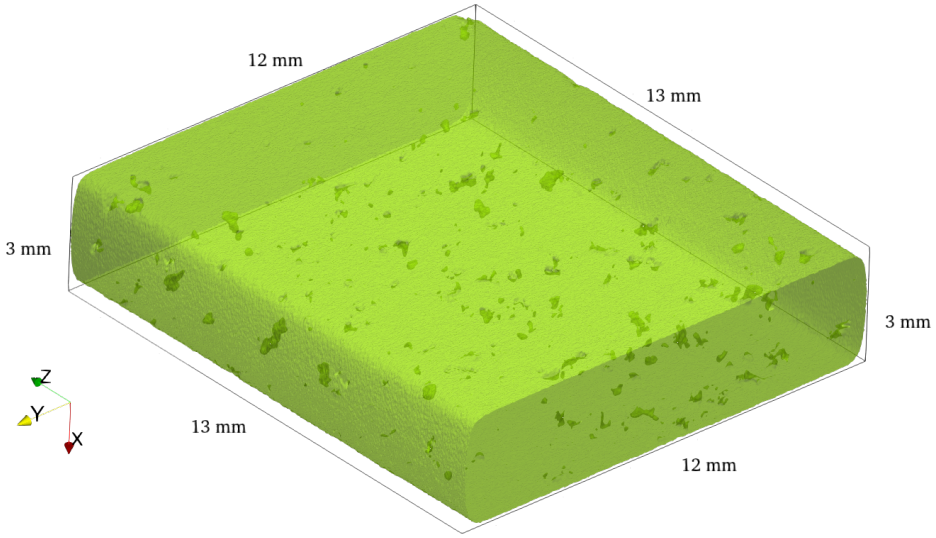

Figure 2.2: Tomography of $12 \times 13 \times 3\,\mathrm{mm}^3$ region of a planar specimen made using the same porous material as the cylindrical specimens used for fatigue experiments

3 Multi-scale probabilistic fatigue lifetime model

3.1 Micro and meso scale defects

A probabilistic multi-scale approach is proposed for the fatigue lifetime prediction of specimens containing a distribution of pores and microstructural heterogeneity. The first scale, henceforth termed the micro-scale, accounts for the effect of microstructural heterogeneity on the fatigue lifetime. The microstructural heterogeneity is not explicitly modelled; its effect is considered by making the fatigue lifetime model probabilistic [Doudard et al., 2004, Ni and Mahadevan, 2004, Pessard et al., 2011, Koutiri et al., 2013, Li et al., 2016]. This approach is adopted as the exact state of the microstructure is not known and would be too costly to model at the scale of the specimens undergoing fatigue loading. The lifetime distribution of an elementary volume subjected to a uniform stress depends on its volume and on the mechanical load to which it is subjected; further details of the construction of this probabilistic model will be explained in the next subsection.

The second scale, defined as the meso-scale, comprises tomography-informed pore distributions that are embedded in the base material containing the microstructural heterogeneity. This is shown schematically in Fig. 2.3. The effects of the pore distribution on the fatigue lifetime are considered by explicitly modelling these pores via a finite element model (see Fig. 2.4). The sizes, shapes, and locations of pores with respect to other pores and the surfaces of the specimen all influence the fatigue lifetime. The meso-scale part of the model accounts for uncertainty due to varying pore distributions by synthetically generating them.

Due to the presence of explicitly represented pores in the fatigue specimen, the mechanical stress in the synthetic specimens is heterogeneous. At macroscopic stress greater than σ_y, local plasticity is expected to develop around the pores due to stress concentrations. The micro-scale model may be used element-wise to obtain a probability distribution of failure per element.

The overall life of such a porous specimen is derived from the lifetime probability density of the individual finite elements that constitute it, via the standard weakest link assumption [Zok, 2017]. This modelling brick will be detailed after the explanation of the micro and meso scales of the model.

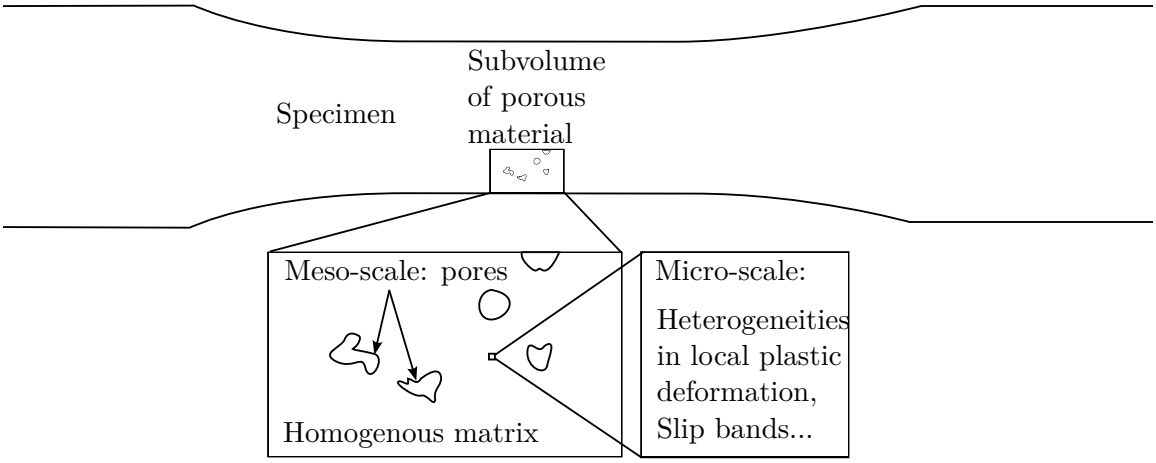

Figure 2.3: Example of a specimen containing a sub-volume of pores, with micro-plasticity activating in the base material between the pores

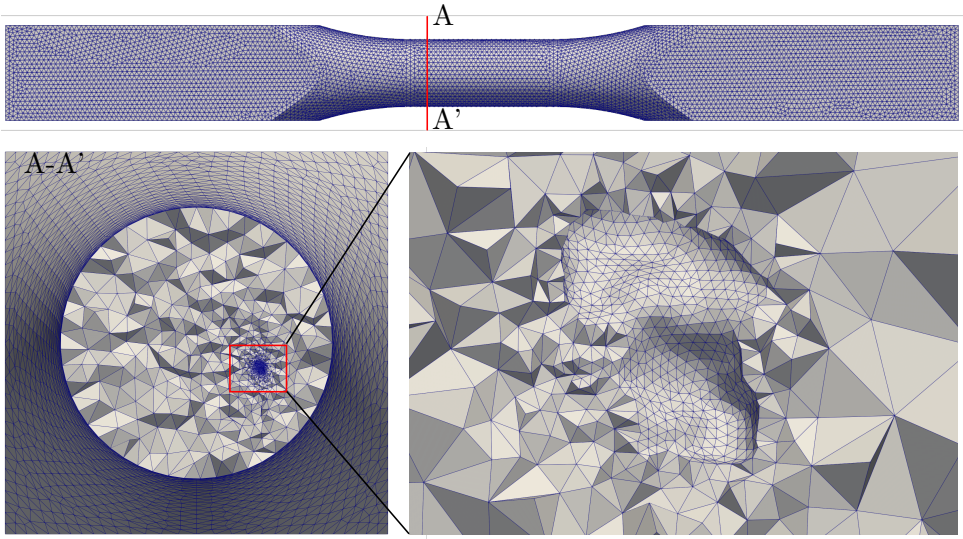

Figure 2.4: Example of a specimen containing a sub-volume of pores as a finite element mesh, with a zoom of the mesh around one pore

3.2 Probabilistic modelling of the life span at the material point level (micro-scale uncertainty modelling)

In this section, a probabilistic element-wise strain life model (with two regimes) is developed. The element-wise model needs to be based on multiaxial criterion, as the local stress state for regions around the pores in specimens depicted in Fig. 2.3 is multiaxial. The fatigue lifetime of an element $* \in \mathcal{E}$ (where $\mathcal{E}$ is the set of finite elements constituting a specimen) is obtained as a probability distribution, given a damage criterion $\frac{\Delta\varepsilon^*}{2}$ and the volume V^* of the element $*$.

Deterministic strain-life approach

The strain life approach assumes that the fatigue lifetime of an element N_{R}^* is governed by half the total strain range experienced by the element ($\frac{\Delta\varepsilon^*}{2}$) by a standard two-line model [ASTM, 2015]:

$$\frac{\Delta\varepsilon^*}{2} = g(N_{\mathrm{R}}^*) = A(N_{\mathrm{R}}^*)^{-\alpha} + B(N_{\mathrm{R}}^*)^{-\beta} + C \tag{2.1}$$

where A and α correspond to the parameters of the high-cycle fatigue (HCF) line, B and β correspond to the parameters of the low-cycle fatigue (LCF) line and C controls the fatigue limit, as illustrated in Fig. 2.5. As local plasticity may appear depending on the loading in the element, $\Delta\varepsilon^*$ is computed in the stabilized cycle with period $\mathcal{T}_c$, in the following manner [Karolczuk and Macha, 2005]:

$$\Delta\varepsilon^* = \left[\max_{t\in\mathcal{T}_c}(n^* \cdot \underset{\sim}{\varepsilon}^*(t) \cdot n^*) - \min_{t\in\mathcal{T}_c}(n^* \cdot \underset{\sim}{\varepsilon}^*(t) \cdot n^*)\right] \tag{2.2}$$

$$\text{where} \quad n^* = \arg\max_{n\cdot n=1}(n \cdot \underset{\sim}{\sigma}^{\#*} \cdot n) \tag{2.3}$$

Here, $\underset{\sim}{\sigma}^{\#*}$ is element's stress tensor coming from a separate elastic computation and n^* is the eigenvector associated to the highest eigenvalue of $\underset{\sim}{\sigma}^{\#*}$. The quadratic form $(n^* \cdot \underset{\sim}{\varepsilon}^*(t) \cdot n^*)$ of the element's total strain tensor $\underset{\sim}{\varepsilon}^*$ is obtained along this critical direction for the full loading sequence. The range of this quantity in the period of the stabilized stress-strain cycle $\mathcal{T}_c$ is computed. This procedure allows to account for the local multiaxiality that may cause a change in the critical direction from element to element. The underlying assumption is that local non-proportionality remains low [Desmorat, 2002].

As $g(N_{\mathrm{R}}^*)$ is monotonic, there exists a function $g^{-1}\left(\frac{\Delta\varepsilon^*}{2}\right)$ defined as:

$$g^{-1} :]C, +\infty) \rightarrow]0, +\infty) \tag{2.4}$$

Probabilistic strain-life approach

The fatigue lifetime model will now be made probabilistic. The fatigue lifetime is considered to be stochastic due to randomness in underlying total damage over all cycles that a specimen with volume V^* may undergo before failing. The total damage $\mathcal{G}$ is modelled as a random variable,

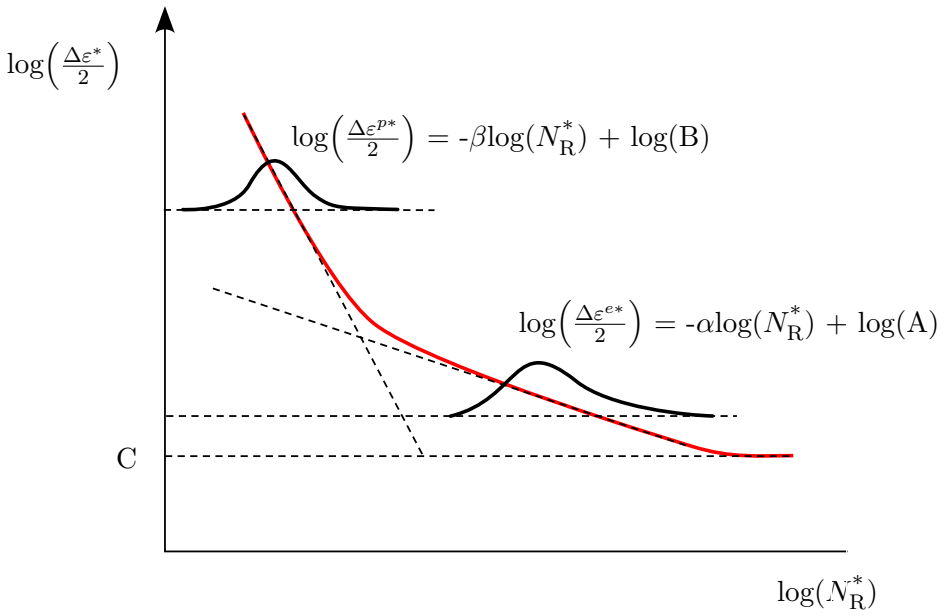

Figure 2.5: Schematic of the probabilistic strain-life model with two straight lines connected with an elbow in the $\log(\frac{\Delta\varepsilon^*}{2})$-$\log(N_{\mathrm{R}}^*)$ plane for modelling the two regimes (for low and high-cycle fatigue), and C giving the fatigue limit

and the form of the associated probability distribution is considered to be a Weibull distribution that respects weakest link scaling [Zok, 2017]:

$$N_{\mathrm{R}}^* \frac{1}{g^{-1}\left(\frac{\Delta\varepsilon^*}{2}\right)} = \mathcal{G} \tag{2.5}$$

with the cumulative distribution function (CDF) of $\mathcal{G}$ being denoted as $F_{\mathcal{G}}(g)$:

$$F_{\mathcal{G}}(g) = 1 - \left\{\exp\left(-\left\{\frac{g}{g_0}\right\}^m\right)\right\}^{\frac{V^*}{V_0}} \tag{2.6}$$

where $g_0 = \frac{1}{(\ln 2)^{1/m}}$, which implies that the median of this Weibull distribution is equal to 1 for a volume $V^* = V_0$. Here, m is the shape parameter of the Weibull distribution. By a change of variables, this leads to the following expression for the fatigue lifetime N_{R}^* (with its CDF being denoted as $F_{N_{\mathrm{R}}^*}(N; \Delta\varepsilon^*, V^*)$):

$$N_{\mathrm{R}}^* \sim \mathcal{W}\left(\lambda = \left\{g^{-1}\left(\frac{\Delta\varepsilon^*}{2}\right)\left\{\frac{1}{\ln 2}\frac{V_0}{V^*}\right\}^{1/m}\right\}, m\right) \tag{2.7}$$

$$F_{N_{\mathrm{R}}^*}(N) = 1 - \exp\left(-\left\{\frac{N}{\lambda}\right\}^m\right) \tag{2.8}$$

where λ is the scale parameter of the Weibull distribution describing the fatigue lifetime of the

element. It is noted that a higher V^* or a higher $\frac{\Delta\varepsilon^*}{2}$ (leading to lower g^{-1}) will cause the Weibull scale parameter λ to decrease, thus causing the lifetime probability distribution to shift to the left.

The set of parameters introduced, including the strain-life parameters and the Weibull shape parameter, is thus:

$$\mu = [m, A, B, \alpha, \beta, C] \tag{2.9}$$

Henceforth, the dependence of $F_{N_{\mathrm{R}}^*}$ on μ will be introduced as $F_{N_{\mathrm{R}}^*}(N; \Delta\varepsilon^*, V^*, \mu)$. The probability density function (PDF) of fatigue lifetime of the element $*$ will be denoted as $f_{N_{\mathrm{R}}^*}(N; \Delta\varepsilon^*, V^*, \mu)$.

3.3 Statistical modeling of the pore distributions at the meso-scale

The meso-scale part of the model takes into account the uncertainty in fatigue lifetime of porous specimens due to varying pore distributions by synthetically generating them. In the context of our research, the precise positions and morphology of pores within the specimens for which we aim to predict lifespan are unknown and not sought, resulting in inherent uncertainty. If the positions and morphologies of the pores were known, the model could be identified directly from the exact tomographies of the tested specimens rather than from synthetic ones. This approach would then align with fatigue studies on deterministic geometries, such as notches [Lanning et al., 2003, Li et al., 2022]. The distinct feature of our work lies in addressing the randomness of pore positions rather than deterministic pore distribution configurations, highlighting the unique challenge of random pore distribution in predicting material fatigue.

The synthetically generated porous specimens have the same geometry as the specimens used for fatigue testing (Fig. 2.1(a)), but with the pores inspired by the computed tomography (Fig. 2.2). These synthetically generated porous specimens thus resemble the traction specimens used for fatigue testing. The resulting meshes have linear elements with a piece-wise constant approximation of the stresses.

Synthetic pore field generator from CT scans

The tomographic scan of the porous specimen used for getting information on pores was shown in Fig. 2.2. A volume threshold is applied on this scan to exclude small pores. A pore is accepted if the radius of a sphere with the same volume as the pore is greater than 50 μm. This is justified by other authors, who show that in presence of large sized porosity, smaller pores have a negligible effect in fatigue life and that in the high cycle fatigue regime, cracks systematically originate from large pores [Kitagawa, 1976, Le et al., 2015, El Khoukhi et al., 2019]. This size filter step is illustrated in Fig. 2.6.

Surface meshes of the remaining pores after the size-filtering step were obtained using smoothing based on a criterion on sharp angles between surfaces of the pores - the original surfaces from the tomography and the remeshed surfaces are shown in Fig. 2.7. This smoothing

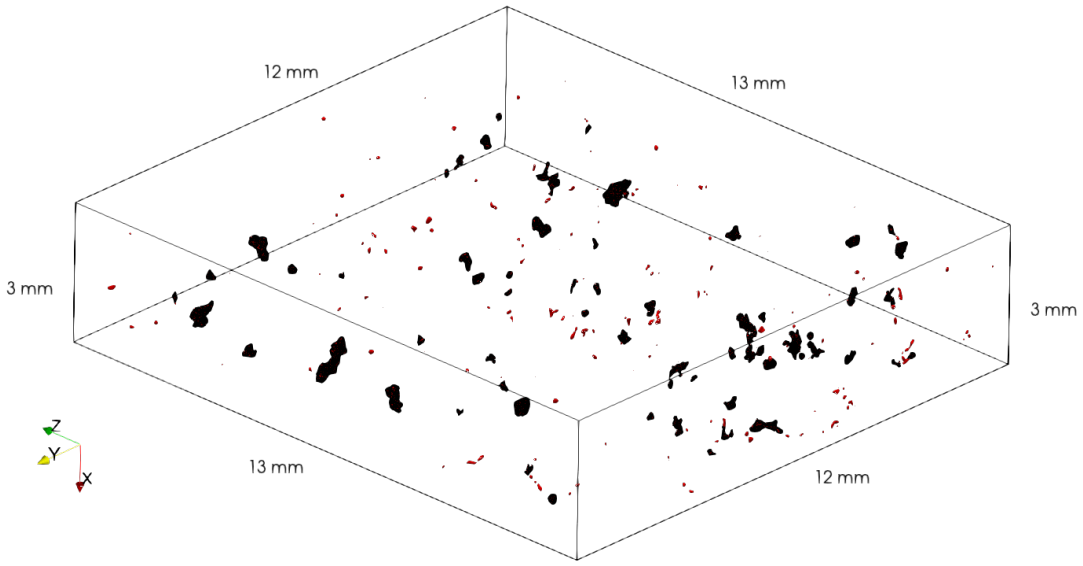

Figure 2.6: Segmented defects, with accepted defects (black) and rejected defects (red) based on their size (acceptance for effective radius of a sphere of same volume as the defect ≥ 50 μm)

is done to facilitate finite element meshing.

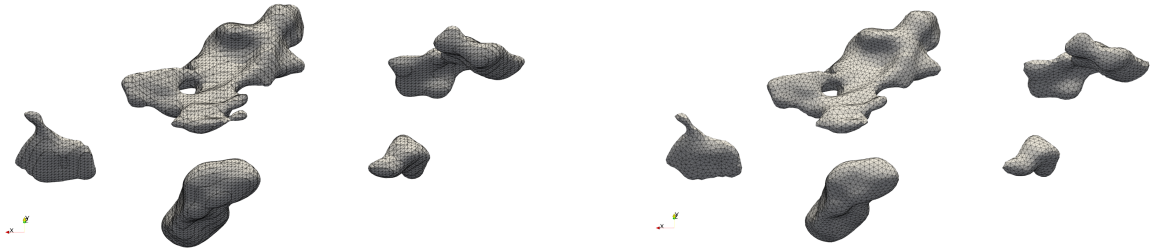

(a) Before smoothing

(b) After smoothing

Figure 2.7: Curvature based surface re-meshing of the defect surfaces

A set of synthetically generated porous specimens (with varying pore distributions) was created by using an algorithm based on this set of size-filtered and smoothed pores. The volume of the gauge section of the cylindrical fatigue specimens, being around 593 mm^3, contains a very large number of pores (and therefore elements). A splitting of the computational domain into sub-volumes is therefore carried out to avoid memory limitations. The following steps were done to synthetically generate porous specimens:

1. A CAD geometry of the cylindrical specimen used for fatigue experiments was created using GMSH [Geuzaine and Remacle, 2020].

2. The gauge section of this CAD geometry was randomly superposed with the representative volume of pores, and the set of pores intersecting with the geometry were retained for meshing.

3. A meshing operation is carried out in the base material between the surfaces of the specimens and the pores, with adequate refinement of the mesh close to the pores, using GMSH. Thus, only one region or sub-volume of the gauge section contains pores, henceforth referred to as a 'porous sub-volume'.

4. The previous two steps were carried out 100 times, to get 100 such specimens each with a different region of pores (illustrated in Fig. 2.8 (a)).

5. Elements in the 'porous subvolumes' of these 100 specimens are extracted. A random combination of porous sub-volumes that equal the volume of the gauge section of the cylindrical specimen makes up one synthetically generated porous specimen (illustrated in Fig. 2.8 (b)).

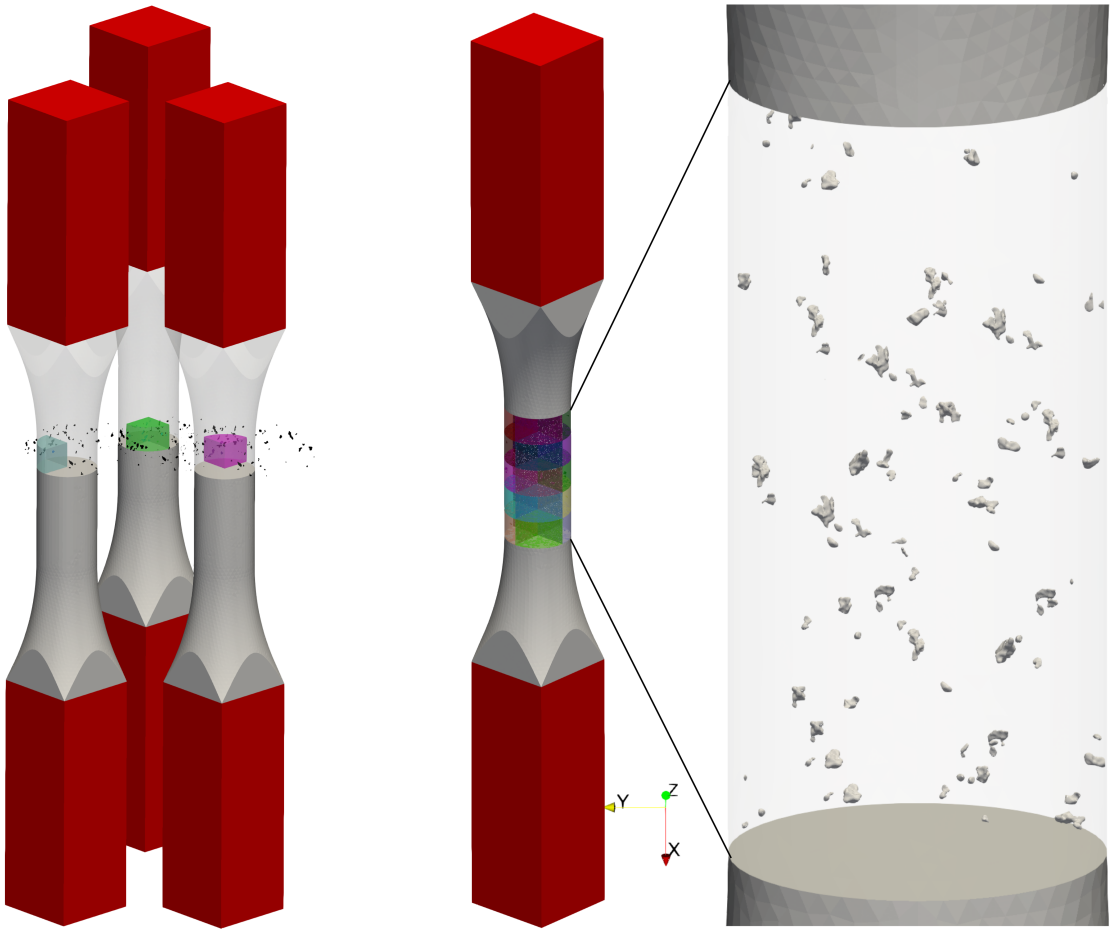

(a) (b)

Figure 2.8: (a) Random intersection of the defects with the geometric CAD representation of the fatigue specimens, with the defects being meshed into the specimen if it falls within the colored sub-volumes (process repeated 100 times) (b) Assembly of randomly selected porous sub-volumes to obtain a synthetically generated porous specimen with defects in its gauge section

Elasto-plastic computations

The multi-scale probabilistic fatigue model developed requires the computation of the local criterion ($\Delta\varepsilon^*$) for all the finite elements comprising the porous specimens due to applied stress amplitude on the specimen (Σ_a) for computation of the specimen's fatigue lifetime probability distribution. As the presence of pores in the specimen causes high stress concentration factors leading to local yielding, we consider a Chaboche-type plastic material behaviour, consisting of non-linear isotropic and kinematic hardening. The equations are recalled in table 2.1.

Table 2.1: Set of equations used for the mechanical behaviour - with $\underline{\underline{\sigma}}$ being the stress tensor, $\underline{\underline{\sigma}}_d$ being the deviatoric stress tensor, $\mathcal{C}$ the stiffness tensor, $\underline{\underline{\varepsilon}}$ the total strain, $\underline{\underline{\varepsilon}}^e$ and $\underline{\underline{\varepsilon}}^p$ the elastic and plastic strain tensors respectively, $\mathcal{J}$ the von Mises yield function, p the cumulative plastic strain, and $\underline{\underline{\varepsilon}}^p_d$ the deviatoric plastic strain [Chaboche, 1989]

Elasticity	$\underline{\underline{\sigma}} = \mathcal{C} : (\underline{\underline{\varepsilon}} - \underline{\underline{\varepsilon}}^p)$
Strain partitioning	$\underline{\underline{\varepsilon}} = \underline{\underline{\varepsilon}}^e + \underline{\underline{\varepsilon}}^p$
Yield function	$f_y(\underline{\underline{\sigma}}; \underline{\underline{X}}, p) = \mathcal{J}\left(\underline{\underline{\sigma}} - \underline{\underline{X}}\right) - \sigma_y - R(p)$
Evolution of yield function	$f_y \dot{p} = 0 \quad \text{and} \quad f_y \leq 0$
Isotropic Hardening	$R(p) = Q\left(1 - \exp\left(-bp\right)\right)$
Kinematic Hardening	$\dot{\underline{\underline{X}}} = \frac{2}{3} C \dot{\underline{\underline{\varepsilon}}}^p - D \underline{\underline{X}} \dot{p}$
Flow rule	$\dot{\underline{\underline{\varepsilon}}}^p = \dot{p} \left(\frac{3}{2} \frac{\underline{\underline{\sigma}}_d - \underline{\underline{X}}}{\mathcal{J}(\underline{\underline{\sigma}}_d - \underline{\underline{X}})} \right)$
Cumulative plastic strain	$\dot{p} = \sqrt{\frac{2}{3} \dot{\underline{\underline{\varepsilon}}}^p_d : \dot{\underline{\underline{\varepsilon}}}^p_d}$

However, time integration of non-linear material behaviour is time-consuming and resource heavy, especially for large meshes. Therefore, a plastic corrector is used, which allows rapid approximation/post-processing of the full-field elasto-plastic response of specimens for any proportional loading sequence when given elastic FEA results at one timestep [Palchoudhary et al., 2024b]. [1] An example of the approximation quality of the criterion with respect to a reference computation is shown in Appendix A on a subvolume of pores (with Fig.

[1] The reader is invited to refer to either the publication or the next chapter in this dissertation for the details of this plastic corrector.

7.13 showing the comparison directly on the fatigue criterion chosen in this chapter, i.e. $\Delta\varepsilon^*$).

The following steps highlight the process:

1. Elasto-static computations are performed on the sub-volumes of the synthetically generated specimens with the FEniCS [Alnaes et al., 2015] software.

2. The approximate elasto-plastic solution is reconstructed in a space-time domain, for several nominal loading levels, by a plastic corrector that approximates elasto-plasticity for any form of proportional applied loading via post-processing of elasto-static finite element results [Palchoudhary et al., 2024b]

3. The local total strain amplitude ($\Delta\varepsilon^*$) is extracted for the stabilized cycle for all the elements comprising the gauge section of the generated specimens and for all the nominal loading levels.

3.4 Probabilistic lifetime model at the structure level : weakest link assumption

A structure with a heterogeneous stress distribution, for example, a structure with pores that are explicitly meshed, or a structure with a notch, will have different values of the criterion ($\Delta\varepsilon^*$) in different elements of the structure for a given applied stress amplitude Σ_a. We formally define a function $\Delta\varepsilon^*(\Sigma_a) : \Sigma_a \mapsto \Delta\varepsilon^*$ that maps the load applied to the structure as boundary condition to the fatigue criterion in element $*$. This function is computed by FEA. The probabilistic strain-life model developed in section 3.2 can subsequently be applied to all the elements of the FE mesh. The CDF of fatigue lifetime of a given element in the geometrically heterogeneous case is thus obtained as $F_{N^*_{\mathrm{R}}}(N; \Delta\varepsilon^*(\Sigma_a), V^*, \mu)$, as given in equation (2.8).

A weakest link hypothesis is used to obtain the fatigue lifetime density of the full structure. In this model, the failure of the structure is given by the failure of the first element of the FE mesh. The weakest link hypothesis assumes that the failure of the elements are statistically independent events. The probability of the survival of a structure s (modelled by the random variable $N^{\mathrm{s}}_{\mathrm{R}}$) is given by:

$$\mathrm{Prob}(N^{\mathrm{s}}_{\mathrm{R}} \geq N) = \prod_{*\in\mathcal{E}} \mathrm{Prob}(N^*_{\mathrm{R}} \geq N) \tag{2.10}$$

where $\mathcal{E}$ is the set of elements comprising the structure. The analytical form of the probability distribution of failure of the structure is the same as that of a 2-parameter Weibull distribution with Weibull scale parameter denoted as λ^s and given by (the proof is given in Appendix B):

$$N^{\mathrm{s}}_{\mathrm{R}} \sim \mathcal{W}\left(\lambda^s = \frac{1}{\left\{\sum_{*\in\mathcal{E}} \frac{1}{\lambda^m}\right\}^{1/m}}, m\right) \tag{2.11}$$

The CDF of fatigue lifetime of the structure is:

$$F_{N_{\mathrm{R}}^{\mathrm{s}}}(N) = 1 - \exp\left(-\left\{\frac{N}{\lambda^s}\right\}^m\right) \tag{2.12}$$

The computation of λ^s is dependent on Σ_a as the computation of λ needs the function $\Delta\varepsilon^*(\Sigma_a)$. It is also dependent on the parameters of the fatigue model. Henceforth, the cumulative distribution function (CDF) and the probability density function (PDF) of the specimen's fatigue lifetime are denoted as $F_{N_{\mathrm{R}}^{\mathrm{s}}}(N;\Sigma_a,\mu)$ and $f_{N_{\mathrm{R}}^{\mathrm{s}}}(N;\Sigma_a,\mu)$, respectively.

4 Identification of the probabilistic lifetime model from experimental data by maximum likelihood estimation

Identification of the probabilistic lifetime model can be done on experimental fatigue lifetime data. In the following we will expose how this can be done in the case of (i) specimens with homogeneous stress distribution in the gauge section (ii) structures with heterogeneous stress distributions and (iii) structures with heterogeneous stress distributions that arise due to pores whose exact geometries and locations are unknown.

4.1 Specimens with homogeneous stress distributions

We recall from section 3.4 that $f_{N_{\mathrm{R}}^{\mathrm{s}}}$ is the PDF of the fatigue lifetime of a structure with a heterogeneous stress distribution. For specimens with a homogeneous stress distribution in their gauge section, i.e. without stress concentrations, the distribution of fatigue lifetime may be obtained without FEA.

The standard log-likelihood function is defined as [Pollak and Palazotto, 2009, Lee et al., 2023]:

$$\ln \mathcal{L}(\mu) = \sum_{i\in\mathcal{H}} \ln f_{N_{\mathrm{R}}^{\mathrm{s}}}(N^i;\Sigma_a^i,\mu) \tag{2.13}$$

where $\mathcal{H}$ is the index set of all the specimens with uniform stress distribution tested for fatigue failure, N^i is the number of cycles to failure for an applied stress amplitude Σ_a^i, and μ is the set of parameters of the fatigue model. A Nelder-Mead algorithm is used for optimisation:

$$\mu = \arg\max_{\tilde{\mu}} \left(\sum_{i\in\mathcal{H}} \ln f_{N_{\mathrm{R}}^{\mathrm{s}}}(N^i;\Sigma_a^i,\tilde{\mu})\right) \tag{2.14}$$

Furthermore, experimental fatigue data-sets usually include some data points corresponding to specimens that did not break before reaching the maximum number of cycles allowed $N_{\max}$. The latter, termed "run-outs", have a finite probability of failing for some number of cycles greater than $N_{\max}$. This probability is expressed as:

$$P(N > N_{\max}) = 1 - F_{N_{\mathrm{R}}^{\mathrm{s}}}(N_{\max};\Sigma_a,\mu) \tag{2.15}$$

4.2 Structures with heterogeneous stress distributions

We remind the reader of the PDF of the fatigue lifetime of structures with a heterogeneous stress distribution $f_{N_{\mathrm{R}}^{\mathrm{s}}}$ from section 3.4. Structures with multiple distinct geometries can be taken into account here, provided that the exact geometries are known. This could, for example, be structures with different notch geometries, or porous specimens whose exact pore distribution is known for each of the specimens tested. In this case, $f^i_{N_{\mathrm{R}}^{\mathrm{s}}}$ for each distinct geometry i with fatigue lifetime N^i at load Σ_a^i is needed for identification of the model. For identification of the parameters of such a model, previous studies have used Bayesian calibration [Liu et al., 2020] or manual adjustment of parameters [Karolczuk and Palin-Luc, 2013], especially on notched geometries. We use the maximum likelihood method:

$$\mu = \arg\max_{\tilde{\mu}} \left(\sum_{i \in \mathcal{I}} \ln f^i_{N_{\mathrm{R}}^{\mathrm{s}}}(N^i; \tilde{\mu}, \Sigma_a^i) \right) \tag{2.16}$$

where $\mathcal{I}$ is the set of all the structures with heterogeneous stress distributions tested for fatigue failure, N^i is the number of cycles to failure at an applied stress amplitude Σ_a^i and $\tilde{\mu}$ is the set of parameters of the fatigue model. A Nelder-Mead process is used for optimisation, outputting parameters μ of the lifetime model that are the most probable given the experimental fatigue results, by maximizing the likelihood function.

To illustrate the computational complexity involved, we note that the computing the Weibull scale parameter of the structure, λ^s, requires summing the Weibull scale parameters, λ, of all elements in the FE mesh (equation (2.11)). This result is then used to compute $f_{N_{\mathrm{R}}^{\mathrm{s}}}$. The scale parameters of the elements in turn require the computation of the inverse function $g^{-1}\left(\frac{\Delta\varepsilon^*}{2}\right)$ for each element (equation (2.7)). The criterion $\Delta\varepsilon^*$ is obtained for all the elements by one elasto-static finite element computation combined with the Neuber-type element-wise plastic correction algorithm, and does not need to be re-computed during the optimisation process. As the inverse function $g^{-1}\left(\frac{\Delta\varepsilon^*}{2}\right)$ depends on some of the parameters of the fatigue model (A, B, α and β), it needs to be re-computed for all the elements at every iteration of the optimisation process.

4.3 Structures with pores whose exact distribution is unknown

We now treat the case of structures with a fixed macroscopic geometry, that contains pores whose exact geometries and locations are unknown. In this case, no observations of the pore distribution in these structures were realized before fatigue testing, which makes the methodology presented in section 4.2, with deterministic geometries, inapplicable. The purpose is to identify a lifetime distribution on fatigue data of structures accounting for all possible pore geometries and localization. This is done by taking an expectation over all the possible configurations of pore distributions in the structures. For example, if $\mathcal{J}$ is the set of all the porous specimens of a given macroscopic geometry tested for fatigue failure, and $\mathcal{K}$ is the set of all possible synthetically generated configurations of porous specimens, the parameters of the lifetime distribution are obtained using the following optimisation statement:

$$\mu = \arg\max_{\tilde{\mu}} \left(\sum_{i \in \mathcal{J}} \ln \left(\mathop{\mathbb{E}}_{k \in \mathcal{K}} f^k_{N^{\mathrm{s}}_{\mathrm{R}}}(N^i; \Sigma^i_a, \tilde{\mu}) \right) \right) \tag{2.17}$$

Where N^i is the number of cycles to failure at an applied stress amplitude Σ^i_a. The expectation is taken over all realisations of the specimen with random meso-scale pore distributions. A Monte Carlo method is used to approximate this expectation over a finite number of synthetically generated porous specimens (denoted as the set $\tilde{K}$):

$$\mu = \arg\max_{\tilde{\mu}} \left(\sum_{i \in \mathcal{J}} \ln \left(\frac{1}{n_{\mathrm{k}}} \sum_{k \in \tilde{K}} f^k_{N^{\mathrm{s}}_{\mathrm{R}}}(N^i; \Sigma^i_a, \tilde{\mu}) \right) \right) \tag{2.18}$$

The computational cost of this optimisation is broken down here. Elasto-static finite element computations are required to be performed once for n_{k} synthetically generated porous specimens. The approximation of the criterion $\Delta\varepsilon^*$ in all the elements of all the synthetic specimens, being a post-processing, takes virtually no time. As explained previously (section 4.2), the inverse function $g^{-1}\left(\frac{\Delta\varepsilon^*}{2}\right)$ needs to be computed for all elements of n_{k} synthetic specimens, at every iteration of the optimisation process, for computation of the approximated expectation of the fatigue lifetime.

The algorithm explained in Algorithm 1 explains how the log-likelihood is computed for this case, including taking run-outs into account.

Algorithm 1 Log-Likelihood (LL) Computation

Ensure: ▷ N, λ are separated into N_{finite}, λ_{finite} (where $N < N_{\max}$) and N_{inf}, λ_{inf} (where $N \geq N_{\max}$)
$\text{LL} \leftarrow 0$
$i \leftarrow 0$
while $i < |N_{\text{finite}}|$ **do**
    $s \leftarrow 0$
    $k \leftarrow 0$
    while $k < n_{\text{k}}$ **do**
        $s \leftarrow s + f_{N_{\text{R}}^{\text{s}}}(N_{\text{finite}}[i], \lambda_{\text{finite}}[k][i], m)$
        $k \leftarrow k + 1$
    $s^{\text{avg}} \leftarrow \frac{s}{n_{\text{k}}}$
    $\text{LL} \leftarrow \text{LL} + \log(s^{\text{avg}} + 10^{-10})$
    $i \leftarrow i + 1$

$i \leftarrow 0$
while $i < |N_{\text{inf}}|$ **do**
    $m_{\text{inf}} \leftarrow 0$
    $k \leftarrow 0$
    while $k < n_{\text{k}}$ **do**
        $m_{\text{inf}} \leftarrow m_{\text{inf}} + (1 - F_{N_{\text{R}}^{\text{s}}}(N_{\max}, \lambda_{\text{inf}}[k][i], m))$
        $k \leftarrow k + 1$
    $m_{\text{inf}}^{\text{avg}} \leftarrow \frac{m_{\text{inf}}}{n_{\text{k}}}$
    $\text{LL} \leftarrow \text{LL} + \log(m_{\text{inf}}^{\text{avg}} + 10^{-10})$
    $i \leftarrow i + 1$

5 Calibration and validation on experimental data

In this section, the behaviour of the optimisation process presented in section 4 will be studied. The complexity of the fatigue model, i.e. number of required model parameters to fit lifetime data, will also be investigated. The data used is the previously presented experimental fatigue data on non-porous and porous specimens (Figure 2.1). Finally, we will try to identify a fatigue model that is transferable between these two types of pore populations.

The set $\tilde{K}$ is created with a total of 45 synthetically generated porous specimens [2] using the method detailed in section 3.3.

Elasto-plastic computations (elasto-static FEA followed by Neuber-type elasto-plastic correction, as explained in section 3.3) were carried out on each of the synthetically generated porous specimens, for 9 nominal loading levels (Σ_a ranging from 20 to 100 MPa). We use the material parameters identified by [Le et al., 2016] for the considered alloy. The parameters of the elasto-plastic model are recalled in table 2.2. The boundary conditions (shown in Figure 2.9) replicates the experimental conditions under which the fatigue data were obtained. Each loading sequence consisted of 20 symmetric tension-compression cycles ($R = -1$), to allow for stabilization of the elasto-plastic response. The fatigue criterion $\Delta\varepsilon^*$ in the stabilized (20^{th}) cycle is extracted. An example of the criterion computation in two synthetically generated specimens for one of the nominal loading levels ($\Sigma_a = 80$ MPa), is shown in Fig. 2.10. In this figure, the axial stress-strain histories for some integration points having high values of $\Delta\varepsilon^*$ are shown, to highlight the stabilization of the stress-strain cycles.

Table 2.2: Parameters of the elasto-plastic model [Le et al., 2016]

Parameter	E (MPa)	σ_y (MPa)	b	Q (MPa)	C (MPa)	D
Value	75500	170	19	20	127499	1334

[2] The size of the set $\tilde{K}$ is limited to 45 as meshing and elasto-static finite element computations are required to be performed once for n_{k} synthetically generated porous specimens. This step can become computationally expensive as the meshing and elastic computation time grows: each synthetic porous specimen contains between 1.5 to 3 million quadrature points

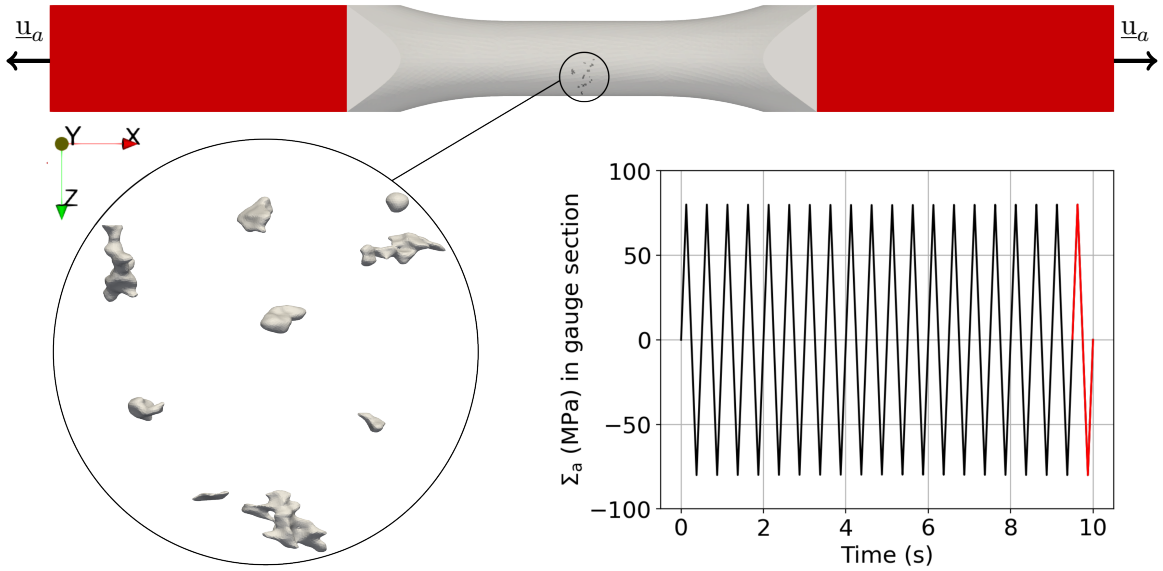

Figure 2.9: Boundary conditions (shown in red) for a specimen containing a sub-volume of tomography-informed pores, showing where cyclic displacement $\underline{u}_a$ is applied, to obtain the different levels of loading desired. In the gauge section of the specimen (away from pores), the von Mises stress reaches the desired stress amplitude levels (here, as an example, $\Sigma_a = 80$ MPa). The 20^{th} cycle (shown in red) is chosen for the computation of $\frac{\Delta\varepsilon^*}{2}$.

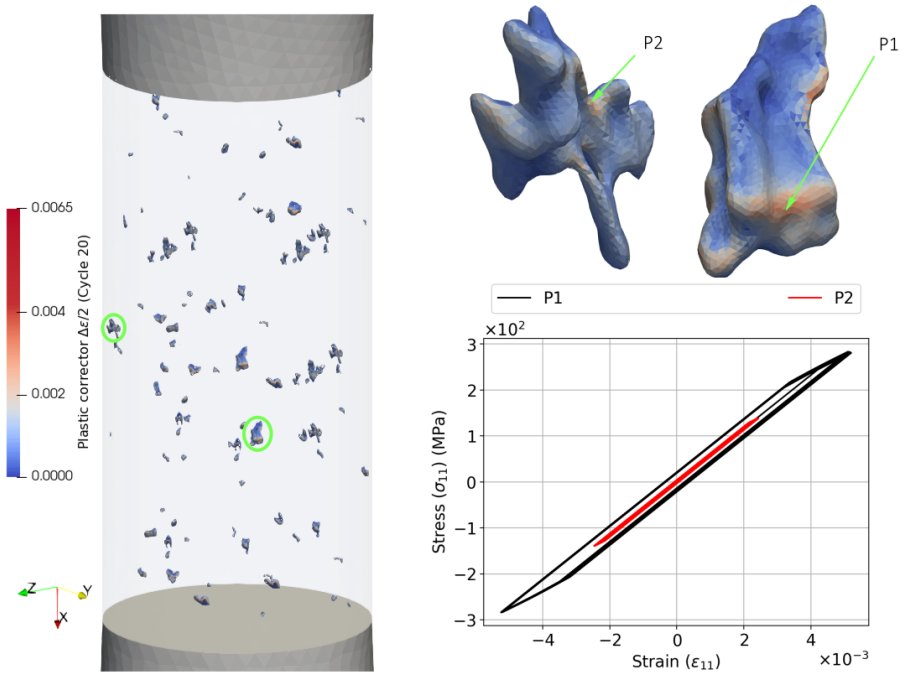

(a) Test specimen 1. $\Sigma_a = 80$ MPa

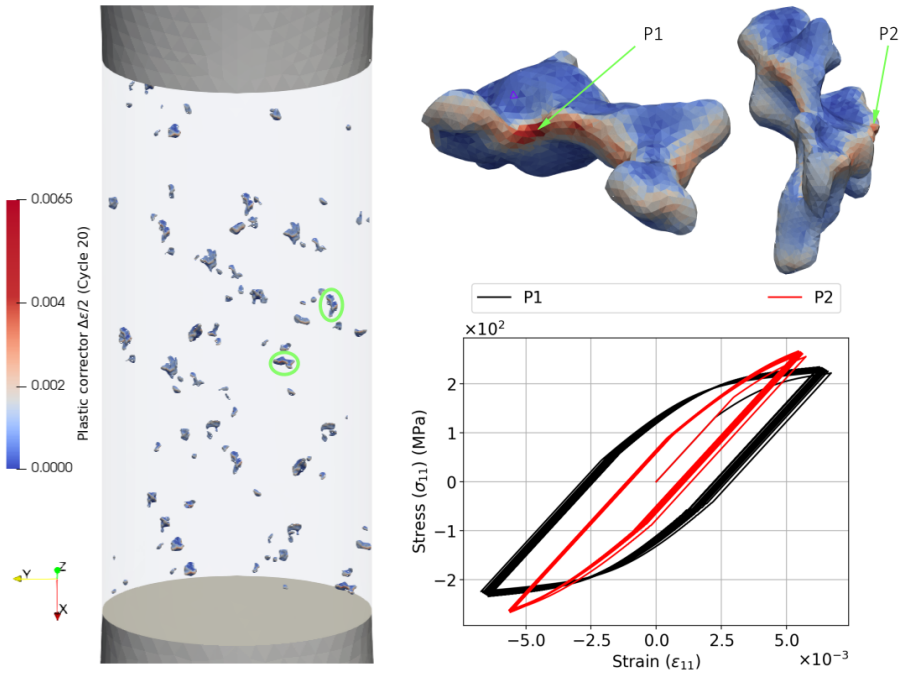

(b) Test specimen 10. $\Sigma_a = 80$ MPa

Figure 2.10: Local criterion ($\frac{\Delta\varepsilon}{2}$) field, in two different synthetically generated porous specimens, named test specimens 1 & 10. The criterion around the most critical defects and the axial stress-strain components at the highest points are shown. Refer to Appendix A for an analysis of the accuracy of the fields computed using the plastic correction algorithm compared to that obtained with a full elasto-plastic finite element analysis.

5.1 Homogeneous stress distributions: non-porous specimens

The multi-scale methodology is not required for identifying the parameters of the fatigue model on non-porous specimens, as the stress field is homogeneous in the gauge section. The maximum likelihood approach developed in section 4.1 is used to identify the parameters μ of the fatigue model. Optimisation is carried out using the experimental fatigue lifetime data of non-porous specimens, as detailed in section 2.

During the identification of the parameters of the fatigue model, we evaluate the impact of using fatigue models of varying complexity. Three cases are presented:

$$\mu = \begin{cases} [m, A, B, \alpha, \beta, C] & \text{(i)} \\ [m, A, \alpha, C, \quad B = 0, \beta = 0] & \text{(ii)} \\ [m, A, \alpha, \quad B = 0, \beta = 0, C = 0] & \text{(iii)} \end{cases} \tag{2.19}$$

These three cases presented here correspond to (i) the fatigue model with parameters for both the LCF and HCF lines (A, α, B, β), and the fatigue limit (C) which we term as the 'two-line fatigue model' (ii) the fatigue model with one line and the fatigue limit which we term as the 'one-line fatigue model' (iii) the fatigue model with one line and no fatigue limit.

Optimisation cost and convergence of solution

For all three models, the optimizer (Nelder-Mead) converges towards solutions with very similar likelihood values. The evolution of the parameters and the solution for the two-line fatigue model (equation (2.19)(i)) is shown in Fig. 2.11. Even for an initialisation that is far away from the solution at convergence, the optimisation process is well behaved, as seen by the intermediate and final solutions in Fig. 2.11(b-f).

The time required to evaluate all the functions during one iteration is dependent on the number of lifetime data points used for identification. For the considered data-set of 34 fatigue lifetime points, the cost of an iteration is around 0.15 seconds, therefore, the full optimisation procedure over 400 iterations takes around 60 seconds.

Comparison between lifetime models of varying complexity

The results of optimisation are presented in Fig. 2.12. For all the models, it is observed that the solutions for the first and second fatigue models (equation (2.19)(i) and (ii)) are similar, which suggests that the parameters B and β, i.e. the second line in the fatigue model, are not required. In our view, this conclusion would have been different had we had access to a richer data-set with more experiments across more loading levels. The third fatigue model (equation (2.19)(iii)) shows a significant decrease in the quality of the fit, indicating the requirement for the parameter C for getting a meaningful fatigue limit beyond which the lifetime is infinite.

Furthermore, the results show that the model is capable of taking into account run-outs. Indeed, all the quantiles of the model continue past the point $N_R = 2 \times 10^6$ cycles, which

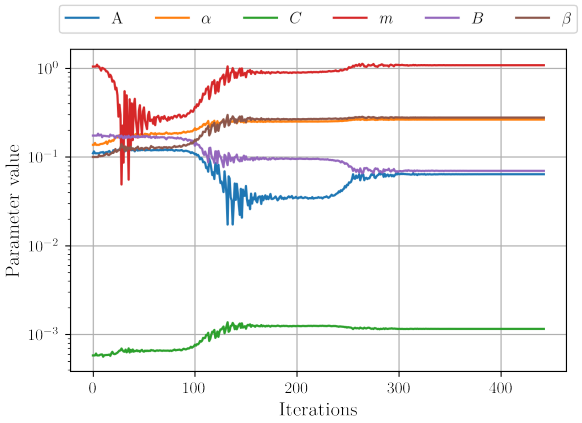

(a) Evolution of parameters

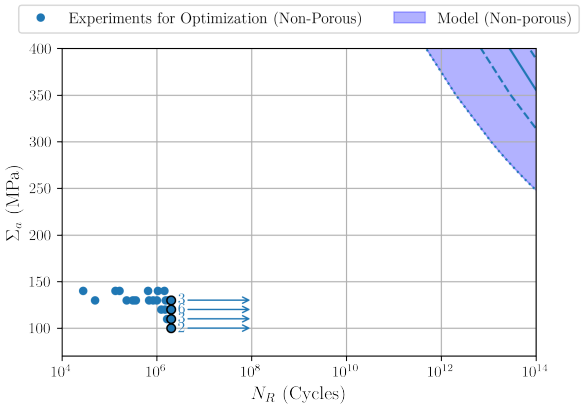

(b) Iteration number 0 (initial guess)

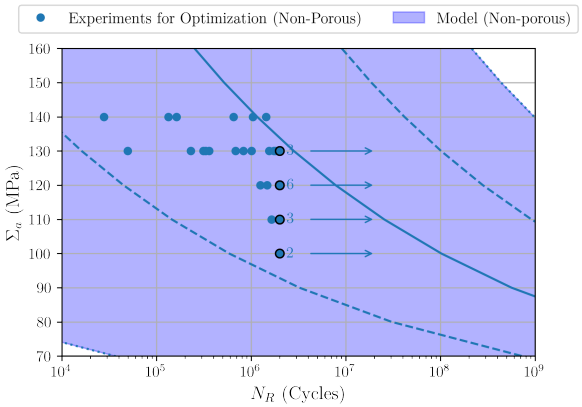

(c) Iteration number 75

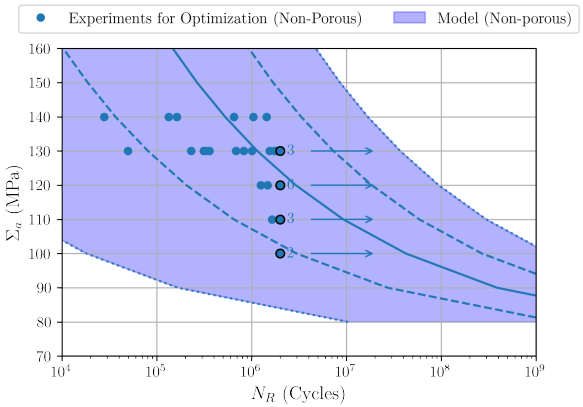

(d) Iteration number 125

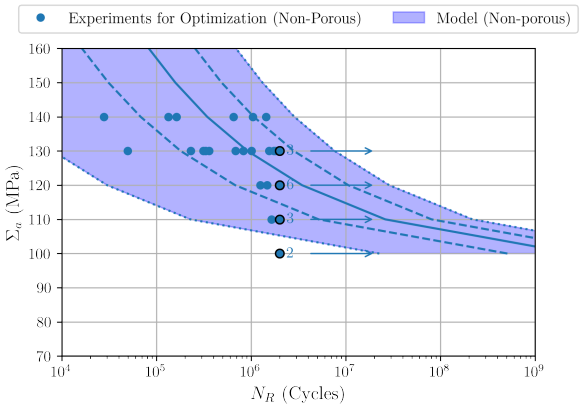

(e) Iteration number 200

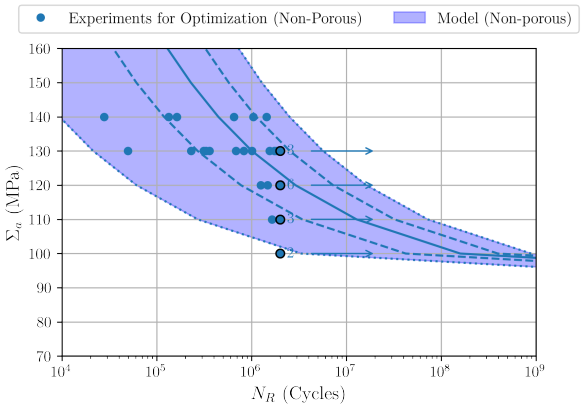

(f) Iteration number 300

Figure 2.11: Evolution and stabilization of the model parameters during optimisation for the two-line fatigue model, $\mu = [m, A, B, \alpha, \beta, C]$. The solid line represents the median, the dashed lines represent the 15% and 85% quantiles, and the dotted lines represent 1% and 99% quantiles. The final parameters (iterations 300 and above) are $A = 6.39 \times 10^{-2}$, $\alpha = 0.264$, $C = 1.16 \times 10^{-3}$, $m = 1.08$, $B = 6.97 \times 10^{-2}$, $\beta = 0.278$.

indicates the capability of the model to assign a finite probability of failure for some number of cycles greater than $N_R = 2 \times 10^6$ cycles.

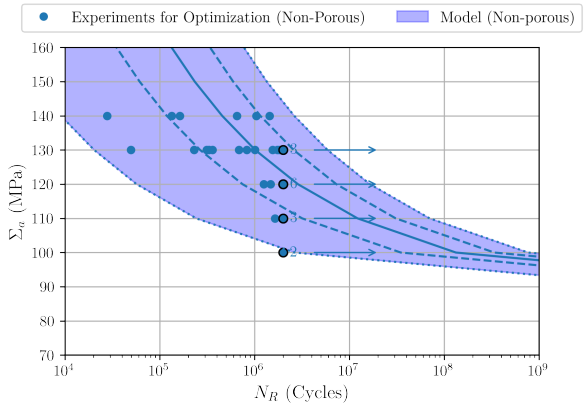

(a) Two-line model, $\mu = [m, A, B, \alpha, \beta, C]$

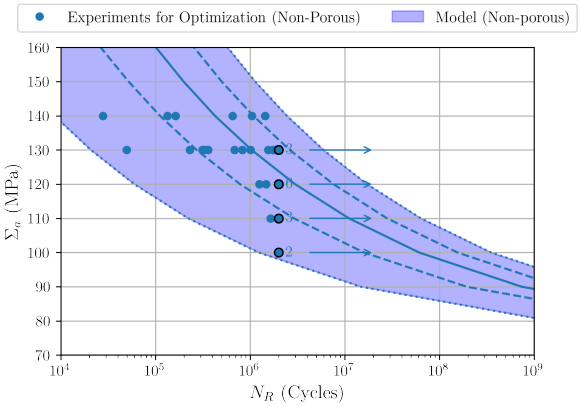

(b) One-line model, $\mu = [m, A, \alpha, C]$

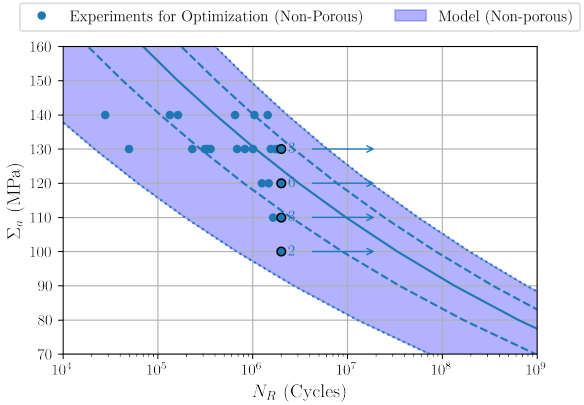

(c) One-line model without the fatigue limit, $\mu = [m, A, \alpha]$

Figure 2.12: Results of the probabilistic strain-life model, with three different fatigue models. The solid line represents the median, the dashed lines represent the 15% and 85% quantiles, and the dotted lines represent 1% and 99% quantiles.

5.2 Structures with pores whose exact distribution is unknown: porous specimens

The fatigue model is now identified on the experimental fatigue lifetime data of porous material presented in Section 2. The multi-scale methodology developed in section 3 for structures with heterogeneous stress distributions due to pores whose exact geometries and locations are unknown is used. The maximum likelihood approach developed in section 4.3 was used as the identification procedure. From the previously defined set $\tilde{K}$, a total of $n_{\mathrm{k}} = 10$ synthetic specimens were randomly selected for each (N^i, Σ_a^i) pair in order to approximate the expectation operator in the expression (2.18) of the likelihood function.[3]

During the identification of the parameters of the strain-life model, we evaluate the impact of using fatigue models of varying complexity. Two cases are presented (as C has previously been proven necessary for obtaining a fatigue limit):

$$\mu = \begin{cases} [m, A, B, \alpha, \beta, C] & \text{(i)} \\ [m, A, \alpha, C, \quad B = 0, \beta = 0] & \text{(ii)} \end{cases} \tag{2.20}$$

As defined previously (section 5.1), the cases correspond to (i) the 'two-line fatigue model' and (ii) the 'one-line fatigue model'.

Optimisation cost and convergence of solution

The parameters stabilise after a certain number of iterations of optimisation, as shown in the Fig. 2.13(a) for the two-line fatigue model. In Fig. 2.13 we show an optimisation process that converges well due to good initialisation. Indeed, if the initialisation is very far away from the expected solution, the optimisation process does not yield satisfactory results.

The cost of evaluating all the functions during one iteration is dependent on the number of synthetically generated specimens n_k taken to compute the expectation of the fatigue lifetime distribution and the number of lifetime data points. It also depends on the number of elements in each synthetically generated specimen, which is around 1.5-2.5 million elements each. For the considered data-set of 32 fatigue lifetime points, the cost of one iteration is around 42 seconds if $n_k = 1$ and 425 seconds for $n_k = 10$. For the presented case ($n_k = 10$), the cost of optimisation over 400 iterations is thus 47 hours.

Wöhler curve representing uncertainty due to pore distributions

Fatigue lifetime distributions for multiple realizations of synthetically generated porous specimens of the same volume but varying pore distributions (examples previously shown in 2.10) were obtained, at various nominal loading levels. The synthetically generated porous specimens

[3]The value of $n_{\mathrm{k}} = 10$ is chosen to balance robustness and computational cost in the model identification process. The robustness increases with n_{k}: each experimental point has a likelihood of failing from a larger variety of pore configurations, which is ideal as the exact pore distribution associated to the failure point is unknown. However, as will be discussed later, the computational cost increases linearly with n_{k}.

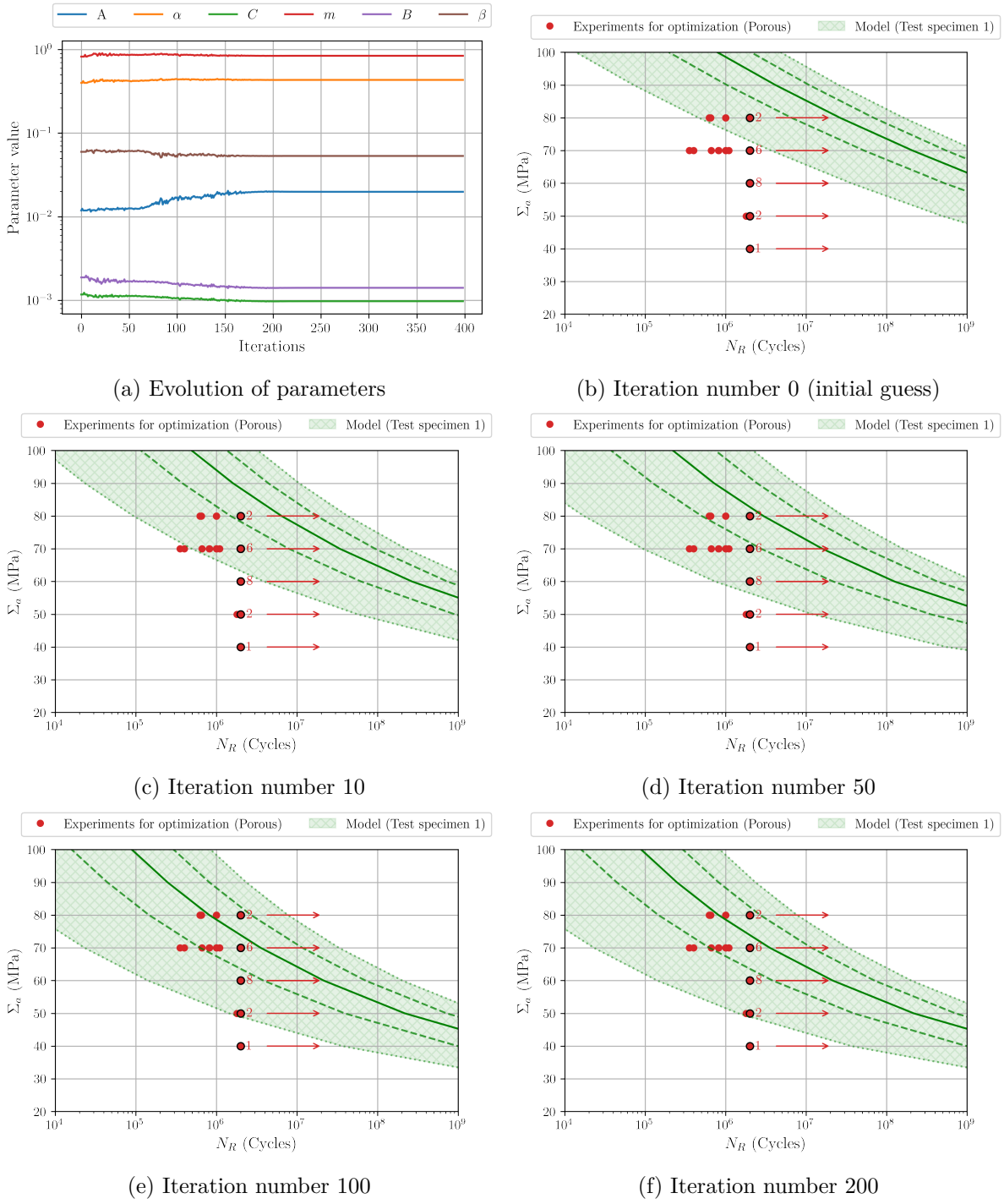

(a) Evolution of parameters

(b) Iteration number 0 (initial guess)

(c) Iteration number 10

(d) Iteration number 50

(e) Iteration number 100

(f) Iteration number 200

Figure 2.13: Evolution and stabilization of the model parameters during optimisation for the two-line fatigue model, $\mu = [m, A, B, \alpha, \beta, C]$ during optimisation on the porous experimental data using the multi-scale method. The final parameters (iterations 200 and above) are $A = 1.98 \times 10^{-2}$, $\alpha = 0.433$, $C = 9.72 \times 10^{-4}$, $m = 0.843$, $B = 1.41 \times 10^{-3}$, $\beta = 0.0533$.

show variations in their fatigue lifetime distributions, as shown in Fig. 2.14 for two different nominal applied stress amplitude levels, or in Fig. 2.15 for the entire Wöhler curve for a couple of specimens.

A fatigue lifetime distribution or Wöhler curve representing uncertainty due to pore distributions can be constructed by combining samples from a certain number of porous specimens. The failure distribution representing this uncertainty in pore distributions is constructed by combining 1000 samples each from 10 different randomly generated porous test specimens (shown by the red histogram in Fig. 2.14(c,d)). The quantiles are then computed on 10000 samples for each nominal stress level, which are joined to construct the quantiles of the porous Wöhler curve (shown by the red area in Fig. 2.15). This failure distribution or Wöhler curve represents uncertainty due to defects at two scales - micro-heterogeneity and varying pore distributions. We note that the uncertainty in fatigue lifetime due to varying pore distributions in the specimen is relatively low as compared to the uncertainty due to the micro-heterogeneity. In other words, at the scale of this specimen, the impact of varying pore distributions on the lifetime is not high. This is because of the volume of the specimen, which is large as compared to the pore size, which increases the likelihood of finding critical pore configurations in all the specimens, and makes all the synthetic specimens have similar stress distributions.

Comparison between lifetime models of varying complexity

The comparison between a two-line strain life model and one line strain life model is shown in Fig. 2.16. The two models (with four and six parameters) yield qualitatively similar probability distributions for the specimen fatigue lifetime (with the 6 parameter model having only a very slightly lower likelihood value than the one obtained using the 4 parameter model). We will further investigate the more general two-line strain-life model with 6 parameters, to allow for the possibility of two distinct regimes.

Lifetime prediction on a non-porous test specimen

Ideally we should also be able to predict the fatigue lifetime of porous materials with different pore distributions than the ones that were experimentally tested. Using the two-line fatigue model identified on the porous data, we try to predict the fatigue behaviour of a non-porous specimen. The results are shown in Fig. 2.17. We see that the prediction on the non-porous specimens is incorrect. The predicted lifetime is lower than what experiments suggest. This could be due to three reasons:

1. Misrepresentation of pores: Several uncertainties and assumptions have been propagated while meshing the pores (smoothing the surfaces, removing smaller pores, etc.). This could explain the discrepancy; the real state of stress due to the pores may not be correctly modelled. It is also possible that the surface roughness plays a role, at a scale that is smaller than that of the tomographic scan of the pores, and is not taken into account in the mesh.

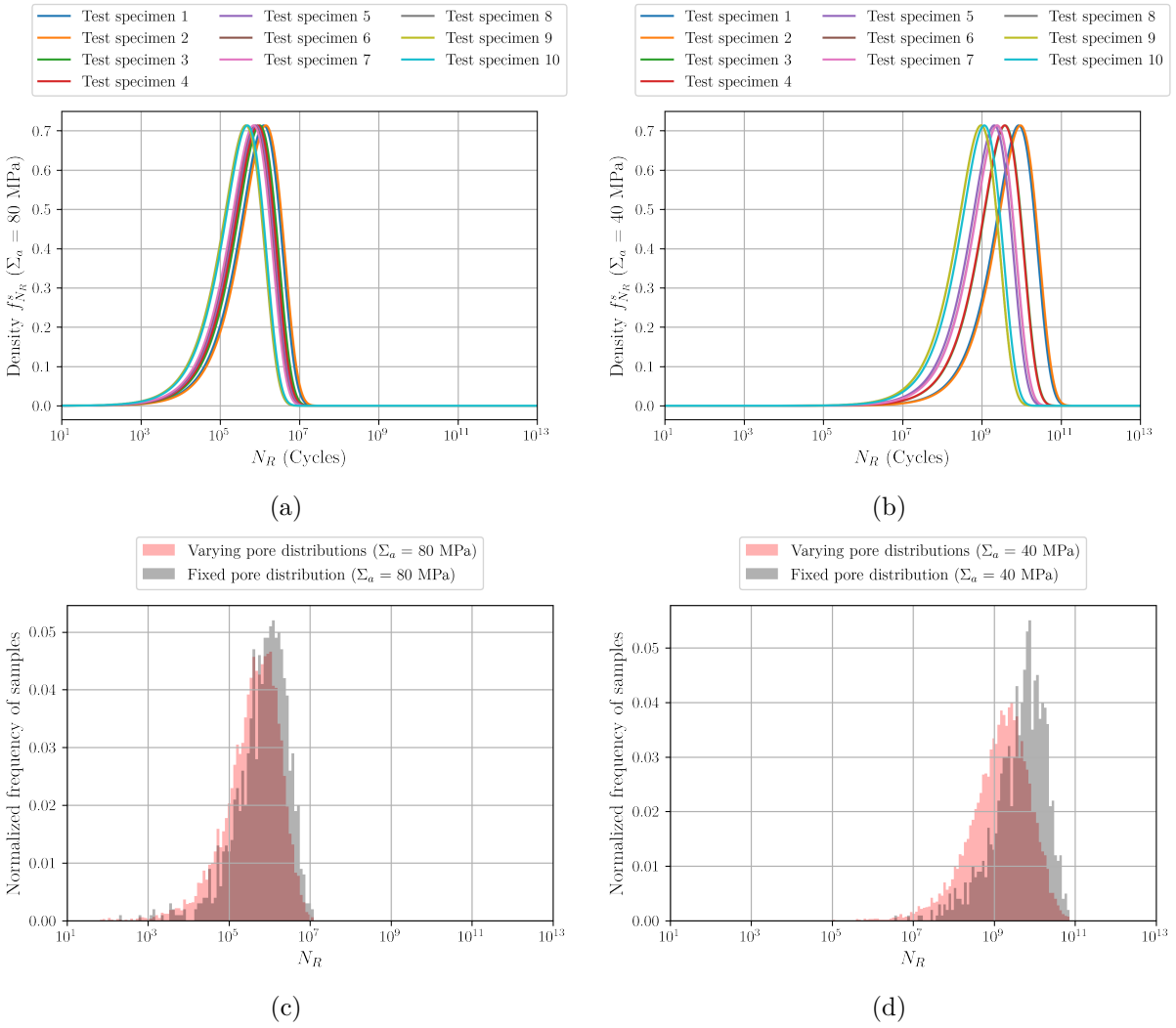

Figure 2.14: For the two-line strain-life model (parameters $\mu = [m, A, B, \alpha, \beta, C]$) identified on porous data: Failure densities for 10 different synthetically generated porous test specimens at (a) $\Sigma_a = 80$ MPa (b) $\Sigma_a = 40$ MPa. Proportion of uncertainty coming from a specimen with a fixed pore distribution (black) compared to specimens with varying pore distributions (red histogram constructed by combining 1000 samples each from 10 different porous test specimens) at (c) $\Sigma_a = 80$ MPa (d) $\Sigma_a = 40$ MPa

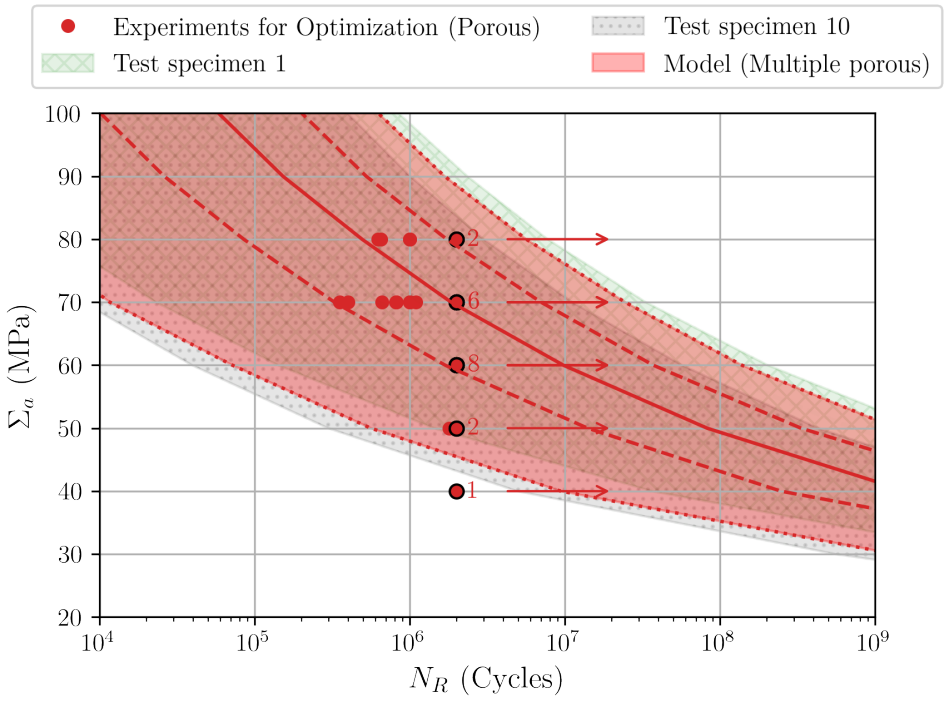

(a)

Figure 2.15: Results of the multi-scale probabilistic strain-life model identified on all available porous data, with all parameters active ($\mu = [m, A, B, \alpha, \beta, C]$). Proportion of uncertainty coming from fixed pore distributions (two test specimens shown in green and grey hatch) to varying pore distributions (red master curve constructed by combining 1000 samples each from 10 different porous test specimens at every applied stress amplitude level). The solid line represents the median, the dashed lines represent the 15% and 85% quantiles, and the dotted lines represent 1% and 99% quantiles.

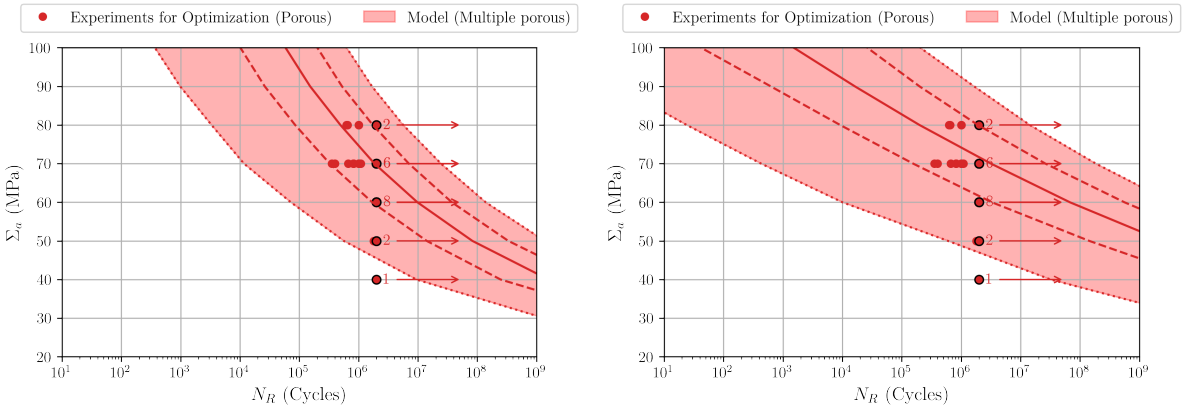

(a) Two-line model, $\mu = [m, A, B, \alpha, \beta, C]$

(b) One-line model, $\mu = [m, A, \alpha, C]$

Figure 2.16: Results of the probabilistic strain-life model using the multi-scale approach, identified on all available porous data, with two fatigue lifetime models. The solid line represents the median, the dashed lines represent the 15% and 85% quantiles, and the dotted lines represent 1% and 99% quantiles.

2. Lack of data: The current data-set for porous materials lacks fatigue lifetime data for when the material around the pores is loaded at the same stress levels (100-140 MPa) as in the data-set for non-porous specimens. To address this, we require experiments in one of two ways. One possible solution is obtaining further experimental data on porous specimens at very low stress levels, such that the material around the pores reaches the required stress levels (100-140 MPa) that the non-porous specimens were subject to. Another solution is to obtain experimental data on non-porous specimens at the required (100-140 MPa) levels. Using this additional data during the optimisation process, we can identify a model that is transferable between material with these two levels of porosity.

3. It could also be possible that the two base materials are different, or that the material in the vicinity of pores behaves differently under fatigue loading. Also, the hydro-static pressure may have an effect on fatigue behaviour, but is not taken into account in the fatigue model criterion.

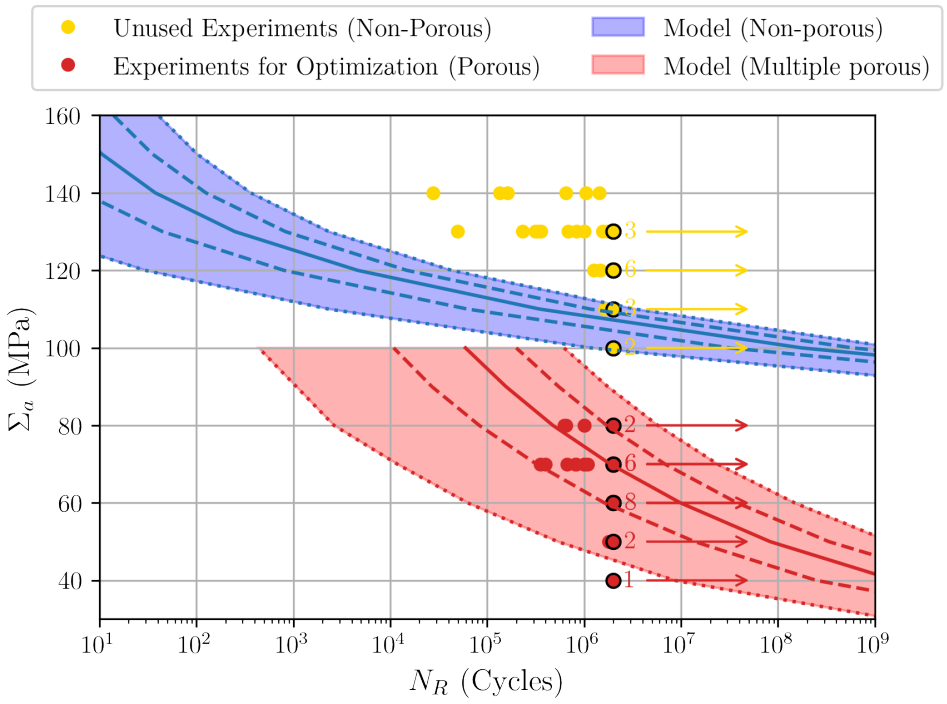

(a)

Figure 2.17: Prediction of the multi-scale probabilistic strain-life model identified on all available porous data, with all parameters active ($\mu = [m, A, B, \alpha, \beta, C]$), on a non-porous specimen. The solid line represents the median, the dashed lines represent the 15% and 85% quantiles, and the dotted lines represent 1% and 99% quantiles.

5.3 Towards a model transferable between different pore populations using lesser experimental data

In this section, we demonstrate that identifying a model that is transferable between different types of pore populations is facilitated by the multi-scale methodology proposed in this chapter.

A simplified method to model the fatigue behaviour of materials with different pore populations is to treat them as separate materials with different fatigue properties, and each material is thus fit separately with separate fatigue models. To do this, a large number of data-points would be required for identifying the parameters of the fatigue models for each of these materials.

The multi-scale approach, however, considers different pore populations to have the same base material. Fatigue lifetime data associated with different data-sets pertaining to different pore populations therefore share the same underlying statistics. Thus, the multi-scale approach is expected to require less data for identifying a model that is transferable between different types of pore populations.

Only the two-line fatigue model will be considered for the following numerical examples, in order to allow for the presence of two distinct regimes:

$$\mu = [m, A, B, \alpha, \beta, C] \tag{2.21}$$

We now consider the fatigue lifetime data-set associated with non-porous and porous material presented in section 2. A reduction of the non-porous fatigue lifetime data-set $\mathcal{I}$ is done by randomly picking one experimental point for each applied stress amplitude level. The resulting reduced non-porous dataset $\mathcal{I}^{\text{red}}$ is shown in Fig. 2.18 (a).

Identification of lifetime model on reduced data-set: multi-scale method

Here, we are identifying the fatigue lifetime model on both structures with homogeneous stress distributions (non-porous specimens) and structures with pores whose exact distribution is unknown (porous specimens) simultaneously. The function to minimize is taken as a sum of the functions defined in section 4:

$$\mu = \arg\max_{\tilde{\mu}} \left(\sum_{i \in \mathcal{I}^{\text{red}}} \ln f_{N_{\text{R}}^{\text{s}}}(N^i; \tilde{\mu}, \Sigma_a^i) + \sum_{i \in \mathcal{J}} \ln \left(\frac{1}{n_{\text{k}}} \sum_{k \in \tilde{K}} f_{N_{\text{R}}^{\text{s}}}^k (N^i; \tilde{\mu}, \Sigma_a^i) \right) \right) \tag{2.22}$$

The reduced set of non-porous fatigue experiments $\mathcal{I}^{\text{red}}$ is used in the optimisation process. The same set $\tilde{K}$ used in the previous section is taken for the synthetically generated porous specimens, and $n_{\text{k}} = 10$.

The model parameters are jointly identified on the reduced non-porous data-set $\mathcal{I}^{\text{red}}$ and the porous data-set $\mathcal{J}$. The result of the optimisation process is shown in Fig. 2.18. The fit is consistent on both the non-porous as well as porous cases, despite the reduction of non-porous data. This indicates that fewer fatigue experiments are required to identify the parameters when using the multi-scale approach. This is because the multi-scale approach considers porous

and non-porous specimens as the same material, and information from the two sets of data are statistically correlated.

Identification of lifetime model on reduced data-set: homogenised method

Identifying a probabilistic fatigue model on the reduced data-set $\mathcal{I}^{\text{red}}$ is difficult due to an insufficient data-set, which makes several solutions possible. When considering the porous material as a new 'homogenised' material, porous specimens may be considered to contain homogenised material with equivalent fatigue properties. A homogenised model is identified without using the multi-scale method, using the 0D identification procedure detailed in section 4.1 on the set $\mathcal{J}$ of porous experimental data. This gives the fit shown by the red curve in Fig. 2.19. While the fit is good on the porous specimens given the data, the model remains non-transferable to other types of pore populations. This is seen when extrapolating the homogenised porous model to the stress levels at which non-porous specimens were tested. The homogenised porous model overlaps with the non-porous experimental data, which is against the generally observed trend of porous material failing sooner than non-porous material.

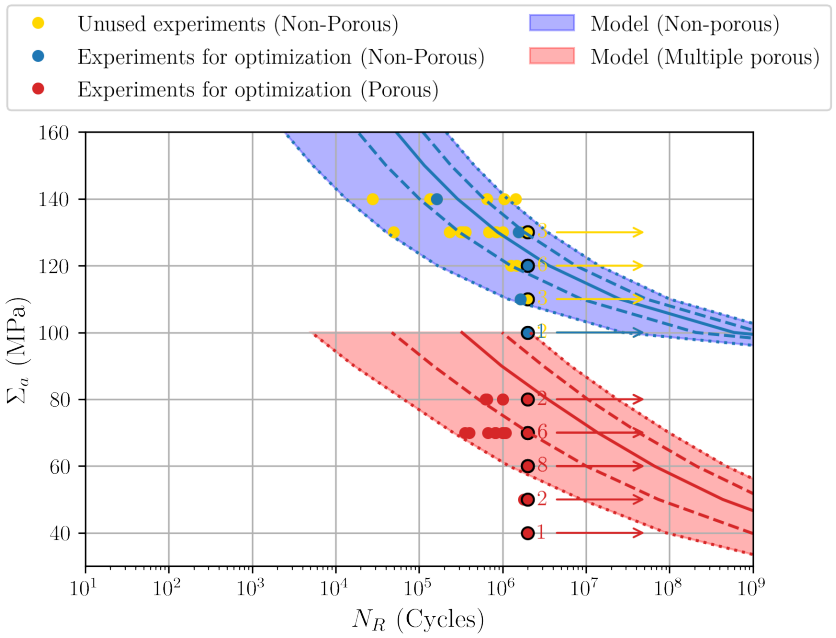

Figure 2.18: Identified fatigue model on the reduced data-set $\mathcal{I}^{\text{red}}$ of 5 random non-porous data points and the data-set $\mathcal{J}$ of all the available 32 porous data points, using the multi-scale method. The parameters found following the optimisation procedure are $A = 2.61 \times 10^{-3}$, $\alpha = 0.198$, $C = 6.59 \times 10^{-4}$, $m = 0.881$, $B = 3.37 \times 10^{-3}$.

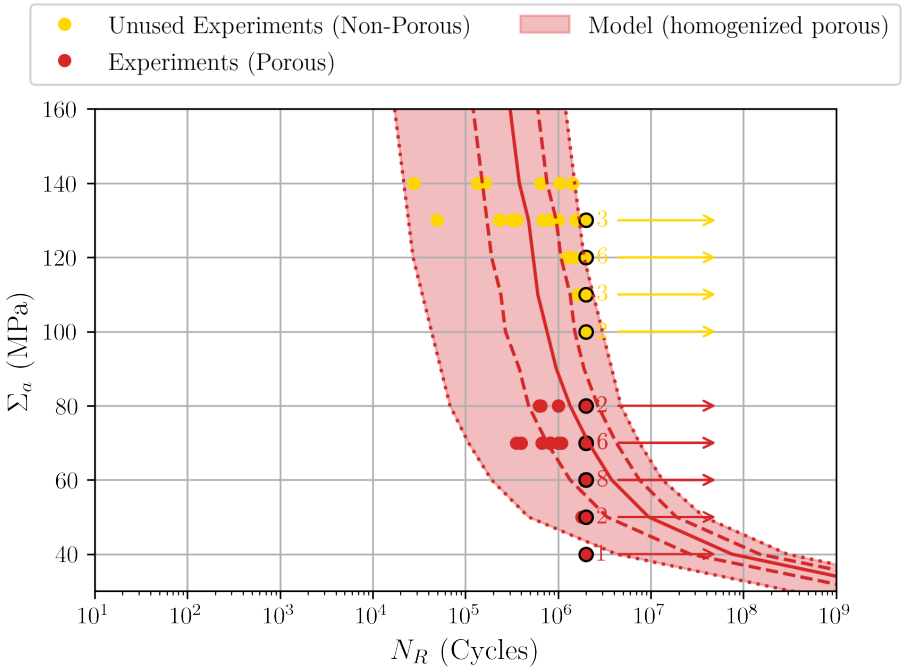

Figure 2.19: Identified fatigue model on the data-set $\mathcal{J}$ of all the available 32 porous data points, considering the porous material as a homogenised material, using a 0D identification method

6 Numerical investigations of multi-scale method properties

In this section, certain properties of the multi-scale method will be investigated. The dependence of the mesh size on the fatigue lifetime curve will be shown. The capacity of the model to take into account the volumetric size effect in fatigue will be shown. Finally, an attempt to replace the multi-scale method by using a naive homogenization technique will be presented.

6.1 Mesh convergence

The influence of the mesh size on the median of the lifetime predicted by the model is studied in this subsection. A synthetic specimen with one pore was meshed at different levels of refinement. The two-line fatigue model with parameters taken from section 5.3 is taken. Figure 2.20 shows four different refinement levels, with the size of the smallest element going from 5 microns to 29 microns. Figure 2.21 shows the effect of these mesh sizes on the median lifetime, across several load levels. As seen in this figure, the median fatigue lifetime curve exhibits a dependence on mesh size. The lifetime curve for the mesh with the smallest element size of 5 μm is identical to that for the 10 μm mesh. The optimal mesh size, beyond which further refinement does not change the solution, therefore lies between 10 and 19 μm.

6.2 Volumetric size effect (iso-stress condition)

As an automatic outcome of the model, specimens with different volumes but loaded under the same stress amplitude show a statistical size effect. Fig. 2.22 shows the Wöhler curves of three synthetically generated porous specimens with volumes $V/2$, V and $2V$. The same pore population in the smallest specimen was 'tiled' multiple times to get bigger specimens, to isolate only the specimen volume size effect (and not add lifetime variability due to changing pore distributions as demonstrated in section 5.2). Across all load levels, specimens with successively higher volumes show a decreasing fatigue lifetime. This is the well known statistical size effect in fatigue, i.e. bigger specimens have a larger probability of finding a critical flaw [Makkonen, 2001, El Khoukhi et al., 2021a].

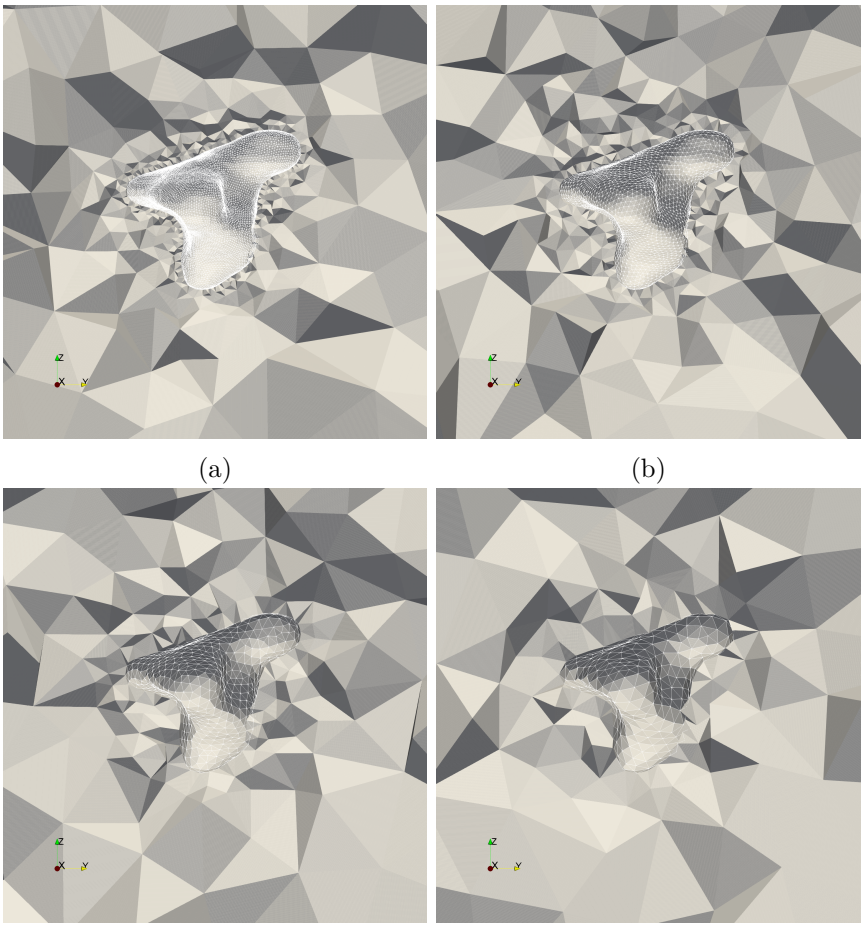

(a) (b)

(c) (d)

Figure 2.20: Mesh refinement around a pore, with the smallest element having size (a) 5 μm (b) 10 μm (c) 19 μm (d) 29 μm

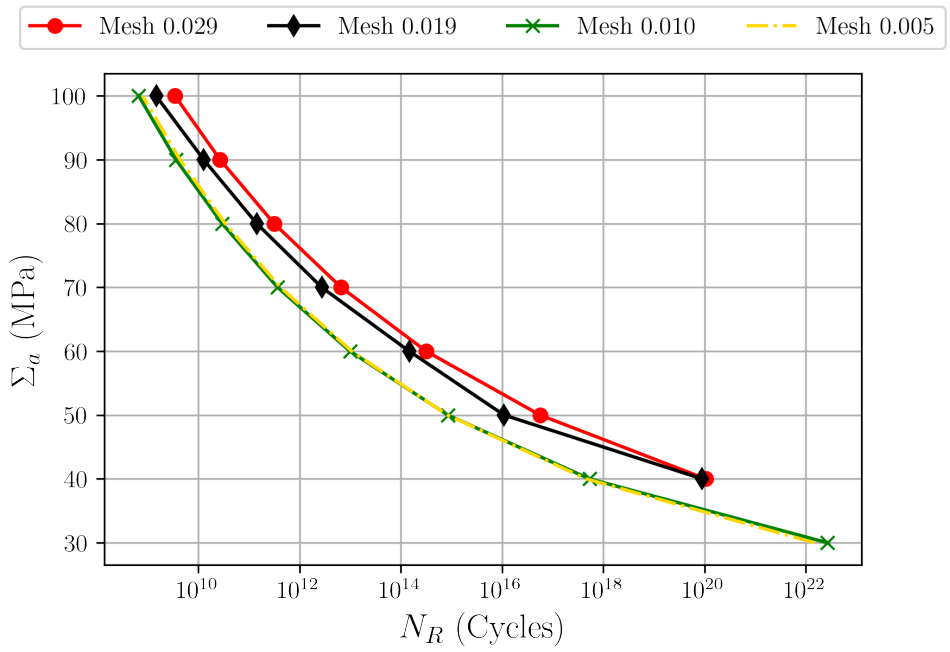

Figure 2.21: Effect of mesh size on the median lifetime for a given set of two-line strain life model parameters

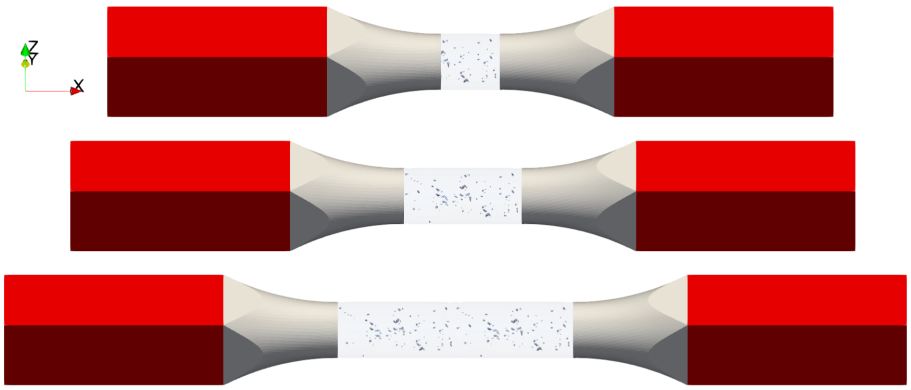

(a) Synthetically generated porous specimens of volume $V/2$, V and $2V$ (owing to different lengths of gauge sections but same cross sectional area), undergoing the same loading (same applied stress amplitudes)

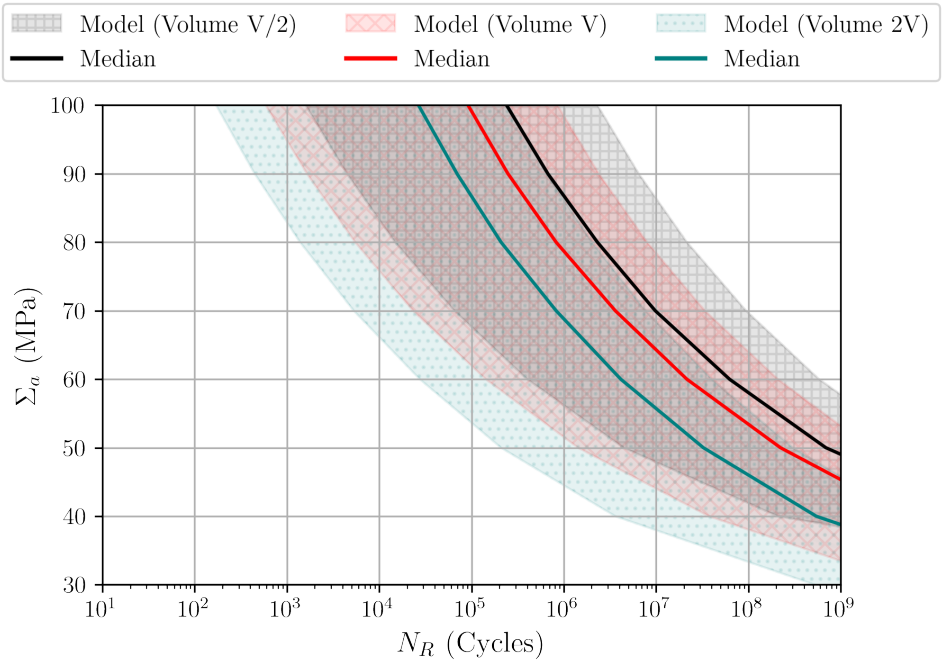

(b) Wöhler curves obtained by the model on the three specimens, with solid lines showing the median fatigue lifetimes and hatch filled areas demarcating the area contained between 1% and 99% quantiles of the fatigue lifetime distributions

Figure 2.22: Demonstration of the statistical size effect due to varying volumes

6.3 Naive homogenization to replace multi-scale method

The multi-scale method developed in this chapter is expensive to compute for entire structures, as several configurations of pore distributions need to be evaluated. In this section, we will try to replace the multi-scale method, termed **A**, with a simplified, homogenised fatigue model, termed **B**. For the identification of the homogenised model, we will generate synthetic data using the multi-scale method, for several realizations of pore distributions in a given geometry. The question is whether the homogenised model will accurately approximate the fatigue lifetime solution when applied to different geometries. The two-line fatigue model will be used for this study, with a fixed set of parameters (similar to those in section 5.3).

Generation of synthetic fatigue lifetime data using the multi-scale method

We will now generate synthetic data using the multi-scale method **A**. A total of 10 cylindrical synthetically generated porous specimens were considered for data generation (examples of the geometries have previously been shown in section 2.10). For each synthetically generated porous specimen, 1000 samples each across 9 nominal loading levels were generated using this model, as shown by the green markers in Figure 2.23.

Identification of a homogenised 0D fatigue model

Using the 0D identification procedure as described in section 4.1, the parameters of a fatigue lifetime model that maximized the likelihood of the synthetic generated data were obtained. This model **B** is a homogenised porous fatigue lifetime model. To check the quality of this homogenised model, a 3D mesh of a homogeneous pore-free cylindrical specimen of the same size and geometry as the porous cylindrical specimens was created (shown in Figure 2.23(a)), and the model **B** was used to obtain predictions on it using the weakest link method developed in section 3.4. The results, shown in Figure 2.23(b), indicate that the homogenised model **B** works well to replace the multi-scale method for the given geometry.

Notched geometry

A geometry with a macroscopic notch was created, as shown in Fig. 2.24. The sub-volume of pores used to create a porous version of this geometry was taken from the same tomography used to create the cylindrical porous specimens. Next, several configurations of the notched specimen were created:

1. Porous notched specimen with the normal expected pore density, with pores interacting with the notch
2. Porous notched specimen with a surface-breaking pore interacting with the notch artificially removed
3. Notched specimen without pores

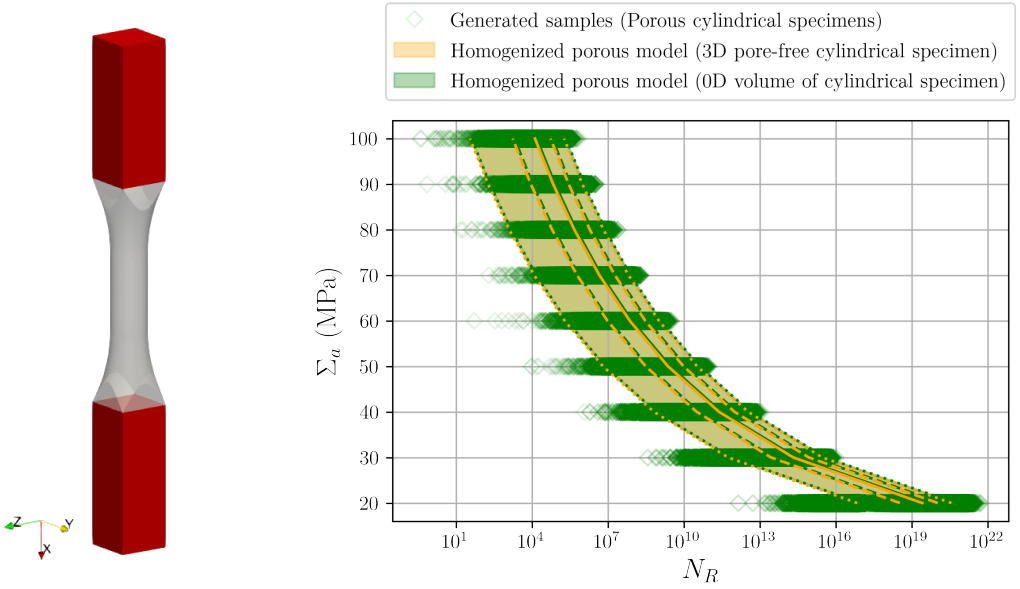

(a) 3D mesh of a pore-free cylindrical specimen

(b) Generated synthetic lifetime data from cylindrical porous specimens, identified homogenised model and predictions of the homogenised model on the 3D mesh of the pore-free cylindrical specimen

Figure 2.23: Identification of the parameters of a 0D homogenised porous fatigue model **B** on generated synthetic lifetime data from the model **A**, and validation on a 3D FE pore-free cylindrical specimen of the same shape and volume as the original cylindrical porous specimens

The criterion of the lifetime model was obtained on all these geometries via the plastic corrector methodology. The elements in the notched region were extracted for lifetime prediction, with the assumption that fatigue lifetime failure is influenced only by this volume. The extracted volumes of the different versions are shown in Fig. 2.25. In the specimen with the normal expected pore density, there are two pores interacting with the notch that give rise to very high levels of plasticity. Concerning the specimen with removed surface-breaking pore interacting with the notch, there is a lesser amount of plasticity due to reduced pore-notch interaction. The specimen without pores has the least amount of plasticity, developing only due to the notch.

Transferability check of homogenised model to notched geometry

We are now in a position to check the transferability of the homogenised model **B**. Lifetime predictions (shown in 2.26) were obtained using the following configurations:

1. Model **A** on the notched volume with normal density of pores (red)

2. Model **A** on the notched volume with one less surface-breaking pore in the notch region (green)

3. homogenised model **B** on the notched volume with no pores (black)

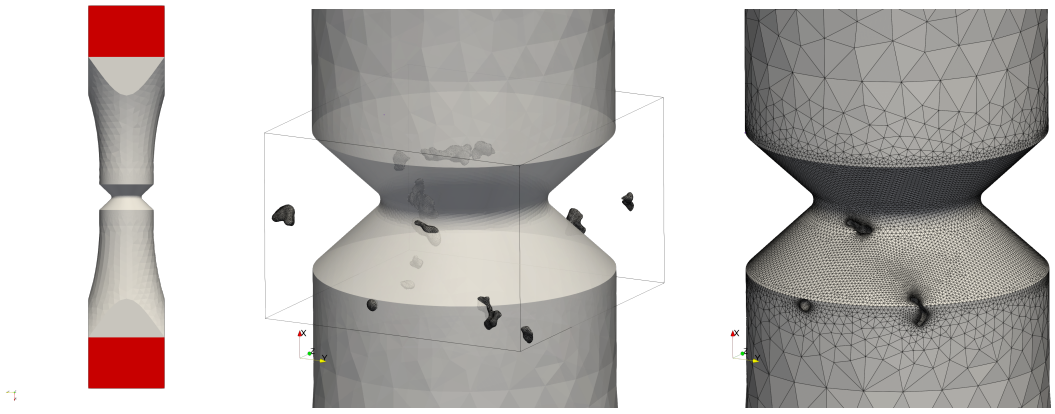

(a) (b) (c)

Figure 2.24: Creation of a notched specimen (a) boundary conditions (b) sub-volume of pores used for creation of a porous notched specimen (c) resulting mesh of the porous notched specimen

The first case i.e. obtained using the original model **A** on the volume with the normal expected pore density, can be considered as the reference solution. The predictions using the same model **A** on the volume with a surface-breaking pore interacting with the notch artificially removed shows a increase in the fatigue lifetime, due to lesser stresses in the notch region. However, both of these predictions show lesser lifetimes of the porous notch volume as compared to the homogenised porous model **B**. This indicates that the homogenised model **B** identified on cylindrical specimens is not transferable to other geometries.

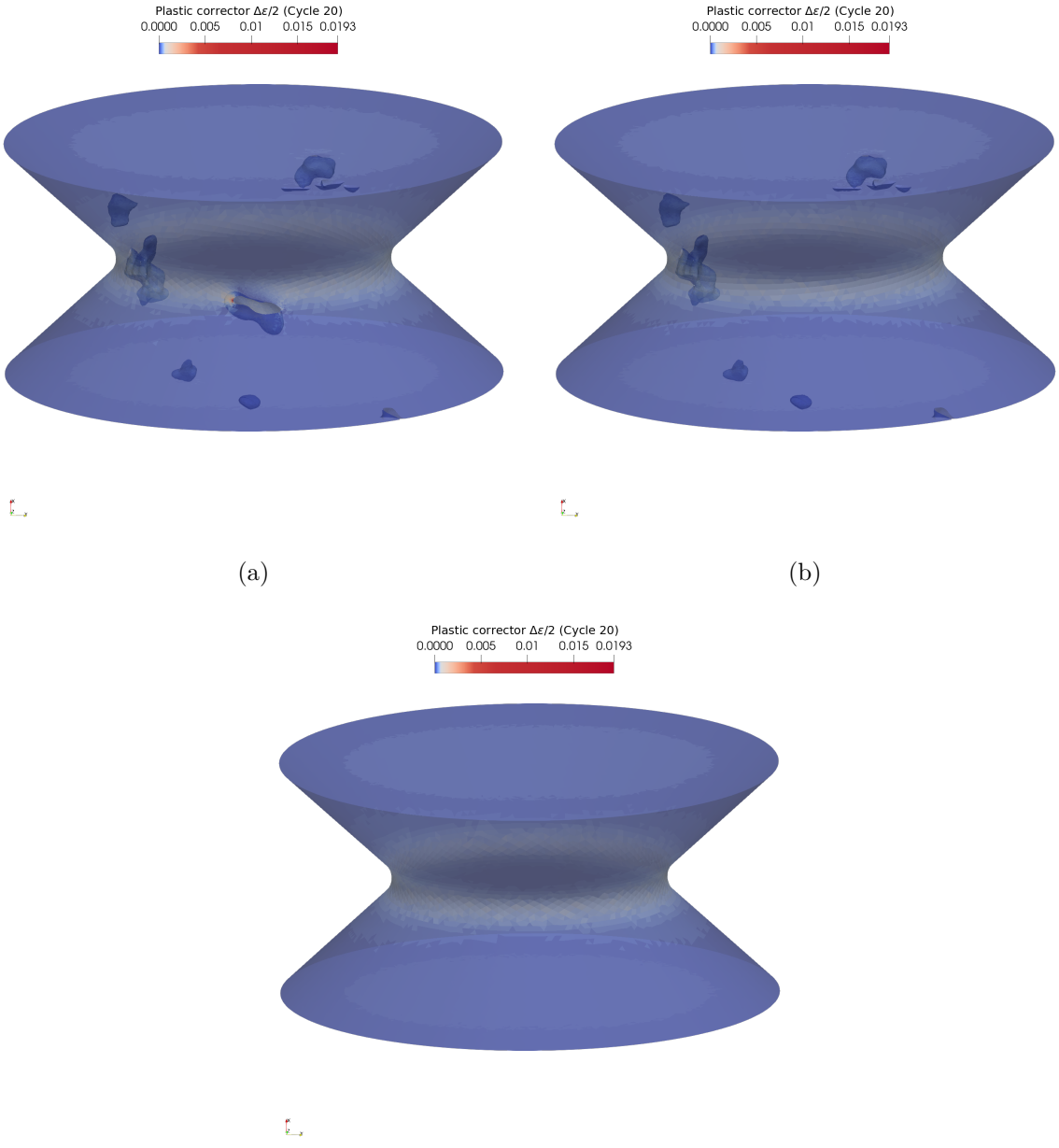

(a) (b)

(c)

Figure 2.25: Extracted volume (for lifetime prediction) of different versions of the notched specimen (a) normal density of pores (b) reduced pores interacting with notch (c) no pores

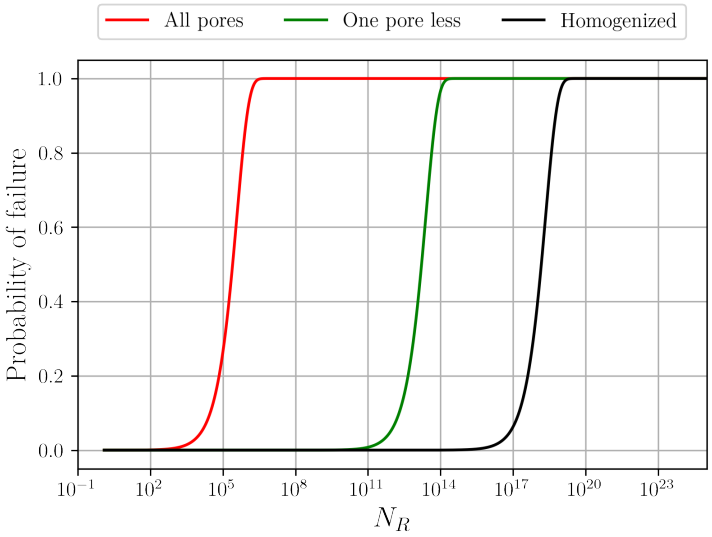

(a)

Figure 2.26: Lifetime predictions using model **A** on the notched volume with normal density of pores (red) model **A** on the notched volume with one less pore interacting with the notch (green) homogenised model **B** on a notched volume with no pores (black)

7 Overview of findings and elements of discussion

7.1 Need for meshing pores

The multi-scale method can be applied to arbitrary geometries for fatigue lifetime predictions. However, there is a need to explicitly mesh the pores in these geometries. This is because a homogenised model (simulating porous material behaviour on the fatigue lifetime) that remains transferable across varying geometries of structures is difficult to obtain. The reason for this difficulty is that the homogenised model identified for one geometry cannot capture the pore-notch interaction in the notched geometries, as discussed in section 6.3. Thus, there is a need to mesh the pores when using the multi-scale method for fatigue lifetime predictions on arbitrary geometries containing porous material.

7.2 Choice of fatigue model complexity

When optimisation is performed on only the non-porous data points (results shown in Fig. 2.12), we observe that the strain-life model with two lines (parameters A, α, B, β and C) and the model with one line (parameters A, α and C) have the same quality of fit, i.e. there is no need for the second line when fitting data in only one regime (HCF regime). However, if more data is present, especially in the LCF regime, it is likely that both lines of the strain life model would be required to obtain a consistent fit. Fig. 2.12(c) shows a significant decrease in the quality of the fit when the parameter C is omitted, which highlights its importance for getting a sensible fatigue limit. The probabilistic fatigue curves show a decrease in the uncertainty with increasing applied stress amplitude, which is a widely observed phenomenon in fatigue, and enforced with $g^{-1}(\frac{\Delta\varepsilon}{2})$ in the numerator of the Weibull scale parameter, i.e. the scale reduces for higher loads and lower N_R for a fixed shape parameter.

When optimisation is performed on only the porous data points (results shown in Fig. 2.16) both the two-line model and one line model seem to give good fits. However, as the porous data points contain information about both LCF and HCF behaviour of the alloy, it is better to work with the two-line strain-life model. Material points around pores that are highly loaded should behave in the LCF regime and points in the non-loaded zones should behave in the HCF regime.

7.3 Enabling transferability of fatigue models between different types of pore populations

Any fatigue lifetime model that needs to be accurate across different loading regimes (LCF and HCF) first needs to be properly identified with experimental data across the entire load spectra. The multi-scale method's capability of treating different alloys of porous material as made of the same base material is thus advantageous. The base material is considered to have a unique behaviour, thus sparse data on different types of pore populations across various loading spectra can be exploited with ease. This is because the multi-scale method, by design, only requires a small representative tomography of the pore population for each grade of porosity. Additionally, the required FEA computations on statistically representative pore fields are accelerated by the

plastic corrector [Palchoudhary et al., 2024b].

The numerical results on the aluminium data-set demonstrate this: the model is able to treat the non-porous grade and the porous grade to be made of the same base material, and identification of a transferable model between these two grades is possible with lesser data than the simplified approach of treating the porous material as a different material than the non-porous one.

7.4 Diversity of exploitable lifetime data for a model transferable between pore populations

Two types of lifetime data are usable to identify a fatigue lifetime model with the proposed multi-scale approach. For example, to identify the model in the HCF regime, one may either load porous specimens at very low levels of stress such that the base material around the pores is loaded in the HCF regime, or by loading specimens made of the base material itself in the HCF regime. This can be particularly helpful if lifetime data on the base material (without porosity) is expensive or time consuming to obtain, or if a limited amount of lifetime data is present for each category of porosity.

For the example presented in this chapter in section 5.2, the two-line fatigue model (identified on the limited set of porous fatigue experiments, across a small range of loading levels) lacks information on distinguishing between the fatigue regimes. However, when the model is given some non-porous fatigue lifetime points at lower stress levels (in section 5.3), it learns to better differentiate between the two regimes of fatigue behaviour of the base material. The base material behaviour in the HCF regime is identified using these non-porous points. In porous specimens, the base material near pores, being loaded at a higher level, informs the LCF fatigue behaviour. In other words, the model learns about different regimes of fatigue behaviour of the base material from the lifetime data of the two grades of porosity.

8 Conclusions

In this chapter, we propose a probabilistic fatigue lifetime model combined with a multi-scale method to model the lifetime of structures with pores whose exact distribution is unknown. The effect of the pores on the fatigue lifetime is modelled using statistical methods based on a small representative tomography of the porous material. The multi-scale aspect is facilitated by a FEA accelerator for lifetime criterion computations when non-linearity is present in the material model.

The identification procedure involves a maximum likelihood estimate, utilizing pre-computed statistically representative heterogeneous 3D elasto-plastic fields obtained via FEA during optimisation. Run-outs are used as valid experimental data by assigning them a finite probability of future failure.

The multi-scale approach developed in this chapter allows materials with varying grades of porosity to be treated as if made of the same base material, thus enabling the use of lifetime data from materials with different pore populations for the identification of a singular fatigue

lifetime model. This approach reduces the overall lifetime data required for identifying the fatigue lifetime model as compared to approaches that treat each porous grade as a different material.

Additionally, by construction, the model accounts for the statistical size effect in fatigue, where larger volumes fail earlier under iso-stress conditions. Furthermore, the model allows for the approximation of Wöhler curves across arbitrary geometries, enabling lifetime estimation even without the need for full tomography of the structure. This is achieved using a small representative volume containing information about the pores, making the model both efficient and effective. The prediction time is comparable to the cost of an elastic-static FEA computation, as the plasticity in the stabilized cycle is computed through the use of a plastic corrector [Palchoudhary et al., 2024b] - this will be the focus of the following chapter. However, the model does require meshes where pores are explicitly represented, as a simple homogenization of the porous material does not reproduce the multi-scale method's prediction for all geometries. Additionally, the optimisation process, particularly when solving fatigue lifetime computation via residual minimization, is resource-intensive.

Chapter 3

A plastic correction algorithm for full-field elasto-plastic finite element simulations

Résumé

Ce chapitre présente un nouvel algorithme de correction plastique locale qui vise à accélérer les simulations élasto-plastiques par éléments finis pour les problèmes structurels présentant une plasticité localisée (autour, par exemple, d'entailles ou de défauts géométriques). La méthode proposée appartient à la catégorie des méthodes multiaxiales généralisées de type Neuber, qui traitent les résultats d'une prédiction élastique de manière ponctuelle afin de calculer une approximation de la solution élasto-plastique complète. L'algorithme proposé repose sur une règle de proportionnalité locale qui, dans le contexte de la plasticité J2, nous permet d'exprimer le problème de la correction plastique en termes d'amplitude des tenseurs mécaniques complets uniquement. Ce problème de correction légère peut être résolu numériquement à l'aide d'un intégrateur temporel entièrement implicite qui présente des similitudes avec l'algorithme de retour radial. Les capacités numériques de l'algorithme proposé sont démontrées pour une structure entaillée et un spécimen contenant une distribution de pores sphériques, soumis à une charge monotone et cyclique. Comme deuxième point d'innovation, nous montrons que l'algorithme de correction plastique locale proposé peut être encore accéléré en employant une simple stratégie de méta-modélisation, sans pratiquement aucune erreur supplémentaire. Enfin, nous développons et étudions les mérites d'une couche corrective basée sur l'apprentissage profond et conçue pour l'erreur d'approximation du correcteur plastique. Une architecture convolutionnelle est utilisée pour analyser les voisinages des points matériels et produit une correction scalaire des prédictions ponctuelles de type Neuber. Cette brique optionnelle de la méthodologie de correction plastique proposée repose sur la disponibilité d'un ensemble de solutions d'éléments finis élasto-plastiques complètes à utiliser comme ensemble de données d'apprentissage.

1 Introduction

In the previous chapter, a lifetime model was introduced that operates on the stress-strain history in the entire computational domain, notably the base material around pores. These fields are expensive to obtain because of the high number of degrees of freedom needed to accurately represent the pores in the finite element meshes, the presence of local non-linearity in the material model (such as localized plasticity), and the necessity of achieving a stabilised cycle due to the transitional hardening phase. This chapter proposes an acceleration of elasto-plastic computations in structures via a plastic corrector. The method uses a Neuber-type plastic correction heuristic coupled with machine learning methods that allows rapid approximation of the elasto-plastic fields in any structure, under proportional loading conditions. This chapter is an adaptation of the article titled 'A plastic correction algorithm for full-field elasto-plastic finite element simulations : critical assessment of predictive capabilities and improvement by machine learning' written during the PhD program [Palchoudhary et al., 2024b].

The first point of innovation proposed in this chapter is the development of a multiaxial Neuber-type plastic correction method that may be used to produce approximations of elasto-plastic quantities at every quadrature point of a finite element mesh. As such, the developed methodology will not rely on particular strain state assumptions regarding the recovery of elasto-plastic solutions at traction-free boundaries. Our proposal is to use a local proportionality rule for the deviatoric stress and strain tensors, which will therefore be linearly related to their counterparts as calculated using an elasto-static analysis. Remarkably, in the context of J2 plasticity (we use a Chaboche model with kinematic and isotropic hardening), the local proportionality rule results in scalar constitutive equations for the deviatoric strain and stress amplitudes, without further assumption on plastic flow, which was already identified in [Desmorat, 2002]. Complemented by a scalar Neuber-type rule, the constitutive equations may be solved locally, the load stemming directly from that heuristic rule. We use the standard change of peaks method [Chaudonneret and Culié, 1985] to account for load cycles with non-zero mean stresses. We will analyse the accuracy of full 3D elasto-plastic solutions computed using the Neuber-type approximation, i.e. at and away from notches and free boundaries. This full-field aspect is particularly relevant to fields whereby fracture criteria are based on full-field elasto-plastic solutions, for example non-local fatigue models that use elasto-plastic fields around critical points [Taylor, 2005], or weakest-link models that compute probabilities of failure via a weighted average of mechanical stresses over the entire computational domain [Beremin et al., 1983, Zok, 2017].

The second point of novelty is a machine-learning-based acceleration of the proposed plastic corrector, which is particularly useful for finite element models exhibiting a large number of degrees of freedom and long time analyses. This is because the local time integration of the elasto-plastic equations, using the plastic correction methodology mentioned previously, remains computationally expensive. We show that under the previously stated rules (J2 plasticity, proportionality of deviatoric strain and stress tensors, scalar Neuber rule), and for a given load history, any output of the plastic correction algorithm exhibits a (nontrivial) scalar dependency to the von Mises stress of the elastic finite element simulation. Therefore, we suggest a meta-

modelling strategy in the form of a Gaussian process regression [Rasmussen and Williams, 2006], that will be trained to produce the elasto-plastic quantity of interest given a von Mises stress stemming from the elasto-static simulation as input. A dataset is generated by populating the real positive axis and computing the corresponding outputs using the plastic corrector. Few (30 to 150) such datapoints are necessary for a one-dimensional regression. We show that training the Gaussian process regression on such a small dataset is sufficient to act as a virtually cost-free surrogate for all remaining local plastic corrections, without sacrificing accuracy. As a consequence, the cost of acquiring approximated elasto-plastic quantities for specimens with single or multiple stress concentrators reduces to the cost of the elastic finite element simulation, as the number of degrees of freedom of the finite element model increases.

As a third and more exploratory part of the development, we propose a methodology of plastic correction using neural networks, which we coin Neural plastic corrector (NPC). The Neural Network developed here will be used to correct the output of the proposed Neuber-type methodology in order to better reproduce the mechanical fields delivered by a full elasto-plastic finite element analysis. While the Neuber-type method described thus far never requires elasto-plastic finite element simulations to be performed, the NPC is based on training with examples (supervised learning), and is therefore based on the availability of reference elasto-plastic solutions that will be used as a dataset. The Neuber corrector being local by nature, we aim to correct it by using information about the local topology of material point neighbourhoods, which will be analysed in an end-to-end fashion by a Convolutional Neural Network (CNN). More precisely, we will first voxelise the neighbourhood of any point of interest. We will then project the result of the previously described Neuber-type methodology to be improved onto the voxelised neighbourhood. Finally, we will provide this gridded data as input to a Neural network and train it to predict a correction to the elasto-plastic quantity of interest obtained approximately using the Neuber-type plastic corrector. Whilst the previously introduced Neuber-type method may be applied to general structures exhibiting stress concentrations, the Neural plastic corrector will be dedicated to the analysis of specimens with randomly placed pores, such as those that may be of interest when simulating the failure of porous alloys obtained by casting, welding or additive manufacturing [Bercelli et al., 2021, Merot et al., 2024, Palchoudhary et al., 2024a]. In this context, the necessity to analyse specimens, or batches of specimens, containing large quantities of defects may justify the deployment of an AI that learns from a small to medium quantity of reference elasto-plastic simulations in order to predict the elasto-plastic output of subsequent simulations. We do not anticipate a strong generalisation ability of the NPC, consistently with observations and analyses made in our previous work [Krokos et al., 2021, Krokos et al., 2024], albeit in a different mechanical context. However, we will show that the output of the Neuber-type methodology may be improved upon by the proposed AI, using a reasonable amount of data for training, and that using the output of our Neuber-type methodology as full-field input to the CNN is indeed beneficial as compared to using inputs of the NPC with a lesser mechanical content.

This chapter is divided into four sections: the first section introduces the proposed Neuber-type plastic corrector scheme. The second section is devoted to results and error analysis of the

plastic correction algorithm for two different problems : A structure with a notch undergoing monotonic loading, and a specimen made of a porous alloy with a spherical pore population undergoing monotonic and cyclic loading. The third section introduces the meta-modelling strategy proposed to accelerate the plastic correction algorithm, and the fourth section presents the Neural Plastic Correction strategy. The three elements introduced in the chapter are separately validated in the section where they are respectively presented. The chapter is concluded by a discussion and perspectives of future studies.

2 Full field Neuber-type plastic corrector

2.1 Linear elasticity problem

Neuber-type methods approximate plasticity by locally processing the stress and strain fields stemming from a single elasto-static finite element analysis. We set up a linear elastic problem in an isotropic material, with stiffness tensor $\mathcal{C}$ and Lamé coefficients λ, μ, over a time interval $[0, T]$, whereby proportional loading conditions are assumed at the global level, i.e. that of the structure. The time-dependent displacement, stress and strain tensors for the elasto-static simulation are denoted by $\underline{u}^{\#}(t)$, $\underline{\underline{\sigma}}^{\#}(t)$ and $\underline{\underline{\varepsilon}}^{\#}(t)$, respectively. The identity tensor is denoted by $\mathbb{I}$. The boundary $\partial\Omega$ of computational domain Ω is additively split into a Dirichlet part $\partial\Omega_u$ and a Neumann part $\partial\Omega_t$. The equations of linearised elasticity are introduced as follows:

$$\operatorname{div} \underline{\underline{\sigma}}^{\#}(t) + f(t)\,\underline{\bar{\xi}} = 0 \tag{3.1}$$

$$\underline{\underline{\sigma}}^{\#}(t) = \mathcal{C} : \underline{\underline{\varepsilon}}^{\#}(t) = \lambda \mathrm{Tr}(\underline{\underline{\varepsilon}}^{\#}(t))\mathbb{I} + 2\mu\underline{\underline{\varepsilon}}^{\#}(t) \tag{3.2}$$

$$\underline{\underline{\varepsilon}}^{\#}(t) = \frac{1}{2}(\nabla \underline{u}^{\#}(t) + \nabla \underline{u}^{\#}(t)^T) \tag{3.3}$$

$$\underline{u}^{\#}(t) = f(t)\,\underline{\bar{u}}_a \qquad \text{over} \quad \partial\Omega_u \tag{3.4}$$

$$\underline{\underline{\sigma}}^{\#}(t) \cdot \underline{n} = f(t)\,\underline{\bar{t}}_a \qquad \text{over} \quad \partial\Omega_t \tag{3.5}$$

In the previous set of equations, $f : [0, T] \mapsto \mathbb{R}$ is an arbitrary function of time that may be set to simulate, for example, proportionally monotonic and cyclic loading. $\underline{\bar{\xi}}$ is a vector-valued field of volume forces, $\underline{\bar{u}}_a$ is a vector-valued field of applied displacements, and $\underline{\bar{t}}_a$ is a vector-valued field of applied traction loads. The previous elastic time-dependent problem is proportional, in the sense that all prescribed loading conditions, be it Neumann, Dirichlet conditions or volume sources, are introduced as fixed vector-valued fields multiplied by a function of time f.

Therefore, $\underline{u}^{\#}(t)$, $\underline{\underline{\sigma}}^{\#}(t)$ and $\underline{\underline{\varepsilon}}^{\#}(t)$ may be obtained by solving the equation of elasto-statics for $f = 1$, and processed in the following way to recover the history of elastic solutions over $[0, T]$:

$$\underline{u}^{\#}(t) = f(t)\,\underline{\bar{u}}^{\#} \tag{3.6}$$

$$\underline{\underline{\sigma}}^{\#}(t) = f(t)\,\underline{\underline{\bar{\sigma}}}^{\#} \tag{3.7}$$

$$\underline{\underline{\varepsilon}}^{\#}(t) = f(t)\,\underline{\underline{\bar{\varepsilon}}}^{\#} \tag{3.8}$$

where $\underline{\bar{u}}^{\#}$, $\underline{\underline{\bar{\sigma}}}^{\#}$ and $\underline{\underline{\bar{\varepsilon}}}^{\#}$ are, respectively, the displacement field, the stress tensor and the strain tensor fields obtained by setting $f = 1$. (note: a bar symbol ($\bar{\bullet}$) is used to denote quantities that are obtained by solving the equations of elasto-statics with $f = 1$).

If the elastic deviatoric stress and strain tensors obtained for $f = 1$ are denoted by $\underline{\underline{\bar{\sigma}}}_d^{\#}$ and $\underline{\underline{\bar{\varepsilon}}}_d^{\#}$ respectively, then the elastic deviatoric tensors at any time t (denoted by $\underline{\underline{\sigma}}_d^{\#}(t)$ and $\underline{\underline{\varepsilon}}_d^{\#}(t)$) are obtained by the following scaling:

$$\underline{\underline{\sigma}}_d^{\#}(t) = f(t)\,\underline{\underline{\bar{\sigma}}}_d^{\#} \tag{3.9}$$

$$\underline{\underline{\varepsilon}}_d^{\#}(t) = f(t)\,\underline{\underline{\bar{\varepsilon}}}_d^{\#} \tag{3.10}$$

2.2 Von Mises plasticity constitutive model

A von Mises plasticity model with a non-linear kinematic hardening and a non-linear isotropic hardening is chosen for the description of the evolution of the yield surface [Chaboche, 1989]. The deviator of the stress tensor $\underline{\underline{\sigma}}$ is henceforth denoted by $\underline{\underline{\sigma}}_d$, the total strain by $\underline{\underline{\varepsilon}}$ and the plastic strain tensor by $\underline{\underline{\varepsilon}}^p$. Elasticity is given by

$$\underline{\underline{\sigma}} = \mathcal{C} : (\underline{\underline{\varepsilon}} - \underline{\underline{\varepsilon}}^p) \tag{3.11}$$

The von Mises stress is given as:

$$\mathcal{J}(\underline{\underline{\sigma}}_d - \underline{\underline{X}}) = \sqrt{\frac{3}{2}(\underline{\underline{\sigma}}_d - \underline{\underline{X}}) : (\underline{\underline{\sigma}}_d - \underline{\underline{X}})} \tag{3.12}$$

where $\underline{\underline{X}}$ is the non-linear kinematic hardening tensor. The expression for the plastic strain rate $\dot{\underline{\underline{\varepsilon}}}^p$ is given as:

$$\dot{\underline{\underline{\varepsilon}}}^p = \dot{p}\left(\frac{3}{2}\frac{\underline{\underline{\sigma}}_d - \underline{\underline{X}}}{\mathcal{J}(\underline{\underline{\sigma}}_d - \underline{\underline{X}})}\right) \tag{3.13}$$

The evolution of $\underline{\underline{X}}$ is given by the following expression:

$$\dot{\underline{\underline{X}}} = \frac{2}{3}C\dot{\underline{\underline{\varepsilon}}}^p - D\underline{\underline{X}}\dot{p} \tag{3.14}$$

where $\dot{p}$ is the time evolution of the cumulative plastic strain p, and C and D are kinematic hardening material parameters. The isotropic hardening $R(p)$ is given by the following expression:

$$R(p) = Q(1 - \exp(-bp)) \tag{3.15}$$

where Q and b are isotropic hardening material parameters. The deviator of the plastic strain tensor is used to define the cumulative plastic strain rate:

$$\dot{p} = \sqrt{\frac{2}{3}\dot{\underline{\underline{\varepsilon}}}_d^p : \dot{\underline{\underline{\varepsilon}}}_d^p} \tag{3.16}$$

The evolution of the yield surface $f_y(\underset{\sim}{\sigma}_d; \underset{\sim}{X}, p)$ is required to satisfy the following two constraints:

$$f_y(\underset{\sim}{\sigma}_d; \underset{\sim}{X}, p) = \mathcal{J}(\underset{\sim}{\sigma}_d - \underset{\sim}{X}) - \sigma_y - R(p) \leq 0 \tag{3.17}$$

$$f_y \dot{p} = 0 \tag{3.18}$$

2.3 Modified Neuber rule

Neuber rule for deviatoric stress and strain tensors

The Neuber-type rule proposed in this chapter operates on the deviatoric parts of the stress and strain tensors [Buczynski and Glinka, 2003]:

$$\hat{\underset{\sim}{\sigma}}_d : \hat{\underset{\sim}{\varepsilon}}_d = \underset{\sim}{\sigma}_d^{\#} : \underset{\sim}{\varepsilon}_d^{\#} \tag{3.19}$$

where $\hat{\underset{\sim}{\sigma}}_d$, $\hat{\underset{\sim}{\varepsilon}}_d$ stand for the approximated deviatoric stress and strain tensors, respectively (note: a hat symbol ($\hat{\bullet}$) is used to denote quantities that are approximated by the plastic corrector).

Tensors $\underset{\sim}{\sigma}_d^{\#}$, $\underset{\sim}{\varepsilon}_d^{\#}$, which are obtained by solving elasto-statics instead of elasto-plasticity, are time-dependent, but the (t) notation has been dropped for conciseness.

Cyclic loading is handled with the classical change of origin at every peak, as proposed by Chaudonneret [Chaudonneret and Culié, 1985]:

$$(\hat{\underset{\sim}{\sigma}}_d - \hat{\underset{\sim}{\sigma}}_{d,o}) : (\hat{\underset{\sim}{\varepsilon}}_d - \hat{\underset{\sim}{\varepsilon}}_{d,o}) = (\underset{\sim}{\sigma}_d^{\#} - \underset{\sim}{\sigma}_{d,o}^{\#}) : (\underset{\sim}{\varepsilon}_d^{\#} - \underset{\sim}{\varepsilon}_{d,o}^{\#}) \tag{3.20}$$

In the previous equation, quantities $\hat{\underset{\sim}{\sigma}}_{d,o}$, $\hat{\underset{\sim}{\varepsilon}}_{d,o}$ stand for the approximated deviatoric stress and strain tensors at the last peak of loading. The tensors $\underset{\sim}{\sigma}_{d,o}^{\#}$, $\underset{\sim}{\sigma}_{d,o}^{\#}$ stand for the deviatoric stress and strain tensors coming from the elastic finite element solution evaluated at the last peak.

Proportional evolution rule for deviatoric stress and strain tensors

It is important to note that stresses and strains in a structure depend on the geometry, the material behaviour and the boundary conditions. When there is a change in the ratio of any two components of the stress tensor at a given material point, these local stresses become non-proportional, by definition. If there is plastic flow anywhere in the structure, local non-proportionality may arise even in the case where the external loading is proportional.

The Neuber rule developed so far and the constitutive relations operate on symmetric second order tensors. We assume local proportionality [Desmorat, 2002], that is, while the local evolution of the actual deviatoric stress and strain tensors at a point may be arbitrarily complex, we postulate that the evolution is well approximated by assuming that it remains in the direction of the deviatoric stress and strain tensors obtained from elasto-statics, i.e. there is no shift in the direction in which plasticity develops.

Therefore, the deviatoric stress tensor may be written as a scaling of the stress tensor stem-

ming from elasto-statics, which reads as

$$\hat{\underset{\sim}{\sigma}}_d(t) = s(t)\bar{\underset{\sim}{\sigma}}_d^{\#} \tag{3.21}$$

and similarly for the deviatoric strain tensor,

$$\hat{\underset{\sim}{\varepsilon}}_d(t) = e(t)\bar{\underset{\sim}{\varepsilon}}_d^{\#} \tag{3.22}$$

where the scalar variables s and e are introduced as scaling factors to be determined.

Neuber rule in terms of proportionality ratios

Taking the local proportionality rules into account, the Neuber rule reduces to a constraint on scalar variables s and e. By substituting equations (3.9) and (3.10), and (3.21) and (3.22) into equation (3.19), the monotonic Neuber rule, in the case of monotonic loading functions, becomes:

$$s\,e\,\bar{\underset{\sim}{\sigma}}_d^{\#} : \bar{\underset{\sim}{\varepsilon}}_d^{\#} = f^2\,\bar{\underset{\sim}{\sigma}}_d^{\#} : \bar{\underset{\sim}{\varepsilon}}_d^{\#} \tag{3.23}$$

which yields

$$s\,e = f^2 \tag{3.24}$$

where we remind the reader that s, e and f are time-dependent variables (the (t) notation has been dropped for conciseness).

For cyclic loading, we introduce s_o and e_o, which are the values of the scalar variables s and e at the last peak. Substituting equations (3.9) and (3.10), and (3.21) and (3.22) into equation (3.20):

$$(s\bar{\underset{\sim}{\sigma}}_d^{\#} - s_o\bar{\underset{\sim}{\sigma}}_d^{\#}) : (e\bar{\underset{\sim}{\varepsilon}}_d^{\#} - e_o\bar{\underset{\sim}{\varepsilon}}_d^{\#}) = (f\bar{\underset{\sim}{\sigma}}_d^{\#} - f_o\bar{\underset{\sim}{\sigma}}_d^{\#}) : (f\bar{\underset{\sim}{\varepsilon}}_d^{\#} - f_o\bar{\underset{\sim}{\varepsilon}}_d^{\#}) \tag{3.25}$$

$$\bar{\underset{\sim}{\sigma}}_d^{\#} : \bar{\underset{\sim}{\varepsilon}}_d^{\#}(s - s_o)(e - e_o) = \bar{\underset{\sim}{\sigma}}_d^{\#} : \bar{\underset{\sim}{\varepsilon}}_d^{\#}(f - f_o)(f - f_o) \tag{3.26}$$

$$(s - s_o)(e - e_o) = (f - f_o)^2 \tag{3.27}$$

The scalar constraint between (deviatoric) stress and strain amplitudes is illustrated in Figure 3.1 in the context of cycling loading. During the first branch of loading (denoted by the superscript 1), the quantities s_o and e_o take on the initial values of s_o^1 and e_o^1, i.e. 0, and s and e evolve as s^1 and e^1. When the peak of loading is reached, and a load reversal is made for a second branch of loading (denoted by the superscript 2), the values of s_o and e_o are updated to the previous peak values, shown in the figure as s_o^2 and e_o^2. Next, s and e evolve as s^2 and e^2 according to the updated origin. This process is repeated, with the quantities s_o and e_o successively taking on the values of s and e at every peak of loading following all the load reversals defined in the function $f(t)$. Equation (3.27) will be complemented by the elasto-plastic constitutive equations to yield a constitutive update algorithm.

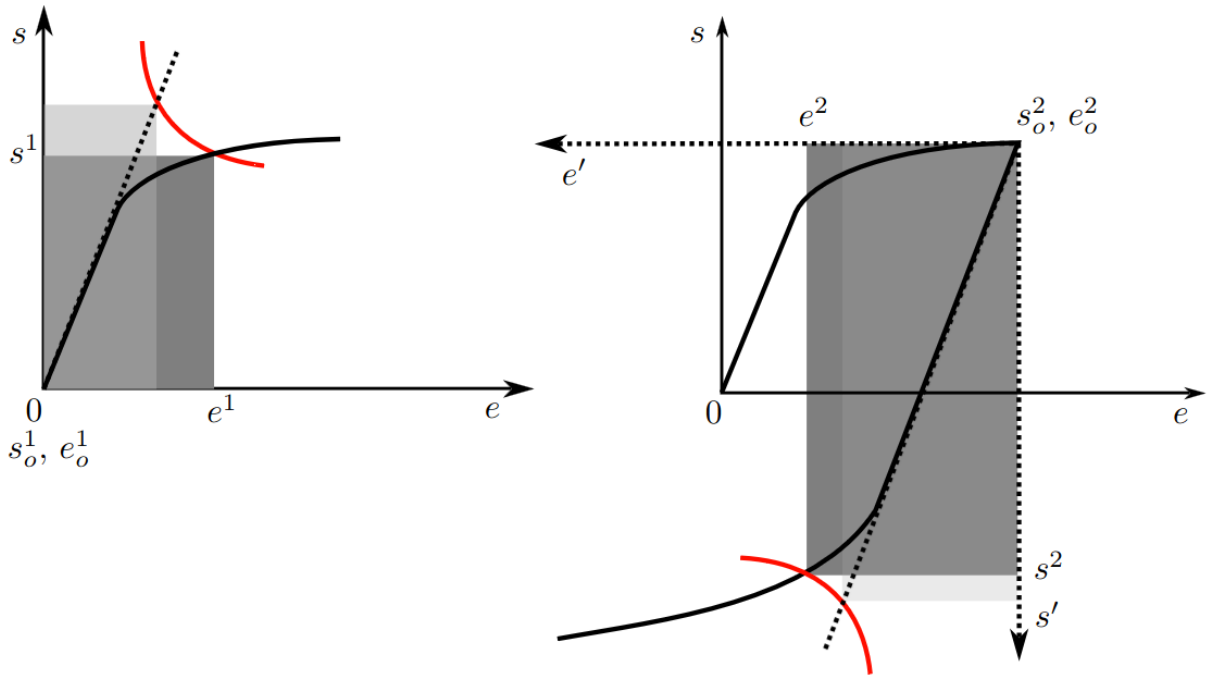

Figure 3.1: An illustration of the plastic correction algorithm during the (a) first branch of loading (b) second branch of loading, with s_o and e_o updated to their respective values at the last peak

2.4 Elasto-plastic constitutive equations under proportional tensor evolutions

The aim of this section is to reduce the tensorial equations of the constitutive law (presented in section 2.2) to scalar equations, using the rules of proportionality stated in equations (3.21) and (3.22), leading to a set of reduced constitutive equations in a set of scalar variables including s and e. The reader is reminded that a hat symbol ($\hat{.}$) is used to denote quantities approximated by the plastic corrector.

Stress-strain relation

The approximated stress tensor is given by:

$$\hat{\underline{\underline{\sigma}}} = 2\mu(\hat{\underline{\underline{\varepsilon}}} - \hat{\underline{\underline{\varepsilon}}}^p) + \lambda \mathrm{Tr}(\hat{\underline{\underline{\varepsilon}}} - \hat{\underline{\underline{\varepsilon}}}^p)\mathbb{I} \tag{3.28}$$

The approximated stress tensor $\hat{\underline{\underline{\sigma}}}$ can be split into its approximated deviatoric $\hat{\underline{\underline{\sigma}}}_d$ and hydrostatic $\hat{\underline{\underline{\sigma}}}_h$ parts:

$$\hat{\underline{\underline{\sigma}}} = \hat{\underline{\underline{\sigma}}}_d + \hat{\underline{\underline{\sigma}}}_h \tag{3.29}$$

where the approximated deviatoric stress tensor $\hat{\underline{\underline{\sigma}}}_d$, under isochoric plastic flow, becomes:

$$\hat{\underline{\underline{\sigma}}}_d = 2\mu(\hat{\underline{\underline{\varepsilon}}}_d - \hat{\underline{\underline{\varepsilon}}}_d^p) \tag{3.30}$$

The deviatoric strain is approximated by assuming proportional evolution to the deviatoric strain coming from the elasto-static simulation (refer to Section 2.3). By virtue of equations (3.13) and (3.30) the plastic deviatoric strain evolves proportionally to the deviatoric strain coming from the elasto-static simulation, $\bar{\underset{\sim}{\varepsilon}}^{\#}_d$. A scalar variable e^p can be introduced to encode this:

$$\hat{\underset{\sim}{\varepsilon}}^p_d(t) = e^p(t)\bar{\underset{\sim}{\varepsilon}}^{\#}_d \tag{3.31}$$

The approximated stress and strain tensors in equation (3.30) are replaced with the scalar variables s, e and e^p and the corresponding quantities from elasto-statics $\bar{\underset{\sim}{\sigma}}^{\#}_d$ and $\bar{\underset{\sim}{\varepsilon}}^{\#}_d$:

$$s\bar{\underset{\sim}{\sigma}}^{\#}_d = 2\mu(e\bar{\underset{\sim}{\varepsilon}}^{\#}_d - e^p\bar{\underset{\sim}{\varepsilon}}^{\#}_d) \tag{3.32}$$

A projection of equation (3.32) in the direction of $\bar{\underset{\sim}{\varepsilon}}^{\#}_d$ is carried out:

$$s\bar{\underset{\sim}{\sigma}}^{\#}_d : \bar{\underset{\sim}{\varepsilon}}^{\#}_d = 2\mu(e\bar{\underset{\sim}{\varepsilon}}^{\#}_d : \bar{\underset{\sim}{\varepsilon}}^{\#}_d - e^p\bar{\underset{\sim}{\varepsilon}}^{\#}_d : \bar{\underset{\sim}{\varepsilon}}^{\#}_d) \tag{3.33}$$

As $\bar{\underset{\sim}{\sigma}}^{\#}_d : \bar{\underset{\sim}{\varepsilon}}^{\#}_d = 2\mu\bar{\underset{\sim}{\varepsilon}}^{\#}_d : \bar{\underset{\sim}{\varepsilon}}^{\#}_d$ (owing to the properties of isotropic linear elasticity), equation (3.33) reduces to:

$$s = e - e^p \tag{3.34}$$

This equation for s can be extended to the cyclic variant $(s - s_o)$ by writing:

$$s - s_o = (e - e_o) - (e^p - e^p_o) \tag{3.35}$$

Here, alongside the updating strategy of s_o and e_o previously described in section 2.3, e^p_o is also updated with the value of e^p at the last peak, every time a load reversal takes place.

Von Mises Stress

By virtue of equations (3.14) and (3.31), the approximated kinematic hardening tensor evolves proportionally to the deviatoric strain stemming from the elasto-static computation. A scalar variable x can be introduced to encode this:

$$\underset{\sim}{X}(t) = x(t)\bar{\underset{\sim}{\varepsilon}}^{\#}_d \tag{3.36}$$

Then, equation (3.12), with equations (3.21) and (3.36), now reads:

$$\hat{\mathcal{J}}(s,x) = \sqrt{\frac{3}{2}(s^2\bar{\underset{\sim}{\sigma}}^{\#}_d : \bar{\underset{\sim}{\sigma}}^{\#}_d - 2sx\bar{\underset{\sim}{\sigma}}^{\#}_d : \bar{\underset{\sim}{\varepsilon}}^{\#}_d + x^2\bar{\underset{\sim}{\varepsilon}}^{\#}_d : \bar{\underset{\sim}{\varepsilon}}^{\#}_d)} \tag{3.37}$$

From $\bar{\sigma}^{\#}_{VM} = \sqrt{\frac{3}{2}\bar{\underset{\sim}{\sigma}}^{\#}_d : \bar{\underset{\sim}{\sigma}}^{\#}_d}$ and $\bar{\underset{\sim}{\sigma}}^{\#}_d = 2\mu\bar{\underset{\sim}{\varepsilon}}^{\#}_d$ we retrieve $\bar{\underset{\sim}{\sigma}}^{\#}_d : \bar{\underset{\sim}{\sigma}}^{\#}_d = \frac{2}{3}(\bar{\sigma}^{\#}_{VM})^2$, $\bar{\underset{\sim}{\sigma}}^{\#}_d : \bar{\underset{\sim}{\varepsilon}}^{\#}_d = \frac{1}{3\mu}(\bar{\sigma}^{\#}_{\mathrm{VM}})^2$ and $\bar{\underset{\sim}{\varepsilon}}^{\#}_d : \bar{\underset{\sim}{\varepsilon}}^{\#}_d = \frac{1}{6\mu^2}(\bar{\sigma}^{\#}_{\mathrm{VM}})^2$.

This finally leads to:

$$\hat{\mathcal{J}}(s,x) = \left|s - \frac{x}{2\mu}\right| \bar{\sigma}^{\#}_{\mathrm{VM}} \tag{3.38}$$

Kinematic hardening

We now need to derive the scalar evolution equation for $\dot{x}$ as a function of x and e^p. From equation (3.14), with equations (3.31) and (3.36), we have

$$\dot{x}\bar{\underset{\sim}{\varepsilon}}_d^{\#} = \frac{2}{3}C\dot{e}^p\bar{\underset{\sim}{\varepsilon}}_d^{\#} - D\dot{\hat{p}}x\bar{\underset{\sim}{\varepsilon}}_d^{\#} \tag{3.39}$$

and therefore, after multiplying the right and left hand-side by $\bar{\underset{\sim}{\varepsilon}}_d^{\#}$ and dividing both sides by $\bar{\underset{\sim}{\varepsilon}}_d^{\#} : \bar{\underset{\sim}{\varepsilon}}_d^{\#}$, we found that

$$\dot{x} = \frac{2}{3}C\dot{e}^p - Dx\dot{\hat{p}} \tag{3.40}$$

Flow rule

We now reformulate the flow rule in terms of scalar variables s, x and e^p. From equation (3.13), with equations (3.21), (3.31) and (3.36), we have that:

$$\dot{e}^p\bar{\underset{\sim}{\varepsilon}}_d^{\#} = \dot{\hat{p}}\left(\frac{3}{2}\frac{s\bar{\underset{\sim}{\sigma}}_d^{\#} - x\bar{\underset{\sim}{\varepsilon}}_d^{\#}}{\hat{\mathcal{J}}(s,x)}\right) \tag{3.41}$$

A projection of this equation (3.41) in the direction of $\bar{\underset{\sim}{\varepsilon}}_d^{\#}$ is carried out:

$$\dot{e}^p\bar{\underset{\sim}{\varepsilon}}_d^{\#} : \bar{\underset{\sim}{\varepsilon}}_d^{\#} = \dot{\hat{p}}\left(\frac{3}{2}\frac{s\bar{\underset{\sim}{\sigma}}_d^{\#} : \bar{\underset{\sim}{\varepsilon}}_d^{\#} - x\bar{\underset{\sim}{\varepsilon}}_d^{\#} : \bar{\underset{\sim}{\varepsilon}}_d^{\#}}{\hat{\mathcal{J}}(s,x)}\right) \tag{3.42}$$

Substituting the contracted products for $\bar{\underset{\sim}{\sigma}}_d^{\#} : \bar{\underset{\sim}{\varepsilon}}_d^{\#}$ and $\bar{\underset{\sim}{\varepsilon}}_d^{\#} : \bar{\underset{\sim}{\varepsilon}}_d^{\#}$, we get:

$$\dot{e}^p = \dot{\hat{p}}\left(\frac{3}{2}\frac{2\mu s - x}{\hat{\mathcal{J}}(s,x)}\right) \tag{3.43}$$

Cumulative plastic strain

The deviator of the plastic strain tensor is used for the computation of the approximated cumulative plastic strain rate $\dot{\hat{p}}$. The reformulation from the tensorial equation to the scalar equation uses the scalar variable e^p, and reads as follows

$$\dot{\hat{p}} = \sqrt{\frac{2}{3}(\dot{e}^p)^2\bar{\underset{\sim}{\varepsilon}}_d^{\#} : \bar{\underset{\sim}{\varepsilon}}_d^{\#}} \tag{3.44}$$

or in a simplified form:

$$\dot{\hat{p}} = \frac{1}{3\mu}|\dot{e}^p|\bar{\sigma}_{\mathrm{VM}}^{\#} \tag{3.45}$$

Solution algorithm

The Neuber rule and constitutive equations derived under the local proportionality rule are summarised in table 3.1. We provide these relationships in terms of mechanical tensors, but

also in terms of reduced scalar variables s, e, e^p, x and $\hat{p}$. It is clear that the reduced scalar variables depend solely on the elasto-static solution through the von Mises stress ($\bar{\sigma}^{\#}_{\mathrm{VM}}$). This dependency to a scalar quantity from the elasto-static simulation is key to the success of the meta-modelling approach developed later on in the chapter.

The system of plastic correction equations needs to be solved for each quadrature point of the finite element mesh. For arbitrary (proportional) load functions $f(t)$, this is done by computing the value of $e^p(t)$ at a series of time steps, using the fully implicit time stepping scheme described in the appendix C.

We can finally reconstruct the approximated elasto-plastic tensor variables $(\hat{\underset{\sim}{\sigma}}(t), \hat{\underset{\sim}{\varepsilon}}(t), \hat{\underset{\sim}{\varepsilon}}^p(t), \hat{p}(t), \hat{\underset{\sim}{X}}(t))$ from the scalar quantities computed using the plastic corrector, i.e. $(s(t), e(t), e^p(t), \hat{p}(t), x(t))$. For example, to compute a component of the stress tensor, we can first reconstruct $\hat{\underset{\sim}{\sigma}}(t) = s(t)\hat{\underset{\sim}{\sigma}}_d + f(t)\mathrm{Tr}(\bar{\underset{\sim}{\sigma}}^{\#})\mathbb{I}$ and then report the time evolution of desired component of this approximated stress tensor.

Table 3.1: Plastic correction equations written in terms of tensor variables ($\hat{\underset{\sim}{\sigma}}_d$,$\hat{\underset{\sim}{\varepsilon}}_d$,$\hat{\underset{\sim}{\varepsilon}}^p$,$\hat{p}$,$\hat{\underset{\sim}{X}}$) to the left, and in terms of scalar variables (s,e,e^p,$\hat{p}$,x) to the right. f is the global loading function, which is time dependent, and $\bar{\sigma}^{\#}_{\mathrm{VM}}$ denotes the von Mises stress stemming from the elastic finite element simulation performed with $f = 1$.

Type	Tensorial variables	Scalar variables
Neuber rule	$\hat{\underset{\sim}{\sigma}}_d : \hat{\underset{\sim}{\varepsilon}}_d = \underset{\sim}{\sigma}^{\#}_d : \underset{\sim}{\varepsilon}^{\#}_d$	$se = f^2$
Elasticity	$\hat{\underset{\sim}{\sigma}} = 2\mu(\hat{\underset{\sim}{\varepsilon}} - \hat{\underset{\sim}{\varepsilon}}^p) + \lambda \mathrm{Tr}(\hat{\underset{\sim}{\varepsilon}} - \hat{\underset{\sim}{\varepsilon}}^p)\mathbb{I}$	$s = (e - e^p)$
Yield function	$f_y(\hat{\underset{\sim}{\sigma}}; \hat{\underset{\sim}{X}}, \hat{p}) = \mathcal{J}\left(\hat{\underset{\sim}{\sigma}} - \hat{\underset{\sim}{X}}\right) - \sigma_y - R(\hat{p})$	$\hat{f}_y(s; x, \hat{p}) = \hat{\mathcal{J}}(s, x) - \sigma_y - R(\hat{p})$
Evolution of yield function	$f_y(\underset{\sim}{\sigma}_d; \underset{\sim}{X}, \hat{p})\dot{\hat{p}} = 0 \quad \text{and} \quad f_y(\underset{\sim}{\sigma}_d; \underset{\sim}{X}, \hat{p}) \leq 0$	$\hat{f}_y(s; x, \hat{p})\dot{\hat{p}} = 0 \quad \text{and} \quad \hat{f}_y(s; x, \hat{p}) \leq 0$
von Mises stress	$\mathcal{J}(\hat{\underset{\sim}{\sigma}}_d - \hat{\underset{\sim}{X}}) = \sqrt{\frac{3}{2}(\hat{\underset{\sim}{\sigma}}_d - \hat{\underset{\sim}{X}}) : (\hat{\underset{\sim}{\sigma}}_d - \hat{\underset{\sim}{X}})}$	$\hat{\mathcal{J}}(s, x) = \left\lvert s - \frac{x}{2\mu} \right\rvert \bar{\sigma}^{\#}_{\mathrm{VM}}$
Isotropic hardening	$R(\hat{p}) = Q(1 - \exp(-b\hat{p}))$	$R(\hat{p}) = Q(1 - \exp(-b\hat{p}))$
Kinematic hardening	$\dot{\hat{\underset{\sim}{X}}} = \frac{2}{3} C \dot{\hat{\underset{\sim}{\varepsilon}}}^p - D \hat{\underset{\sim}{X}} \dot{\hat{p}}$	$\dot{x} = \frac{2}{3} C \dot{e}^p - D x \dot{\hat{p}}$
Flow rule	$\dot{\hat{\underset{\sim}{\varepsilon}}}^p = \dot{\hat{p}} \left(\frac{3}{2} \frac{\hat{\underset{\sim}{\sigma}}_d - \hat{\underset{\sim}{X}}}{\mathcal{J}(\hat{\underset{\sim}{\sigma}}_d - \hat{\underset{\sim}{X}})} \right)$	$\dot{e}^p = \dot{\hat{p}} \left(\frac{3}{2} \frac{2\mu s - x}{\hat{\mathcal{J}}(s, x)} \right)$
Cumulative plastic strain	$\dot{\hat{p}} = \sqrt{\frac{2}{3} \dot{\hat{\underset{\sim}{\varepsilon}}}^p_d : \dot{\hat{\underset{\sim}{\varepsilon}}}^p_d}$	$\dot{\hat{p}} = \frac{1}{3\mu} \lvert \dot{e}^p \rvert \bar{\sigma}^{\#}_{\mathrm{VM}}$

3 Numerical investigations and results

The aim of this section is to evaluate the accuracy of the plastic corrector with respect to reference computations, which consist of full elasto-plastic FE simulations using the Z-Set suite [Besson et al., 2012]. Two test cases, a notched structure and a specimen with spherical pores, will be presented with detailed full-field and point-wise comparisons of variables like the cumulative plastic strain. A third test case, that of a specimen with pores of realistic morphology, meshed based on images from X-ray tomography, is presented in Appendix A. The meshes for the test cases were created with GMSH [Geuzaine and Remacle, 2020], and elasto-static simulations needed for the plastic corrector methodology were performed with FEniCS [Baratta et al., 2023].

The parameters used for the reference elasto-plastic equations (equations (3.11)-(3.18)) and the plastic corrector equations (detailed in table 3.1) chosen for this investigation, for test cases 1 and 2, are summarized in table 3.2.

Table 3.2: Parameters of the reference elasto-plastic equations detailed in equations (3.11)-(3.18) and the plastic corrector equations detailed in table 3.1, used for test cases 1 and 2

E MPa	σ_y MPa	b	Q MPa	C MPa	D
200000	100	10	100	40000	400

3.1 Test cases

Notched structure

Test case 1 is a notched structure, illustrated in Figure 3.2(a). For the plastic corrector, an elasto-static FEA computation is computed with prescribed displacements $\underline{\bar{u}}_a = [u_x, 0, 0]$ for $x \geq L_c$ and $\underline{\bar{u}}_a = [-u_x, 0, 0]$ for $x \leq -L_c$ such that $\bar{\sigma}^{\#}_{\mathrm{VM}}$ at the notch area is at the yield stress of the material (this computation corresponds to $f = 1$). The function $f(t)$ is then chosen to monotonically increase such that $f(t)\bar{\sigma}^{\#}_{\mathrm{VM}}$ reaches 155% of the yield stress of the material at the notch tip. This monotonic load function is shown in Figure 3.2(b). The full-field $\bar{\sigma}^{\#}_{\mathrm{VM}}$ in the structure is used for the plastic corrector approximations. The reference elasto-plastic computation is performed in such a way as to achieve the same loading level as in the plastic corrector computation.

Specimen with spherical pores

Test case number 2 is a specimen with a spatial distribution of spherical pores in the gauge section shown in Figure 3.3. The spherical pores are of a fixed size, and their centers were generated using random sampling. For the plastic corrector, an elasto-static FEA computation is computed with prescribed displacements $\underline{\bar{u}}_a = [u_x, 0, 0]$ for $x \geq L_c$ and $\underline{\bar{u}}_a = [-u_x, 0, 0]$ for $x \leq -L_c$ such that $\bar{\sigma}^{\#}_{\mathrm{VM}}$ in the gauge section, away from pores, is at the yield stress of the material (this computation corresponds to $f = 1$). The function $f(t)$ is evaluated twice, generating loading sequences of 2 cycles and 20 cycles. At the peak of these cyclic loads, $f(t)\bar{\sigma}^{\#}_{\mathrm{VM}}$

is chosen to reach 80% of the yield stress of the material in the gauge section away from pores. These cyclic load functions are shown in Figure 3.3(b-c). Due to the presence of pores in the specimen, the local loading exceeds the yield stress in several regions. The full-field $\bar{\sigma}^{\#}_{\mathrm{VM}}$ in the specimen is used for the plastic corrector approximations. For the reference elasto-plastic computation, the same type of loading as in the plastic corrector is applied.

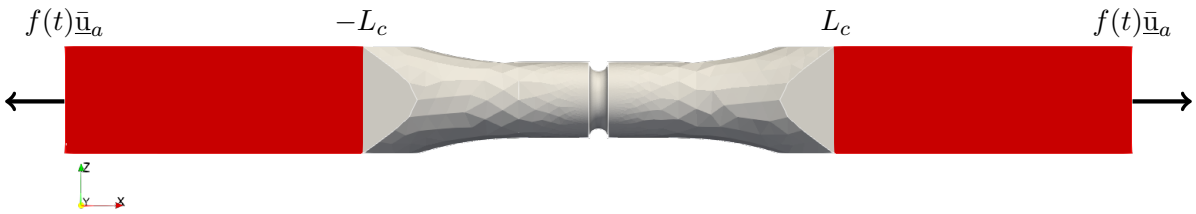

(a) Notched structure, with displacement $\bar{u}_a$ at $f = 1$ scaled by $f(t)$ on highlighted red regions, in opposite directions

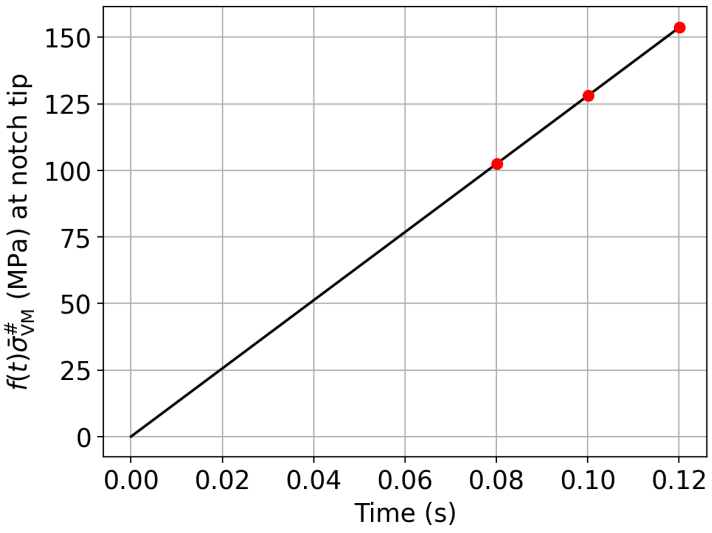

(b) At the notch tip, the von Mises stress from the elastic computation $\bar{\sigma}^{\#}_{\mathrm{VM}}$ at $f = 1$ is scaled by $f(t)$. $f(t)\bar{\sigma}^{\#}_{\mathrm{VM}}$ goes up to 155% of the yield stress at the peak of loading. The red points indicate the specific time-steps at which the cumulative plastic strain results from the full-field plastic corrector will be compared against the reference cumulative plastic strain.

Figure 3.2: Test case 1: Geometry, boundary conditions and applied loading

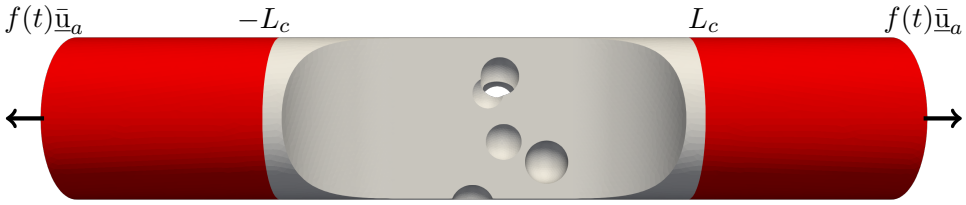

(a) Specimen with spherical pores in gauge section, with displacement $\bar{u}_a$ at $f = 1$ scaled by $f(t)$ on highlighted red regions, in opposite directions

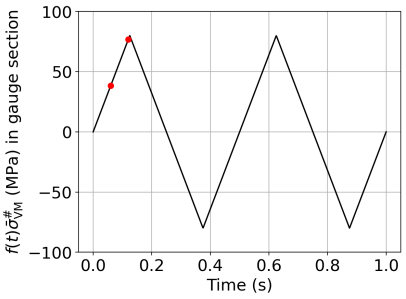

(b) Load function 1: In the gauge section away from pores, the von Mises stress from the elastic computation $\bar{\sigma}^{\#}_{\mathrm{VM}}$ at $f = 1$ is scaled by $f(t)$. The plastic corrector and reference cumulative plastic strain will be compared at the specific time-steps indicated in red

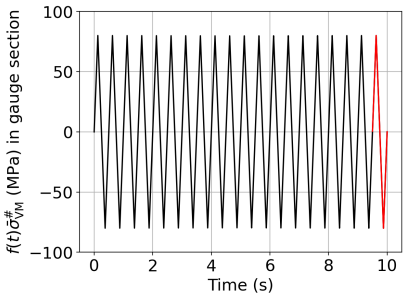

(c) Load function 2: In the gauge section away from pores, the von Mises stress from the elastic computation $\bar{\sigma}^{\#}_{\mathrm{VM}}$ at $f = 1$ is scaled by $f(t)$. The plastic corrector and the reference cumulative plastic strain range over the 20th cycle (red), will be compared

Figure 3.3: Test case 2: Geometry, boundary conditions and applied loading

3.2 Accuracy of the plastic corrector predictions

The accuracy of some quantities of interest computed using the plastic corrector will now be examined for the previously presented test cases. For test case 1, the evolution of the cumulative plastic strain, at a point of the notch tip and for the full 3D geometry will be shown, for monotonic loading. For test case 2, the evolution of the cumulative plastic strain will be shown in the 3D geometry encompassing the pores, for both monotonic and cyclic loading. The accuracy of the deviatoric stresses and strains will also be evaluated for a few points around the pores. Finally, the accuracy of the cumulative plastic strain range (denoted by $\Delta p = p_{\max}^{\text{cycle}} - p_{\min}^{\text{cycle}}$) over the 20^{th} cycle will be evaluated. The 20^{th} cycle is chosen here because in subsequent cycles, the stress strain responses do not change significantly from one cycle to the next, i.e. the cycling response is stabilised. Quantities of interest extracted from such stabilised cycles are notably suitable for the computation of fatigue criteria [Schijve, 2009].

Time-evolution of cumulative plastic strain

The field of cumulative plastic strain approximated by the plastic corrector, at three time steps of the loading sequence, is shown for test case 1 in Figure 3.4 and compared with reference computations at the same levels of applied loading. The time steps correspond to the notch von Mises stress (of the elastic FEA computation) reaching 102%, 127% and 152% of the elastic yield limit. The plastic corrector predicts overall higher cumulative plastic strain in the notch region, as compared to the reference elasto-plastic solution. Scatter plots of the cumulative plastic strain in all integration points in the mesh are shown in Figure 3.5. The approximated solution of the plastic corrector algorithm aligns closely with the reference solution. However, there exists some scatter, which is expected due to the cumulative errors linked to the rules of the plastic correction algorithm. The reference computation has points that undergo plastic accommodation, which is not captured in the Neuber-type computation, therefore leading to over-estimation by the plastic correction algorithm. This is a known phenomenon and has been reported before [Chouman et al., 2014]. Secondly, the Neuber approach also under-estimates the cumulative plastic strain at some points as it is localised and does not take into account redistribution of stresses that occur in the reference computation [Molski and Glinka, 1981].

The time-evolution of a maximally loaded point on the notch region is shown in Figure 3.6. The plastic corrector over-estimates the cumulative plastic strain throughout the loading sequence because stress redistribution was not considered. The relative error is very high at first, due to very low values of plasticity. During loading at the notch between $127\% - 152\%\sigma_y$, the relative error lowers to around 15-20%. These over-estimations match with the literature [Molski and Glinka, 1981, Jones et al., 1998].

For test case 2, the cumulative plastic strains obtained using the plastic corrector at a couple of time steps of the applied loading (corresponding to 40% and 80% of the yield stress of the material) are shown in Figure 3.7 and compared with reference computations at the same levels of applied loading. Plasticity develops around the pores, and the plastic corrector once again predicts overall higher cumulative plastic strain in a slightly larger region, as compared to the reference. Scatter plots of the cumulative plastic strain in all integration points in the mesh are

shown in Figure 3.8. The full-field predictions match well with the reference, especially for the time instants corresponding to lower levels of loading. This is because the plastic corrector's accuracy improves when the plasticity is relatively confined. However, a slight over-estimation by the plastic correction algorithm is observed.

The time-evolution of a maximally loaded point near a pore is shown in Figure 3.9(a-b). Similar to case 1, the plastic corrector over-estimates the cumulative plastic strain throughout the loading sequence. Interestingly, the relative error is lower at the beginning of loading and rises afterwards, contrary to case 1. The relative error in the prediction at the highest stressed points is around $35 - 40\%$ during the cyclic loading. The error oscillates with load reversals, with the oscillations reducing with successive cycles. The same analysis is done with a point seeing lesser loading, shown in Figure 3.9(c-d). Conversely, the plastic corrector under-estimates the cumulative plastic strain throughout the loading sequence. Under-estimation at points away from highly loaded regions is also a result of stress re-distribution, and has rarely been reported in the literature as Neuber-type methods have primarily been studied for highly loaded points or surfaces.

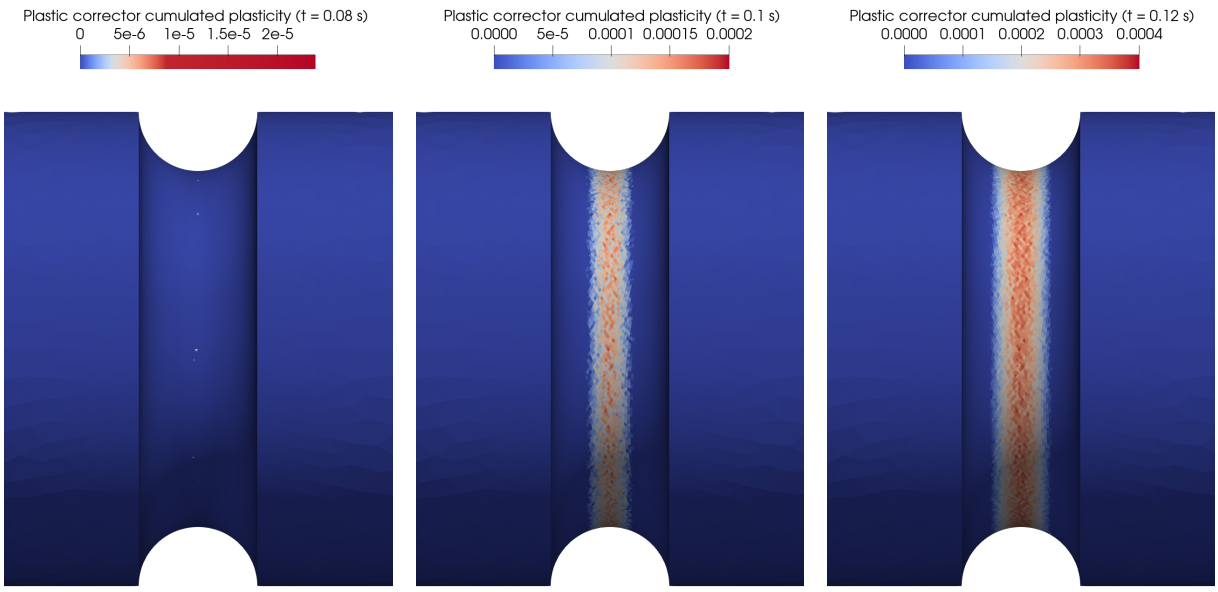

(a) Plastic corrector, t=0.08 s, notch load 102%σ_y

(b) Plastic corrector, t=0.10 s, notch load 127%σ_y

(c) Plastic corrector, t=0.12 s, notch load 152%σ_y

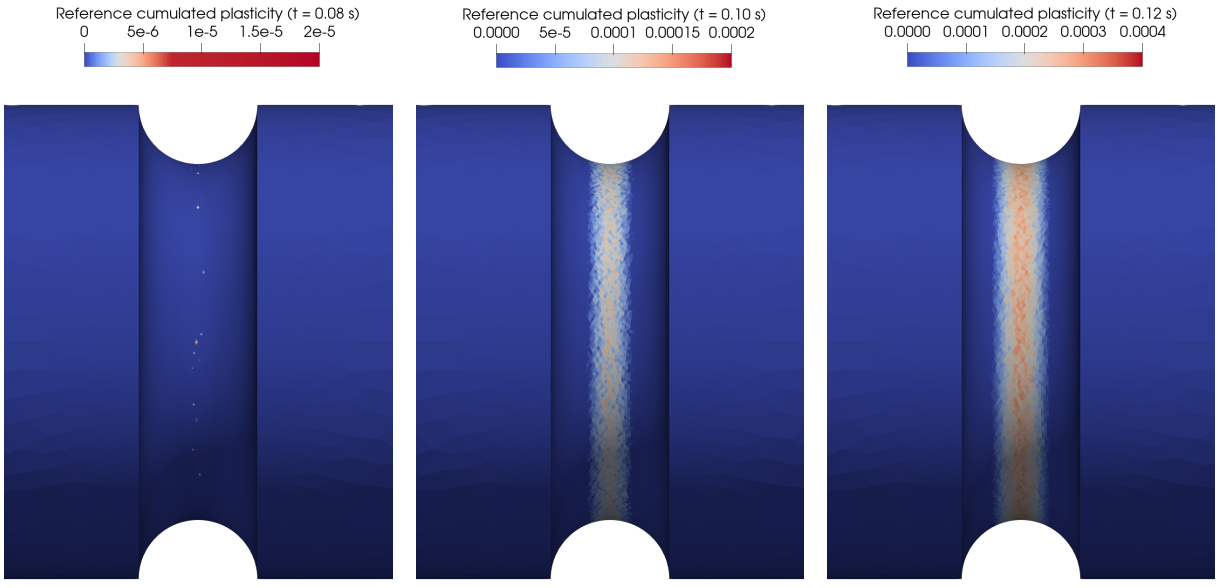

(d) Reference, t=0.08 s, notch load 102%σ_y

(e) Reference, t=0.10 s, notch load 127%σ_y

(f) Reference, t=0.12 s, notch load 152%σ_y

Figure 3.4: Test case 1 (notched geometry): Time-evolution of cumulative plastic strain.

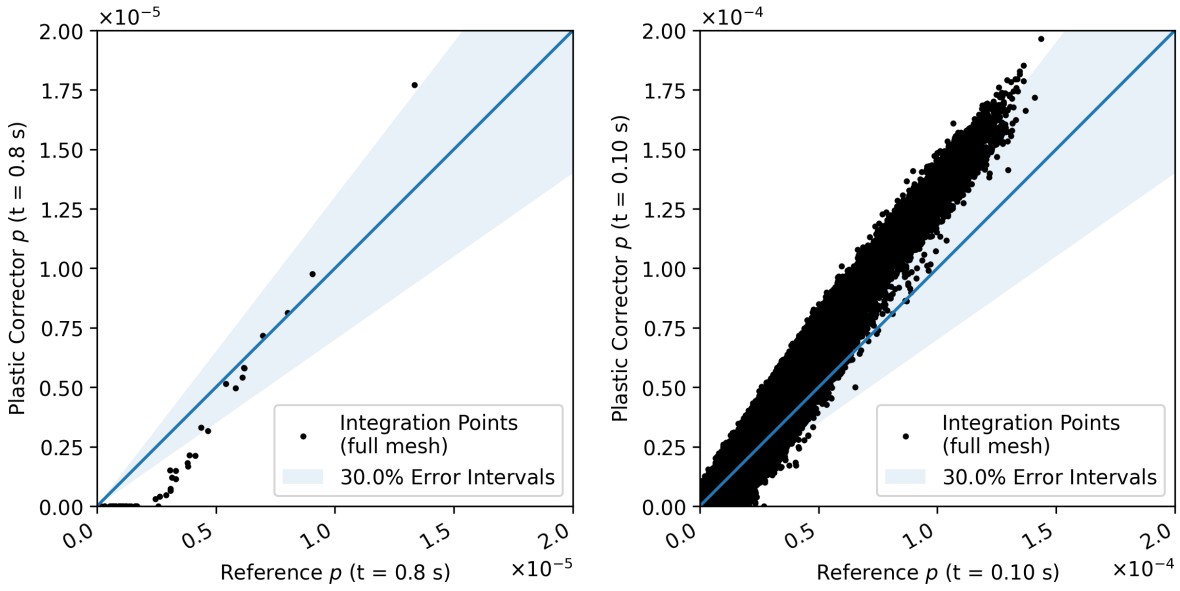

(a) Notch load 102%σ_y (t=0.08 s)

(b) Notch load 127%σ_y (t=0.10 s)

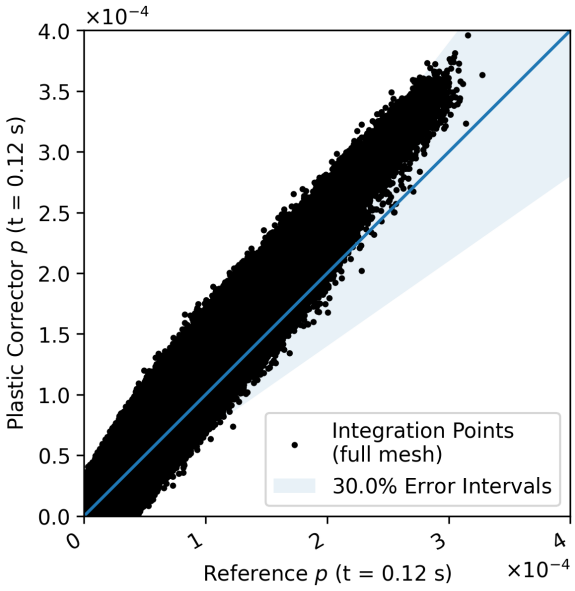

(c) Notch load 152%σ_y (t=0.12 s)

Figure 3.5: Test case 1 (notched geometry): Scatter plots of cumulative plastic strain in all integration points, at three time-steps during monotonic loading

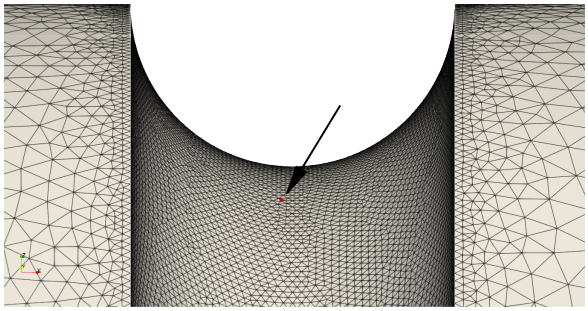

(a) Selected point in the mesh, shown by the arrow at the selected point

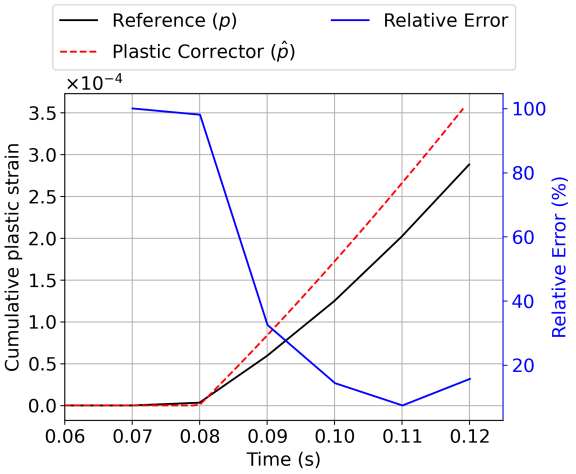

(b) Time-evolution of the cumulative plastic strain

Figure 3.6: Test case 1 (notched geometry): Comparison of the time-evolution of the cumulative plastic strain at the notch tip obtained by the plastic corrector and the reference computation during monotonic loading.

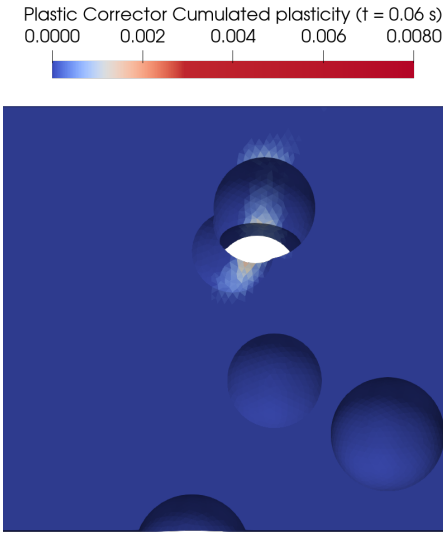

(a) Plastic corrector at t=0.06 s (applied loading $0.4\sigma_y$)

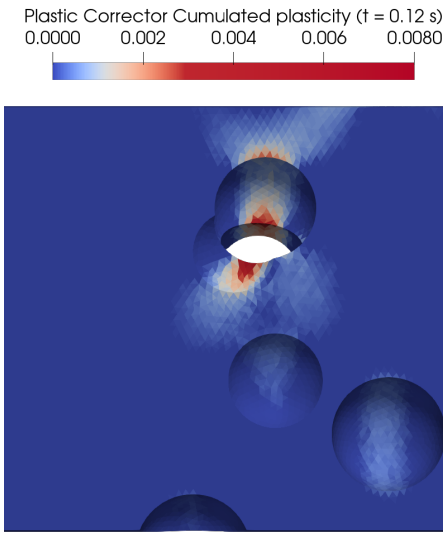

(b) Plastic corrector at t=0.12 s (applied loading $0.8\sigma_y$)

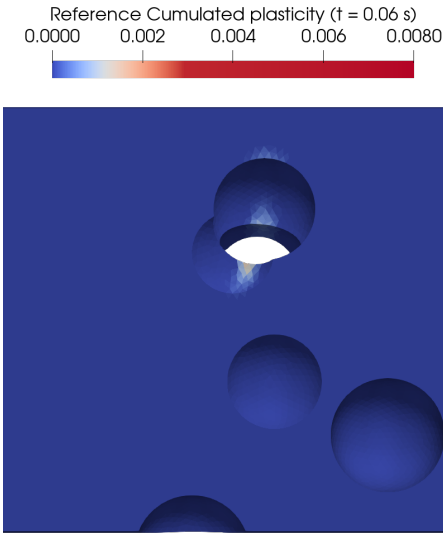

(c) Reference computation at t=0.06 s (applied loading $0.4\sigma_y$)

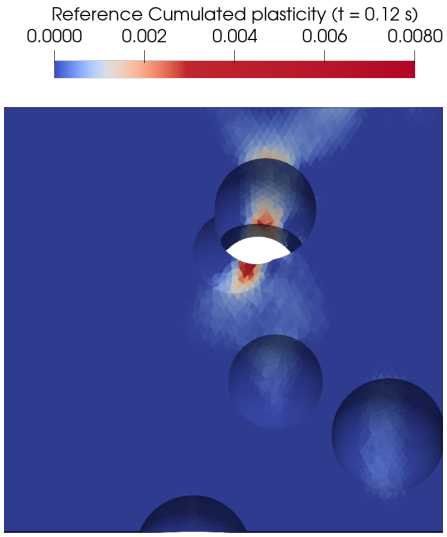

(d) Reference computation at t=0.12 s (applied loading $0.8\sigma_y$)

Figure 3.7: Full-field cumulative plastic strain results computed by the plastic correction algorithm compared to the reference, for two time steps corresponding to successively higher levels of loading.

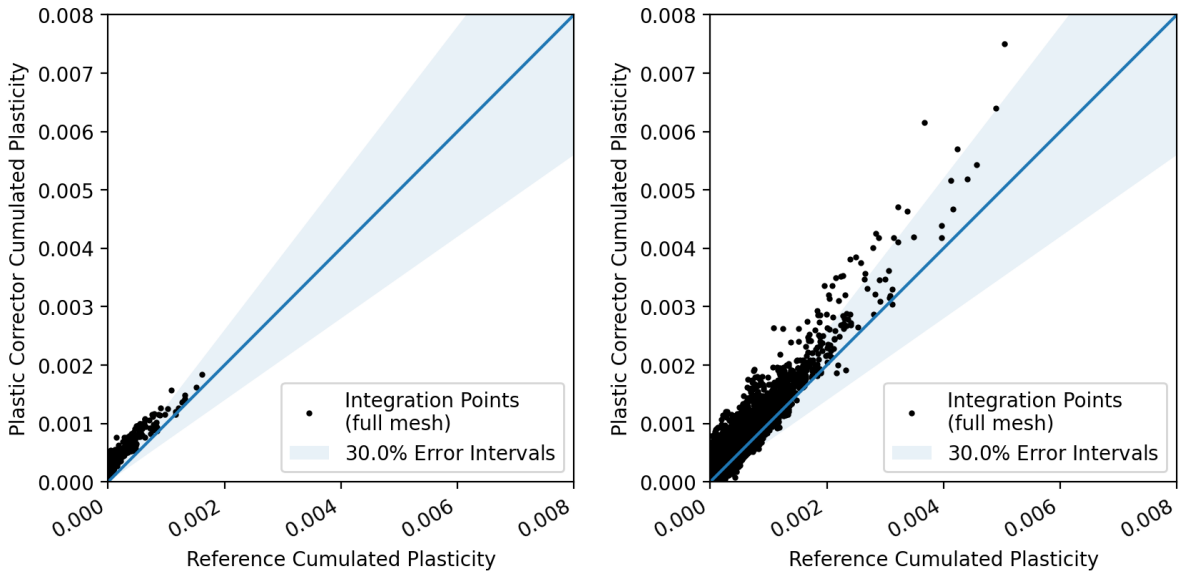

(a) t=0.06 s (applied loading $0.4\sigma_y$)

(b) t=0.12 s (applied loading $0.8\sigma_y$)

Figure 3.8: Scatter plots of cumulative plastic strain in all integration points, at time steps corresponding to successively higher levels of loading.

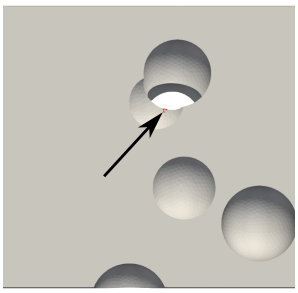

(a) Selected point in the mesh with high loading and high relative error in p

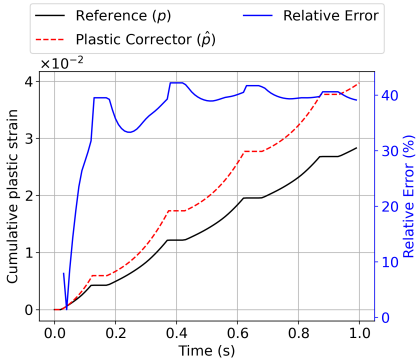

(b) Evolution of cumulative plastic strain at the shown point with high loading and high error

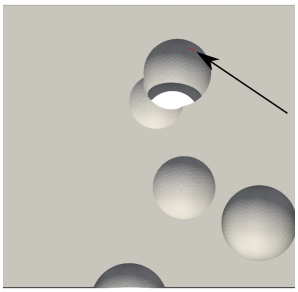

(c) Selected point in the mesh with low loading and low relative error in p

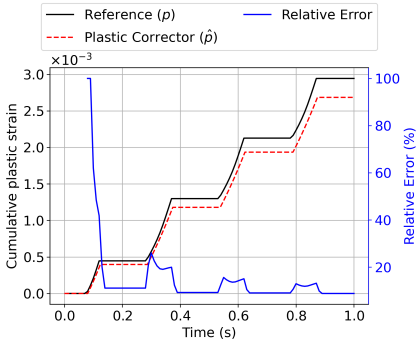

(d) Evolution of cumulative plastic strain at the shown point with low loading and low error

Figure 3.9: Comparison of the time-evolution cumulative plastic strain obtained by the plastic corrector and a reference computation at two points in the mesh of test case 2, showing an over-estimation and under-estimation of the plastic corrector

Time-evolution of stresses and strains

We limit the study of stresses and strains to the more complex loading case, i.e. the test case 2 with spherical pores. We evaluate the accuracy of the plastic corrector on components of the deviatoric stress and strain tensors. The same two points are selected as the previous section, i.e. a highly loaded one with high relative error in cumulative plastic strain (Figure 3.10(a)) and another point with lesser loading and lower relative error (Figure 3.11(a)).

Figure 3.10(b-c) shows the evolution of the axial and shear components of the stress and strain tensors for the point under high local loading.

While the stresses are relatively well approximated, the strains have a much higher error – this is a known result [Desmorat, 2002, Chouman et al., 2014, Jones et al., 1998]. The axial component is overestimated by the plastic corrector. As aforementioned, the Neuber-type method used does not take into account redistribution of stresses. The shear component is not well predicted due to the proportional evolution rule in the plastic corrector – this will be explained in detail in a later section.

Figure 3.11(b-c) shows the evolution of the axial and shear components of the stress and strain tensors for the point under low local loading.

Both the axial and shear components are reasonably well-estimated by the plastic corrector. This is because this point, experiencing lesser loading than the first one, is not as affected by the proportional evolution rule – again, this is proved later on.

Finally, the von Mises stress approximated by the plastic corrector is compared to the reference computation in Figure 3.12. The results show an excellent match between the plastic corrector and the reference, for progressively higher loading.

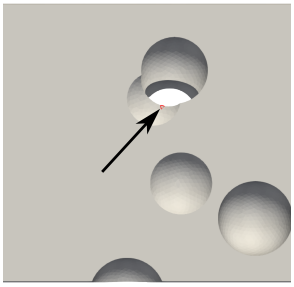

(a) Selected point in the mesh with high error

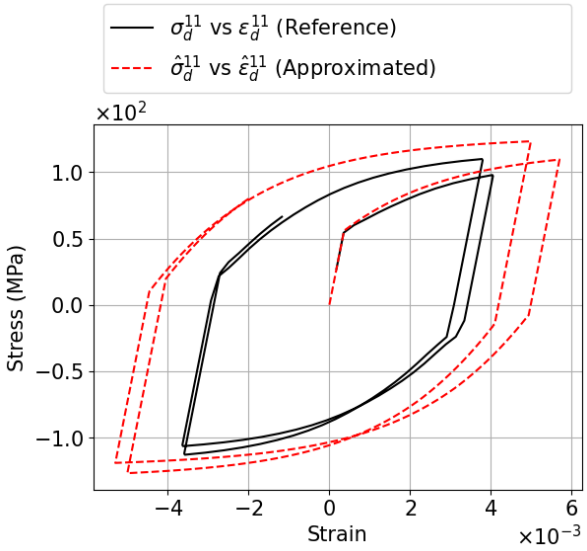

(b) Axial component

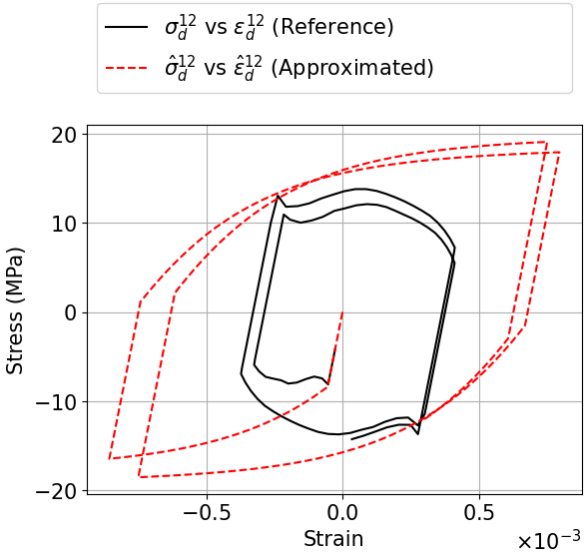

(c) Shear component

Figure 3.10: Point in the mesh of test case 2 with a high amount of plasticity and high error in p (30% relative error between reference p and plastic corrector $\hat{p}$ at t=0.12 s): evolution of the individual components of the approximated deviatoric stress and strain tensors by the plastic corrector (denoted by $\hat{\sigma}_d^{ij}$, $\hat{\varepsilon}_d^{ij}$) compared to the respective reference curves obtained via a complete elasto-plastic computation (denoted by σ_d^{ij}, ε_d^{ij})

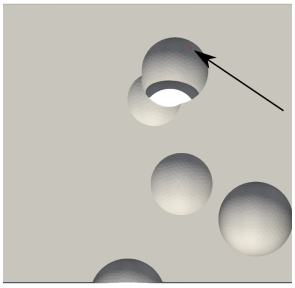

(a) Selected point in the mesh with low error

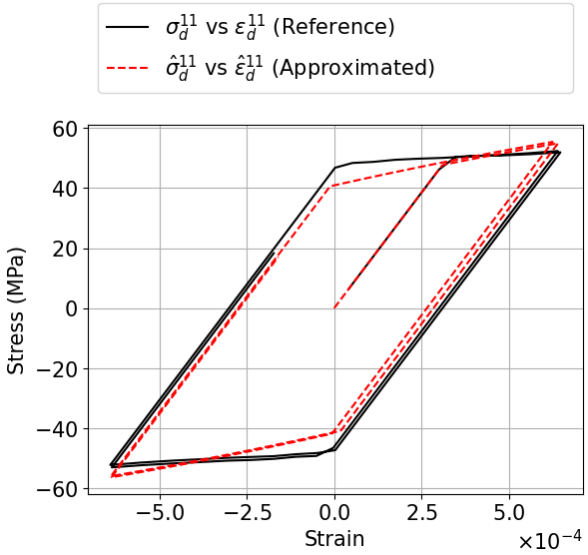

(b) Axial component

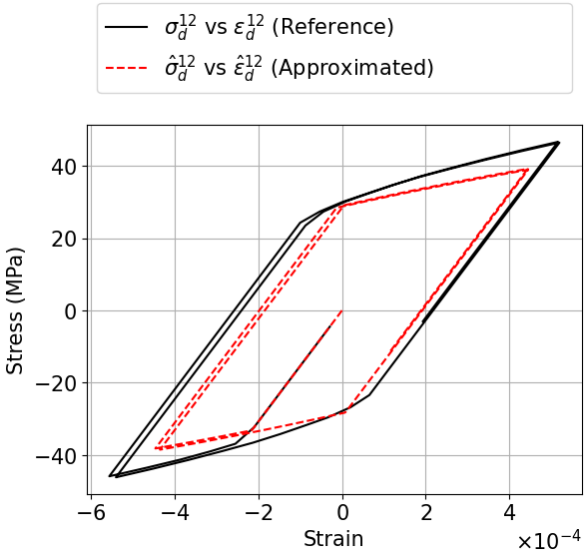

(c) Shear component

Figure 3.11: Point in the mesh of test case 2 with a low amount of plasticity and low error in p (9% relative error between reference p and plastic corrector $\hat{p}$ at t=0.12 s): evolution of the individual components of the approximated deviatoric stress and strain tensors by the plastic corrector (denoted by $\hat{\sigma}_d^{ij}$, $\hat{\varepsilon}_d^{ij}$) compared to the respective reference curves obtained via a complete elasto-plastic computation (denoted by σ_d^{ij}, ε_d^{ij})

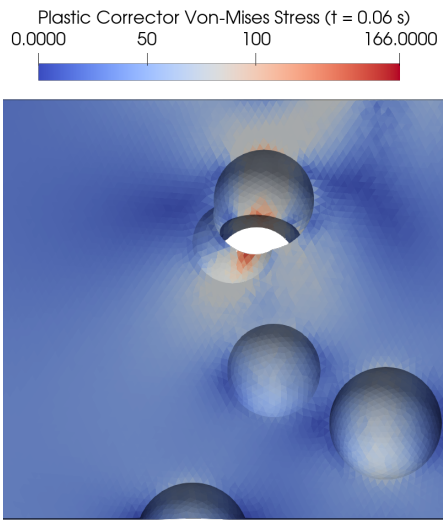

(a) Plastic corrector at t=0.06 s (applied loading $0.4\sigma_y$)

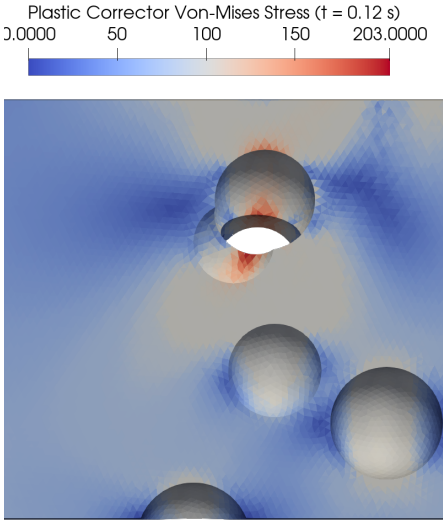

(b) Plastic corrector at t=0.12 s (applied loading $0.8\sigma_y$)

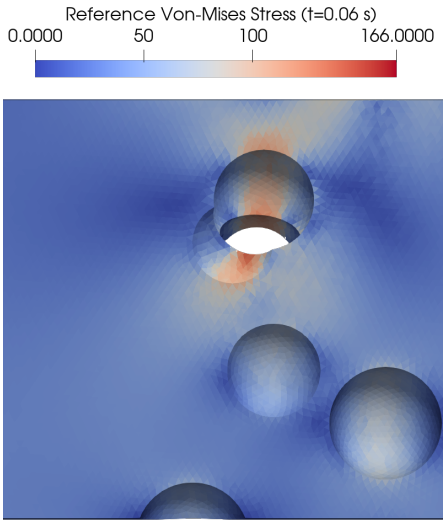

(c) Reference computation at t=0.06 s (applied loading $0.4\sigma_y$)

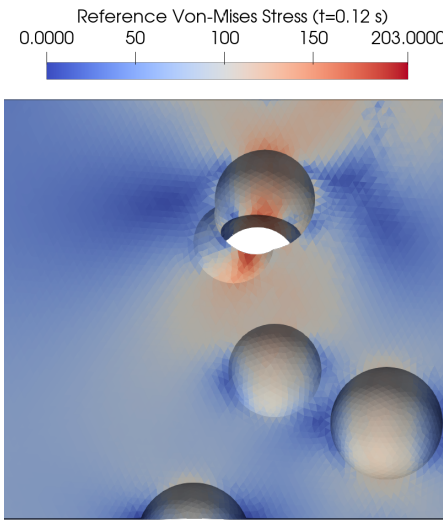

(d) Reference computation at t=0.12 s (applied loading $0.8\sigma_y$)

Figure 3.12: Full-field von Mises stress results computed by the plastic correction algorithm compared to the reference, for two time steps corresponding to successively higher levels of loading.

Cumulative plastic strain range in the 20^{th} cycle

The field of cumulative plastic strain range Δp over the 20^{th} cycle, obtained by the plastic correction algorithm and the reference elasto-plastic FE computation, is shown respectively in ch3/fig 3.13(a) and 3.13(b) for the test case number 2, specimen with spherical pores. A comparison of the values at all the quadrature points in the mesh is shown in Figure 3.13(c). A good overall match is found in the values of the cumulative plastic strain range obtained by the plastic correction algorithm and the reference computation. Like the previously presented cases, there is over and under-estimation by the plastic corrector – the number of over-estimated points is significantly higher than the under-estimated ones. The order of relative error in the loaded zones is around $30 - 40\%$. However, we acknowledge that the errors may be much higher if the material presents ratcheting behaviour, which was not the case here [Chouman et al., 2014].

3.3 Computational time needed for a full-field plastic corrector computation

A breakdown of the computational costs required for obtaining the elasto-plastic solution by the two methods, i.e. a full reference computation and a plastic corrector computation, is compared in table 3.3. The mesh considered is the same porous mesh as test case 2, and has around 661k quadrature points (one per linear element). The loading considered here comprises 1000 time-steps.

Table 3.3: CPU times (in seconds) for full-field p computation for the test case 2: mesh of a specimen with spherical pores (661771 quadrature points, 1000 time-steps)

Operation	Reference FEA (s)	Plastic corrector (s)
Elastic FEA for $\bar{\sigma}^{\#}_{\text{VM}}$	-	236
Elasto-plastic computation	52850	156
Total CPU time	52850	392

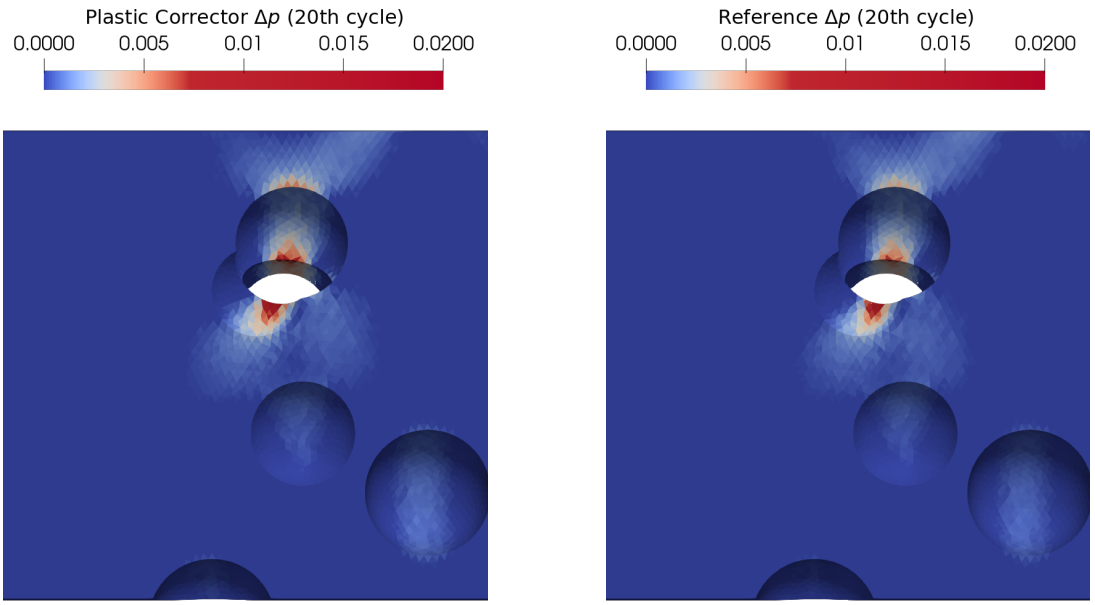

(a) Plastic corrector

(b) Reference computation

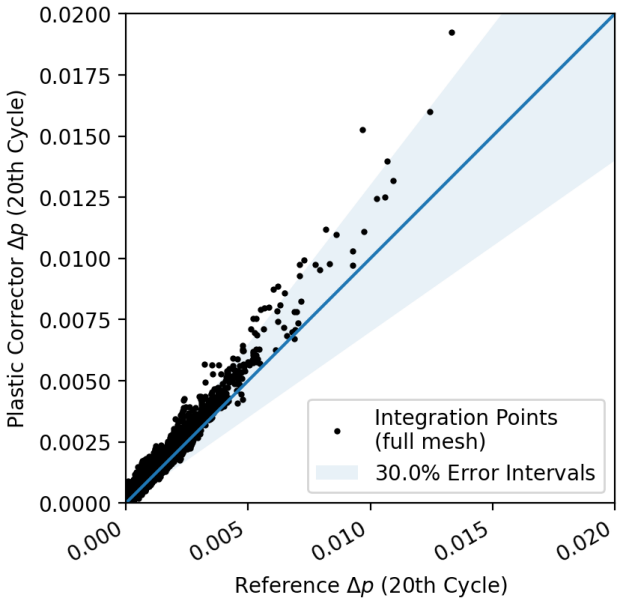

(c) Scatter plot of Δp values in all the integration points in mesh

Figure 3.13: Full-field comparison of Δp in the 20^{th} cycle in the test case 2 mesh

3.4 Errors due to the rule of local proportionality

We will now analyze the error that arises solely from the local proportionality rule. Our objectives are to evaluate (i) the contribution of this proportionality rule to the error in the plastic corrector method and (ii) the characteristics of this error. To achieve this, we will construct a projected elasto-plastic solution based exclusively on the local proportionality rule, omitting the Neuber-type rule. Specifically, we will project the reference stress history at a given point onto the direction of the stress derived from the elastic computation. This projected stress will be compared to the stress calculated using the plastic corrector, which incorporates both the Neuber-type rule and the local proportionality rule. This comparison will allow us to isolate the part of the error that is due to the local proportionality rule. Additionally, we will compare the projected stress computed using only the proportionality rule to the reference stress to assess the acceptability of the proportionality rule in terms of error. Deviations between the stresses computed with these two methods will indicate significant local non-proportionality, which our algorithm may not adequately capture. We will show the characteristics of this error, i.e. the conditions and reasons for which usage of the proportionality rule could result in high relative error.

The projected stress tensor resulting from the local proportionality rule is computed using the following projection of the reference stress $\underset{\sim}{\sigma}_d$:

$$\hat{\underset{\sim}{\bar{\sigma}}}_d = \frac{(\underset{\sim}{\bar{\sigma}}_d : \underset{\sim}{\sigma}_d)}{(\underset{\sim}{\bar{\sigma}}_d : \underset{\sim}{\bar{\sigma}}_d)} \underset{\sim}{\bar{\sigma}}_d \tag{3.46}$$

Quantities denoted by $\hat{\bullet}$ represent projected quantities assuming local proportionality; this approximation is thus different from the plastic corrector approximations developed in the previous sections as it directly operates on the reference stress (which is, of course, not available in practice). The absolute error ξ and the relative error ξ_{rel} between the projected deviatoric stress tensor using the hypothesis of proportionality ($\hat{\underset{\sim}{\bar{\sigma}}}_d$), and the reference deviatoric stress tensor via a full non-linear FE computation ($\underset{\sim}{\sigma}_d$) can be calculated as follows:

$$\underset{\sim}{\xi} = \underset{\sim}{\sigma}_d - \hat{\underset{\sim}{\bar{\sigma}}}_d \tag{3.47}$$

The relative error in stress is computed by taking the Frobenius norm of the tensors:

$$\xi_{rel} = \frac{\|\underset{\sim}{\xi}\|_F}{\|\underset{\sim}{\sigma}_d\|_F} \tag{3.48}$$

Contribution of the local proportionality rule to the error in the plastic corrector solution

We will now analyze the contribution of the proportional evolution rule in terms of error in the plastic corrector solution, at a few points of the computational domain of test case 2. The same two points previously analyzed in Figure 3.9(a,c) are considered. Figure 3.14(a-b) shows a comparison of the evolution of the axial and shear components of the deviatoric stress tensors for the first point near a pore, with high plasticity and high error, computed using (i) purely

the proportional evolution rule (denoted by $\hat{\hat{\sigma}}_d^{ij}$) (ii) the plastic corrector (denoted by $\hat{\sigma}_d^{ij}$) (iii) reference (denoted by σ_d^{ij}). For the components computed using purely the local proportional evolution rule, we observe that the axial component is very well predicted. The shear component is badly predicted, but the maximum stress value is acceptable. This shows that in the plastic corrector solution, the proportional evolution rule does not contribute significantly to the overall solution, and it is the Neuber-type rule that causes most of the error. A similar comparison is done for the second point with low plasticity and low error (Figure 3.15(a-b)). For this point, both the axial and shear components computed with the local proportional evolution rule are reasonably well predicted, and also do not differ from the plastic corrector solution.

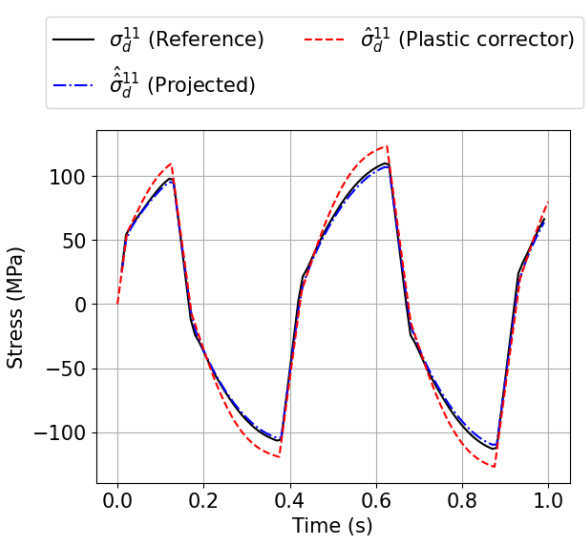

(a) Axial component

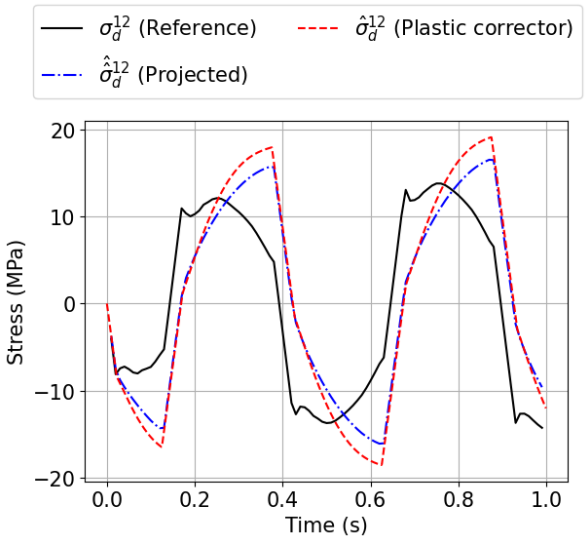

(b) Shear component

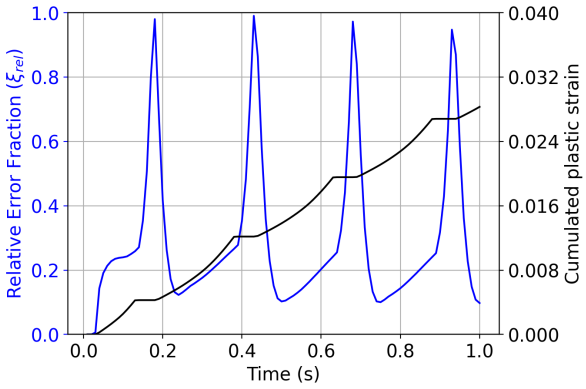

(c) Time evolution of ξ_{rel} and p

Figure 3.14: For a point with high plasticity (shown in Figure 3.9(a)): Evolution of the individual components of the projected deviatoric stress tensor (denoted by $\hat{\hat{\sigma}}_d^{ij}$) compared to the respective reference curves obtained via a complete elasto-plastic computation without any reduction (denoted by σ_d^{ij}). The plastic corrector solution is recalled in red. The relative error fraction for the stresses is shown alongside the cumulative plastic strain.

The relative error ξ_{rel} due to the local proportionality rule is shown for the two points in ch3/fig 3.14(c) and 3.15(c), alongside their cumulative plastic strain. The load reversal naturally

causes ξ_{rel} to increase sharply. ξ_{rel} becomes close to 1, which indicates a 100% relative error. The explosion of relative errors at these load inversion points is because the stress values are very close to zero (see ch3/fig 3.14(a,b) and 3.15(a,b)). The absolute error at these inversion points is very low. This shows that even if the relative error is significant, in reality, its effect is negligible.

Furthermore, the cumulative plastic strain does not increase during these load reversals. In other words, the error during load reversal does not contribute significantly to the error in plasticity computations. For the first point with a higher p error, cumulative plastic strain starts increasing again despite a high ξ_{rel}. For the second point, with lower p error, we observe that the ξ_{rel} always stays low during increase in plasticity. Thus, some points of loading, which are closer to a proportional loading sequence, are better predicted than others.

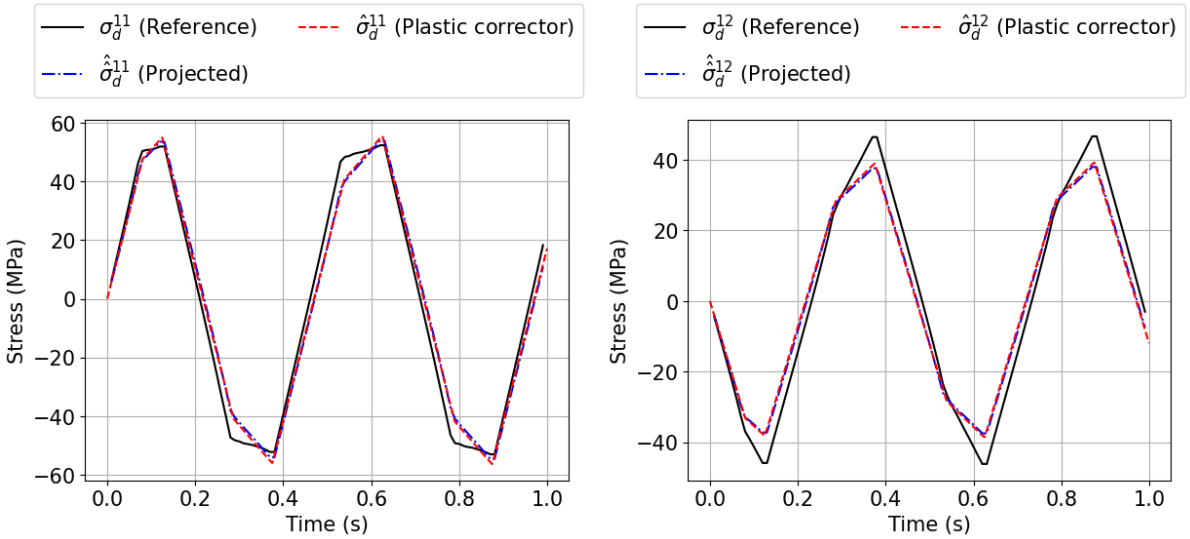

(a) Axial component

(b) Shear component

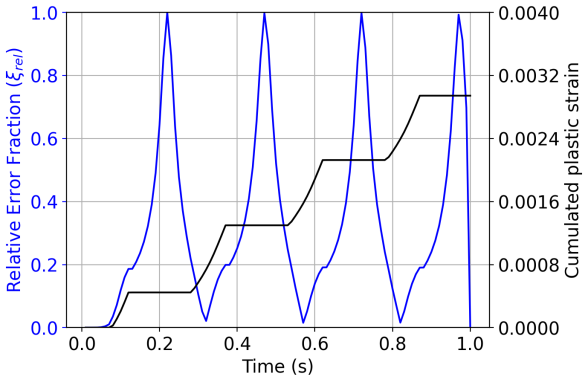

(c) Time evolution of ξ_{rel} and p

Figure 3.15: For a point with low plasticity (shown in Figure 3.9(c)): Evolution of the individual components of the projected deviatoric stress tensor calculated by assuming a hypothesis of proportionality (denoted by $\hat{\hat{\sigma}}_d^{ij}$) compared to the respective reference curves obtained via a complete elasto-plastic computation without any reduction (denoted by σ_d^{ij}). The plastic corrector solution is recalled in red. The relative error fraction for the stresses is shown alongside the cumulative plastic strain.

Relative error due to the local proportionality rule evaluated in the full mesh

Only test case number 2, i.e. the specimen with spherical pores, is considered. The relative error ξ_{rel} due to the local proportionality rule is calculated for all the loading history. The percentage of points in the mesh that stay below 15% relative error during the loading sequence is shown in Figure 3.16. During the first branch of monotonic loading, around 70-75% of all the points in the mesh remain below 15% relative error, and during the load reversal, this number goes down to 20%. As previously discussed, this occurs because the near-zero stress values at these load inversion points lead to a sharp increase in relative errors. The percentage of points below 15% relative error goes back up to 70% after the load reversal, when plasticity starts developing again.

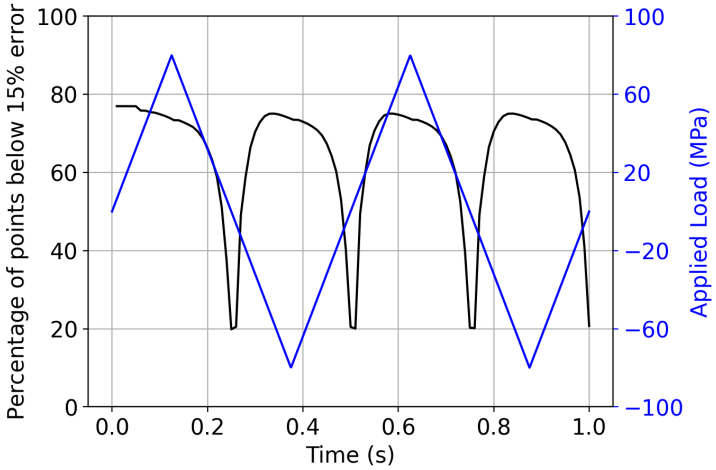

Figure 3.16: Time evolution of the percentage of elements in the FE computation (test case 2: spherical pores) below 15% relative error, alongside the applied loading history in the gauge section away from pores

4 Machine learning-based acceleration of plastic corrector computations

We wish to compute a scalar quantity of interest (QoI) from the elasto-plastic solution at arbitrary time $t \in [0, T]$. More precisely, we wish to extract a scalar value $Q \in \mathbb{R}$ from $(\hat{\underline{\sigma}}(t), \hat{\underline{\varepsilon}}(t), \hat{\underline{\varepsilon}}^p(t), \hat{p}(t), \hat{\underline{X}}(t))$ at an arbitrary number of quadrature points of the finite element mesh.

During the process of acquiring the QoI, the computation of $(s(t), e(t), e_p(t), \hat{p}(t), x(t))$ requires implicit time integration, as described in section 2.4 and the appendix C, and needs to be done for every quadrature point of the finite element mesh, which may lead to significant computational expense, especially for long time analysis. Remarkably, variables $(s(t), e(t), e_p(t), \hat{p}(t), x(t))$ are dependent on the solution of the elastic finite element prediction through the von Mises stress only, which can be seen by inspection of the system of equations in Table 3.1, right column. Therefore, any elasto-plastic quantity of interest, which depends solely on these proportionality ratios also depends on the sole von Mises stress $\bar{\sigma}^{\#}_{\mathrm{VM}}$ stemming from the elastic finite element computation, for a given $f(t)$.

We propose to acquire the scalar QoI with a one-dimensional Gaussian process regression (GP) algorithm [Rasmussen and Williams, 2006] trained on plastic corrector computations. One may use several independent GP regression models for several quantities of interest.

Gaussian process regression algorithm

The GP needs to capture the dependence of the scalar QoI on $\bar{\sigma}^{\#}_{\mathrm{VM}}$. To this end, we need to define a training interval for $\bar{\sigma}^{\#}_{\mathrm{VM}}$. A uniformly distributed set of n_s von Mises stress values, between 0 and s^+ times the σ_y, is created in logarithmic space. As stress values can span several orders of magnitude, usage of logarithmic space ensures that the GP has good interpolation ability. These values are input to the plastic corrector to calculate the QoI. $\bar{\sigma}^{\#}_{\mathrm{VM}}$ and QoI constitute the training data for the GP. For numerical stability, we applied a logarithmic transformation to both the input and target data. Any zero values in the target data were replaced with a small positive value to avoid undefined logarithmic values. The model was then fitted to the log-transformed data.

Once trained, the GP can be applied to all integration points within a given mesh of a structure without requiring any time integration.

Numerical example on a QoI

As an example we train a GP to predict e^p at the 1000^{th} time-step of a given $f(t)$ (shown in Figure 3.17(a)) for the mesh of a specimen with spherical pores (test case 2). The training data set for learning the scalar relation between $\bar{\sigma}^{\#}_{\mathrm{VM}}$ and e^p is created using $n_s = 150$ points and $s^+ = 12$. This is shown in Figure 3.17(b). The choice of 150 points ensures sufficient resolution for accurately capturing the relationship between the two quantities, which is either zero or a simple monotonically increasing function. The upper limit, set at 12 times the yield stress, is chosen to be slightly higher than the maximum stress concentration factor induced by the pores

in the mesh, which is approximately 8.

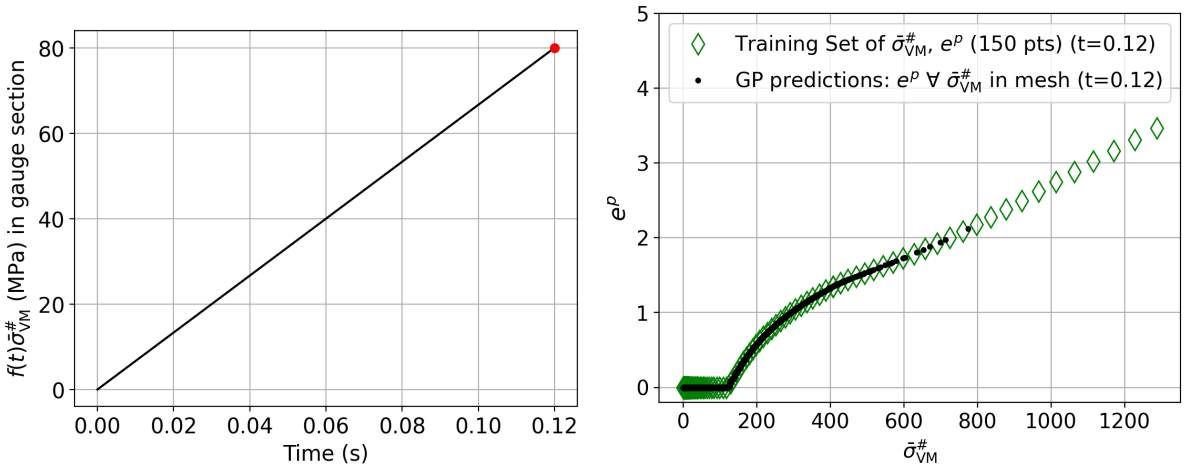

(a) (b)

Figure 3.17: (a) The load function chosen, with 1000 time-steps, with e^p being extracted at the last time-step at the peak of loading (highlighted in red) (b) Training data created for the Gaussian Process (GP) using the plastic corrector, along with the GP's predicted e^p for the last time-step

A comparison between the results obtained via the plastic correction algorithm and the predicted results via the Gaussian process regression is shown in Figure 3.18 for all integration points. The results show virtually no difference, indicating that the 1D meta-model can be used to further accelerate computation of scalar QoIs of the plastic corrector with no added error.

The Gaussian process regression only needs a few seconds in total to use for the prediction of a scalar QoI, including the cost of computing the training set via the plastic corrector, training time (computation and factorisation of data covariance matrix), and prediction time (shown in table 3.4).

Table 3.4: CPU times (in seconds) for QoI computation for the test case 2: mesh of a specimen with spherical pores (661771 quadrature points, 1000^{th} time-step). The training set comprises 150 points integrated over all 1000 time-steps.

Operation	Computing training set	Training	QoI computation	Total CPU time
Plastic corrector	-	-	156	156
Gaussian process regression	0.6	0.3	1.7	2.6

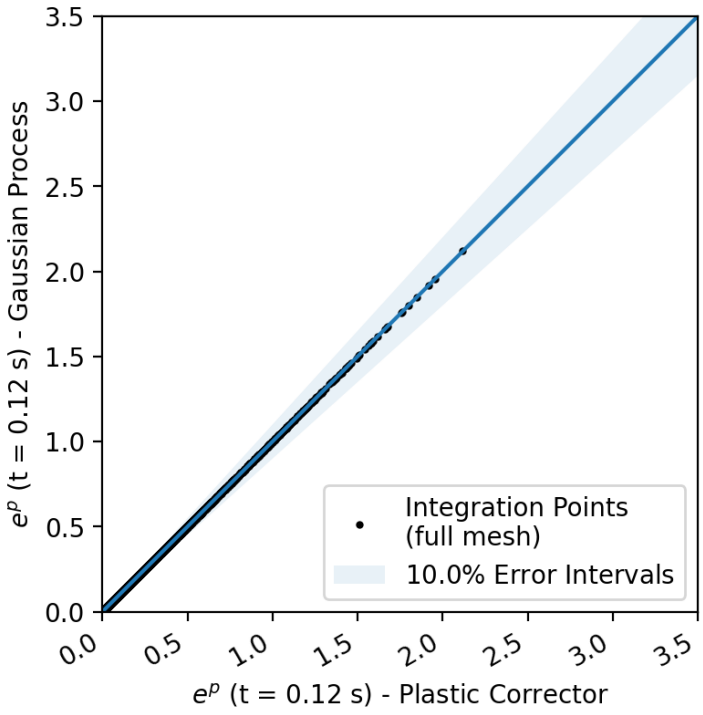

Figure 3.18: Validation of the Gaussian process regression: Comparison between the results obtained via the plastic correction algorithm (pure Neuber-type algorithm) and the predicted results via the Gaussian process regression.

5 Neural plastic corrector: learning from examples

The aim of this section is to investigate the relative merits of the previously described Neuber-type plastic corrector that corrects elasto-static simulations and that of an AI-based alternative that learns plastic corrections from full elasto-plastic simulations, before attempting to merge the two approaches.

The application of machine learning as a surrogate or correction technique for finite element analysis (FEA) has been successful across various fields, including the acceleration of nonlinear computations in porous specimens [Krokos et al., 2024], structural analysis [Nie et al., 2019, Deshpande et al., 2024] and other nonlinear mechanics problems [Raissi et al., 2019, Bai et al., 2024]. However, these methods tend to perform poorly when applied to cases that are geometrically very different from the cases in the training set [Krokos et al., 2021]. Taking this knowledge on-board, we restrict our AI approach using Convolutional Neural Networks (CNNs) to the correction of elasto-plastic fields in specimens with given nominal geometries but with random geometrical defects, the morphology and positioning statistics of which are known in advance. We will concentrate here on a tensile specimen including uniformly distributed spherical pores of fixed radius.

The AI strategy is the following: we voxelise the neighbourhood of points for which plastic correction is to be performed. Next, we provide either (i) the von Mises stress from the elastic computation or (ii) the result of the proposed Neuber-type plastic corrector as input to a CNN designed to predict a pointwise output of interest stemming from an elasto-plastic simulation. Training is done by acquiring reference quantities of interests (QoI) from a series of full elasto-plastic simulations using the Z-Set suite [Besson et al., 2012], for a sufficiently large number of specimens with random pore placement.

5.1 Dataset generation

The objective here is to generate a robust dataset that contains sufficient mechanical information about pore-surface and pore-pore interactions, so that the QoI in specimens containing a new distribution of spherical random pores is well predicted.

The Convolutional Neural Network (CNN) used here is designed to work with 3D images. A procedure was developped in order to convert finite element results into uniform grids of voxels (see Figure 3.19(a-b)). CNNs are resource-heavy when working with 3D images. Therefore, a size restriction is necessary for the images to fit in memory. We choose the CNN prediction of the QoI at a given voxel to be conditioned on the surrounding sub-volume of 16x16x16 voxels of the low-fidelity simulation. This sub-volume is assumed to contain enough information about the mechanical behaviour of the voxel's surroundings. In other words, the influence of the mechanical state beyond this sub-volume on the center point is assumed to be sufficiently well-represented by the mechanical fields that will be provided as input channel for the 16x16x16 input volume. The QoI in the subvolumes is normalised by the maximum value of the QoI across the training set. Empty space due to the pores or due to regions beyond the specimen's surfaces are encoded with a negative value, as input to our CNN is positive. If a negative input is to

be given, an additional binary channel can be used to encode the geometric information of the specimens [Krokos et al., 2021].

Next, the QoI computed by the plastic corrector is extracted specifically for the points that experience plastic deformation (i.e. all points with the von Mises stress exceeding σ_y). A K-medoids clustering algorithm (scikit-learn) is used to extract clusters from these points. K-medoids is preferred because it chooses actual data points as cluster centers, rather than creating new, synthetic points like K-means. This approach ensures that each cluster center is a real sample from the dataset, and is necessary as the mechanical field around the cluster center is needed. The number of clusters per realisation of a random porous specimen was chosen to be 200, to extract a reasonable amount of data per specimen. An example of the cluster points in a mesh is shown in Figure 3.19(c).

Finally, an input-output pair consists of a 16x16x16 volume of real values (the von Mises stress from the elastic prediction, or the actual QoI computed using the Neuber-type plastic corrector), associated with a reference value for the QoI corresponding to the center of this volume.

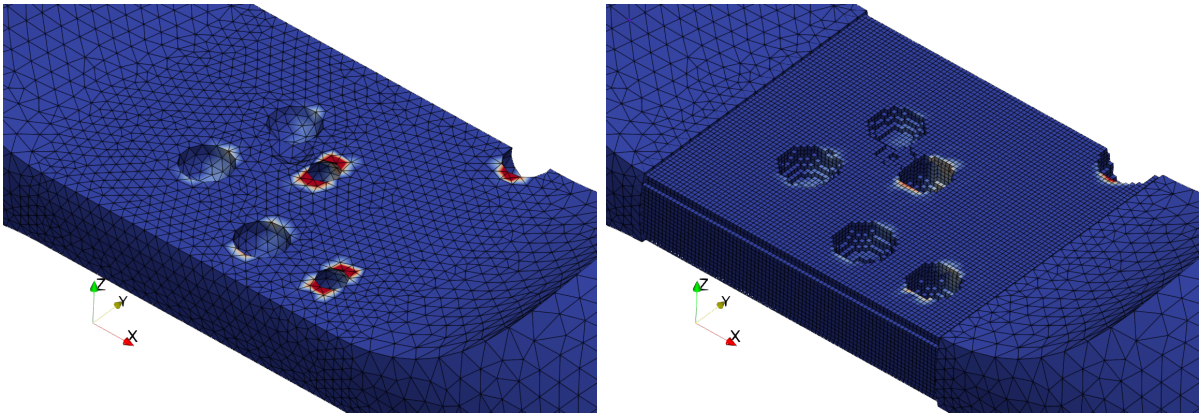

(a) Finite Element results on a continuous space

(b) Transformation to a uniform grid of voxels

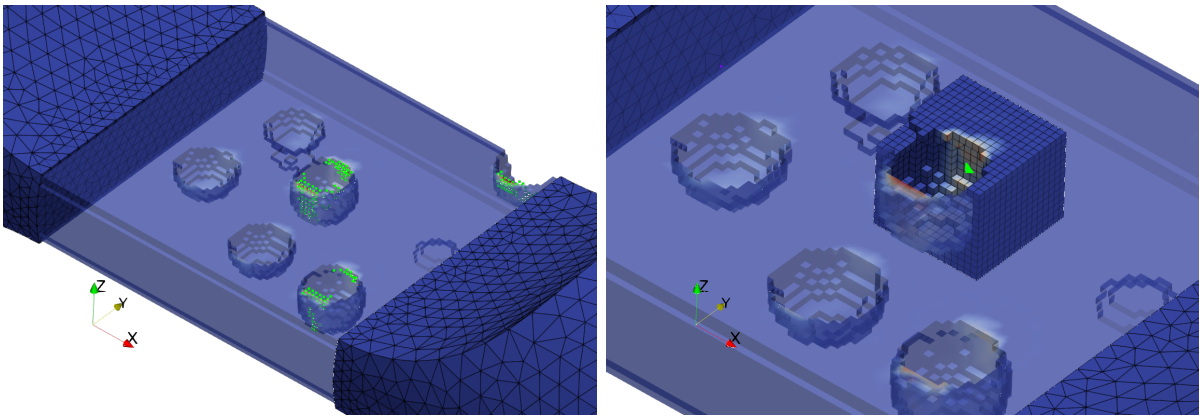

(c) Clusters using the K-medoids algorithm, at which the QoI is to be predicted

(d) A subvolume of voxels around a cluster voxel, serving as low-fidelity input to CNN

Figure 3.19: Obtaining training data from a mesh for the Convolutional Neural Network

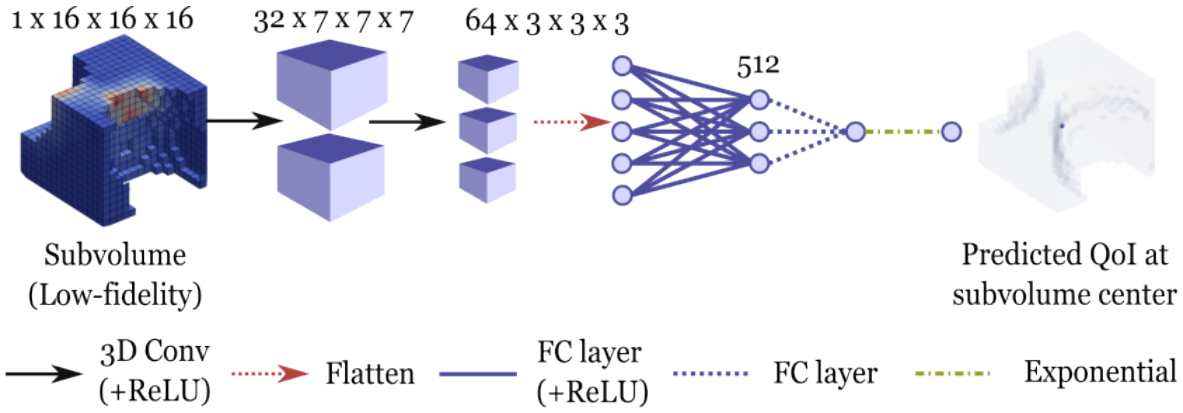

Figure 3.20: Architecture of the CNN developed for multi-fidelity corrections of a quantity of interest (QoI)

5.2 Architecture

The input of the CNN (Figure 3.20) consists of 16x16x16 subvolumes of low-fidelity information around a voxel of the QoI to be corrected. The convolutional blocks used consist of 3D convolutional operations with zero padding and a stride of two voxels, which reduces the size of the volumes after each block, followed by ReLU activation functions. After two blocks, the volumes are flattened and reduced through a fully connected layer followed by a ReLU activation function, and a last fully connected layer reduces the dimensions of the pseudo-output to unity. An exponential function can be used on the pseudo-output, to ensure that the CNN predictions remain positive, which is activated if the QoI is required to be strictly positive. The model parameters consist of the weights of the kernel and the fully connected layers. The output of the network is the value of the predicted QoI at the centre of the given subvolume. A Mean Squared Error between the CNN predictions and the reference data summed over the batch (size of 32) is used as the loss function for training.

5.3 Numerical results

For the numerical study, the intrinsic dissipated energy ϕ integrated over a loading cycle from time t_i to t_f [Besson et al., 2010] is considered as a QoI to be corrected via a CNN:

$$\phi = \int_{t_i}^{t_f} \left(f_y(\underset{\sim}{\sigma}; \underset{\sim}{X}, p) + \sigma_y + \frac{(R(p))^2}{2Q} + \frac{D}{2C}(\mathcal{J}(\underset{\sim}{X}))^2 \right) \dot{p}\, dt \tag{3.49}$$

with $\mathcal{J}(\underset{\sim}{X}) = \sqrt{\frac{3}{2}\underset{\sim}{X} : \underset{\sim}{X}}$.

Impact of mechanical inputs on the performance of the CNN

The CNN is trained using the von Mises stress from the elasto-static simulation ($\bar{\sigma}^{\#}_{\mathrm{VM}}$) as input. The CNN learns to predict the reference dissipation ϕ. We evaluate the accuracy of the CNN on only the clusters of the K-medoids algorithm, as we expect that this reflects well the CNN accuracy on full fields due to the good representative nature of the clusters. Figure 3.21 shows

the CNN predictions on the clusters of a mesh that is not in the training set after being trained on a progressively increasing number (20 to 100) of meshes. The results show that the accuracy of the prediction increases as a function of the amount of training data used. These results highlight that the CNN is able to predict the QoI using only $\bar{\sigma}^{\#}_{\mathrm{VM}}$ as input.

Next, the CNN is trained using the plastic corrector dissipation ($\hat{\phi}$) as input to the CNN. The CNN learns to predict the difference between the plastic corrector dissipation $\hat{\phi}_i$ and the reference dissipation ϕ. After the prediction, this difference is then subtracted from the plastic corrector dissipation $\hat{\phi}_i$ to get the final CNN-predicted dissipation. We focus on learning the difference because it typically yields better results than directly learning the QoI [Chinesta et al., 2020]. Figure 3.22 (a) shows the plastic corrector dissipation as a function of the reference dissipation, and ch3/fig 3.22 (b)-(e) show the CNN predictions on the K-medoid clusters of a mesh that is not in the training set after being trained on a progressively increasing number (20 to 380) of meshes. The results show the accuracy of the predictions improved as a function of the amount of training data used. The CNN trained with 380 meshes has 89% of cluster points of a mesh, not included in the training set, falling in a ±20% error cone, and the highest values of dissipation, which are generally of the most interest, have less than a percent of error.

Figure 3.22 (f) shows the mean square error (MSE) calculated on all the clusters of the mesh that is not in the training set, as a function of the number of meshes used for training. The downward trend of the CNNs trained with the two inputs is a clear indicator that the CNN is able to perform better if given more data during training.

We observe that training the CNN with the plastic corrector is beneficial when there is a low amount of available training data. The percentage of cluster points of a mesh not included in the training set, falling in a ±20% error cone, for the CNN trained on different amounts of training data, is shown in the second column of Table 3.5. The CNN trained with $\bar{\sigma}^{\#}_{\mathrm{VM}}$ as input, on 20 meshes, performs significantly worse than the CNN trained with $\hat{\phi}$ as input. The difference of the accuracy of the predictions between the CNNs, however, becomes smaller and smaller as the amount of training data increases. In our opinion, this is because the corrections provided by the proposed Neuber-type approach are purely local. The plastic corrections do not contain any additional information as compared to elastic results about the source of the discrepancy between the input and output of the CNN model from the topology of the neighbourhood of a point.

Accuracy of the CNN predictions for a non-spherical defect

We now illustrate the behaviour of the CNN, trained successfully on a data-set consisting of 380 specimens with spherical pores, when making predictions on a specimen containing a defect of non-spherical morphology. To this hand, we will generate a new specimen with a single non spherical defect whose geometry is illustrated in Figure 3.23(a). The geometric morphology of this defect comes from a computed tomography scan of a cast aluminium alloy. We ask the CNN to perform the plastic correction on all the points of the mesh that plastify (shown by the red points in Figure 3.23(a)). After being corrected by CNN, the number of predictions that are within the 20% error cone reaches 40.4%, starting from 40.8% for correction-less Neuber-type

Table 3.5: Percentage of cluster points in a mesh not included in the training set falling in a ±20% error cone for the networks trained with different inputs ($\bar{\sigma}^{\#}_{\mathrm{VM}}$ and $\hat{\phi}$) at different amounts of training data used

Training data used(number of meshes)	Input $\bar{\sigma}^{\#}_{\mathrm{VM}}$(% points)	Input $\hat{\phi}$(% points)
20	62%	80.5%
40	73%	77.5%
60	69%	76.0%
80	76.5%	79.0%
100	89%	87.5%
380	-	89.0%

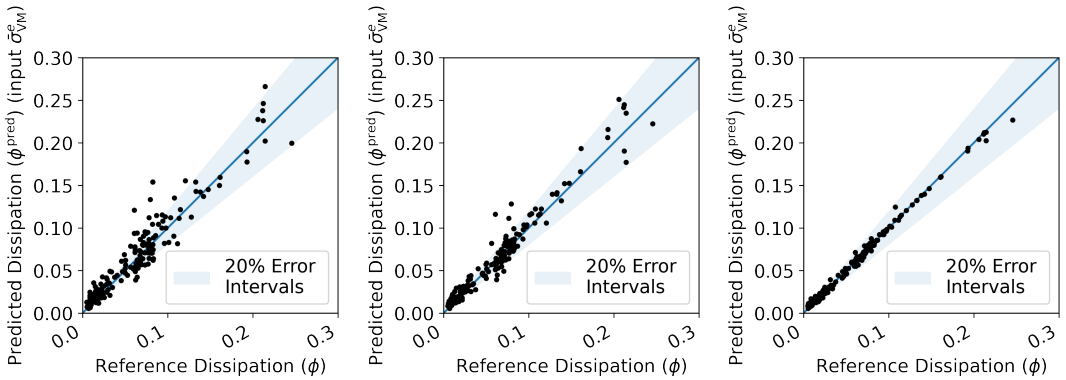

(a) 20 meshes (b) 40 meshes (c) 100 meshes

Figure 3.21: Using von Mises stress coming from elasto-static simulations ($\bar{\sigma}^{\#}_{\mathrm{VM}}$) as input: CNN predictions of dissipation for the clusters of a new, unseen mesh, after training for 2000 epochs on a varying number of meshes.

predictions, as shown in Figure 3.23. This behavior is in agreement with previous scientific findings [Krokos et al., 2021] that report a poor performance of neural networks when used to make predictions for cases outside the distribution of the training set.

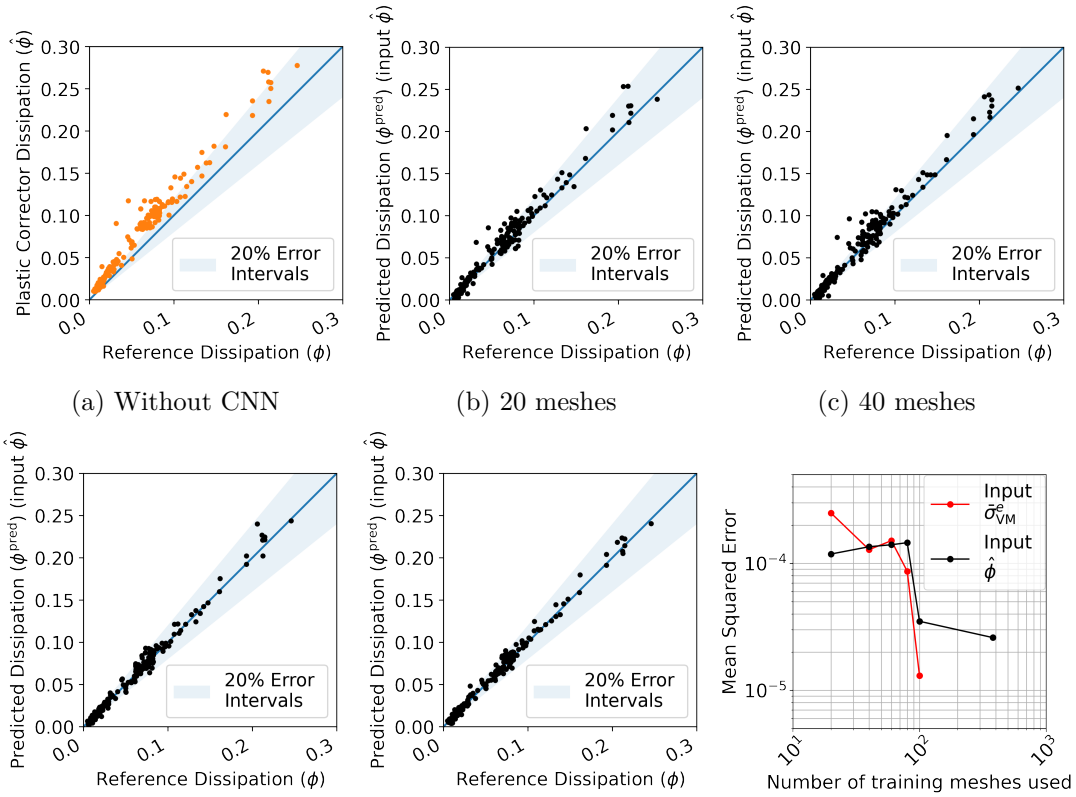

(a) Without CNN (b) 20 meshes (c) 40 meshes

(d) 100 meshes (e) 380 meshes (f) Sensitivity analysis

Figure 3.22: Using plastic corrector dissipation ($\hat{\phi}$) as input: CNN predictions of dissipation in the clusters of a new, unseen mesh: (a) Plastic corrector, before passing into CNN, (b-e) CNN predictions after training for 2000 epochs on a varying number of meshes, and (f) Sensitivity analysis showing decrease of the MSE between the CNN predictions and reference data with increase in training data.

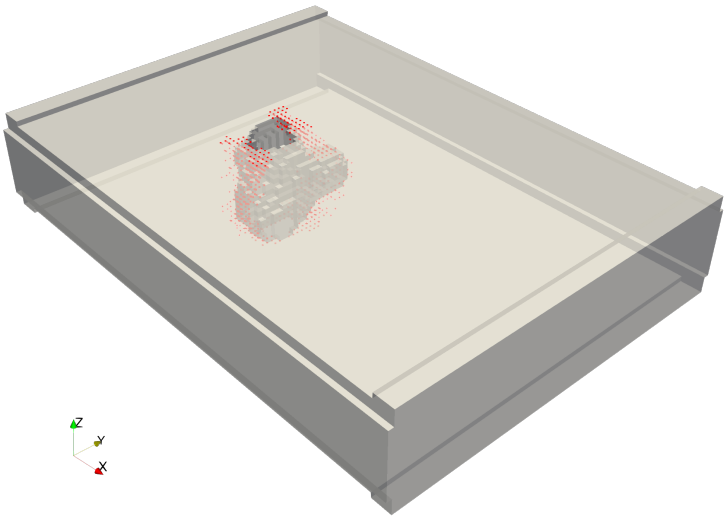

(a) Points in mesh selected for correction

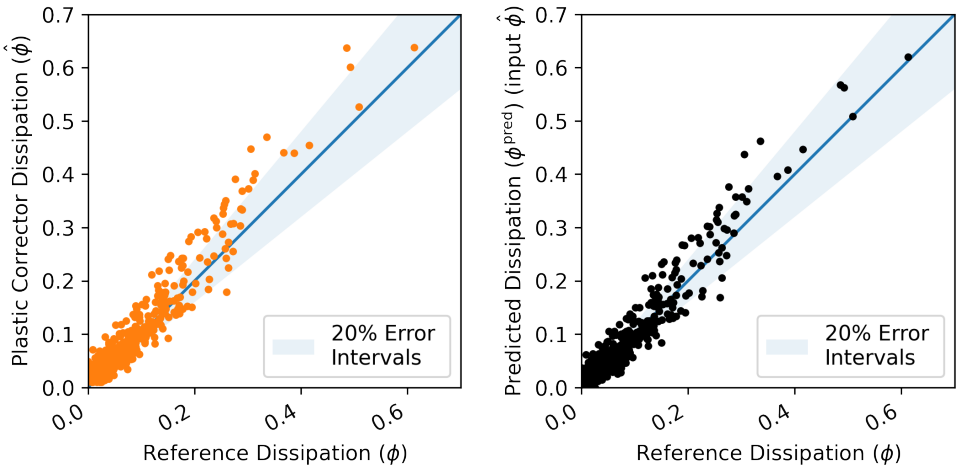

(b) Before passing into CNN

(c) CNN predictions

Figure 3.23: Accuracy of the CNN trained on 380 specimens with spherical pores on a specimen containing a defect of non-spherical morphology. The highlighted red points indicate points that undergo plastic deformation, that are selected for correction, in a mesh not included in the training set with a defect of complex morphology

6 Conclusion

A plastic correction algorithm has been proposed that rapidly post-processes elasto-statics simulations to approximate the full-field elasto-plastic response of structures subjected to proportional loading. The classical Neuber's rule has been modified to operate on the deviatoric part of stress and strain tensors. Cyclic loading is handled via a change of origin at every loading peak, using the method in [Chaudonneret and Culié, 1985]. A pointwise rule of proportional evolution of the deviatoric stress and strain tensors is used to reduce J2 elasto-plastic constitutive laws to a set of equations operating on scalar representations of stresses and strains. A fully implicit time integration algorithm for this system of equations has been developed, which leads to approximations of elasto-plastic solutions for arbitrary (proportional) loading sequences.

Numerical investigations on two test cases, one being a notched structure and the other one being a specimen with spherical pores, have shown good overall approximations of cumulative plastic strain fields, for both monotonic and cyclic loading, with errors in the notched structure matching previous studies [Molski and Glinka, 1981, Jones et al., 1998]. The overly stiff behavior observed in these plastic corrector predictions arises because plastic accommodation and stress redistribution effects have not been taken into account. [Molski and Glinka, 1981, Chouman et al., 2014]. For cyclic loading sequences, quantities computed over later cycles, like the cumulative plastic strain range, are reasonably well approximated. The plastic corrector's accuracy improves when the plasticity is relatively confined.

Furthermore, we have attempted to isolate the error due to the local proportional evolution rule in the plastic corrector algorithm. Investigations reveal that the proportionality rule contributes significantly less error compared to the Neuber-type rule. We have also shown that the major part of the error owed to the rule of local proportional evolution occurs during load reversal, when there is no accumulating plasticity.

Despite the plastic corrector's low computational cost compared to a full nonlinear finite element simulation, time-integration over long time histories may remain expensive. However, as a consequence of the rules underlying the proposed plastic corrector (J2 plasticity, pointwise proportionality of deviatoric strain and stress tensors, scalar Neuber rule), any output of the plastic correction algorithm depends on the elastic finite element simulation via the von Mises stress only. We have shown that this property can be exploited to build 1D meta-models that accelerate the plastic correction method even further, for any quantity of interest, by sampling the output of the plastic corrector for a relatively small number of von Mises stresses, training the meta-model and using it at almost no cost in place of the time integration algorithm.

Lastly, we have investigated the possibility of performing plastic correction using deep learning. These neural networks need reference elasto-plastic computations on a set of geometries for training, and do not generalise well to other types of geometries. We have shown that the output of the Neuber-type plastic corrector can be improved by using a CNN that leverages information about the local topology of material point neighbourhoods. We have also shown that the output of our Neuber-type methodology, as full-field input to the CNN, is indeed beneficial compared to using inputs of the NPC with a lesser mechanical content, i.e. the von Mises

stress from elasto-static simulations. We have shown that the benefit rapidly becomes negligible with an increase in the training data. Thus, the plastic corrector offers an advantage for deep learning-based corrections, particularly when the amount of training data is limited.

To further advance the research presented in this chapter, several directions can be pursued. First, the accuracy of the plastic corrector could be evaluated on cyclic loading sequences with non-zero mean values and irregular shapes. Second, the plastic corrector algorithm could be extended to accommodate non-proportional applied loading conditions, with an assessment of the algorithm's robustness and limitations under these scenarios. Finally, the potential of the plastic corrector in predicting elasto-viscoplastic material behavior and creep could be explored by incorporating time-dependent plasticity and viscous flow effects into the algorithm.

Part 2:

Self-heating for the detection of pores and proposed numerical developments towards rapid lifetime estimation for alloys with defects

Chapter 4

Experimental characterization of self-heating due to cyclic loading

Résumé

Ce chapitre explore le phénomène d'auto-échauffement dans les alliages d'aluminium et d'IN718 soumis à des chargements cycliques. La campagne expérimentale cherche à établir un lien entre l'élévation de température et les caractéristiques des défauts, notamment la porosité. Les résultats montrent que dans les alliages d'aluminium, la localisation thermique autour des pores n'est pas possible en raison de la conductivité thermique élevée, tandis que dans les alliages IN718 de faible conductivité, les données d'auto-échauffement permettent de détecter et localiser les pores. Les conclusions de cette étude soutiennent le potentiel d'utiliser les mesures d'auto-échauffement comme un outil diagnostique pour caractériser les défauts dans les alliages métalliques soumis à la fatigue.

1 Introduction

During cyclic loading, plasticity causes structures to dissipate energy, leading to a rise in temperature within the material. This phenomenon, known as self-heating, can provide insights into fatigue lifetime behaviour, as discussed in Chapter 1. Moreover, the magnitude and distribution of dissipation within the structure—and consequently the temperature increase—can be affected by the presence of defects such as pores, as the material surrounding these pores experiences higher loading. Self-heating experiments have previously been carried out for porous alloys in an attempt characterize damage [Ezanno et al., 2010, Bustos et al., 2023]. However, not many studies report the temperature response as a function of varying porosity levels or different pore configurations. A study on a bronze-aluminium alloy with a few isolated pores showed no effect on the temperature rise [Bercelli et al., 2021], and another on several porosity grades of a titanium alloy reported no differences either [Brot et al., 2024].

In this context, the primary objective of this chapter is to experimentally characterise the self-heating behaviour of the cast aluminium alloys introduced in Chapter 2, with two levels of porosity (one practically pore-free and the other with a 0.3% volume fraction of porosity), and to assess the differences between them. The potential application of the results from this experimental campaign for fatigue lifetime characterisation will be discussed in Chapter 5. Furthermore, as a secondary objective, this chapter will explore the potential for localising pores within a specimen based on the thermal signature on its surface during self-heating. This thermal signature depends on several factors, including the characteristics of the applied load [Munier et al., 2014], the conductivity of the alloy, and the distance of the pores from the surface. By testing various configurations of artificial pore positions, in inconel (IN718) specimens created through the Laser Powder Bed Fusion (LPBF) process, we aim to determine the limits of pore detection through self-heating experiments, given an alloy with low conductivity.

2 Experimental Protocol

This section will detail the materials, specimen geometries used, and the experimental protocol for self-heating experiments.

2.1 Materials and loading conditions

2.1.1 Aluminium alloys

The same aluminium alloys presented in Section 2 of Chapter 2 are used for the self-heating experiments. We recall the offset yield limit $R_{\text{p0.2}} = 240$ MPa and the elastic yield limit $\sigma_y = 170$ MPa.

Specimen geometry and preparation

The aluminium specimens used for self-heating experiments were provided by Stellantis. The geometry of the aluminium specimens used for self-heating experiments is shown in Figure 4.1. These planar aluminum specimens were polished with 1000, 2000 grit abrasive paper for one

minute each followed by 9 μm, 6 μm and 3 μm diamond paste for 15 minutes each. Black paint was then uniformly spray-painted onto the gauge section of the specimen to ensure an emissivity close to 1 [Leveuf et al., 2018] and to prevent reflections.

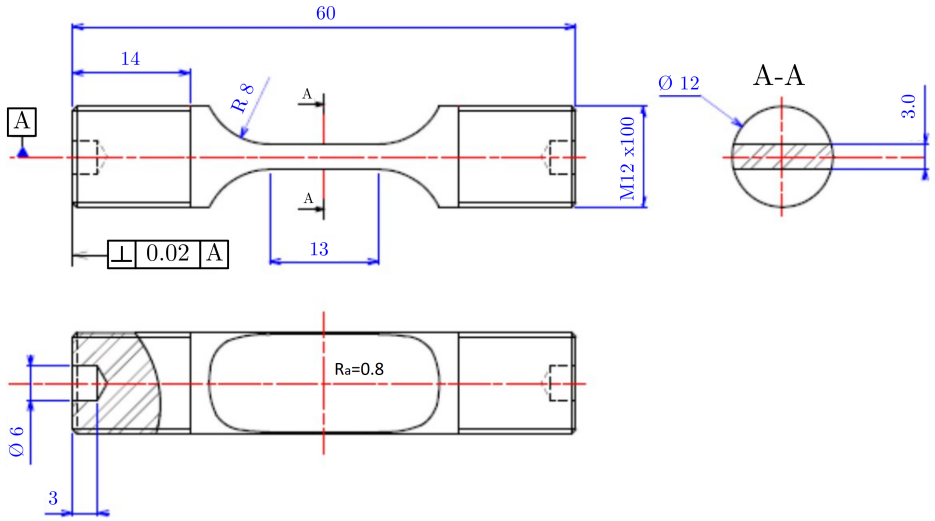

Figure 4.1: Specimen geometry used for self-heating experiments - aluminium alloys

Loading conditions

The experiments were conducted at a room temperature of 25°C. Successively increasing cyclic loading stages were applied to the specimens, with an applied stress amplitude $\Sigma_0 = \frac{\Delta\Sigma}{2}$ where $\Delta\Sigma$ is the applied stress range. The loading stages (shown in Figure 4.2) consisted of 5000 cycles with a load ratio (R) of -1 and a load frequency of 20 Hz. These stages were chosen to initially have a higher increment (12 MPa) between stages for very low loading (7-42% of σ_y) and then a smaller increment (6 MPa) for higher loading stages (42-60% of σ_y). This was done in order to obtain more points for capturing the transition between self-heating regimes and in anticipation of a second regime with a steeper slope [Doudard et al., 2004, Bercelli, 2021]. The experiment was stopped if the specimen failed before completion of all the loading stages. After each loading stage, a hold at zero kN was performed for a period twice as long as the loading stage, i.e. 500 seconds, to allow natural cooling, ensuring that the temperature of both the specimen and the clamps returned to the baseline temperature.

2.1.2 IN718-LPBF alloys

The specimens made of an inconel alloy (designated as IN718). The specimens were manufactured using the laser powder bed fusion (LPBF) process and underwent a heat treatment process.

Specimen geometry and preparation

The geometry of the IN718 specimens used for the self-heating experiments is shown in Figure

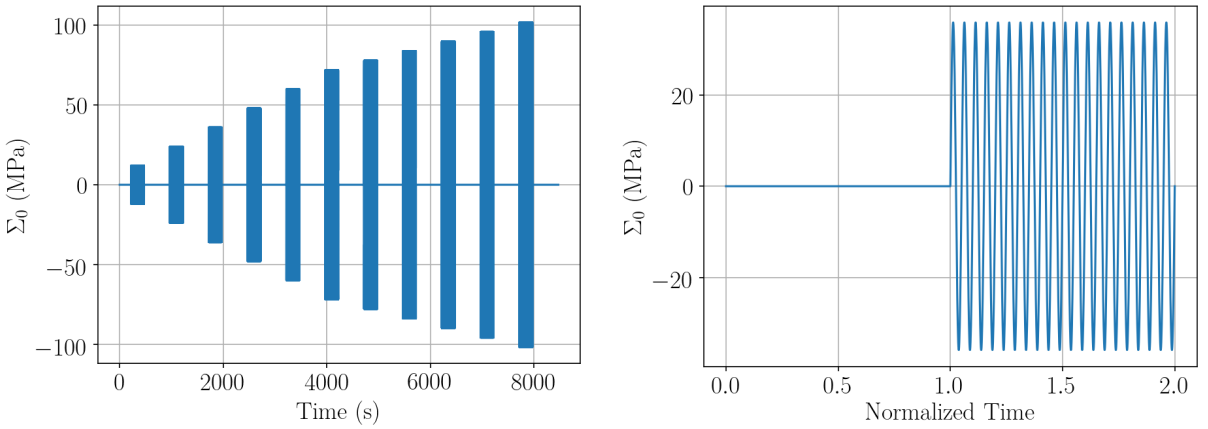

(a) Cyclic loading stages and wait periods

(b) Zoomed-in view of a time-interval showing the cyclic loading form imposed

Figure 4.2: Loading stages for the aluminium alloys

4.3. The specimens are tested here are typically used for fatigue testing, with a gauge section diameter of 4.37 mm, a gauge length of 12 mm. The entire geometry of the specimen (gauge section, threads, etc.) is obtained using additional machining after the additive manufacturing process. The cylindrical specimens were tested in their as-received condition, with black paint uniformly spray-painted onto the gauge section to ensure an emissivity close to 1 and to prevent reflections.

Artificial pores were drawn in the computer aided design (CAD) of the specimens, which were thus incorporated into the specimen geometry during the L-PBF process [Andreau et al., 2019]. Three types of pore configurations were created. The final position and geometry of the pores naturally depend on both the additive manufacturing protocol and the final machining. Their approximate positions are shown in Figure 4.3. These three configurations feature defects at varying distances from the surface and are described as follows:

1. **DS03 specimen**: Three surface-breaking spherical pores, each with a diameter of 0.6 mm, are positioned such that their centres theoretically lie on the surface of the specimen. The smallest distance between the boundaries of two adjacent pores (also called the ligament between pores) is 0.3 mm, resulting in a 0.6 mm centre-to-centre distance. These pores are located in the middle of the gauge section.

2. **DL03 specimen**: Three internal spherical pores, each with a diameter of 0.6 mm, are aligned along the diametric axis of the specimen's cross-section. The smallest distance between the boundaries of two adjacent pores is 0.3 mm, resulting in a 0.6 mm centre-to-centre distance. They are situated in the middle of the gauge section, with the distance from the pore boundary closest to the surface being 0.98 mm.

3. **DE specimen**: A single sub-surface ellipsoidal defect with a major axis diameter of 0.7 mm and a minor axis diameter of 0.3 mm is situated inside the specimen. The major axis of this ellipsoid is aligned with the diametric axis of the specimen's cross-section, with its

centre located just beneath the surface in the middle of the gauge section. The smallest distance between the pore boundary and the surface is 0.37 mm.

For specimens with internal pores (DL03 and DE), the pores were situated exactly in the middle of the gauge section. This is shown in Figure 4.6(c-d).

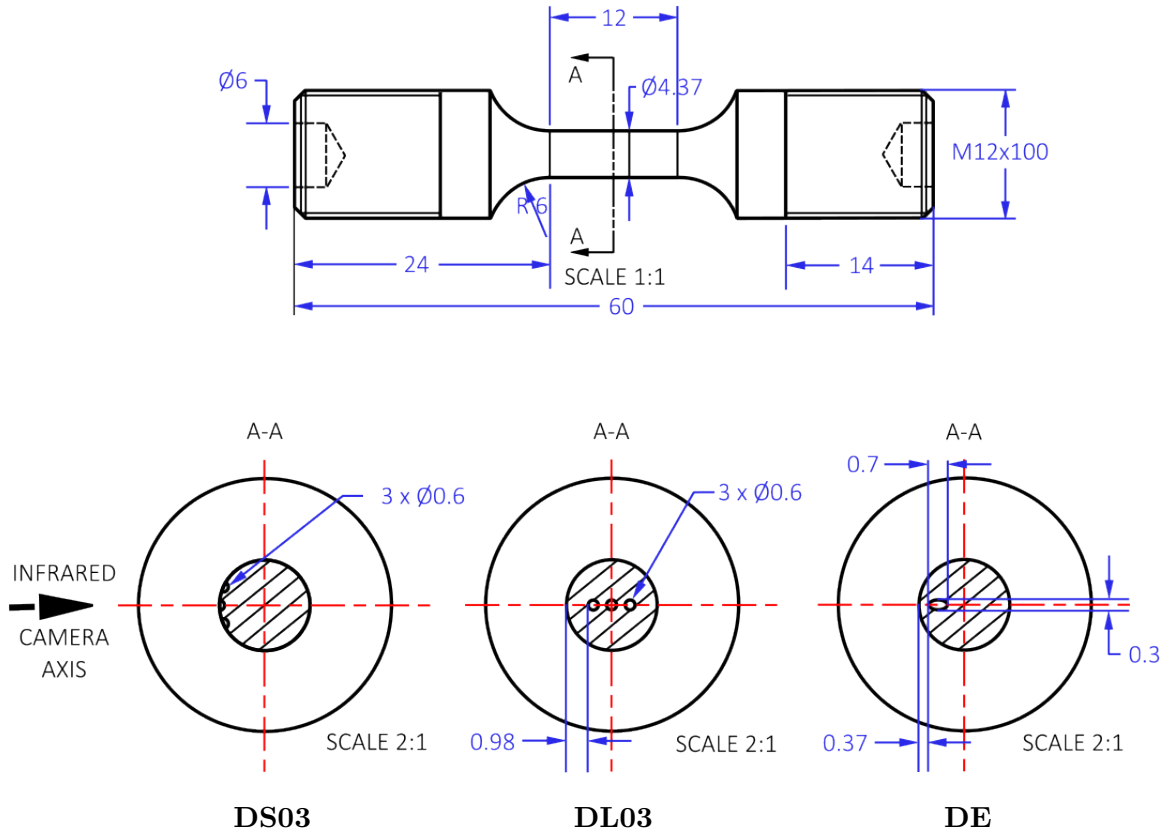

Figure 4.3: IN718 alloy specimen geometry, with three different configuration of pores (dimensions in mm)

Loading conditions

Successively increasing cyclic loading stages were applied to the specimens with hold at zero kN for natural cooling between stages. The first loading stage was chosen at around 30% of $R_{p0.2}$ of the alloy for a good signal-to-noise ratio. Indeed, discerning a temperature elevation due to pores becomes difficult due to noise at lower loading levels. The increment between loading stages was kept constant at 121 MPa (i.e. 10% $R_{p0.2}$), until failure occurred, in order to obtain the amount of temperature elevation at successively higher loading stages. The experiments were carried out under the following conditions: room temperature of 25 °C, a load ratio (R) of either 0 (for the DS03 and DL03 specimen, see Figure 4.4) or -1 (for the DE specimen, see Figure 4.5), and a load frequency of 20 Hz.

For the IN718 specimens with internal pores, the position of the pores was marked on the surface of the specimens in advance. For the DL03 specimen, the orientation of the three

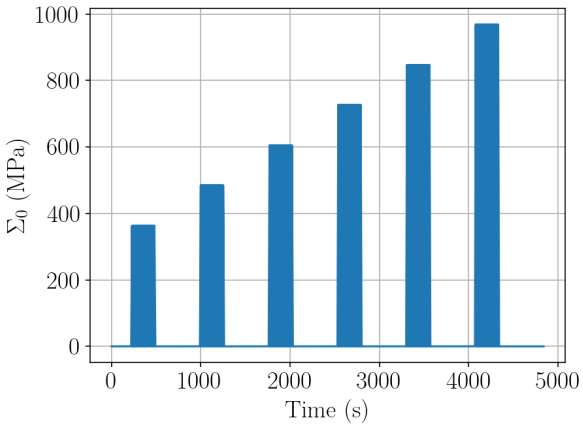

(a) Cyclic loading stages and wait periods

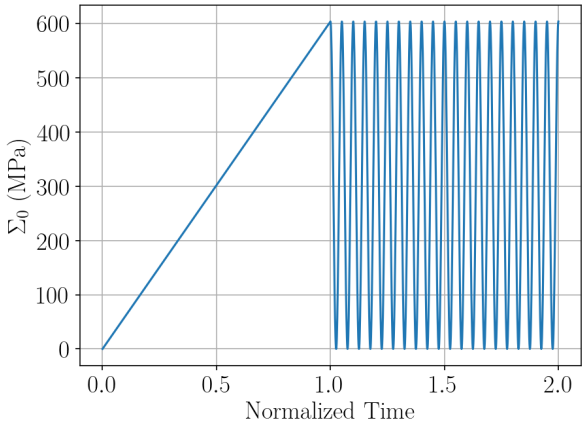

(b) Zoomed-in view of a time-interval showing the cyclic loading form imposed

Figure 4.4: Loading stages for the IN718 specimens with three surface breaking defects (DS03) and three internal defects (DL03)

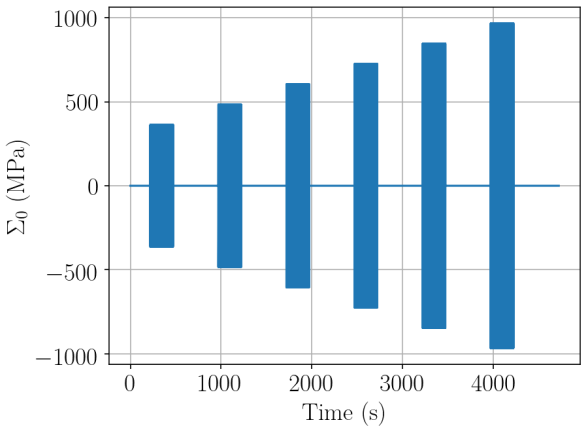

(a) Cyclic loading stages and wait periods

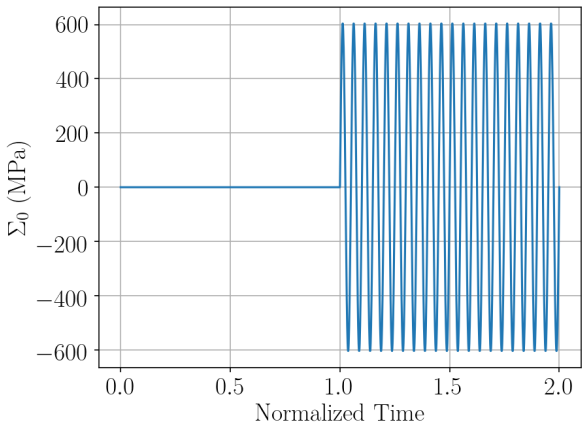

(b) Zoomed-in view of a time-interval showing the cyclic loading form imposed

Figure 4.5: Loading stages for the IN718 specimen with a subsurface elliptical defect (DE)

subsurface spherical pores was marked on using an etching on the upper face of one of the threaded ends at the time of manufacturing (see the top view of the specimen in Figure 4.6(a)). A similar marking was done for the DE specimen (see the top view of the specimen in Figure 4.6(b)). The alignment of the principal axis of the infrared camera with the axis connecting these spherical defects is therefore made possible (illustrated before in Figure 4.3). At the end of the experiment, an optical image taken of the fracture surface confirmed the orientation of the pores with respect to the infrared camera axis, as well as the inter-pore spacing and pore-to-surface distance. The fracture surfaces of the DS03, DL03 and DE specimens are shown in Figure 4.7.

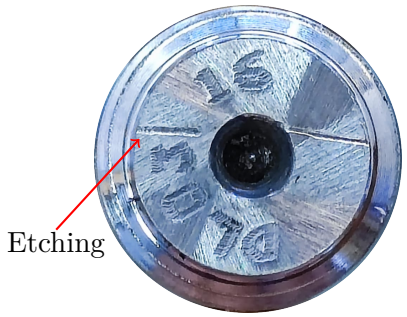

(a) DL03 specimen, top view

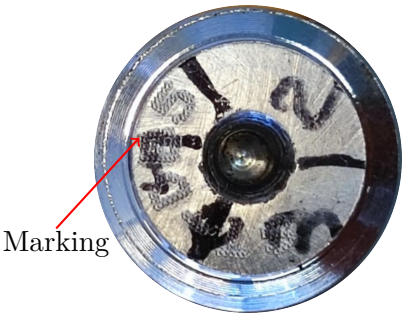

(b) DE specimen, top view

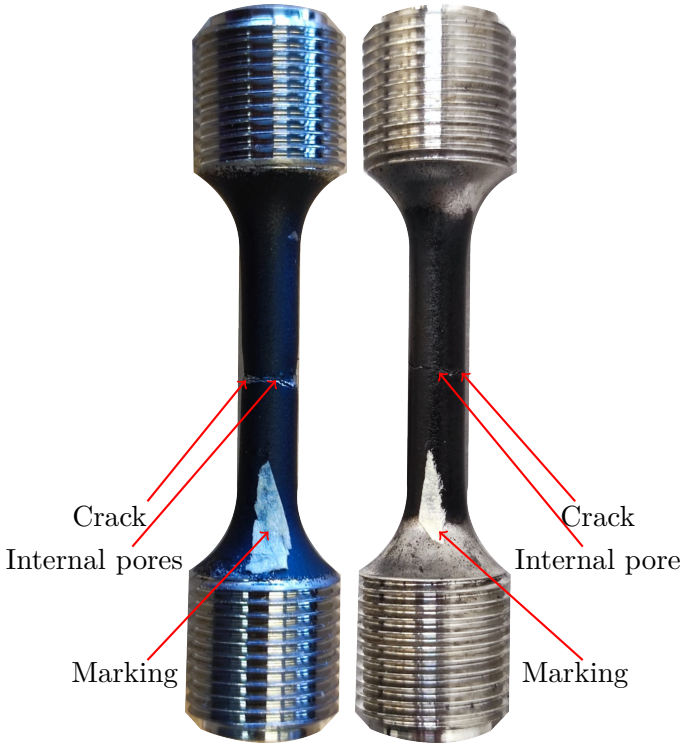

(c) Front view (DL03)

(d) Front view (DE)

Figure 4.6: (a,b) Etchings and markings that show the internal pore orientations of the DL03 and DE specimens, and (c-d) supplementary marking in the lower part of the gauge section of the two specimens to aid camera positionining (images taken post-failure)

2.2 Testing protocol

The fatigue testing machine for all experiments was an Instron 8502 equipped with a 50 kN load cell. The experimental setup is shown in Figure 4.8. Air conditioning, set to 25 °C, was used to maintain a constant temperature in the room, while light sources, including sunlight and artificial lighting, were controlled to remain stable throughout the experiments. This precaution helps avoid thermal drift of the machine that may affect temperature measurements. The room was fully sealed to prevent any temperature fluctuations. If the fatigue testing machine was

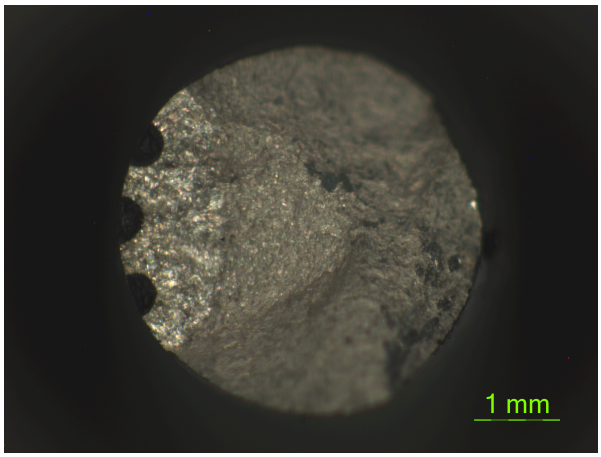

(a) DS03 specimen

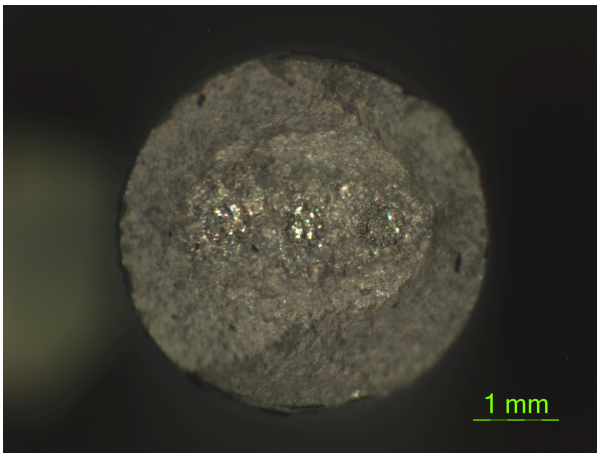

(b) DL03 specimen

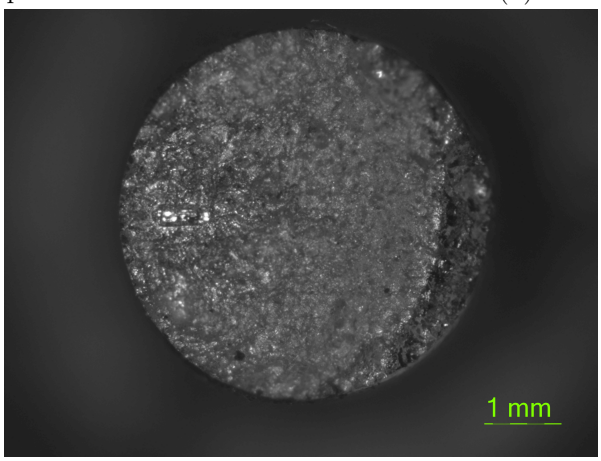

(c) DE specimen

Figure 4.7: Fracture surfaces of the DS03, DL03, and DE specimens after the self-heating experiments, confirming the inter-pore spacing, pore shapes and pore-to-surface distance, as well as confirming the correct positioning of infrared camera placement

turned off, it was first cycled without any specimen to heat the piston, ensuring the machine reached the required operating temperature before starting the actual test.

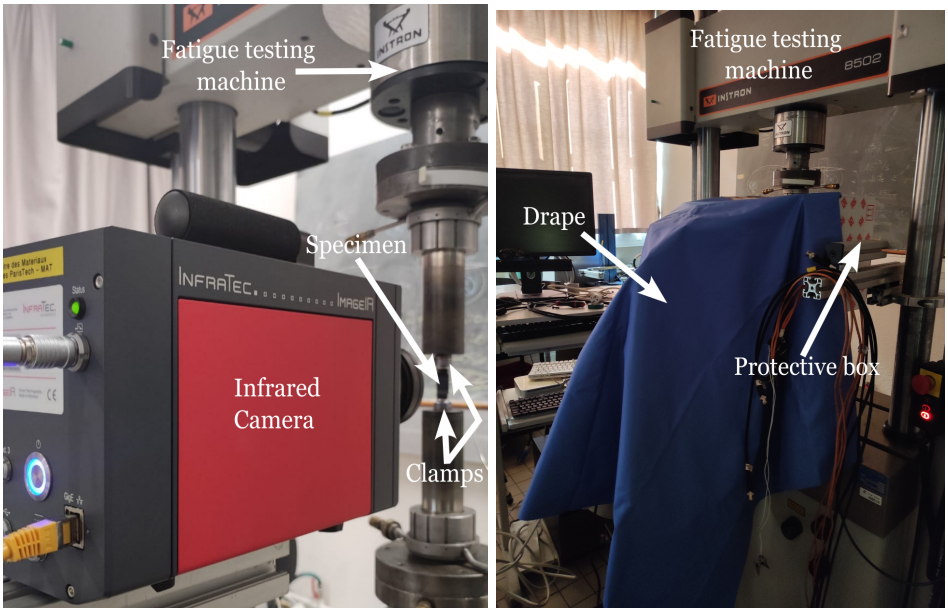

(a) Setup of the infrared camera and the specimen in the fatigue testing machine

(b) Protective drapes and boxes to avoid artifacts in temperature measurements

Figure 4.8: Setup for self-heating experiments using infrared thermography

The prepared specimen is mounted onto the machine, and both the camera and specimen are covered by a thick drape and a protective box with its interiors painted black (see Figure 4.8(b)). This was done to avoid reflected fluxes by the surrounding environment on the object, as is sometimes done for self-heating experiments [Carteron, 2020]. The protective elements reduce the noise captured by the infrared camera, improve the contrast between the specimen and the background, limit the reflected flux (radiation) and prevent fluctuations due to convective flows (for example, air currents). This step is followed by a minimum waiting period of 4 hours to allow the temperature difference between the bottom and top clamps to stabilize. During this time, the temperature gradient is monitored in real-time to ensure there is no difference between the temperature profiles of the clamps and the specimen before the experiment is started.

2.3 Measurement methods and acquisition protocol

An infrared camera was used for measuring the temperature evolution of the specimen and the clamps. The details of the camera are provided in table 4.1.

For self-heating experiments, which are generally done at high load frequency, the average rise of the temperature over time is of interest, and not the temperature cycling due to thermo-elastic coupling. At the same time, it is necessary to correctly identify the thermo-elastic coupling for treatment of temperature profiles for the accurate identification of the temperature rise due to purely self-heating. The stroboscopic effect can be utilized to capture the extents of temperature variations due to thermo-elastic coupling. The acquisition of the temperature maps

Table 4.1: Infrared Camera Specifications

Name	IR InfraTec 8350
Description	Infrared camera for full-field temperature measurement
Detector	MCT detector, 640x512 pixels
Resolution (max.)	32 px/mm (with 50 mm Telephoto Lens + 8 mm Extension Rings + 300 mm Close-Up Lens)
Working distance (at max. resolution)	104 mm
FOV (at max. resolution)	20 mm x 16 mm
Acquisition frequency (max.)	200 Hz for a window of 640x512 pixels

was performed with a randomized time interval between acquisitions (50 ms, 60 ms, 55 ms, etc.) to achieve this. The acquisition of images, started before cyclic loading, is continued during the loading and cooling stages and stopped after all the load stages have been completed.

3 Self-heating results: Aluminium alloys

For the self-heating experiments on the aluminium alloys, the infrared camera resolution was set to 8 px/mm, with a total image size of 90x220 pixels (11x28 mm). This field of view was specifically chosen to have the specimen as well as the clamps in the thermal image, in order to be able to correct for the heating of the clamps.

Both the porous and non-porous aluminium alloys were tested to check the temperature response due to self-heating. No temperature localization due to pores was observed for the porous aluminium alloy, which matches results found by other authors on aluminium alloys who cite very low signal to noise ratio due to high conductivity of these alloys [Morabito et al., 2007]. Other authors claim a compensation of the higher dissipation around pores by the missing volume of material [Messager, 2020].

Self-heating measurements are typically reported in a $\bar{\theta}$ - Σ_0 space, where $\bar{\theta}$ is the steady-state temperature rise of the specimen, usually taken after a few thousand cycles of loading. This is done in order to identify a parameter in the micro-inclusion model [Doudard et al., 2004] controlling the scatter in high-cycle fatigue, which was described in Chapter 1, and will be applied in Chapter 5. To this end, the following paragraphs will detail the analysis procedure used to obtain this graph. Maps of temperature difference were computed by pixel-wise subtraction:

$$\theta(N) = T(N) - \bar{T}_0 \tag{4.1}$$

where $T(N)$ is the temperature in the image at the N^{th} cycle. Likewise, the temperature map just before heating starts, in with temperature $\bar{T}_0$, is the initial state of the system. An example of $\bar{T}_0$ is shown in Figure 4.9(a) and $\bar{T}(N = 3500)$ is shown in Figure 4.9(b), with the difference $\bar{\theta}(N = 3500)$ shown in Figure 4.9(c). Note that the overhead bar ($\bar{\bullet}$) symbol is used for quantities without time dependence.

Next, specific regions were selected for extracting the value of averaged temperature difference of the specimen and clamps (the average is taken over all the pixels in the region). The region size for this operation was 6.4×6.4 mm (the size of the regions is shown in Figure 4.9(c)). This average temperature rise over time is shown for one of the tested porous specimens in Figure 4.10(a). In order to isolate the temperature rise purely due to self-heating and suppress the oscillations due to thermo-elastic coupling, the rolling mean of the temperature time series is calculated by taking the mean of the values within a specified window size for each point in the time series. An example is shown in Figure 4.10(a). The rolling window size is fixed at 100 readings. The same rolling mean is also applied to the temperature of the two clamps.

The mean temperature of the two clamps (obtained using a rolling mean) is subtracted from the mean temperature of the specimen (also obtained using a rolling mean) to determine the corrected temperature rise of the specimen due to self-heating (an example is shown in Figure 4.10(b)). The corrected temperature rise profiles of the specimen were superimposed such that all the heating curves start at the same point (Figure 4.10(c)). The steady state temperature, denoted as $\bar{\theta}$ was taken as the temperature after 3500 cycles of loading. Finally, $\bar{\theta} - \Sigma_0$ curves were obtained, shown for all the specimens tested in Figure 4.11. The results show the existence of two regimes of self-heating for the non-porous alloy. Furthermore, the non-porous material exhibits approximately the same level of temperature rise as the porous alloy. Higher levels of loading in the porous alloy could not be achieved due to failure. Although no self-heating experiments on this specific alloy were found in the literature for comparison purposes, the authors of [Ezanno et al., 2013] indicate the presence of two regimes on a cast copper-aluminium alloy, even in the presence of casting defects, which was not the case here.

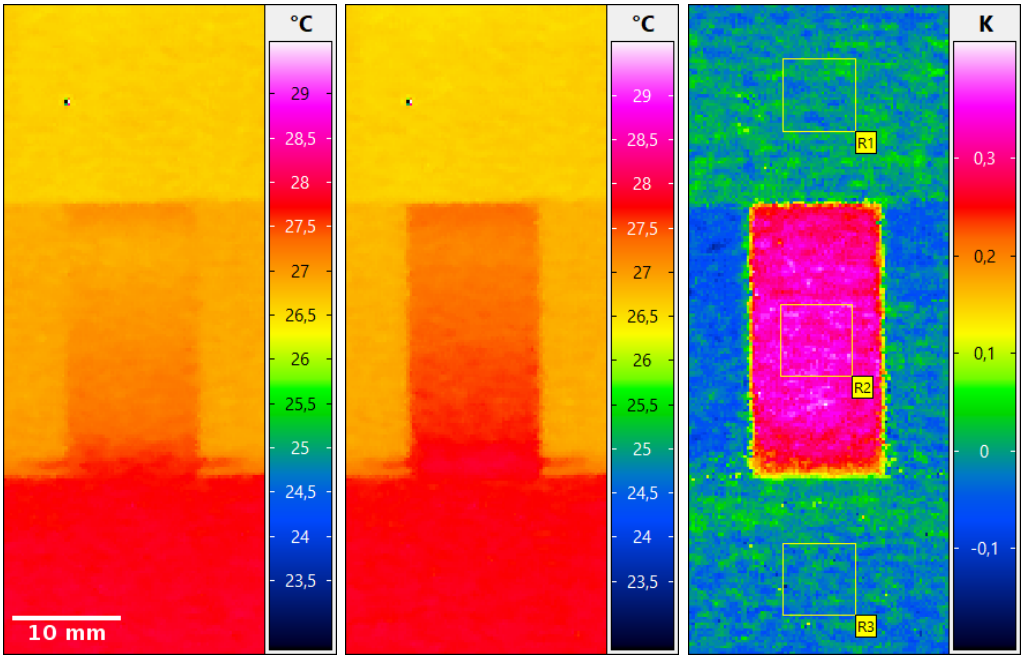

(a) Temperature map with initial temperature $\bar{T}_0$ before the start of cyclic loading

(b) Temperature map with temperature $\bar{T}(N = 3500)$ after 3500 cycles at 20 Hz (considered as steady state)

(c) Map of temperature difference, with temperature rise $\bar{\theta}(N = 3500) = \bar{T}(N = 3500) - \bar{T}_0$, and regions chosen for the area-wise averaging of temperature difference of specimen and clamps

Figure 4.9: Pixel-wise temperature difference for obtaining $\bar{\theta}$ maps, and regions chosen for extracting the average temperature variation

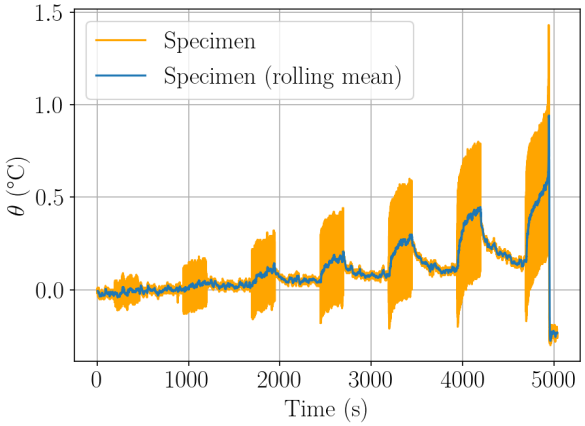

(a) Mean filtering of specimen temperature rise acquisitions

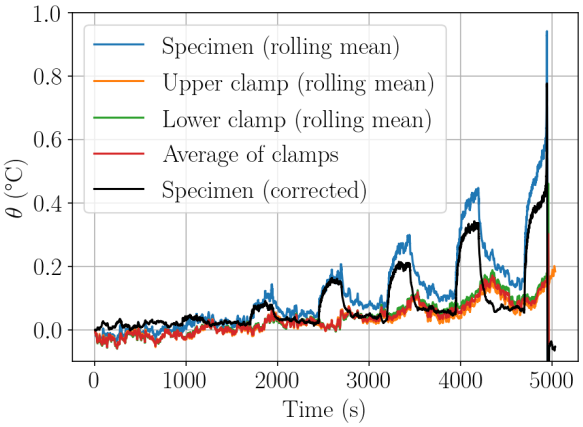

(b) Subtraction of the average clamp temperature rise from the mean specimen temperature rise

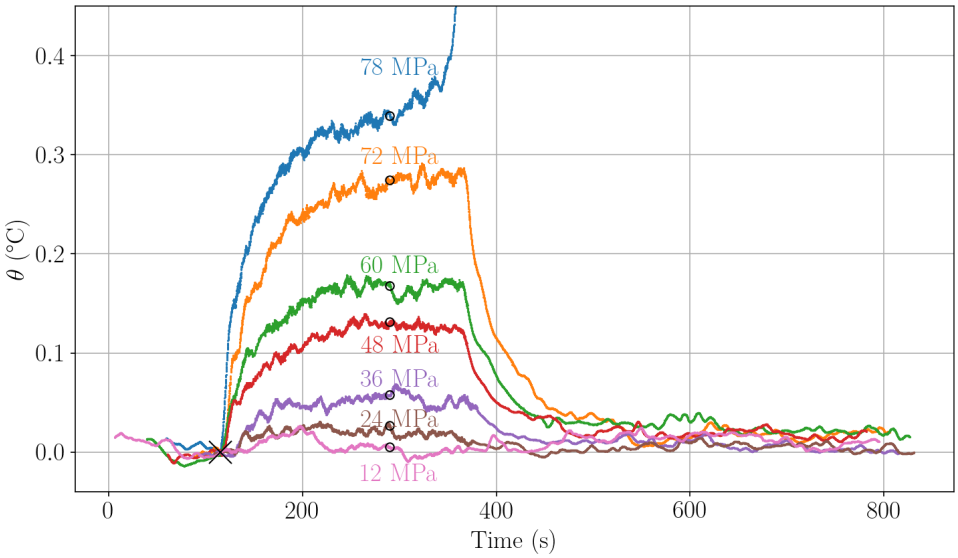

(c) Superimposition of the corrected specimen temperature rise for different loading levels. The × is the point used for superimposition of the profiles, and the circles are the time points for which θ is considered stabilized.

Figure 4.10: Treatment of temperature acquisitions

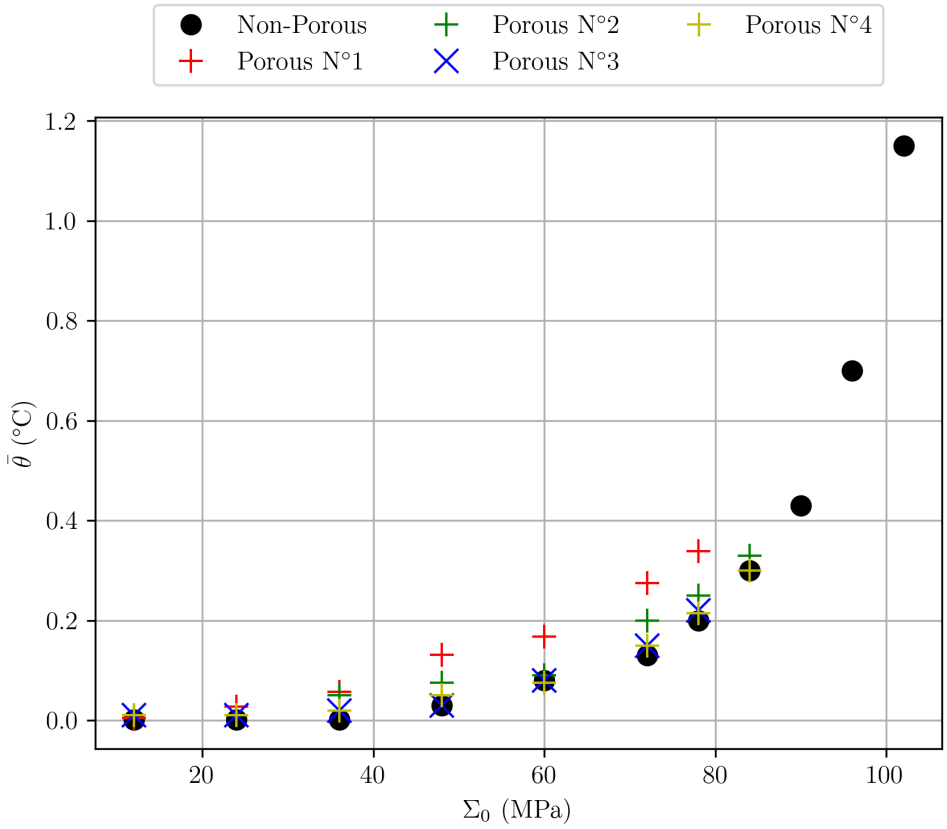

(a)

Figure 4.11: Results of self-heating experiments carried out on one non-porous specimen and 4 porous specimens, in the $\bar{\theta}$ - Σ_0 space

4 Self-heating results: IN718-LPBF alloys

For the self-heating experiments on the IN718 alloys, the infrared camera resolution was set at 31 px/mm, with a total image size of 640x512 pixels (20.6x16.5 mm). This field of view was specifically chosen to have the maximum resolution possible for detection of pores in the specimen. Maps of temperature difference were computed by pixel-wise subtraction in the same fashion as described in equation (4.1).

Surface-breaking pores (DS03 specimen)

Two points are considered for analysis, one point in one of the surface-breaking pores, and the other one away from the pores, but still in the gauge section of the specimen (see Figure 4.12). The temperature evolution of these two points during cyclic loading is shown in Figure 4.13(c-d). The steady state temperature difference $\bar{\theta}$, here computed after 5000 cycles, is shown in Figure 4.14. The results clearly show a higher temperature rise for the point in the pore as compared to the point away from the pore, for all the loading levels. In the temperature rise maps shown in Figure 4.14(b-f), the pores are detectable at a load as low as 30% $R_{p0.2}$. However, the signal-to-noise ratio is not very high at this small load.

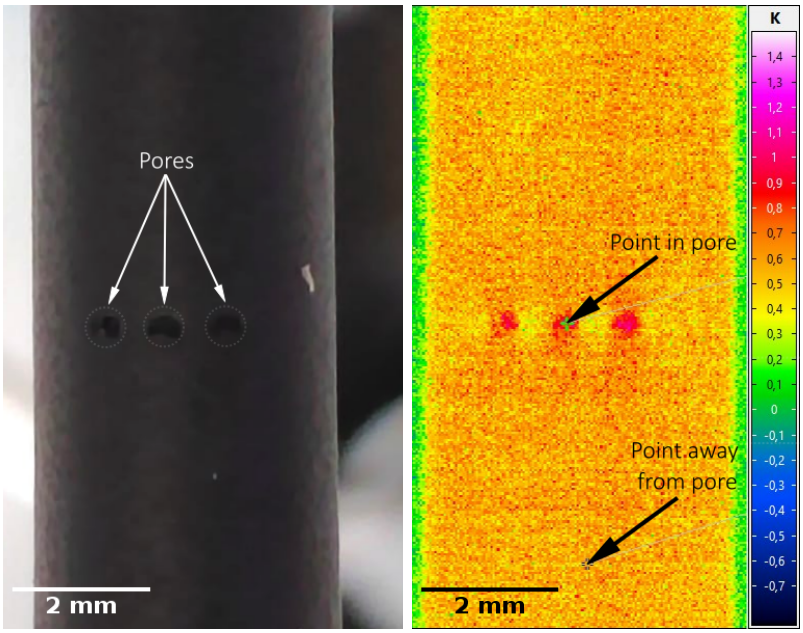

(a) Optical image of pores in the DS03 specimen's gauge section, with the surface-breaking pores encircled

(b) Points in the specimen's gauge section selected for analysis: a point near and away from a surface-breaking pore, shown on the $\bar{\theta}$ map for loading at 60%$R_{p0.2}$

Figure 4.12: Optical and thermal difference image showing the points chosen for analysis, in a pore and away from the pores

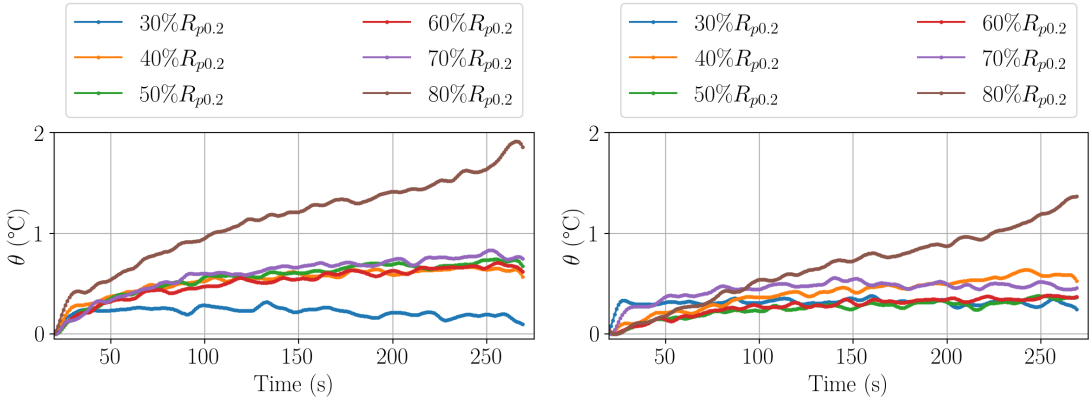

(a) Point in pore (b) Point away from pore

Figure 4.13: Comparison of self-heating near and away from a surface-breaking pore

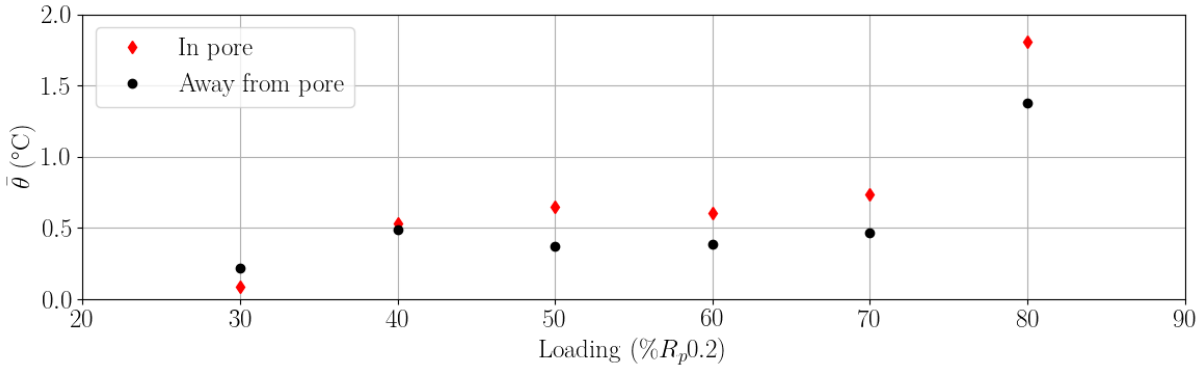

(a) Comparison of self-heating (at t=250 s, i.e. 5000 cycles at 20 Hz) near and away from a surface-breaking pore

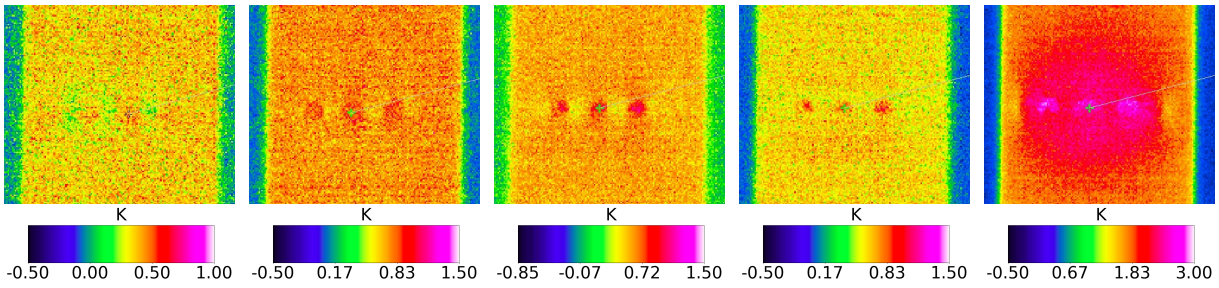

(b) 30%$R_{p0.2}$ (c) 50%$R_{p0.2}$ (d) 60%$R_{p0.2}$ (e) 70%$R_{p0.2}$ (f) 80%$R_{p0.2}$

Figure 4.14: Self-heating in and away from a surface-breaking pore, with full-field $\bar{\theta}(N = 5000)$ maps showing stronger localization due to the pores with higher applied loading

Internal pores: subsurface spheres (DL03 specimen)

A difference in temperature rise due to self-heating was observed between the region with pores and the pore-free region, even at the lowest level of loading (30% $R_{p0.2}$, see Figure 4.15). However, this minimal temperature difference does not necessarily indicate a successful localisation of the pores, and could be due to the boundary conditions. Indeed, the elevated temperature of the specimen in the middle of the gauge section could be due to conduction through the ends of the specimen, which can act as heat sinks. The temperature profiles for the lowest load level are shown in Figure 4.16. No temperature variation is found between the seven profiles, i.e., the pores cannot be localised along the width of the specimen (the horizontal axis). However, the temperature rises slightly in the centre of the profile after cyclic loading is applied (the temperature is shown after 2000, 4000, and 5000 cycles at 20 Hz). Again, it is not possible to say if this rise is due to the boundary conditions applied to the specimen or actually due to the pores. To distinguish between the heating caused by the presence of pores and the heating at the centre of the specimens due to boundary conditions, a pore-free specimen needs to be tested. Unfortunately, such an experiment could not be conducted due to the unavailability of a pore-free specimen. Subsequent loading stages show the same behaviour, with a much clearer rise in temperature at the pore locations — this clearer signature, however, is a combined effect of the boundary conditions, higher dissipation due to increased loading and internal crack propagation (see Figure 4.17 for the loading stage corresponding to 90% $R_{p0.2}$).

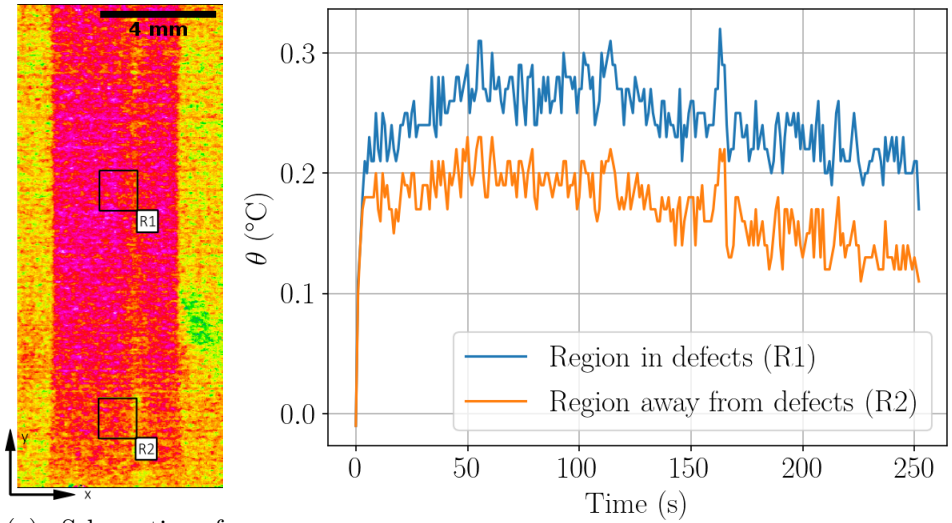

(a) Schematic of selected regions R1 and R2

(b) Comparison of self-heating in regions R1 and R2 over time, for the 30% $R_{p0.2}$ loading stage

Figure 4.15: Comparison of evolution of surface temperature in pore and pore-free regions (R1 and R2 respectively) of the specimen with a subsurface elliptical pore

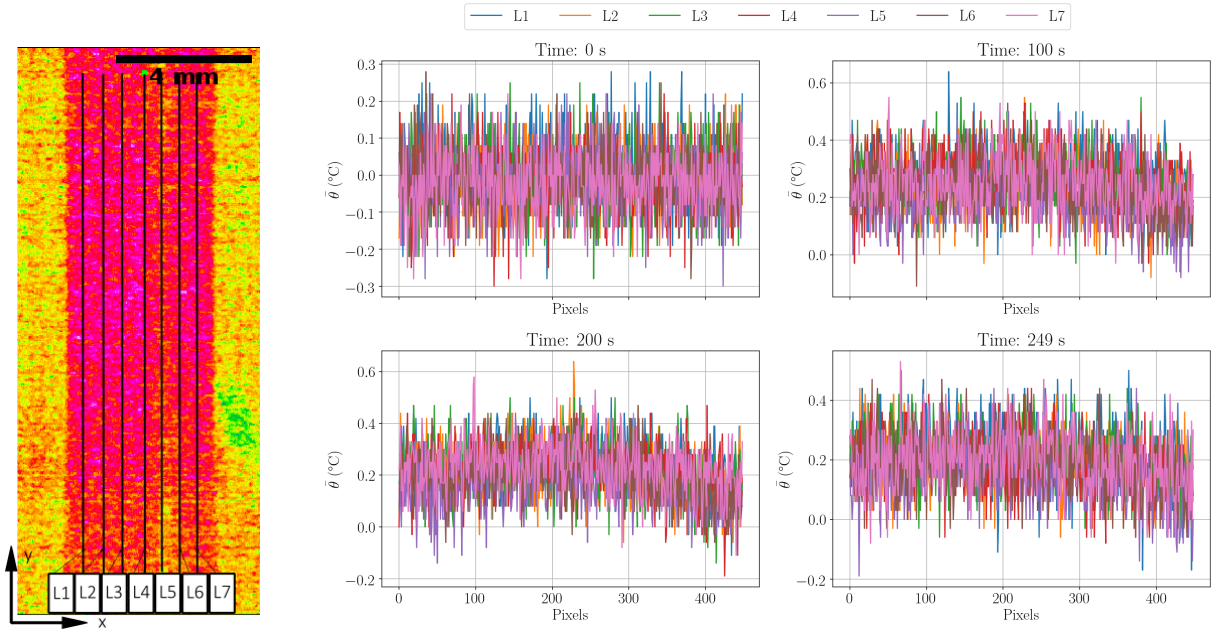

(a) Schematic of 7 profiles taken in the specimen

(b) Temperature evolution during stage 1 of cyclic loading: 30% $R_{p0.2}$, superposition of temperature of 7 profiles. The temperature at different intervals of time is shown: in the initial state, at 50, 200, and 249 seconds.

Figure 4.16: Evolution of temperature in the specimen with a subsurface spherical pores at 1 mm below the surface (loading at 30% $R_{p0.2}$)

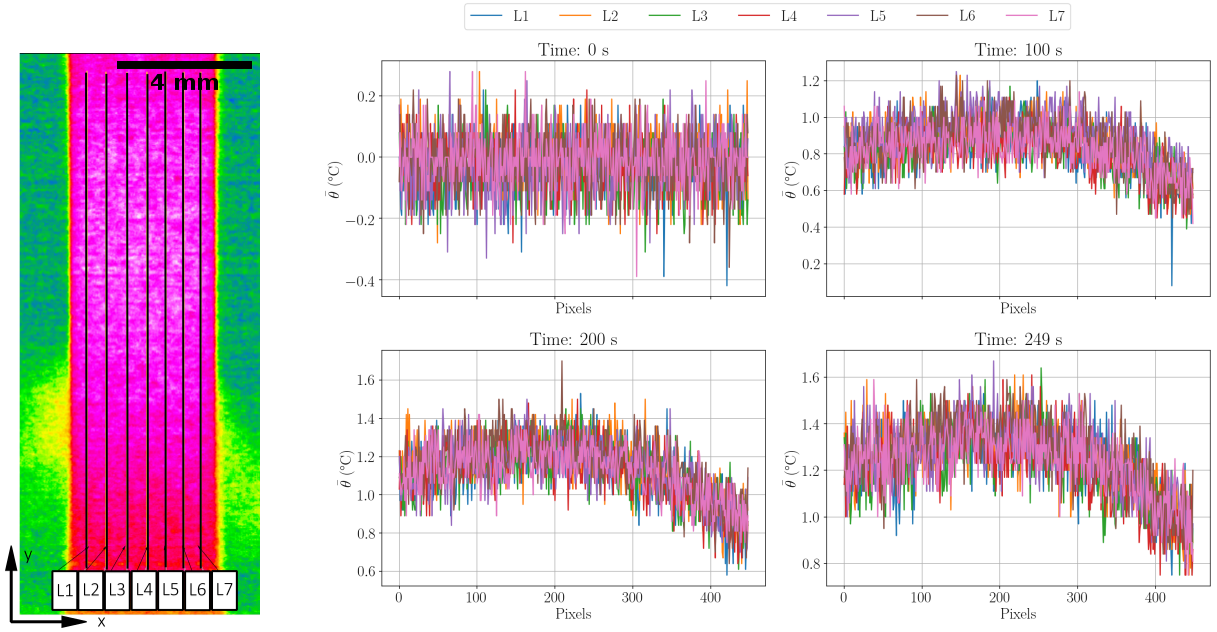

(a) Schematic of 7 profiles taken in the specimen

(b) Temperature evolution during stage 1 of cyclic loading: 90% $R_{p0.2}$, superposition of temperature of 7 profiles. The temperature at different intervals of time is shown: in the initial state, at 50, 200, and 249 seconds.

Figure 4.17: Evolution of temperature in the specimen with a subsurface spherical pores at 1 mm below the surface (loading at 90% $R_{p0.2}$)

Internal pores: subsurface ellipse (DE specimen)

The position of the subsurface elliptical defect was marked on the surface of the specimen in advance, using radiography. The principal axis of the infrared camera was aligned with the major axis of the elliptical defect (illustrated in Figure 4.3). With infrared thermography monitoring, an increase in temperature in the specimen is observed, which becomes higher for higher load steps (see Figure 4.18). The average temperatures of the region R1 with the pore and the region R2 in the gauge section away from the pore is similar for stages 1-3, and starts to noticeably differ from stage 4 onward. The average temperatures in these regions tend towards a stabilization for loading stages 1-4 after approximately 5000 cycles. The temperature during stage 5 never stabilizes, indicating an advanced stage of crack propagation. For these reasons, stage 4 will be analyzed to see if it is possible to identify the location of the internal defect before significant damage occurs.

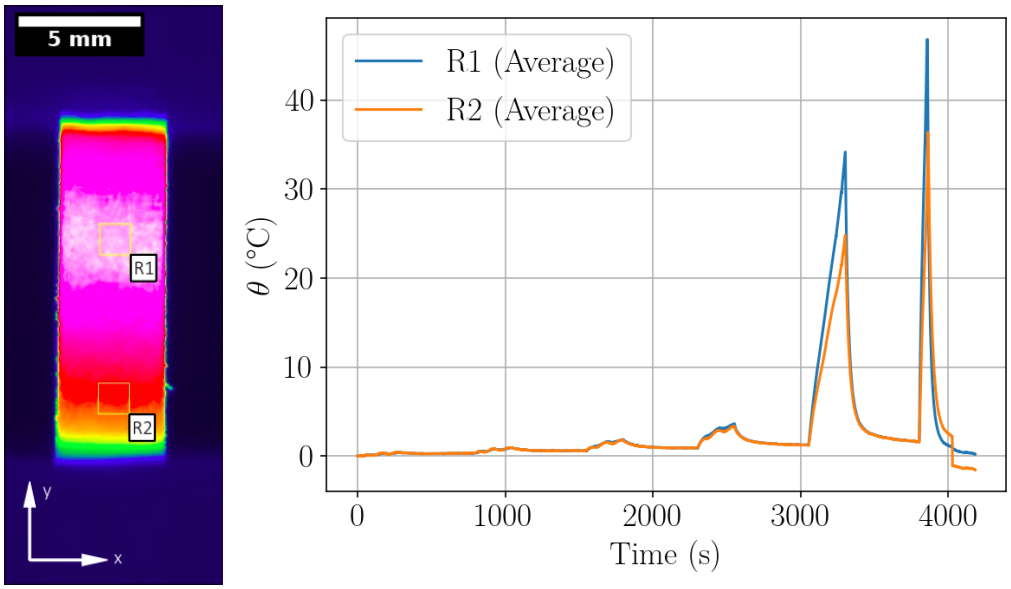

(a) Schematic of selected regions R1 and R2

(b) Comparison of self-heating in regions R1 and R2 over time, for all the cyclic load stages

Figure 4.18: Comparison of evolution of surface temperature in pore and pore-free regions (R1 and R2 respectively) of the specimen with a subsurface elliptical pore

Because of high local loading, the internal pore dissipates more heat than the rest of the useful region. However, the pore is located at a distance of 0.373 mm from the surface, making heat diffusion difficult to precisely locate the exact position of the defect in the x-y plane. This makes the analysis of profiles necessary, as shown in Figure 4.19. The evolution of temperature along profiles L1-L7 with time is measured. The temperature is heterogeneous and maximal in the middle of the specimen, which is consistent with the actual position of the ellipse that had been marked on the surface using radiography results. There is, of course, an effect of the boundary conditions on the heating, as in the DL03 specimen presented in the previous section (section 4). However, the temperature rise in the location of the pores is more pronounced in the DE specimen as compared to the DL03 specimen, despite the lower loading level of the

DE specimen (60% $R_{p0.2}$, Figure 4.19) as compared to the DL03 specimen (90% $R_{p0.2}$, Figure 4.17), which demonstrates a stronger temperature rise due to the pores as compared to the heating due to the boundary conditions. Therefore, it is indeed possible to locate the elliptical pore along the y-axis. It is unknown if significant internal crack propagation occurred during this stage, thus increasing the temperature difference. This is consistent with studies by other authors on another additive manufactured alloy with low conductivity, who report a possibility of subsurface crack detection [Bercelli, 2021]. However, as there is no difference in temperature among the 7 lines at any given time-instant or stage of self-heating, it is impossible to locate the elliptical pore along the x-axis. This can be attributed to the low angular resolution, and the fact that the diameter of the specimen (x-axis) is small compared to its height (y-axis).

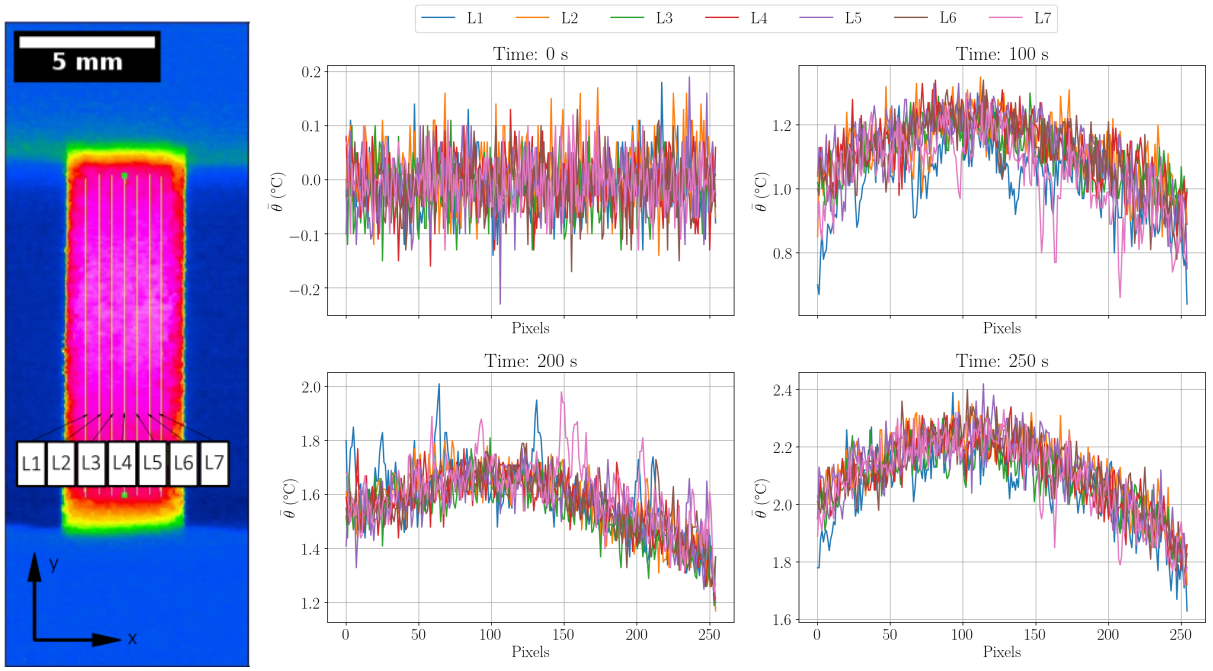

(a) Schematic of 7 profiles taken in the specimen

(b) Temperature evolution during stage 4 of cyclic loading: ±723 MPa (middle and bottom), superposition of temperature of 7 profiles. The temperature at different intervals of time is shown: in the initial state, at 50, 200, and 248 seconds.

Figure 4.19: Evolution of temperature in the specimen with a subsurface elliptical pore

5 Conclusions

This chapter focused on the characterization of self-heating of two alloys. The self-heating results on the aluminium alloys show that the presence of pores has very little to no impact on the mean temperature rise in the aluminium alloy, which is in accordance with the literature. However, for the less conductive IN718-LPBF alloy, the level of temperature rise is dependent on the distance between the pore and the surface, which makes detection of surface-breaking and subsurface pores possible at relatively low loading levels. However, this method of pore detection in this alloy reaches its limits when the pore or crack is situated more than a millimeter deep from the surface. Furthermore, a pore-free sample should be tested in order to correct the

temperature for the effects of the boundary conditions, in order to establish the correct limits for internal pore detection. In addition, since internal crack propagation influences the temperature rise, future studies should incorporate a method to measure internal crack propagation, either through a calibrated potential drop technique or tomography. This would help establish the correct limits of resolution of the method, i.e. temperature rise as a function of the distance of the internal pore or crack from the surface. Finite element simulations also offer a potential solution to the challenge of establishing resolution limits. If the material's elasto-viscoplastic parameters are known, a thermo-mechanical model can be developed to simulate the temperature rise caused by internal pores and propagating cracks. These simulations can then be compared with experimentally measured temperature increases to validate the model.

Chapter 5

Self-heating for fatigue lifetime estimation using the probabilistic micro-inclusion model and proposed improvements

Résumé

Ce dernier chapitre présente un modèle probabiliste basé sur la micro-mécanique (proposé par Doudard et al. en 2004) pour estimer la durée de vie en fatigue des alliages, où l'identification est basée sur des mesures de l'auto-échauffement. Une nouvelle méthode d'estimation par maximum de vraisemblance est proposée pour identifier les paramètres du modèle, et une comparaison est faite avec l'approche d'identification existante. Le modèle est étendu pour prendre en compte la plasticité à l'échelle macroscopique, et les distributions hétérogènes des contraintes sont traitées à l'aide de l'approche multi-échelle présentée dans le chapitre 2, ce qui permet de l'appliquer aux matériaux poreux.

1 Introduction

The previous chapter presented the experimental setup, protocols, and results related to self-heating during fatigue testing. This chapter will focus on a model that can utilize self-heating data to help identify a fatigue lifetime model. Specifically, the stochastic micro-inclusion model will be explored, which incorporates both fatigue and self-heating experimental results to determine a probabilistic Wöhler curve, as described in [Doudard et al., 2004, Doudard et al., 2005]. A maximum likelihood estimation (MLE) method for identifying the parameters of the micro-inclusion model is proposed, and its advantages over the existing identification approach is evaluated. The potential advantages of the MLE method compared to existing methods are also discussed, particularly in scenarios involving noisy or uncertain temperature measurements of the self-heating phenomenon, or when only very limited fatigue data-sets are available.

As a second proposition, an extension of the micro-inclusion model will be made to account for structures with heterogeneous stresses, using the multi-scale method developed in Chapter 2. Furthermore, the criterion of the micro-inclusion model will be modified to include a second criteria based on macro-scale plasticity, which occurs beyond the material's yield limit. The need for this modified criterion is justified by the inadequate performance of the original model when applied to simultaneously model the fatigue behavior of non-porous and porous specimens (demonstrated on the data-set presented in Chapter 2). The extended model is also used with the multi-scale method presented in Chapter 2, and validated on the same experimental data-set.

2 Micro-inclusion model: theory

The micro-inclusion model [Doudard et al., 2004, Doudard et al., 2005] operates on an assumption of separation of scales. It assumes that fatigue lifetime of a homogeneously loaded specimen, as observed at the macro scale, is governed by an underlying stochastic damaging process at the micro-scale. A Poisson process is assumed for the appearance of micro-inclusions in a volume that follow a kinematic hardening law beyond their yield stresses. The intensity of their appearance is a power law of the applied stress amplitude, and the weakest link hypothesis is used to describe rupture, which leads to a Weibull distribution of the yield stress of the weakest inclusion. A criteria based on a critical value of accumulated plastic strain for the weakest site governs the micro fatigue life [Ezanno et al., 2013]. While several fatigue lifetime criteria exist, the criteria used is based on a critical value of cumulated plastic strain for a site, that is considered to govern the fatigue life in a given volume [Desmorat et al., 2007, Ezanno et al., 2013]. A complete description of the equations of the model is given in complementary section 1. Henceforth, the cumulative density function of failure of a volume V subject to stress Σ_0 given by the micro-inclusion model is denoted by $F_{N_R}(N; \mu, \Sigma_0, V)$.

Complement 1: Micro-inclusion model for probabilistic fatigue lifetime

For a given volume V, it is assumed that the probability of having k active microplastic sites, which are seen as elasto-plastic inclusions, is modelled by a random variable X, and

follows a Poisson process with intensity Λ:

$$\text{Prob}(X = k) = \frac{\Lambda^k}{k!} \exp(-\Lambda) \tag{5.1}$$

where the intensity of the Poisson process Λ is assumed to be a power law of the stress Σ_0 experienced by volume V:

$$\Lambda = \frac{V}{V_0} \left(\frac{\Sigma_0}{S_0} \right)^m \tag{5.2}$$

where m and $V_0 S_0^m$ are parameters of the model that govern the relation between the intensity of the process and the stress. A weakest link assumption is applied, i.e. the weakest site in the set of sites S in the volume should govern the fatigue life. Each site s can be considered to have a yield stress $\sigma_y^{(s)}$, and the yield stress of the weakest site is given by Σ_∞ which is modelled as a random variable:

$$\Sigma_\infty = \min_{s \in S} \sigma_y^{(s)} \tag{5.3}$$

In doing so, one can express the probabilities in terms of yield stress of the weakest inclusion Σ_∞ instead of the number of active sites:

$$\begin{aligned} \text{Prob}(\Sigma_\infty < \Sigma_0) &= \text{Prob}(\exists \geq 1 \text{ site with } \sigma_y^{(s)} < \Sigma_0) \\ &= 1 - \text{Prob}(X = 0) \\ &= 1 - \exp\left(-\frac{V}{V_0} \left(\frac{\Sigma_0}{S_0} \right)^m \right) \end{aligned} \tag{5.4}$$

Thus, the yield stress of the weakest site as a function of the stress Σ_0 in the element becomes a 2-parameter Weibull with a scale parameter m and a shape parameter λ given as:

$$\Sigma_\infty \sim \mathcal{W}\left(\lambda = \left(\frac{V_0 S_0^m}{V} \right)^{1/m}, m \right) \tag{5.5}$$

with the cumulative distribution function denoted by $F_{\Sigma_\infty}(\Sigma)$ and probability density function denoted by $f_{\Sigma_\infty}(\Sigma)$.

To express this density in terms of the number of cycles to failure N_R, a criterion [Ezanno et al., 2013] that considers crack initiation and rupture to be governed by a critical value of accumulated plastic strain in the weakest micro-inclusions [Desmorat et al., 2007] is taken. The fatigue lifetime is considered to be finite if the weakest inclusion has a yield stress less than the stress Σ_0 experienced by the loaded volume, and infinity otherwise. Owing to the probabilistic nature of the appearance of the weakest inclusion, the fatigue lifetime is also probabilistic, and is modelled as a random variable:

$$N_\text{R} = \begin{cases} \frac{A}{(\Sigma_0 - \Sigma_\infty)^2}, & \text{if } \Sigma_\infty < \Sigma_0 \\ +\infty, & \text{if } \Sigma_\infty \geq \Sigma_0 \end{cases} \tag{5.6}$$

The lifetime density function $f_{N_R}(N)$ is obtained via a change of variables. We define:

$$g(\Sigma_\infty) = \frac{A}{(\Sigma_0 - \Sigma_\infty)^2} \tag{5.7}$$

$$g^{-1}(N) = \Sigma_0 - \sqrt{\frac{A}{N}} \tag{5.8}$$

$$f_{N_R}(N) = \begin{cases} \{f_{\Sigma_\infty} \circ g^{-1}(N)\} \left.\frac{dg^{-1}(N)}{dN}\right|_N + \text{Prob}(\Sigma_\infty > \Sigma_0)\delta_{N_R=a}(N), & \text{if } N > \frac{A}{{\Sigma_0}^2} \\ 0, & \text{if } N \leq \frac{A}{{\Sigma_0}^2} \end{cases} \tag{5.9}$$

where $\delta_{N_R=a}(N)$ represents the dirac delta, and a denotes the number of cycles at which the fatigue experiments were stopped. The lifetime distribution function is obtained by integration of the density function:

$$F_{N_R}(N) = \begin{cases} \left\{1 - \exp\left(-\left\{\frac{g^{-1}(N)}{\lambda}\right\}^m\right)\right\} + \text{Prob}(\Sigma_\infty > \Sigma_0))H_{N_R=a}(N), & \text{if } N > \frac{A}{{\Sigma_0}^2} \\ 0, & \text{if } N \leq \frac{A}{{\Sigma_0}^2} \end{cases} \tag{5.10}$$

$$\text{Where } H_{N_R=a}(N) = \begin{cases} 1, & \text{if } N > a \\ 0, & \text{if } N \leq a \end{cases} \tag{5.11}$$

$$\begin{aligned} \text{Prob}(\Sigma_\infty > \Sigma_0) &= 1 - \text{Prob}(\Sigma_\infty < \Sigma_0) \\ &= \exp\left(-\left\{\frac{\Sigma_0}{\lambda}\right\}^m\right) \end{aligned} \tag{5.12}$$

The set of parameters μ thus introduced is summarized as:

$$\mu = [m, V_0 S_0^m, A] \tag{5.13}$$

Later on, the dependence of f_{N_R} and F_{N_R} on μ will be introduced as $f_{N_R}(N; \Sigma_0, V, \mu)$ and $F_{N_R}(N; \Sigma_0, V, \mu)$.

The micro-inclusion model has a dissipation associated to plastic activity in the inclusions due to mechanical loading. The dissipation is used as a source term in the heat equation, and the solution to this equation gives the steady state temperature $\bar{\theta}_{\text{sim}}$ in the considered volume as a function of this dissipation. Full details of this development can be found in complementary section 2.

Complement 2: Dissipation due to the micro-inclusions

For a linear kinematic hardening law, the intrinsic dissipated energy for one inclusion can be computed as a function of the material parameters, and a global dissipated energy density

is expressed as [Doudard et al., 2004]:

$$\Delta = \frac{4m}{h(m+1)(m+2)} \frac{\Sigma_0^{m+2}}{S_0^m} \tag{5.14}$$

If the energy density due to the micro-inclusion hypothesis is multiplied by the volume V of a specimen, one may obtain the dissipation in the specimen ω:

$$\omega = V\Delta \tag{5.15}$$

One may then solve the heat equation with characteristic time τ with this dissipation ω as the source term, and obtain a theoretical steady state temperature $\bar{\theta}_{\text{sim}}$ in the specimen. The dissipation is scaled by the load frequency f_r, density ρ and specific heat capacity c:

$$\dot{\theta}_{\text{sim}} + \frac{\theta_{\text{sim}}}{\tau} = \omega \frac{f_r}{\rho c} \tag{5.16}$$

The solution to this differential equation can be given by:

$$\theta_{\text{sim}}(t) = \tau\omega \frac{f_r}{\rho c} \left[1 - \exp\left(-\frac{t}{\tau}\right)\right] \tag{5.17}$$

The steady state temperature, after enough time has passed, is obtained as:

$$\bar{\theta}_{\text{sim}} = \tau\omega \frac{f_r}{\rho c} \tag{5.18}$$

The set of parameters ν thus introduced is:

$$\nu = [m, V_0 S_0^m, h] \tag{5.19}$$

Thus, $\bar{\theta}_{\text{sim}}$ is a function of the stress Σ_0, the volume V, and the parameter set ν.

3 Identification of the micro-inclusion model from experimental data

3.1 Existing method

The existing identification method for the original micro-inclusion model as proposed by the authors of [Doudard et al., 2004] consists of two steps. First, the Weibull parameter m is identified using the self-heating experiments. By virtue of equations (5.14), (5.15) and (5.18), the steady state temperature is expressed as a function of the stress amplitude:

$$\bar{\theta}_{\text{sim}} = \frac{\tau V f_r}{\rho c} \frac{4m}{h(m+1)(m+2)} \frac{\Sigma_0^{m+2}}{S_0^m} \tag{5.20}$$

The value of m is identified via least squares fitting of the previous equation (5.20) in the $\log(\bar{\theta}_{\text{exp}})$ - $\log(\Sigma_0)$ space, on the points in the second regime of self-heating. The intercept of

the equation is used for the identification of h, which is not a necessary step for obtaining the Wöhler curve.

From the analysis of the fatigue data plotted in a Wöhler curve, the parameter A and the mean fatigue limit $\bar{\Sigma}_\infty$ are obtained. From the mean fatigue limit, the parameter $V_0 S_0^m$ is given by the expression:

$$V_0 S_0^m = \left(\frac{\bar{\Sigma}_\infty}{\Gamma(1 + \frac{1}{m})} \right)^m V^* \tag{5.21}$$

where Γ represents the gamma function. The expression (5.21) is found using the expressions for the mean of Σ_∞, (which is a Weibull distribution), and the expression for the scale parameter λ in equation (5.5).

3.2 Proposed method using maximum likelihood estimation (MLE)

We first represent the temperature measurement as a probability distribution, which will (a) enable the modelling of uncertainty in the measurement and (b) allow the construction of a likelihood function for the temperature, allowing for the joint identification of all model parameters based on temperature measurements and fatigue data. The measured steady-state temperature difference during self-heating experiments $\bar{\theta}_{\text{exp}}$ can be considered to be a noisy version of the simulated temperature (where $\bar{\epsilon}$ is the noise, modelled by a normal distribution with standard deviation σ_ϵ):

$$\bar{\theta}_{\text{exp}} = \bar{\theta}_{\text{sim}} + \bar{\epsilon} \quad \text{where} \quad \epsilon \sim \mathcal{N}(0,\, \sigma_\epsilon^2) \tag{5.22}$$

$\bar{\theta}_{\text{exp}}$ is thus a normal distribution with mean $\bar{\theta}_{\text{sim}}$ and standard deviation σ_ϵ:

$$\bar{\theta}_{\text{exp}} \sim \mathcal{N}(\bar{\theta}_{\text{sim}},\, \sigma_\epsilon^2) \tag{5.23}$$

The probability density function of $\bar{\theta}_{\text{exp}}$ is given by:

$$f_{\bar{\theta}_{\text{exp}}}(\bar{\theta}) = \frac{1}{\sigma_\epsilon \sqrt{2\pi}} \exp\left(-\frac{1}{2} \left(\frac{\bar{\theta} - \bar{\theta}_{\text{sim}}}{\sigma_\epsilon} \right)^2 \right) \tag{5.24}$$

For a specimen with a homogeneous stress in its gauge section, undergoing an applied stress amplitude Σ_a, the loading $\Sigma_0 = \Sigma_a$. As $\bar{\theta}_{\text{sim}}$ is a function of the stress amplitude Σ_a, the volume V, and the parameter set ν, henceforth, $f_{\bar{\theta}_{\text{exp}}}$ will be written as $f_{\bar{\theta}_{\text{exp}}}(\bar{\theta}; \Sigma_0, V, \nu)$.

A pre-identification of the characteristic time τ is done on the cooling part of the self-heating curves, using Newton's law of cooling:

$$\theta_{\text{c}}(t) = \bar{\theta}_{\text{exp}} \exp\left(\frac{-t}{\tau} \right) \tag{5.25}$$

where $\theta_{\text{c}}(t)$ is the transient temperature of the specimen during the natural cooling phase. The standard deviation σ_ϵ is pre-identified from the variations in measured steady-state temperature. Identification of the two parameter sets related to the fatigue (μ) and self-heating (ν) parts of the micro-inclusion model (which collectively contain the parameters m, $V_0 S_0^m$, A, h) will be done

on available experimental fatigue data and self-heating experiments on non-porous specimens, via a maximum likelihood estimate. For this purpose, we construct a log-likelihood function by considering both the fatigue (5.9) and self-heating (5.24) probability density functions:

$$\ln \mathcal{L}(\mu, \nu) = \sum_{i \in \mathcal{I}} \ln f_{N_\mathrm{R}}(N^i; \Sigma_a^i, V^i, \mu) + \sum_{j \in \mathcal{A}} \ln f_{\bar{\theta}_\mathrm{exp}}(\bar{\theta}^j; \Sigma_a^j, V^j, \nu) \tag{5.26}$$

where $\mathcal{I}$ is the set of all the homogeneous experimental specimens tested for fatigue failure, N^i is the number of cycles to failure at an applied stress amplitude Σ_a^i for a specimen with volume V^i. Furthermore, $\mathcal{A}$ is the set of all the self-heating experiments belonging to the second regime, $\bar{\theta}^j_\mathrm{exp}$ is the steady-state self-heating measurement at an applied stress amplitude Σ_a^j on a specimen of volume V^j. Here, μ and ν are the sets of parameters used to evaluate the function. A Nelder-Mead process is used for optimization, which outputs parameters of the micro-inclusion model that are the most probable given the experimental fatigue and self-heating data, by maximizing the likelihood function (here, $\tilde{\mu}$ and $\tilde{\nu}$ represents the different sets of parameters tested by the optimizer):

$$\mu, \nu = \arg\max_{\tilde{\mu}, \tilde{\nu}} \left(\ln \mathcal{L}(\tilde{\mu}, \tilde{\nu}) \right) \tag{5.27}$$

4 Numerical investigations and results of the identification methods

The aim of this section is to show the relative benefits of using the proposed identification method of the parameters of micro-inclusion model on experimental data, as compared to the existing identification approach proposed by the authors in [Doudard et al., 2004]. To this end, the model will be identified using these two methods on the same set of experimental self-heating and fatigue data of the non-porous material, recalled in Fig. 5.1(a-b). The effect of erroneous or uncertain temperature measurement on the identification of the lifetime model will be investigated.

It is noted that the geometry for self-heating experiments is different than that of fatigue experiments, but the volume of the gauge section is nearly equal (Self-heating specimen: $468\,\mathrm{mm}^3$, Fatigue specimen: $593\,\mathrm{mm}^3$). The parameters sets of the micro-inclusion model μ and ν are recalled here:

$$\mu = [m, V_0 S_0^m, A] \tag{5.28}$$

$$\nu = [m, V_0 S_0^m, h] \tag{5.29}$$

4.1 Existing identification method

The identification of m on the second regime of steady-state temperature measurements is demonstrated in Figure 5.1(a). From the analysis of the fatigue data plotted in a Wöhler curve, the parameter A and the mean fatigue limit $\bar{\Sigma}_\infty$ are obtained (shown in Figure 5.1(b)) and the

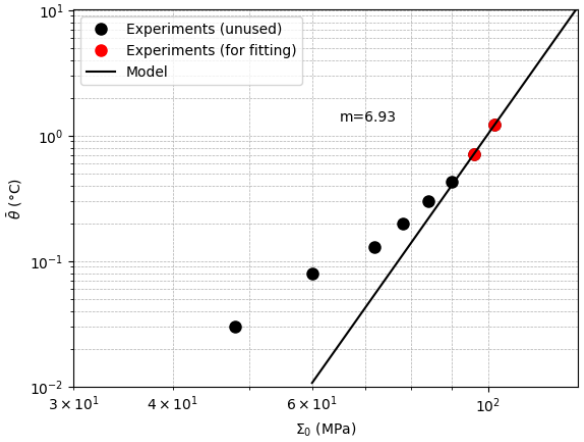

(a) Identification of m on the second regime of self-heating experiments

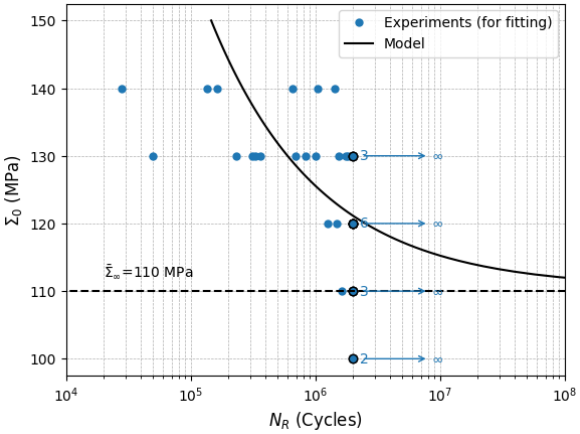

(b) Identification of a mean fatigue limit $\bar{\Sigma}_\infty$ and A from fatigue experiments

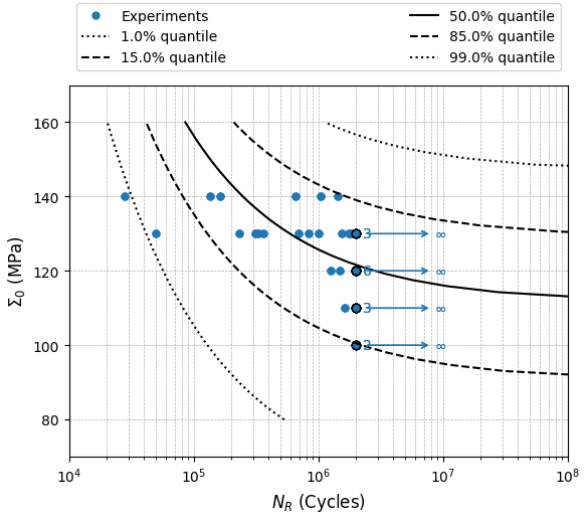

(c) Predicted Wöhler curve with quantiles after the identification process

Figure 5.1: Identification of the parameters of the micro inclusion model using the method proposed by the authors in [Doudard et al., 2004] and the predicted Wöhler curve

parameter $V_0 S_0^m$ is thus computed. With all the parameters identified, the obtained Wöhler curve can be plotted (see Figure 5.1(c)). A very good fit is obtained by using this method. The obtained value of m is in close agreement to values obtained by other authors on other aluminium alloys, for example a cast copper-aluminum alloy [Ezanno et al., 2010].

With this method, the identification of the scatter in lifetime distribution is dependent on the quality of self-heating measurements. If a lot of fatigue data is present, but the self-heating measurements are noisy, the fatigue curve may not be estimated correctly. To illustrate this point, the effect of +/-5% change in the self-heating measurement at the highest load, on the predicted Wöhler curve is shown in Figure 5.2. The uncertainty in temperature measurements cause a change in the identified value of the parameter m, and thus affects the quantiles, notably the 85% and 99% quantiles shift significantly as compared to the base (shown in Figure 5.1)(c).

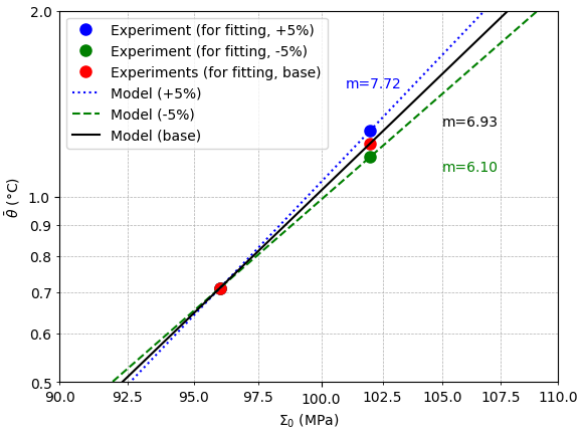

(a) Identification of m on the second regime of self-heating experiments, with +/-5% change in the value of the measurement at the highest loading

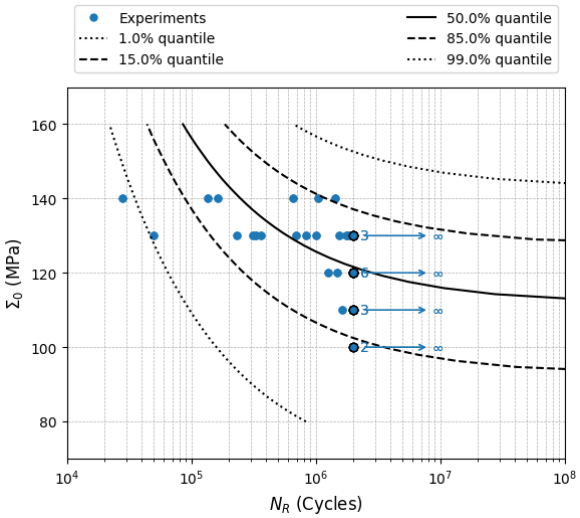

(b) Predicted Wöhler curve with the model with +5% change in temperature measurement

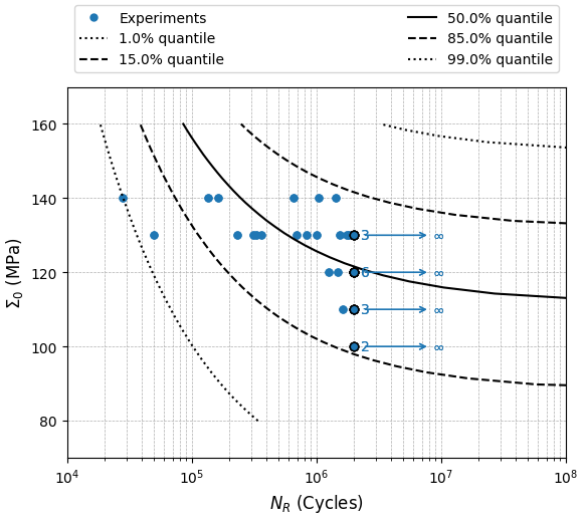

(c) Predicted Wöhler curve with the model with -5% change in temperature measurement

Figure 5.2: Effect of a 5% change in temperature measurement on the identification and the predicted Wöhler curve, using the identification method proposed by [Doudard et al., 2004]

4.2 Proposed MLE identification method

The value of τ is identified on the cooling part of the self-heating curves (see Figure 5.3(b)). The simplified cooling model does not provide a satisfactory fit to the cooling curves; however, we will proceed with the approximated characteristic time for further analysis. The standard deviation σ_ϵ is taken as 0.1 °C (see Figure 5.3(c)). Here, all available fatigue experimental data

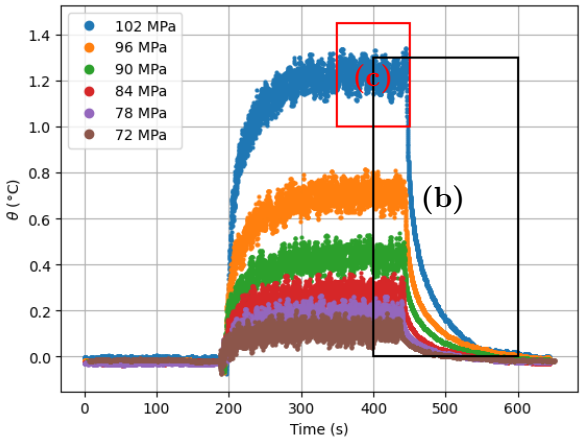

(a) Self-heating curves of the non-porous specimen

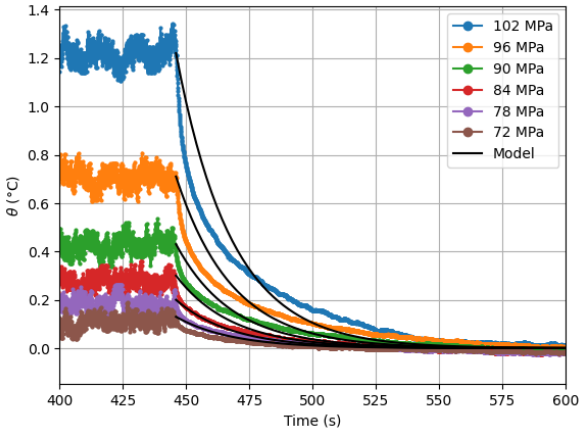

(b) Identification of the characteristic time τ on the cooling curves

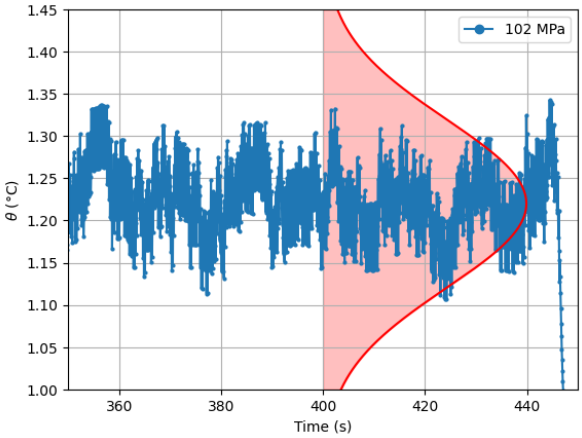

(c) Zoom on the self-heating curve, showing the noise in measurements. The red Gaussian curve shows the distribution of $\bar{\theta}_{\text{exp}}$ centered around a mean value with $\sigma_\epsilon = 0.1$ °C

Figure 5.3: Identification of the characteristic time τ and the noise parameter σ_ϵ on the self-heating data of the non-porous specimen

(corresponding to 34 specimens tested in the high-cycle fatigue regime) were kept in the subset $\mathcal{I}$ for identification. Two steady-state measurements corresponding to the second regime of loading on a specimen were kept in the set A. Several initialization points were tested, and the solution with the lowest likelihood value after the optimization process was retained. The evolution of the parameters throughout the optimization process (resulting in the lowest likelihood value) is shown in Figure 5.4 and the evolution of the solution for a few iterations and final result are

shown in 5.5.

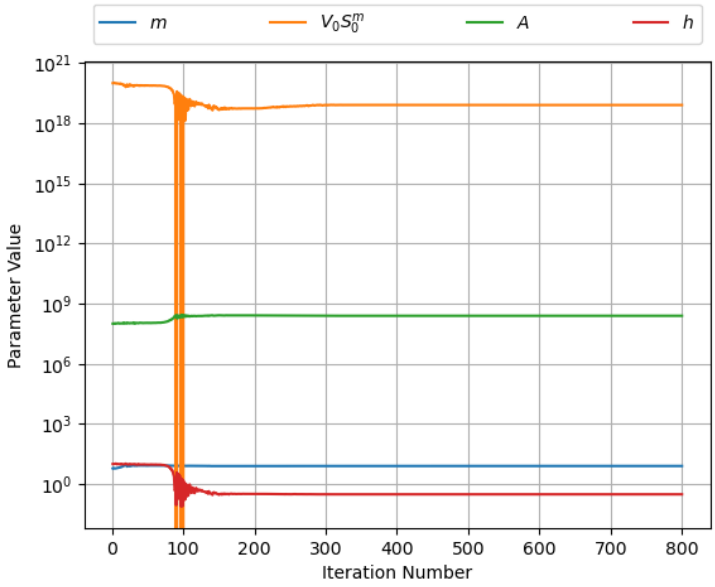

Figure 5.4: Evolution of the micro-inclusion models' parameters during the optimization process using maximum likelihood estimation

In the proposed method, erroneous or uncertain temperature measurements are accounted for by the noise parameter σ_ϵ, which reduces the rigidity in the identification of the parameter m. Figure 5.6(a) shows the model fit after the optimization process using data with +/-5% error in the temperature measured at the highest load. Despite this error, the slope of the line (governed by m) does not change, as it is constrained by the information on m brought in by the fatigue experiments. The fatigue curve (Figure 5.6(b-c)) does not change.

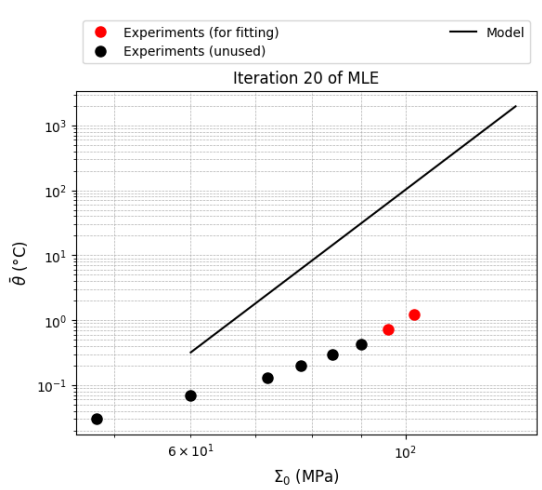

(a) Iteration 20

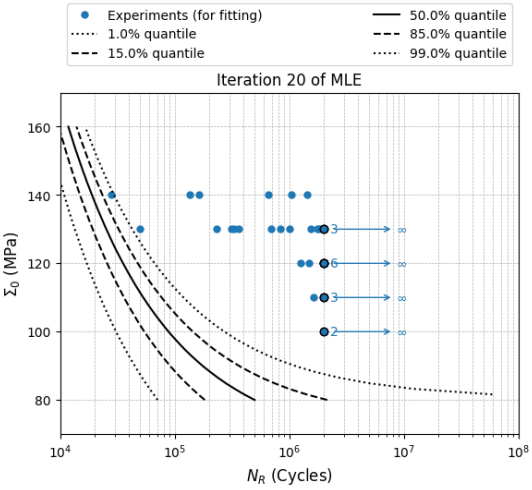

(b) Iteration 20

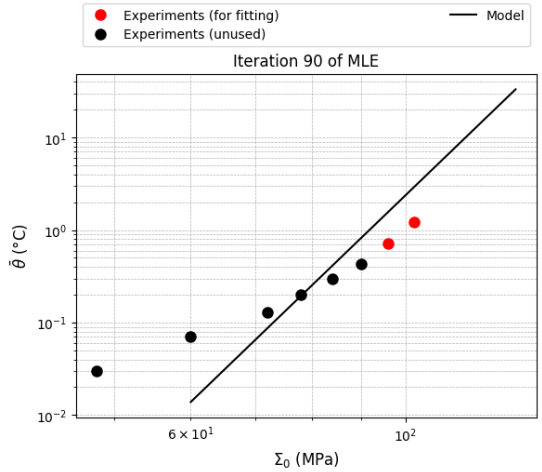

(c) Iteration 90

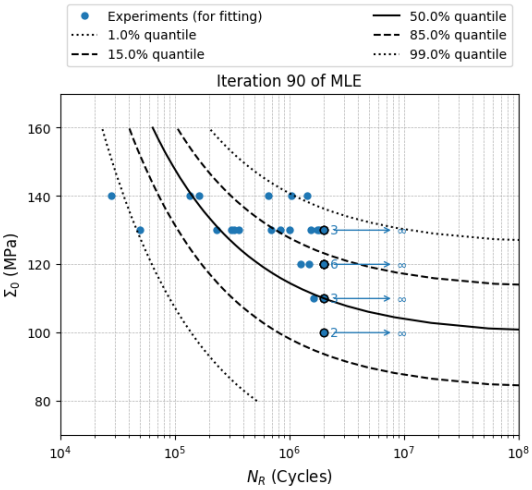

(d) Iteration 90

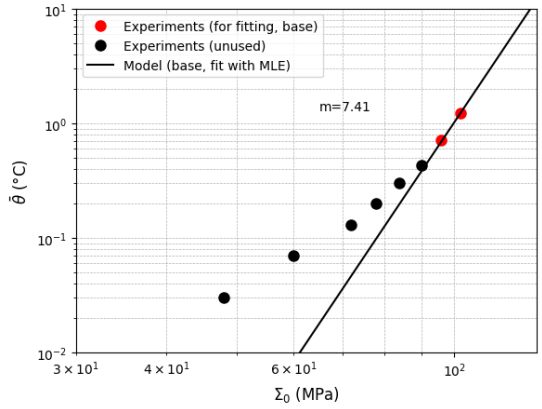

(e) Iteration 800

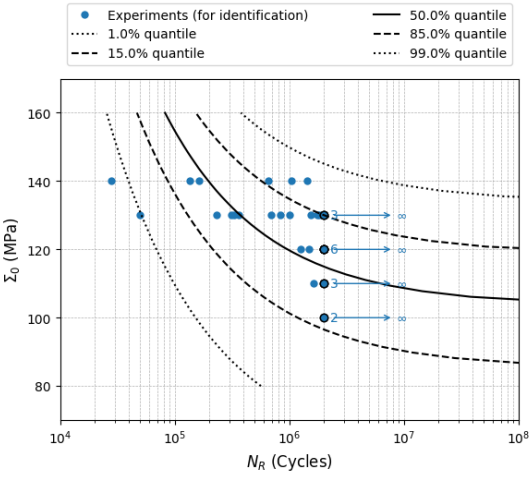

(f) Iteration 800

Figure 5.5: Results of the micro-inclusion model at different iterations of the optimization process, identified using the maximum likelihood method. The identification was performed on all available high-cycle fatigue data (34 points) on non-porous specimens and two steady-state measurements of temperature during the second loading regime of a self-heating experiment on a specimen (a) temperature fit on second regime of loading (b) Wöhler curve fit

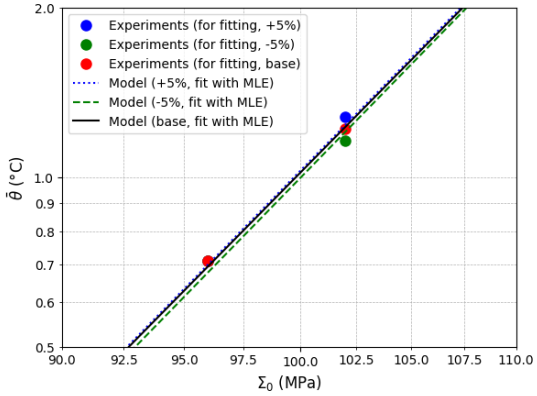

(a) Temperature fit, with +/-5% change in measurement of temperature at the highest loading

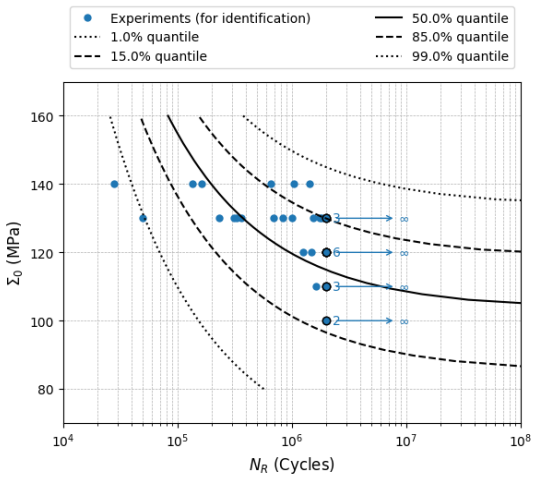

(b) Wöhler curve fit with the model with +5% change in temperature measurement

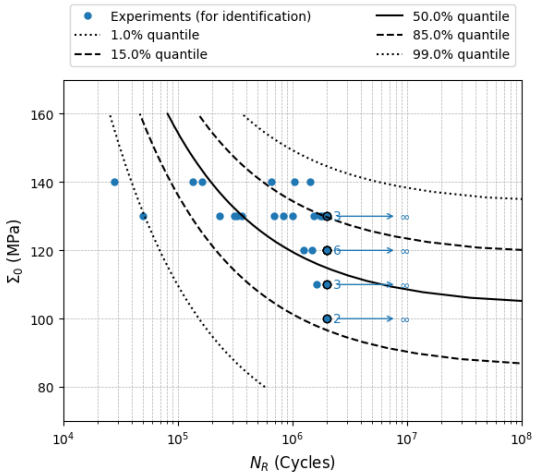

(c) Wöhler curve fit with the model with -5% change in temperature measurement

Figure 5.6: Effect of a +/-5% change in the temperature measurement at the highest load, on the identification and results of the micro-inclusion model, using the maximum likelihood method. The identification was carried out using all available high-cycle fatigue data (34 points) from non-porous specimens, along with two steady-state temperature measurements taken during the second loading regime of a self-heating experiment on a non-porous specimen.

4.3 Performance of the MLE method on extremely limited fatigue data

This subsection critically evaluates the performance of the proposed method using maximum likelihood estimation for identifying the micro-inclusion model, under availability of self-heating information but extremely limited fatigue lifetime data. An extreme scenario is considered where only a single fatigue lifetime data point is available in the high-cycle fatigue regime. This situation makes the existing identification method unusable as it requires at least 10-15 experiments to determine the parameters A and $V_0 S_0^m$ from the Wöhler curve analysis [Doudard et al., 2004, Doudard et al., 2005].

In this case, the value of σ_ϵ is taken to be a low value (0.02 °C) to place high confidence in self-heating measurements. One fatigue experiment (corresponding to a specimen tested in the high-cycle fatigue regime with a finite number of cycles to fatigue failure) was kept in the subset $\mathcal{I}$ for identification. As before, several initialization points were tested. Two of the solutions with the lowest likelihood values after the optimization process are shown in Figure 5.7. The likelihood values for all these solutions are similar, with the value obtained using initialization point 2 being nearly the same value obtained using initialization point 1. However, the fatigue curves are significantly different, with the solution obtained with initialization point 2 significantly underestimating the fatigue lifetime. This is due to insufficient information on the parameter A. Moreover, as expected, the lifetime data point used for identification significantly affects

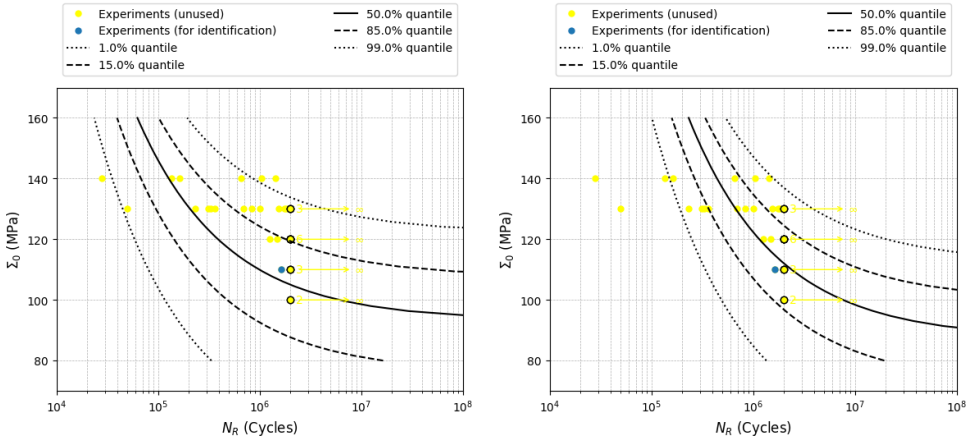

(a) Identified curve with initialization point 1

(b) Identified curve with initialization point 2

Figure 5.7: Impact of varying initialization points on the Wöhler curve obtained through the proposed identification method, in cases where self-heating data is available but only a single fatigue data point exists for identification purposes

the lifetime distribution. Figure 5.8 presents Wöhler curves after optimization performed three times using the same initialization, each time retaining a different random fatigue experiment in the subset $\mathcal{I}$. The resulting Wöhler curves are highly dependent on the specific data point used for identification, with the most accurate curves derived from data points that exhibit central or mean tendencies, like in 5.8(a,c), but not when the data point is an extreme 5.8(b). Collectively, these results highlight a need for a higher number of fatigue experiments when

using the MLE method for identifying the micro-inclusion model, despite the availability of self-heating information.

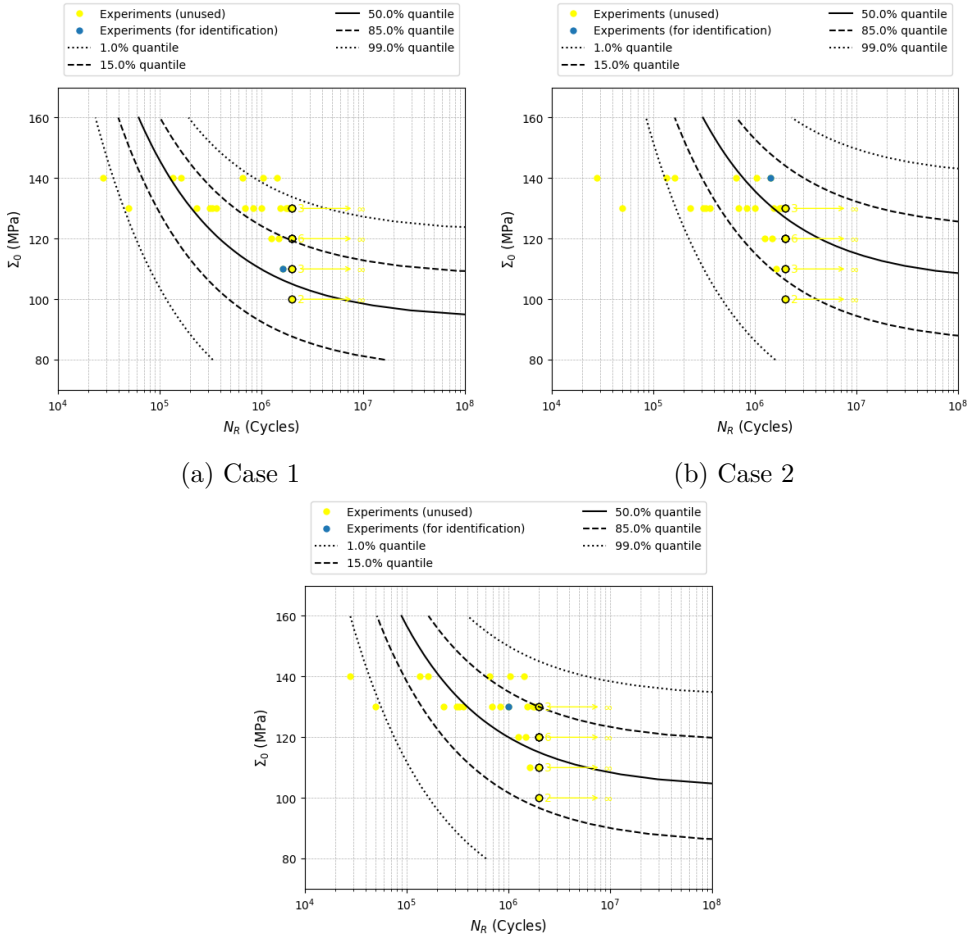

(a) Case 1

(b) Case 2

(c) Case 3

Figure 5.8: The Wöhler curve obtained using the proposed identification method, using two self-heating measurements during the second loading regime and only one fatigue data point (a different point for each of the three cases)

5 Extension of the micro-inclusion model for structures with heterogeneous stresses using the multi-scale method

The micro-inclusion model presented was originally developed for specimens with homogeneous stress distributions [Doudard et al., 2004] with the possibility of handling heterogeneous cases using an effective volume introduced soon after [Doudard et al., 2005]. Here, we will use the multi-scale method developed in Chapter 2 in order to compute the lifetime in the case of a heterogeneous stress distribution. To this end, we will use the micro-inclusion model element wise. Henceforth, as in Chapter 2, a $\bullet^*$ symbol is used to denote any entity $\bullet$ computed for element $* \in \mathcal{E}$ where $\mathcal{E}$ is the set of finite elements constituting a specimen.

To treat multi-axiality, the stress Σ_0^* in element $*$ is modified in the following manner (it collapses to the original criteria $\Sigma_0^* = \Sigma_a$ in uni-axial loading cases):

$$\Sigma_0^* = E\frac{\Delta\varepsilon^*}{2} \tag{5.30}$$

where the total strain amplitude in the stabilized cycle for an element $\Delta\varepsilon^*$ retains the same definition as given in Chapter 2.

A structure with a heterogeneous stress distribution, for example, a structure with pores that are explicitly meshed, or a structure with a notch, will have different values of the the criterion (Σ_0^*) in different elements of the structure for a given applied stress amplitude Σ_a. We formally define the function $\Sigma_0^*(\Sigma_a) : \Sigma_a \mapsto \Sigma_0^*$ that maps the load applied to the structure as boundary condition to the fatigue criterion in element $*$. This function is computed by FEA. The probabilistic lifetime model developed in the previous section (Complement 1) can subsequently be applied to all the elements of the FE mesh. The CDF of the lifetime of the element in the case of heterogeneous stress distribution can be rewritten (from equation (5.10)) as $F_{N_{\mathrm{R}}^*}(N; \Sigma_0^*(\Sigma_a), V^*, \mu)$.

The weakest link hypothesis to get the fatigue lifetime density of the full structure remains the same process, as previously detailed in Chapter 2, using the mixture CDF of the lifetime of the element:

$$F_{N_{\mathrm{R}}^s}(N; \Sigma_a, \mu) = 1 - \prod_*(1 - F_{N_{\mathrm{R}}^*}(N; \Sigma_0^*(\Sigma_a), V^*, \mu)) \tag{5.31}$$

The PDF of the lifetime of the structure is obtained by perturbing the CDF (equation (5.31)), as an analytical model was not derived. [1] This lifetime model is henceforth referred to as the micro model.

6 Mixture model using criteria based on micro and macro-plasticity

The criterion of the micro inclusion model as given by equation (5.30) is not sufficient on its own to simultaneously model the fatigue lifetime of non-porous and porous cases (a demonstration of this will be shown in the numerical results section). Therefore, a second criterion for fatigue lifetime $N_{\mathrm{R}_2}^*$ based on the accumulated plastic strain range (the stabilized value of Δp^*) is introduced for the element-wise model. $N_{\mathrm{R}_2}^*$ is termed as the macro fatigue lifetime. The

[1] The numerical implementation of the mixture PDF of the failure of the structure is done in the following manner:

$$f_{N_{\mathrm{R}}^s}(N) = \frac{1}{N_{\mathrm{pert}} - N}\left(F_{N_{\mathrm{R}}^s}(N_{\mathrm{pert}}) - F_{N_{\mathrm{R}}^s}(N)\right) \tag{5.32}$$

where the perturbation is done in the logarithmic scale to get a smooth probability density function, i.e. $N_{\mathrm{pert}} = \exp(\log(N) + \epsilon_0)$. The perturbation parameter ϵ_0 is set to 0.01.

expression for the macro-plasticity criteria is given as:

$$\Delta p^* = c {N^*_{\mathrm{R}_2}}^{-a} \tag{5.33}$$

where a and c are parameters. This formulation is chosen to obtain a straight line in the $\log(\Delta p^*)$-$\log(N^*_{\mathrm{R}})$ space, as is standard in fatigue lifetime modelling.

Probabilistic approach for macro-plasticity criteria

The fatigue lifetime model will now be made probabilistic. The fatigue lifetime is considered to be stochastic due to the randomness in underlying total damage over all cycles that a specimen with volume V^* may undergo before failing. The total damage $\mathcal{G}$ is modelled as a random variable, and the form of the associated probability distribution is considered to be a Weibull distribution:

$$N^*_{\mathrm{R}_2} \left\{ \frac{c}{\Delta p^*} \right\}^{-1/a} = \mathcal{G} = N^*_{\mathrm{R}_2} \Delta d^* \tag{5.34}$$

where, the damage increment per cycle in the element, denoted by $\Delta d^* = \left\{ \frac{c}{\Delta p^*} \right\}^{-1/a}$, is a function of the cumulative plastic strain range in the stabilized cycle. The volume is taken into account in the scale factor, given by:

$$\lambda_2 = \left\{ \frac{1}{V^*} \right\}^{1/m_2} \tag{5.35}$$

and the cumulative distribution function of the total damage is expressed as:

$$F_{\mathcal{G}}(G) = 1 - \exp\left(- \left\{ \frac{G}{\lambda_2} \right\}^{m_2} \right) \tag{5.36}$$

The cumulative distribution function of the fatigue lifetime is thus expressed as (after a transformation of variables):

$$F_{N^*_{\mathrm{R}_2}}(N) = 1 - \exp\left(- \left\{ \frac{N \Delta d^*}{\lambda_2} \right\}^{m_2} \right) \tag{5.37}$$

The set of parameters is summarized by:

$$\zeta = [c, m_2, a] \tag{5.38}$$

Henceforth, the dependence of $F_{N^*_{\mathrm{R}_2}}$ on ζ will be introduced as $F_{N^*_{\mathrm{R}_2}}(N; \Delta p^*, V^*, \zeta)$. The probability density function (PDF) of fatigue lifetime of the element $*$ will be denoted as $f_{N^*_{\mathrm{R}_2}}(N; \Delta p^*, V^*, \zeta)$.

Mixture model at the material point level

We recall the lifetime from the previous criterion of the micro-inclusion model (section 2), which will henceforth be denoted as the micro fatigue lifetime ($N^*_{\mathrm{R}_1}$). The CDF and PDF of the micro fatigue lifetime is written as $F_{N^*_{\mathrm{R}_1}}(N; \Sigma^*_0, V^*, \mu)$ and $f_{N^*_{\mathrm{R}_1}}(N; \Sigma^*_0, V^*, \mu)$ respectively. A mixture law is used to obtain the CDF of the lifetime of the element $*$, denoted $F_{N^*_{\mathrm{R}}}$, with a smooth

transition between the micro and macro fatigue lifetimes:

$$\begin{aligned} F_{N^*_{\mathrm{R}}}(N;\Sigma^*_0,\Delta p^*,V^*,\mu,\zeta,\gamma,l) =& [1-\alpha(\Sigma^*_0;\gamma,l)]F_{N^*_{\mathrm{R}_1}}(N;\Sigma^*_0,V^*,\mu) \\ &+ \alpha(\Sigma^*_0;\gamma,l)F_{N^*_{\mathrm{R}_2}}(N;\Delta p^*,V^*,\zeta) \end{aligned} \tag{5.39}$$

where the weighting is done locally, i.e. at the level of the element, using the same sigmoïd function $\alpha(\Sigma^*_0;\gamma,l)$ for all elements.

$$\alpha(\Sigma^*_0;\gamma,l) = \frac{1}{2}(\tanh\left(\frac{\Sigma^*_0-\gamma}{l}\right)+1) \tag{5.40}$$

$$\alpha = \begin{cases} 0, & \text{if } \Sigma^*_0 << \sigma_y \\ 1, & \text{if } \Sigma^*_0 >> \sigma_y \end{cases} \tag{5.41}$$

Structure level model

Similar to section 5, the mixed model will be combined with a weakest link assumption to obtain a probabilistic lifetime model at the structure level. We formally define the function $\Delta p^*(\Sigma_a) : \Sigma_a \mapsto \Delta p^*$ that maps the load applied to the structure as boundary condition to the fatigue criterion in element $*$. This function is also computed by FEA. The probabilistic lifetime model using the mixture law developed in the previous section (equation (5.39)) can subsequently be applied to all the elements of the FE mesh. The CDF of the lifetime of the element in the case of heterogeneous stress distribution can be rewritten (from equation (5.39)) as $F_{N^*_{\mathrm{R}}}(N;\Sigma^*_0(\Sigma_a),\Delta p^*(\Sigma_a),V^*,\mu,\zeta,\gamma,l)$.

The weakest link hypothesis to get the fatigue lifetime density of the full structure remains the same process, as previously detailed in section 5, using the mixture CDF of the lifetime of the element:

$$F_{N^s_{\mathrm{R}}}(N;\Sigma_a,\mu,\zeta,\gamma,l) = 1-\prod_*(1-F_{N^*_{\mathrm{R}}}(N;\Sigma^*_0(\Sigma_a),\Delta p^*(\Sigma_a),V^*,\mu,\zeta,\gamma,l)) \tag{5.42}$$

The PDF of the lifetime of the structure is obtained by perturbing the CDF (equation (5.42)), as an analytical model was not derived, using the same process as in footnote 1. Henceforth, lifetime model of the structure developed here will be referred to as the mixed model.

7 Numerical results: Calibration and validation of lifetime models on experimental fatigue data

In this section, the justification for the extension of the micro-inclusion model to include a second criteria based on macro-plasticity and creation of the mixed model will be discussed. The micro-inclusion model will first be identified on non-porous experimental data (presented in Chapter 2, section 2), and using the multi-scale method (section 5), a prediction will be made on a porous specimen. Next, the micro model, using the multi-scale method, will be identified

on porous experimental data and used to make a prediction on a non-porous specimen. The identification procedures remain the same as detailed in Chapter 2, section 4. Finally, the micro-inclusion model will be jointly identified on non-porous and porous data. The quality of the fit and prediction in these three cases will be discussed, before moving on to the identification and results of the mixed model.

7.1 Micro-inclusion model: Need for a modified criteria based on macro-plasticity

The set of parameters of the micro-inclusion model (sections 2 and 5) is recalled here:

$$\mu = [m, V_0 S_0^m A] \tag{5.43}$$

The plastic corrector algorithm (previously detailed in Chapter 3) was used to compute the criteria Σ_0^* and Δp^* in all the elements of the finite element meshes of the synthetic porous specimens (previously presented in Chapter 2, section 5).

Homogeneous stress distributions (non-porous specimens)
The set of micro-model parameters $\mu = [m, V_0 S_0^m, A]$ are identified on non-porous fatigue data. The fit is shown in Figure 5.9a. The fit obtained on non-porous data is very good. However, predictions on porous specimens using the multi-scale method do not match with the experimental data.

Structures with pores whose exact distribution is unknown (porous specimens)
The set of micro-model parameters $\mu = [m, V_0 S_0^m, A]$ are identified on porous experimental fatigue data using the maximum likelihood estimate procedure for structures with pores whose exact distribution is unknown, as detailed in Chapter 2, section 4.3. The value of n_k is kept at 10 synthetic specimens. The fit is shown in Figure 5.9b. While the fit on the porous data is excellent, the lifetime predictions on a non-porous specimen do not match with the experimental data.

Combined identification (non-porous and porous specimens)
The set of micro-model parameters $\mu = [m, V_0 S_0^m A]$ are identified jointly on non-porous and porous experimental fatigue data using the maximum likelihood estimate procedure for heterogeneous cases. The fit, shown in 5.9c, does not distinguish between the porous and non-porous behavior, and is thus inadequate.

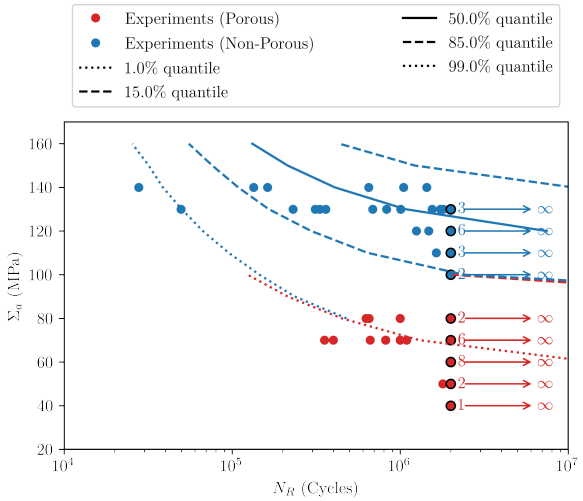

(a) Identification of parameter set μ on non-porous specimens, prediction on porous specimens.

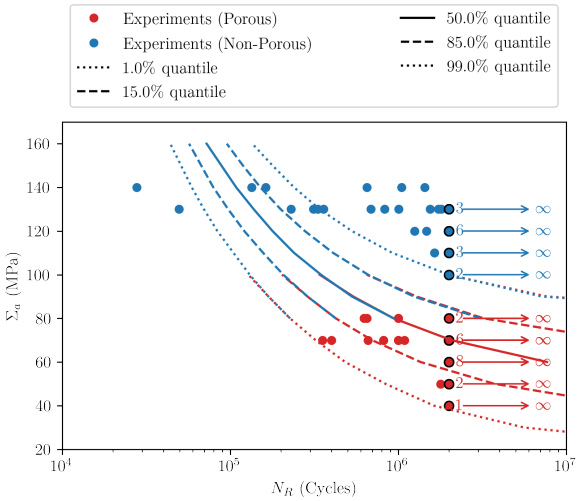

(b) Identification of parameter set μ on porous specimens, prediction on non-porous specimens.

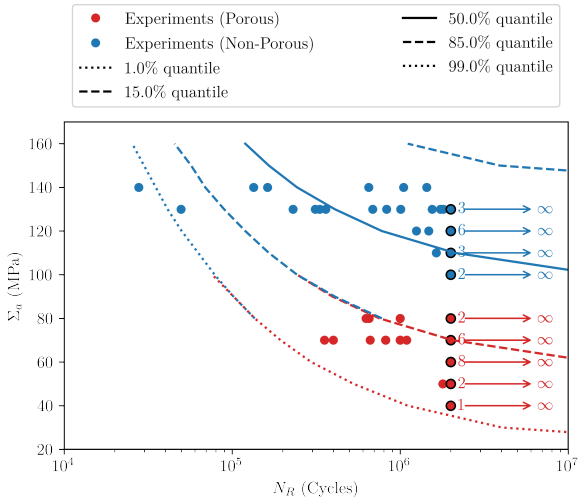

(c) Identification of parameter set μ on both non-porous and porous specimens.

Figure 5.9: Comparison of micro-inclusion model identification and predictions on different specimen types using the two-scale method. The parameter set for optimization is $\mu = [m, V_0 S_0^m, A]$.

7.2 Mixed model

The set of micro-model parameters $\mu = [m, V_0 S_0^m A]$ are identified on non-porous experimental fatigue data using the maximum likelihood estimate procedure for homogeneous cases. The obtained micro-model parameter set is thus calibrated on experiments where there is no development of macro-plasticity. The micro-model parameter set is fixed for the next step, where the macro-model parameter set $\zeta = [C, m_2, a]$ are identified on porous experimental fatigue data using the maximum likelihood estimate procedure for structures with pores whose exact distribution is unknown, as detailed in Chapter 2, section 4.3. The value of n_k is kept at 10 synthetic specimens. The parameters of the transition function γ, l were fixed to $\gamma = \sigma_y = 170$ MPa and $l = 0.69$, which gives a smooth transition between the two models, and ensures that the macro model operates above the yield stress, and the micro model operates below the yield stress.

Several synthetic porous specimens (around 10) each with different distribution of pores (not used during the maximum likelihood estimate for parameter identification) were input to the mixed model. Using the same method presented in Chapter 2, a set of quantiles showing the generalized trend using the numerical samples from each specimen is constructed and shown in Fig. 5.10.

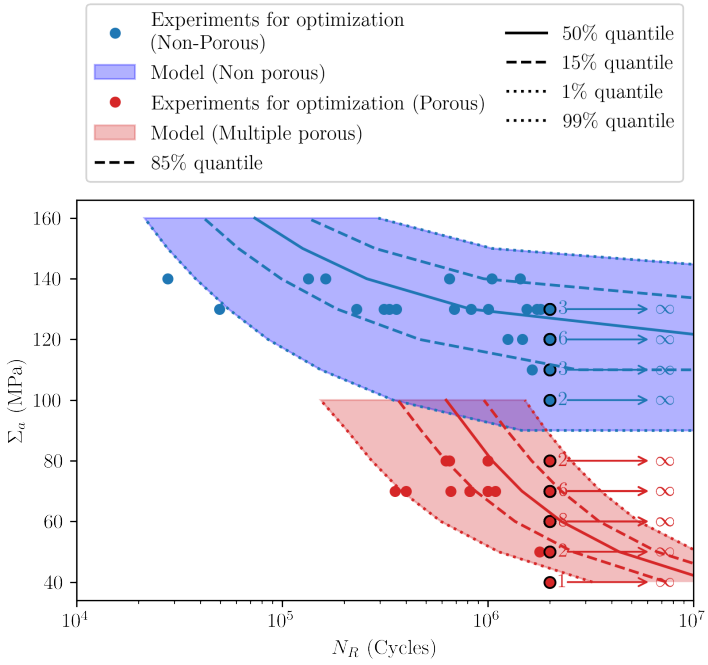

Figure 5.10: Wöhler curve obtained using the mixed model, identified on non-porous and porous specimens

8 Conclusion

In this chapter, temperature measurements from the self-heating experiments conducted in Chapter 4 were incorporated into the identification of a lifetime model, using the micro-inclusion model developed by [Doudard et al., 2004]. A new method for identifying the model parameters

from experimental data, based on maximum likelihood estimation, was proposed. This method involved representing the temperature measurement as a probability distribution, which enabled the modelling of uncertainty in the measurements and allowed for the identification of all model parameters using both temperature measurements and fatigue data together. The advantage of this approach lies in the ability to account for scatter in fatigue when uncertainty in the temperature measurement is high, thereby placing greater emphasis on the fatigue data.

Additionally, an extension to the micro-inclusion model was proposed, using the multi-scale approach introduced in Chapter 2, to account for heterogeneous stress states. However, the model is not sufficiently flexible to distinguish between the fatigue behaviour of porous and non-porous specimens. Therefore, a second criterion, based on macroscopic plasticity beyond the material's yield stress, was introduced. The mixed model, incorporating a transition between the two failure mechanisms around the yield stress using both criteria, was successfully validated against experimental data.

Conclusions and perspectives

1 Conclusions of the study

The first part of this thesis focused on the development of a numerical pipeline for predicting the high-cycle fatigue lifetime of porous alloys based on tomographic images. A multi-scale methodology was proposed in Chapter 2 to account for uncertainties in fatigue lifetime due to the variability of defects at two scales: micro-scale heterogeneity and meso-scale pores. The variability at the micro-scale is not explicitly modelled but is incorporated by applying probabilistic criteria to the lifetime models. For meso-scale pores, the methodology explicitly models pore populations using the finite element (FE) method, based on high-resolution tomographic images. This approach captures the effects of pore morphology, pore interactions, and interactions of the geometry of the specimen with the pores, all of which significantly influence fatigue lifetime (refer to Chapter 1).

The overall lifetime of a porous specimen, with a given pore distribution, is estimated using a weakest link assumption at the level of its finite elements. When the exact pore population is unknown, a statistical method is employed, whereby various pore positions are sampled to estimate the specimen's lifetime. The lifetime model in this framework can be freely selected, and in this study, two models were used: a probabilistic strain-life model and a probabilistic micro-inclusion model [Doudard et al., 2004]. A novel identification method was introduced to directly identify the parameters of these models based on experimental data from porous specimens, using an expectation over pore populations when the precise distribution of pores in each tested specimen is unknown, as discussed in Chapter 2. The model thus calibrated on only porous experimental data under-estimates the lifetime of non-porous specimens, however, when given a few data points of the non-porous specimens during calibration, correctly predicts the lifetime of both the non-porous and porous alloy. These contributions directly address the first challenge outlined in the introduction — i.e. we can predict of the lifetime of a given porous specimen whose exact pore geometries and locations are unknown, but a representative tomography of the porous material is available. This methodology also demonstrates the potential to tackle the third challenge, i.e. the substantial amount of data required for lifetime model calibration. By considering the same base material across different porosity levels, we have shown a reduction in the amount of data necessary to calibrate the lifetime model, as compared to fitting a separate lifetime model for each porosity level. The method also incorporates the statistical

size effect, where larger volumes fail earlier under iso-stress conditions. Furthermore, a simple homogenization of the porous material does not reproduce the multi-scale method's prediction for all geometries.

The proposed methodology involves meshing the pore network within the volume of interest in order to compute the lifetime model criteria. A plastic correction algorithm was introduced in Chapter 3 to alleviate the computational costs associated to non-linear finite element (FE) computations on such meshes. This algorithm post-processes an elastic FE computation to retrieve elasto-plastic results for any proportional loading sequence. The overly stiff behavior observed in these plastic corrector predictions arises because plastic accommodation and stress redistribution effects have not been taken into account. Nevertheless, the correction algorithm shows acceptable performance for arbitrary pore geometries, provided the global loading remains within the high-cycle fatigue regime, i.e. confined plasticity. We have also shown that the rule of local proportionality introduces significantly lesser error than the Neuber rule. Moreover, it was demonstrated that the algorithm can be further accelerated through 1D meta-modelling, which is particularly advantageous for cases where long loading sequences are required before calculating the quantity of interest, such as the stabilised cycle. Virtually no errors are introduced during this process. Additionally, a second machine learning (ML) block was proposed to further refine the plastic correction algorithm's approximations for specific pore populations, such as spherical pores, assuming availability to a set of high-fidelity reference FE simulations for training purposes. We show that the CNN corrections improve with access to more training data. Furthermore, we show that using the plastic correction quantities as inputs to the CNN is beneficial as compared to inputting quantities with a lesser mechanical context, e.g. coming purely from elasticity. This benefit, however, rapidly decreases with an increase in training data. There are further limitations to the CNN, in that it lacks generalisation ability to other geometries of pores not present in the training data-set, and that a re-training of the CNN is required when a different quantity of interest needs to be obtained. Collectively, these contributions collectively address the second challenge outlined in the introduction: the computational costs associated with using models that require high-resolution elasto-plastic simulations at the pore level for lifetime predictions.

The second part of this thesis focused on investigating the potential of using self-heating data for lifetime estimation. In Chapter 4, experimental investigations were conducted to examine the local dissipative sources. For the aluminium alloys, self-heating resulted in a temperature rise in both porous and non-porous alloys, even below their yield stress. For the non-porous alloys, this temperature rise is due to dissipative mechanisms associated to micro-scale defects. Due to high thermal conductivity, there was no temperature localisation caused by the pores, aligning with observations in the literature for similar alloys [Messager, 2020]. Additionally, this high conductivity explains the absence of a significant difference in the average temperature rise between porous and non-porous alloys, despite their different failure mechanisms, as shown by fatigue property investigations. In alloys with lower conductivity, however, the temperature rise localisation due to pore-related dissipative mechanisms is possible, as demonstrated by studies on IN718-LPBF superalloys with controlled pore configurations. Nonetheless, accurate calibration

is necessary to separate the temperature rise caused by boundary conditions and internal crack propagation, in order to determine the resolution limits for pore detection using this method.

Specialised models, which use temperature rise from self-heating to inform scatter in high-cycle fatigue (HCF), already exist, for example the stochastic micro-inclusion model [Doudard et al., 2004], which employs a scale separation to account for dissipation due to variability in micro-scale defects. In Chapter 5, we showed that this approach works well for the non-porous aluminium alloy, helping to reduce the amount of fatigue data required for model calibration. Furthermore, we demonstrated that the robustness of this model could be marginally improved by introducing a parameter to account for noise or uncertainty in temperature measurements. The maximum likelihood method allows the identification of all model parameters using a combination of fatigue and self-heating data, with the advantage of assigning a separate level of confidence to each dataset through the noise parameter. In other words, using this method, the quantiles of the predicted Wöhler curve do not shift with errors in temperature measurements.

The application of this model to porous materials has previously been done as shown in [Bercelli et al., 2021], nevertheless it requires modification for cases involving plasticity. To address this, we proposed an extension of the lifetime model by incorporating a second probabilistic criterion based on cumulative plastic strain, with a transition between the two criteria depending on the material's yield stress. This modified lifetime model, combined with the multi-scale methodology introduced in Chapter 2, was successfully validated on fatigue lifetime data for the aluminium alloy. However, it does have more parameters than the strain-life model. Identifying the modified model on self-heating data from porous specimens has not been undertaken in this thesis, and remains an open issue.

2 Perspectives and Future Work

Several questions arise regarding the usability of the multi-scale method in the absence of high-resolution tomographic images of the pore networks. Optical imaging of the material's surface offers a potential alternative for constructing a pore size distribution, as demonstrated by [Osmond et al., 2018]. This distribution can then be used to simulate digital volumes by sampling from it. However, the size effect observed by these authors must be carefully considered, as the maximum defect sizes observed through surface inspection tend to be smaller than those detected via fracture surface analysis. For applying the multi-scale methodology developed in this work, it is crucial to have some information on the maximum pore size, density, and spatial distribution, which can be obtained from low-resolution tomography. Based on this data, pore populations may be generated as shown in [El Khoukhi et al., 2021a, Matpadi Raghavendra et al., 2023]. In the absence of such data, the foundation for pore population modelling for the multi-scale method becomes less certain.

In the lifetime models used within the multi-scale method, local field values of the fatigue criteria have been employed, necessitating highly refined meshes to ensure convergence of the solution. However, this requirement significantly increases computational costs, especially for

large volumes with complex pore geometries. A promising alternative would be to adopt a non-local approach, such as the method used by [Lacourt, 2019], which smooths the local field values of the criteria around the pores by taking an average of the local field values around the point. The key goal of this approach would be to identify an optimal averaging radius that produces consistent lifetime predictions across different levels of mesh refinement. This would allow for the use of coarser meshes, reducing computational time and resources without sacrificing the accuracy of the lifetime distribution predictions. Furthermore, the weakest link model was applied across all elements within the entire gauge section of the porous specimens. Several authors have recommended focusing solely on the region surrounding the pores [Lacourt, 2019, Bercelli et al., 2021] or the highly stressed areas near the pores for more accurate lifetime predictions in the presence of porosity [Matpadi Raghavendra et al., 2024], albeit with different non-local models. This aspect warrants further investigation.

Moreover, the multi-scale methodology remains somewhat cumbersome, particularly for bigger structures, due to the need to mesh pores at the meso-scale. Therefore, investigating a form of homogenisation or model reduction to replicate the fatigue behaviour of a porous volume depending on its position in the structure is a promising direction. This could involve a model that assigns lower fatigue lifetime predictions at surfaces and higher lifetime estimates in the core of a volume, consistent with experimental results [Pegues et al., 2017, Romano et al., 2019, El Khoukhi et al., 2021a].

Another open question is the validity of the proposed numerical pipeline for low-cycle fatigue. While the multi-scale method, combined with a suitable lifetime model, could be adapted, the Neuber-type method for lifetime criteria may lead to significant errors in this regime, as plasticity is no longer confined [Desmorat, 2002]. Alternative methods of computational acceleration should thus be explored, including the cycle jump method [Sai, 1993] or reduced-order modelling [Lacourt, 2019].

Finally, the modified micro-inclusion model developed in Chapter 5 includes several additional parameters related to the transition and macro-model criteria, as compared to the original micro-inclusion model [Doudard et al., 2004]. We have demonstrated that these parameters can be identified using fatigue data. Although no theoretical framework currently exists to establish a direct link between temperature measurements and fatigue model parameters (as was the case with the micro-inclusion model), further investigation could explore whether these parameters can be identified from self-heating data of porous specimens, using the maximum likelihood estimation procedure outlined in Chapter 5. In this case, the dissipation causing the temperature rise in porous specimens should be attributed to a combination of micro-scale plasticity and macro-scale plasticity around the pores, governed by the same transition parameters. Such a study would align with the objective of further reducing the amount of fatigue data required for fatigue model calibration.

Appendix A

Accuracy of the plastic corrector on a specimen with pores from X-ray tomography loaded in the high-cycle fatigue regime

As a final test case, we present here a specimen containing pores (arising due to the manufacturing process) that were meshed using information from tomography of a porous AlSi7Mg0.3 alloy. This case was chosen to show the particular suitability of application of the plastic corrector for high-cycle fatigue models that require elasto-plastic fields around pores of non-spherical geometry [Bercelli et al., 2021, Lacourt, 2019, Palchoudhary et al., 2024a]. The parameters of the Chaboche law are chosen according to reference [Le, 2016], and are summarised in table 7.1.

For the plastic corrector, an elasto-static FEA computation is computed with prescribed displacements $\underline{\bar{u}}_a = [u_x, 0, 0]$ for $x \geq L_c$ and $\underline{\bar{u}}_a = [-u_x, 0, 0]$ for $x \leq -L_c$ such that $\bar{\sigma}^{\#}_{\mathrm{VM}}$ in the gauge section away from the pores is at the yield stress of the material (this computation corresponds to $f = 1$). The function $f(t)$ is chosen to have 20 cycles. At the peak of the cyclic load, $f(t)\bar{\sigma}^{\#}_{\mathrm{VM}}$ is chosen to reach 47% of the yield stress of the material in the gauge section away from pores. The boundary conditions are shown in Figure 7.11.

For the reference elasto-plastic computation, prescribed displacements are applied to both ends of the porous specimen in the same way. The von Mises stress in the gauge section away from pores reaches 47% of the material's yield stress at peak loads in the cycles, assuming the body behaves elastically.

The plastic corrector and reference computations for the cumulative plastic strain range Δp in the 20^{th} cycle for this mesh are respectively shown in Figure 7.12(a) and 7.12(b). A scatter plot comparing Δp in all the integration points in the mesh is shown in Figure 7.12(c). The accuracy of the full-field approximation indicates that the plastic corrector performs well for varying material parameters and on different sizes and geometries of pores. Despite the nominal loading being $0.47\sigma_y$, there are regions with higher stress concentrations arising due to a maximum stress concentration factor of $k_t \sim 4.3$. The plastic corrector approximates the solution well in these regions despite the high k_t as the plasticity remains confined due to the small size of the pores.

Table 7.1: Parameters of the elasto-plastic model detailed in equations (3.11)-(3.18) [Chaboche, 1989, Le et al., 2018]

E MPa	σ_y MPa	b	Q MPa	C MPa	D
75500	170	19	20	127499	1334

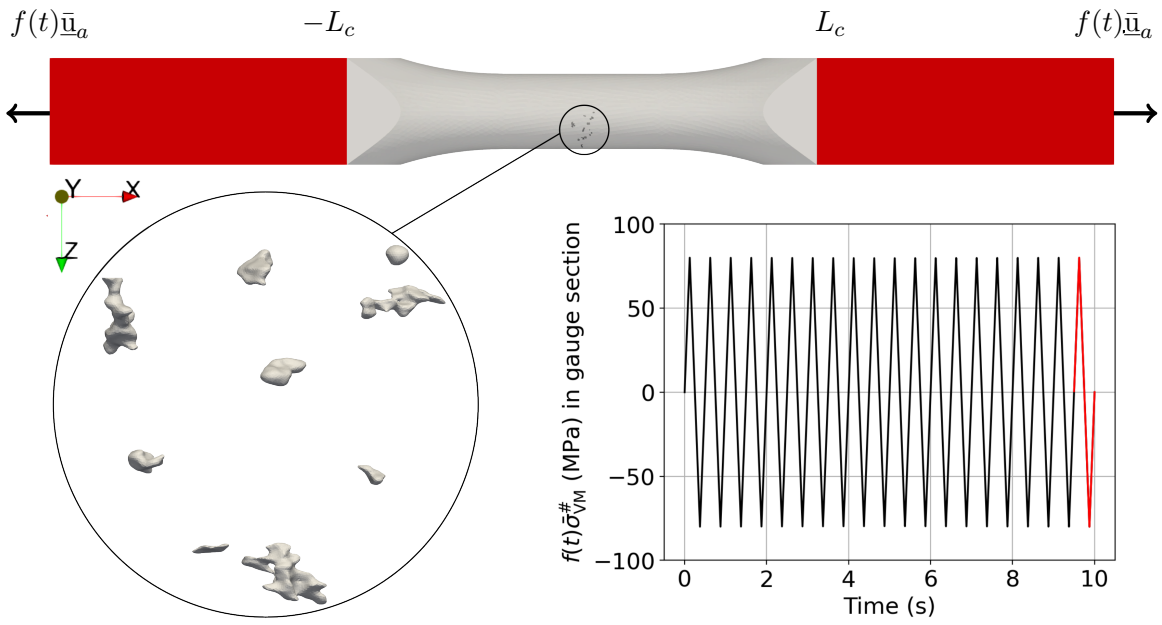

Figure 7.11: Boundary conditions (shown in red) for a specimen containing a sub-volume of tomography-informed pores, showing where displacement is applied to get a cyclic loading in the gauge section of the specimen (away from pores) with peak equal to 47% of the yield stress of the material. The 20^{th} cycle is chosen for the computation of Δp.

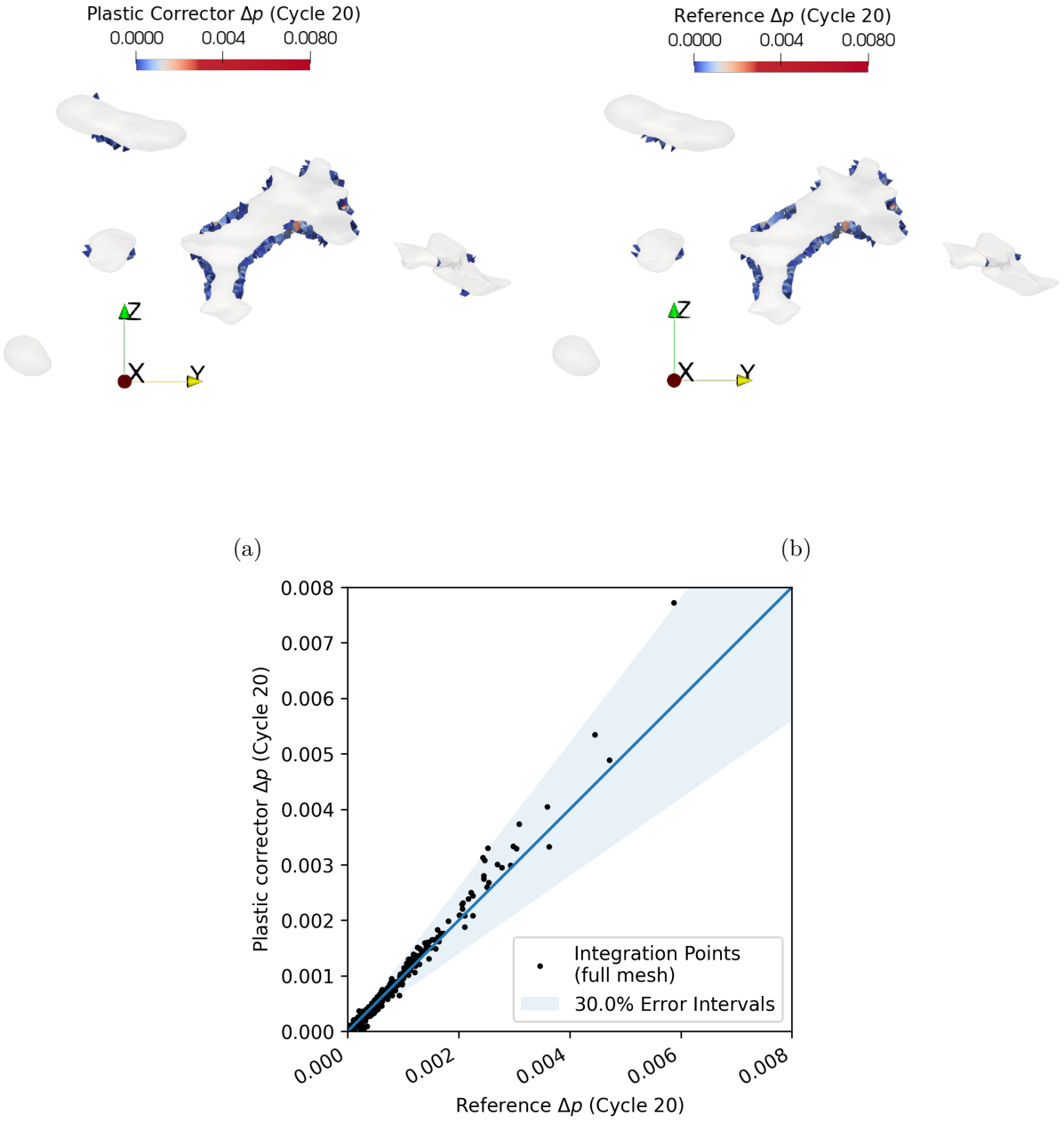

Figure 7.12: (a-b) A comparison between Δp in the 20^{th} cycle calculated via the plastic corrector and a reference computation via Z-Set [Besson et al., 2012] in a few pores of a specimen containing a subvolume of pores (with the maximum stress concentration factor being $k_t \sim 4.3$). The loading corresponds to 80 MPa in the gauge section at the peak of cyclic loading, away from pores (around 47% of σ_y) (c) A scatter plot comparing Δp calculated via the plastic corrector and a reference computation via Z-Set [Besson et al., 2012] in all the integration points of the specimen containing the subvolume of pores.

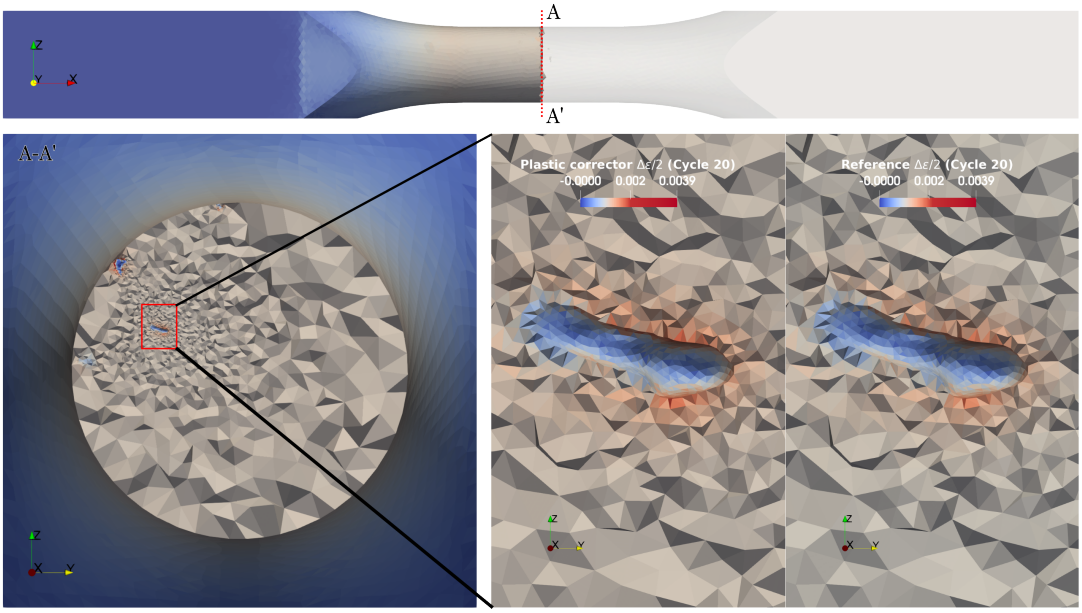

(a)

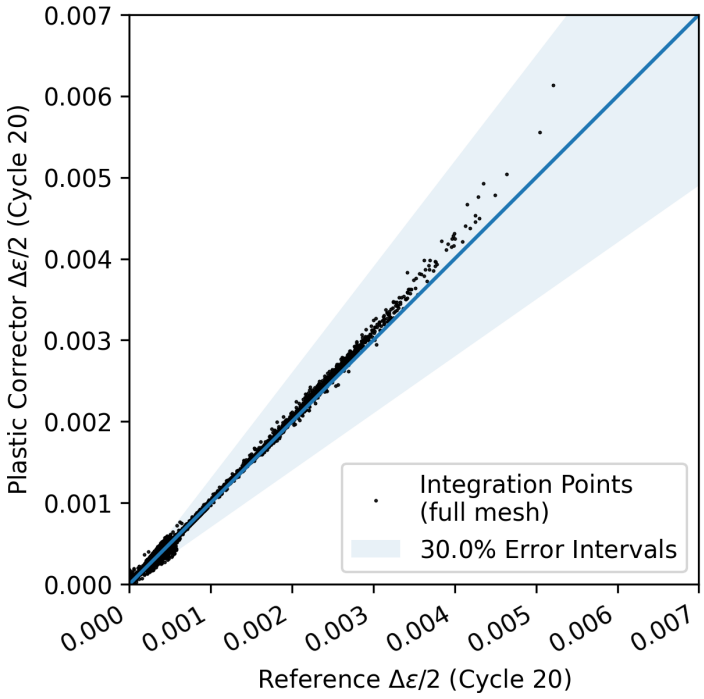

(b)

Figure 7.13: (a) A comparison between the fatigue criterion $\Delta\varepsilon$ in the 20^{th} cycle calculated via the plastic corrector and a reference computation via Z-Set [Besson et al., 2012] in a specimen containing a different subvolume of pores (with the maximum stress concentration factor being $k_t \sim 4$). The loading corresponds to 80 MPa in the gauge section at the peak of cyclic loading, away from pores (around 47% of σ_y) (b) A scatter plot comparing $\Delta\varepsilon$ calculated via the plastic corrector and a reference computation via Z-Set [Besson et al., 2012] in all the integration points of the specimen containing the subvolume of pores.

Appendix B

Analytical form of the failure density of a specimen undergoing heterogeneous stresses

The life of the porous specimen is dependent on the elements that constitute its volumes:

$$\text{Prob}(N_{\text{R}}^{\text{s}} \geq N) = \prod_{*\in\mathcal{E}} \text{Prob}(N_{\text{R}}^{*} \geq N) \tag{8.44}$$

Therefore, the cumulative probability distribution (CDF) of the specimen failing is given by:

$$F_{N_{\text{R}}^{\text{s}}}(N) = 1 - \prod_{*\in\mathcal{E}} \left(1 - F_{N_{\text{R}}^{*}}(N)\right) \tag{8.45}$$

The CDF of failure of an element was defined as:

$$F_{N_{\text{R}}^{*}}(N) = 1 - \exp\left(-\left\{\frac{N}{\lambda}\right\}^{m}\right) \tag{8.46}$$

Substituting this expression in the expression for the CDF of the specimen, we get:

$$F_{N_{\text{R}}^{\text{s}}}(N) = 1 - \prod_{*\in\mathcal{E}} \left(\exp\left(-\left\{\frac{N}{\lambda}\right\}^{m}\right)\right) \tag{8.47}$$

$$F_{N_{\text{R}}^{\text{s}}}(N) = 1 - \exp\left(\sum_{*\in\mathcal{E}} \left(-\left\{\frac{N}{\lambda}\right\}^{m}\right)\right) \tag{8.48}$$

$$F_{N_{\text{R}}^{\text{s}}}(N) = 1 - \exp\left(-N^{m} \sum_{*\in\mathcal{E}} \left\{\frac{1}{\lambda}\right\}^{m}\right) \tag{8.49}$$

This is equivalent to a Weibull distribution with Weibull scale parameter denoted as λ^{s}:

$$F_{N_{\text{R}}^{\text{s}}}(N) = 1 - \exp\left(-\left\{\frac{N}{\lambda^{s}}\right\}^{m}\right) \tag{8.50}$$

$$\lambda^{s} = \frac{1}{\left\{\sum\limits_{*\in\mathcal{E}} \frac{1}{\lambda^{m}}\right\}^{1/m}} \tag{8.51}$$

$$N_{\mathrm{R}}^{\mathrm{s}} \sim \mathcal{W}\left(\lambda^{s}, m\right) \tag{8.52}$$

The probability density function (PDF) and the cumulative distribution function (CDF) of the specimen's fatigue lifetime are denoted by $f_{N_{\mathrm{R}}^{\mathrm{s}}}(N;\Sigma_a,\mu)$ and $F_{N_{\mathrm{R}}^{\mathrm{s}}}(N;\Sigma_a,\mu)$ to show the dependence of these functions on the set of parameters μ and the applied stress amplitude Σ_a.

Appendix C

Algorithm for solving the plastic corrector equations

This section details the algorithm used to solve numerically the equations of the local plastic corrector, for arbitrary (proportional) loading functions $f(t)$.

Monotonic loading

In that case, the proposed Neuber-type rule (from section 2.3) reads as:

$$se = f^2 \tag{9.53}$$

The plastic corrector equations derived in section 2.4 are reminded here for the sake of readability.

$$\text{Stress strain relation} \quad s = (e - e^p) \tag{9.54}$$

$$\text{Yield surface} \quad \hat{f}_y(s; x, \hat{p}) = \hat{\mathcal{J}}(s, x) - \sigma_y - R(\hat{p}) \tag{9.55}$$

$$\text{Yield surface evolution} \quad \hat{f}_y\dot{\hat{p}} = 0 \quad \text{and} \quad \hat{f}_y(s; x, \hat{p}) \leq 0 \tag{9.56}$$

$$\text{von Mises stress} \quad \hat{\mathcal{J}}(s, x) = \left| s - \frac{x}{2\mu} \right| \bar{\sigma}^{\#}_{\text{VM}} \tag{9.57}$$

$$\text{Kinematic hardening} \quad \dot{x} = \frac{2}{3} C\dot{e}^p - Dx\dot{\hat{p}} \tag{9.58}$$

$$\text{Isotropic hardening} \quad R(\hat{p}) = Q(1 - e^{-b\hat{p}}) \tag{9.59}$$

$$\text{Cumulative plastic strain} \quad \dot{\hat{p}} = \frac{1}{3\mu} |\dot{e}^p| \bar{\sigma}^{\#}_{\text{VM}} \tag{9.60}$$

Implicit time integration of this set of equations is done by introducing the following set of discretised equations for s_{i+1}, e_{i+1}, e^p_{i+1}, $\hat{p}_{i+1}$ and x_{i+1} at time $t_{i+1} \in [0\ T]$, scalar quantities e^p_i, $\hat{p}_i$ and x_i at time $0 \leq t_i < t_{i+1}$ being known.

$$s_{i+1}e_{i+1} = f_{i+1}^2 \tag{9.61}$$

$$s_{i+1} = e_{i+1} - e_{i+1}^p \tag{9.62}$$

$$\hat{p}_{i+1} = \hat{p}_i + \left| e_{i+1}^p - e_i^p \right| \frac{1}{3\mu} \bar{\sigma}_{\mathrm{VM}}^{\#} \tag{9.63}$$

$$x_{i+1} = \frac{x_i + \frac{2}{3}C(e_{i+1}^p - e_i^p)}{1 + D(e_{i+1}^p - e_i^p)} \tag{9.64}$$

$$\hat{f}_y(s_{i+1}, x_{i+1}, \hat{p}_{i+1}) \leq 0 \qquad \hat{f}_y(s_{i+1}, x_{i+1}, \hat{p}_{i+1})(\hat{p}_{i+1} - \hat{p}_i) = 0 \tag{9.65}$$

To solve this system of equations, we first need to express s_{i+1} as a function of e_{i+1}^p by making use of equations (9.61), and (9.62):

$$s_{i+1} = \begin{cases} \frac{-e_{i+1}^p + \sqrt{\left(e_{i+1}^p\right)^2 + 4f_{i+1}^2}}{2} & \text{if} \quad f_{i+1} > f_i \\ \frac{-e_{i+1}^p - \sqrt{\left(e_{i+1}^p\right)^2 + 4f_{i+1}^2}}{2} & \text{if} \quad f_{i+1} < f_i \end{cases} \tag{9.66}$$

There are two roots for s. Substituting the expression for e from the scalar stress-strain relation of the material law in the scalar Neuber-type equation, a second order polynomial equation is obtained: The positive sign in the root is taken for increasing f (tensile loading), the negative sign is taken in the case of decreasing f (compression loading).

Now, the following solution algorithm is proposed

1. compute

$$s_{i+1}^{\star} = \begin{cases} \frac{-e_i^p + \sqrt{\left(e_i^p\right)^2 + 4f_{i+1}^2}}{2} & \text{if} \quad f_{i+1} > f_i \\ \frac{-e_i^p - \sqrt{\left(e_i^p\right)^2 + 4f_{i+1}^2}}{2} & \text{if} \quad f_{i+1} < f_i \end{cases} \tag{9.67}$$

2. compute $f_{y,i+1}^* = \hat{f}_y(s_{i+1}^{\star}, x_i, \hat{p}_i)$, i.e. the value of the yield function assuming that no plastic flow takes place between t_i and t_{i+1}.

3. if $f_{y,i+1}^* \leq 0$, set $e_{i+1}^p = e_i^p$

4. if $f_{y,i+1}^* > 0$, find e_{i+1}^p such that

$$\hat{f}_y(s_{i+1}, x_{i+1}, \hat{p}_{i+1}) = 0 \tag{9.68}$$

with s_{i+1} given as a function of e_{i+1}^p in equation (9.66), x_{i+1} given as a function of e_{i+1}^p in equation (9.64) and $\hat{p}_{i+1}$ given as a function of e_{i+1}^p in equation (9.63). The root of this equation is found by a Newton algorithm, which is initialised by setting $e_{i+1}^p = e_i^p$,

$x_{i+1} = x_i$ and $\hat{p}_{i+1} = p_i$. In our implementation, the derivative of $\hat{f}_y$ with respect to e^p_{i+1} is computed by finite differences.

5. set $x_{i+1} = \frac{x_i + \frac{2}{3}C(e^p_{i+1} - e^p_i)}{1 + D(e^p_{i+1} - e^p_i)}$ and $\hat{p}_{i+1} = \hat{p}_i + \left| e^p_{i+1} - e^p_i \right| \frac{1}{3\mu} \bar{\sigma}^{\#}_{\mathrm{VM}}$

Cyclic loading

In that case, the proposed Neuber-type rule (from section 2.3) reads as:

$$(s - s_o)(e - e_o) = (f - f_o)^2 \tag{9.69}$$

From the plastic corrector equations derived in section 2.4, the scalar stress-strain relation extended for cyclic loading is:

$$(s - s_o) = (e - e_o) - (e^p - e^p_o) \tag{9.70}$$

The rest of the plastic corrector equations are the same as equations (9.55)-(9.60). The equations (9.69) and (9.70) involve the quantities s_o, e_o, e^p_o and f_o which are updated with s_i, e_i, e^p_i and f_i respectively, each time a load reversal occurs. The time discretisation of these equations is given here:

$$(s_{i+1} - s_o)(e_{i+1} - e_o) = (f_{i+1} - f_o)^2 \tag{9.71}$$

$$s_{i+1} - s_o = (e_{i+1} - e_o) - (e^p_{i+1} - e^p_o) \tag{9.72}$$

And the expression for s_{i+1} as a function of e^p_{i+1} by making use of equations (9.71), and (9.72):

$$s_{i+1} - s_o = \begin{cases} \frac{-(e^p_{i+1} - e^p_o) + \sqrt{\left((e^p_{i+1} - e^p_o)\right)^2 + 4(f_{i+1} - f_o)^2}}{2} & \text{if} \quad f_{i+1} > f_i \\ \frac{-(e^p_{i+1} - e^p_o) - \sqrt{\left((e^p - e^p_o)_{i+1}\right)^2 + 4(f_{i+1} - f_o)^2}}{2} & \text{if} \quad f_{i+1} < f_i \end{cases} \tag{9.73}$$

The same implicit time integrator used for the monotonic case presented in the previous paragraph is used to find the value of e^p point-wise at each time-step.

Python implementation A Python implementation of this algorithm is made available under LGPL licence. The code and detailed usage instructions can be found in this GitHub repository (https://github.com/AbhishekPalchoudhary/PlasticCorrector/tree/main). The repository includes scripts and instructions for point-wise plastic correction and correction of full elastic FEA computations. Examples are also included. This will enable reproduction of our results and enable further exploration of the algorithm's capabilities.

Liste des publications

Articles à comité de lecture

A. Palchoudhary, S. Peter, C. Ovalle, V. Maurel, P. Kerfriden. "*A plastic correction algorithm for full-field elasto-plastic finite element simulations : critical assessment of predictive capabilities and improvement by machine learning*". Computational Mechanics.
DOI: https://doi.org/10.1007/s00466-024-02561-6

Articles en préparation

A. Palchoudhary, C. Ovalle, V. Maurel, P. Kerfriden. "*A multi-scale probabilistic methodology to predict high-cycle fatigue lifetime for alloys with process-induced pores*". Journal to be decided.
DOI: https://doi.org/10.48550/arXiv.2409.16565

Conférences internationales (premier auteur)

A. Palchoudhary, C. Ovalle, V. Maurel, P. Kerfride. "*A fast Neuber-type Finite Element simulator to calibrate a multi-mechanism fatigue model of alloys in the presence of process-induced pores*". 13th International Fatigue Congress, Hiroshima, Japan, 2023.

Bibliography

[Adib and Pluvinage, 2003] Adib, H. and Pluvinage, G. (2003). Theoretical and numerical aspects of the volumetric approach for fatigue life prediction in notched components. *International Journal of Fatigue*, 25(1):67–76.

[Alnaes et al., 2015] Alnaes, M. S., Blechta, J., Hake, J., Johansson, A., Kehlet, B., Logg, A., Richardson, C., Ring, J., Rognes, M. E., and Wells., G. N. (2015). The fenics project version 1.5, archive of numerical software 3.

[Andreau et al., 2019] Andreau, O., Koutiri, I., Peyre, P., Penot, J.-D., Saintier, N., Pessard, E., De Terris, T., Dupuy, C., and Baudin, T. (2019). Texture control of 316l parts by modulation of the melt pool morphology in selective laser melting. *Journal of Materials Processing Technology*, 264:21–31.

[Antoni, 2019] Antoni, N. (2019). A novel rapid method of purely elastic solution correction to estimate multiaxial elastic-plastic behaviour. *Journal of Computational Design and Engineering*, 6(3):269–283.

[ASTM, 2015] ASTM, E. (2015). 739-91. standard practice for statistical analysis of linear or linearized stress-life (sn) and strain-life (ε-n) fatigue data. *ASTM International*.

[B., 1956] B., C. (1956). Effect of large hydrostatic pressures on the torsional fatigue strength of an alloy steel. *Proceedings of the Inter-national Conference on Fatigue of Metals, Institution of Mechanical Engineers*, pages 138–149.

[Bai et al., 2024] Bai, J., Liu, G.-R., Rabczuk, T., Wang, Y., Feng, X.-Q., and Gu, Y. (2024). A robust radial point interpolation method empowered with neural network solvers (rpim-nns) for nonlinear solid mechanics. *Computer Methods in Applied Mechanics and Engineering*, 429:117159.

[Baratta et al., 2023] Baratta, I. A., Dean, J. P., Dokken, J. S., Habera, M., Hale, J. S., Richardson, C. N., Rognes, M. E., Scroggs, M. W., Sime, N., and Wells, G. N. (2023). DOLFINx: The next generation FEniCS problem solving environment. preprint.

[Bercelli, 2021] Bercelli, L. (2021). *Étude des propriétés en fatigue polycyclique des matériaux et des structures obtenus par le procédé de fabrication additive arc-fil*. Theses, ENSTA Bretagne - École nationale supérieure de techniques avancées Bretagne.

[Bercelli et al., 2021] Bercelli, L., Moyne, S., Dhondt, M., Doudard, C., Calloch, S., and Beaudet, J. (2021). A probabilistic approach for high cycle fatigue of wire and arc additive manufactured parts taking into account process-induced pores. *Additive Manufacturing*, 42:101989.

[Beremin et al., 1983] Beremin, F. M., Pineau, A., Mudry, F., et al. (1983). A local criterion for cleavage fracture of a nuclear pressure vessel steel. *Metallurgical Transactions A*, 14:2277–2287.

[Besson et al., 2010] Besson, J., Cailletaud, G., Chaboche, J.-L., and Forest, S. (2010). *Non-Linear Mechanics of Materials*. Springer, Dordrecht.

[Besson et al., 2012] Besson, J., Leriche, R., Foerch, R., and Cailletaud, G. (2012). Object-oriented programming applied to the finite element method part ii. application to material behaviors. *Revue Européenne des Éléments*, 7:567–588.

[Billaudeau et al., 2004] Billaudeau, T., Nadot, Y., and Bezine, G. (2004). Multiaxial fatigue limit for defective materials: mechanisms and experiments. *Acta Materialia*, 52(13):3911–3920.

[Bracquart et al., 2018] Bracquart, B., Mareau, C., Saintier, N., and Morel, F. (2018). Experimental study of the impact of geometrical defects on the high cycle fatigue behavior of polycrystalline aluminium with different grain sizes. *International Journal of Fatigue*, 109:17–25.

[Brot et al., 2024] Brot, G., Bonnand, V., Favier, V., Koutiri, I., Pacou, D., Dupuy, C., and Lefebvre, F. (2024). Self-heating testing of additively manufactured ti-6al-4v with different microstructures and porosity levels. *Procedia Structural Integrity*, 57:53–60. Fatigue Design 2023 (FatDes 2023).

[Brown and Miller, 1973] Brown, M. and Miller, K. (1973). A theory for fatigue under multiaxial stress-strain conditions. *Proceedings of the Institute of Mechanical Engineers*, 187:745–756.

[Buczynski and Glinka, 2003] Buczynski, A. and Glinka, G. (2003). An analysis of elasto-plastic strains and stresses in notched bodies subjected to cyclic non-proportional loading paths. In Carpinteri, A., de Freitas, M., and Spagnoli, A., editors, *Biaxial/Multiaxial Fatigue and Fracture*, volume 31 of *European Structural Integrity Society*, pages 265–283. Elsevier, Amsterdam, Netherlands.

[Buffière et al., 2001] Buffière, J.-Y., Savelli, S., Jouneau, P., Maire, E., and Fougères, R. (2001). Experimental study of porosity and its relation to fatigue mechanisms of model al–si7–mg0.3 cast al alloys. *Materials Science and Engineering: A*, 316(1):115–126.

[Bustos et al., 2023] Bustos, I., Bergant, M., and Yawny, A. (2023). On the suitability of applying thermographic methods for the rapid estimation of the fatigue limit of additively manufactured ti-6al-4v. *International Journal of Fatigue*, 174:107709.

[Caradec et al., 2023] Caradec, Q., Breuzé, M., Maitournam, H., Prabel, B., and Fayard, J.-L. (2023). Finite element simulation of high cycle fretting wear using an implicit adaptive cycle jump. *Wear*, 522:204703. 24th International Conference on Wear of Materials.

[Carteron, 2020] Carteron, L. (2020). *De l'apport des mesures de champs de température sous sollicitations cycliques pour la caractérisation et la modélisation des propriétés en fatigue des assemblages soudés*. PhD thesis, ENSTA Bretagne. Thèse de doctorat dirigée par Doudard, Cédric et Calloch, Sylvain Mécanique des solides, des matériaux, des structures et des surfaces Brest, École nationale supérieure de techniques avancées Bretagne 2020.

[Chaboche, 1989] Chaboche, J. (1989). Constitutive equations for cyclic plasticity and cyclic viscoplasticity. *International Journal of Plasticity*, 5(3):247–302.

[Chaudonneret and Culié, 1985] Chaudonneret, M. and Culié, J. (1985). Adaptation of neuber's theory to stress concentration in viscoplasticity. *La Recherche Aérospatiale*, 4:33–40.

[Chen et al., 2023] Chen, K., Qin, H., and Ren, Z. (2023). Establishment of the microstructure of porous materials and its relationship with effective mechanical properties. *Scientific Reports*, 13:18064.

[Cheng et al., 2022] Cheng, J., Hu, X., and Kirka, M. (2022). A cycle-jump acceleration method for the crystal plasticity simulation of high cycle fatigue of the metallic microstructure. *International Journal of Fatigue*, 165:107185.

[Chinesta et al., 2020] Chinesta, F., Cueto, E., Abisset-Chavanne, E., Duval, J.-L., and El Khaldi, F. (2020). Virtual, digital and hybrid twins: A new paradigm in data-based engineering and engineered data. *Archives of Computational Methods in Engineering*, 27:105–134.

[Chouman et al., 2014] Chouman, M., Gaubert, A., Chaboche, J. L., Kanoute, P., Cailletaud, G., and Quilici, S. (2014). Elastic-viscoplastic notch correction methods. *International Journal of Solids and Structures*, 51(18):3025–3041.

[Coffin, 1954] Coffin, L. F., J. (1954). A study of the effects of cyclic thermal stresses on a ductile metal. *Transactions of the American Society of Mechanical Engineers*, 76(6):931–949.

[Dang-Van et al., 1982] Dang-Van, K., Griveau, B., and Message, O. (1982). On a new multiaxial fatigue limit criterion : theory and application, biaxial and multiaxial fatigue. *EGF Publication*, 3:479–496.

[Deshpande et al., 2024] Deshpande, S., Bordas, S. P., and Lengiewicz, J. (2024). Magnet: A graph u-net architecture for mesh-based simulations. *Engineering Applications of Artificial Intelligence*, 133:108055.

[Desmorat, 2002] Desmorat, R. (2002). Fast estimation of localized plasticity and damage by energetic methods. *International Journal of Solids and Structures*, 39(12):3289–3310.

[Desmorat et al., 2007] Desmorat, R., Kane, A., Seyedi, M., and Sermage, J. (2007). Two scale damage model and related numerical issues for thermo-mechanical high cycle fatigue. *European Journal of Mechanics - A/Solids*, 26(6):909–935.

[Dezecot et al., 2016] Dezecot, S., Buffiere, J.-Y., Koster, A., Maurel, V., Szmytka, F., Charkaluk, E., Dahdah, N., El Bartali, A., Limodin, N., and Witz, J.-F. (2016). In situ 3d characterization of high temperature fatigue damage mechanisms in a cast aluminum alloy using synchrotron x-ray tomography. *Scripta Materialia*, 113:254–258.

[Doudard et al., 2005] Doudard, C., Calloch, S., Cugy, P., Galtier, A., and Hild, F. (2005). A probabilistic two-scale model for high-cycle fatigue life predictions. *Fatigue & Fracture of Engineering Materials & Structures*, 28(3):279–288.

[Doudard et al., 2004] Doudard, C., Calloch, S., Hild, F., Cugy, P., and Galtier, A. (2004). Identification of the scatter in high cycle fatigue from temperature measurements. *Comptes Rendus Mécanique*, 332(10):795–801.

[Dowling, 2003] Dowling, N. (2003). 4.03 - local strain approach to fatigue. In Milne, I., Ritchie, R., and Karihaloo, B., editors, *Comprehensive Structural Integrity*, pages 77–94. Pergamon, Oxford.

[D'Accardi et al., 2021] D'Accardi, E., Ulbricht, A., Krankenhagen, R., Palumbo, D., and Galietti, U. (2021). Capability of active thermography to detect and localize pores in metal additive manufacturing materials. *IOP Conference Series: Materials Science and Engineering*, 1038(1):012018.

[El Khoukhi et al., 2021a] El Khoukhi, D., Morel, F., Saintier, N., Bellett, D., Osmond, P., and Le, V.-D. (2021a). Probabilistic modeling of the size effect and scatter in high cycle fatigue using a monte-carlo approach: Role of the defect population in cast aluminum alloys. *International Journal of Fatigue*, 147:106177.

[El Khoukhi et al., 2019] El Khoukhi, D., Morel, F., Saintier, N., Bellett, D., Osmond, P., Le, V.-D., and Adrien, J. (2019). Experimental investigation of the size effect in high cycle fatigue: Role of the defect population in cast aluminium alloys. *International Journal of Fatigue*, 129:105222.

[El Khoukhi et al., 2022] El Khoukhi, D., Morel, F., Saintier, N., Bellett, D., Osmond, P., Le, V.-D., and Adrien, J. (2022). Scatter and size effect in high cycle fatigue of cast aluminum-silicon alloys: A comprehensive experimental investigation. *Procedia Structural Integrity*, 38:611–620. Fatigue Design 2021, International Conference Proceedings, 9th Edition.

[El Khoukhi et al., 2021b] El Khoukhi, D., Saintier, N., Morel, F., Bellett, D., Osmond, P., and Le, V.-D. (2021b). Spatial point pattern methodology for the study of pores 3d patterning in two casting aluminium alloys. *Materials Characterization*, 177:111165.

[Ezanno et al., 2013] Ezanno, A., Doudard, C., Calloch, S., and Heuzé, J.-L. (2013). A new approach to characterizing and modeling the high cycle fatigue properties of cast materials based on self-heating measurements under cyclic loadings. *International Journal of Fatigue*, 47:232–243.

[Ezanno et al., 2010] Ezanno, A., Doudard, C., Calloch, S., Millot, T., and Heuzé, J.-L. (2010). Fast characterization of high-cycle fatigue properties of a cast copper–aluminum alloy by self-heating measurements under cyclic loadings. *Procedia Engineering*, 2(1):967–976. Fatigue 2010.

[Fatemi and Socie, 1988] Fatemi, A. and Socie, D. (1988). A critical plane approach to multiaxial fatigue damage including out-of-phase loading. *Fatigue and Fracture of Engineering Materials and Structures*, 11(3):149–166.

[Geuzaine and Remacle, 2020] Geuzaine, C. and Remacle, J.-F. (2020). Gmsh.

[Gong et al., 2014] Gong, H., Rafi, K., Gu, H., Starr, T., and Stucker, B. (2014). Analysis of defect generation in ti–6al–4v parts made using powder bed fusion additive manufacturing processes. *Additive Manufacturing*, 1-4:87–98. Inaugural Issue.

[Guerchais et al., 2017] Guerchais, R., Morel, F., and Saintier, N. (2017). Effect of defect size and shape on the high-cycle fatigue behavior. *International Journal of Fatigue*, 100:530–539. Multiaxial Fatigue 2016: Experiments and Modeling.

[Herbland, 2009] Herbland, T. (2009). *Une méthode de correction élastoplastique pour le calcul en fatigue des zones de concentration de contraintes sous chargement cyclique multiaxial non proportionnel*. Theses, École Nationale Supérieure des Mines de Paris.

[Hoffmann and Seeger, 1985] Hoffmann, M. and Seeger, T. (1985). A Generalized Method for Estimating Multiaxial Elastic-Plastic Notch Stresses and Strains, Part 1: Theory. *Journal of Engineering Materials and Technology*, 107(4):250–254.

[Hou et al., 2024] Hou, Y., Hu, Z., Wauters, T., and Talemi, R. (2024). Combined effect of random porosity and surface defect on fatigue lifetime of additively manufactured micro-sized ti6al4v components: An investigation based on numerical analysis and machine learning approach. *Theoretical and Applied Fracture Mechanics*, 131:104451.

[Ince and Glinka, 2013] Ince, A. and Glinka, G. (2013). A numerical method for elasto-plastic notch-root stress–strain analysis. *The Journal of Strain Analysis for Engineering Design*, 48(4):229–244.

[Jones et al., 1998] Jones, R., Science, D., (Australia), T. O., Aeronautical, and (Australia), M. R. L. (1998). *Stress and strain estimation at notches in aircraft structures*. DSTO Aeronautical and Maritime Research Laboratory, Melbourne.

[Karolczuk and Macha, 2005] Karolczuk, A. and Macha, E. (2005). A review of critical plane orientations in multiaxial fatigue failure criteria of metallic materials. *International Journal of Fracture*, 134:267–304.

[Karolczuk and Palin-Luc, 2013] Karolczuk, A. and Palin-Luc, T. (2013). Modelling of stress gradient effect on fatigue life using weibull based distribution function. *Journal of Theoretical and Applied Mechanics*, 51:297–311.

[Kitagawa, 1976] Kitagawa, H. (1976). Applicability of fracture mechanics to very small cracks or the cracks in the early stage. In *Proceedings of 2nd ICM, Cleveland*, pages 627–631.

[Koutiri, 2011] Koutiri, I. (2011). *Effet des fortes contraintes hydrostatiques sur la tenue en fatigue des matériaux métalliques*. Thèse de doctorat, Arts et Métiers ParisTech, Mécanique des matériaux [physics.class-ph]. NNT : 2011ENAM0015, pastel-00599125.

[Koutiri et al., 2013] Koutiri, I., Bellett, D., Morel, F., and Pessard, E. (2013). A probabilistic model for the high cycle fatigue behaviour of cast aluminium alloys subject to complex loads. *International Journal of Fatigue*, 47:137–147.

[Krokos et al., 2024] Krokos, V., Bordas, S. P., and Kerfriden, P. (2024). A graph-based probabilistic geometric deep learning framework with online enforcement of physical constraints to predict the criticality of defects in porous materials. *International Journal of Solids and Structures*, 286–287:112545.

[Krokos et al., 2021] Krokos, V., Bui Xuan, V., Bordas, S. P. A., Young, P., and Kerfriden, P. (2021). A bayesian multiscale cnn framework to predict local stress fields in structures with microscale features. *Computational Mechanics*, 69(3):733–766.

[La Rosa and Risitano, 2000] La Rosa, G. and Risitano, A. (2000). Thermographic methodology for rapid determination of the fatigue limit of materials and mechanical components. *International Journal of Fatigue*, 22(1):65–73.

[Lacourt, 2019] Lacourt, L. (2019). *Étude numérique de la nocivité des défauts dans les soudures*. Thèse de doctorat, Université Paris Sciences et Lettres, Matériaux. NNT : 2019PSLEM050, tel-02512870.

[Ladinek et al., 2018] Ladinek, M., Niederwanger, A., Lang, R., Schmid, J., Timmers, R., and Lener, G. (2018). The strain-life approach applied to welded joints: Considering the real weld geometry. *Journal of Constructional Steel Research*, 148:180–188.

[Lanning et al., 2003] Lanning, D. B., Nicholas, T., and Palazotto, A. (2003). Hcf notch predictions based on weakest-link failure models. *International Journal of Fatigue*, 25(9):835–841. International Conference on Fatigue Damage of Structural Materials IV.

[Le, 2016] Le, V. D. (2016). *Etude de l'influence des hétérogénéités microstructurales sur la tenue en fatigue à grand nombre de cycles des alliages d'aluminium de fonderie*. PhD thesis, ENSAM. Thèse de doctorat dirigée par Morel, FranckSaintier, Nicolas et Bellett, Daniel Mécanique-matériaux Paris, ENSAM 2016.

[Le et al., 2015] Le, V.-D., Morel, F., Bellett, D., Pessard, E., Saintier, N., and Osmond, P. (2015). Microstructural-based analysis and modelling of the fatigue behaviour of cast al-si alloys. *Procedia Engineering*, 133:562–575. Fatigue Design 2015, International Conference Proceedings, 6th Edition.

[Le et al., 2016] Le, V.-D., Morel, F., Bellett, D., Saintier, N., and Osmond, P. (2016). Multiaxial high cycle fatigue damage mechanisms associated with the different microstructural heterogeneities of cast aluminium alloys. *Materials Science and Engineering: A*, 649:426–440.

[Le et al., 2018] Le, V.-D., Saintier, N., Morel, F., Bellett, D., and Osmond, P. (2018). Investigation of the effect of porosity on the high cycle fatigue behaviour of cast al-si alloy by x-ray micro-tomography. *International Journal of Fatigue*, 106:24–37.

[Lee et al., 2023] Lee, S., Norovrinchen, O., and Sumiyadorj, C. (2023). Fatigue strength estimation based on the maximum likelihood method. In *Proceedings of the second International Conference on Resources and Technology (RESAT 2023)*, pages 98–106. Atlantis Press.

[Lee et al., 2011] Lee, Y.-L., Barkey, M. E., and Kang, H.-T. (2011). *Metal fatigue analysis handbook: practical problem-solving techniques for computer-aided engineering*. Elsevier.

[Lemaitre et al., 1999] Lemaitre, J., Sermage, J., and Desmorat, R. (1999). A two scale damage concept applied to fatigue. *International Journal of Fracture*, 97(1):67–81.

[Leost et al., 2023] Leost, N., Köster, A., Missoum-Benziane, D., Rambaudon, M., Cameriano, L., Comte, F., Le Pannerer, B., and Maurel, V. (2023). Full-field analysis of damage under complex thermomechanical loading. *International Journal of Fatigue*, 170:107513.

[Lesne and Savalle, 1989] Lesne, P. and Savalle, S. (1989). An efficient cycles jump technique for viscoplastic structures calculations involving large number of cycles. In *Proceedings of 2nd International Conference on Computational Plasticity*, pages 591–602.

[Leveuf et al., 2018] Leveuf, L., Marco, Y., Le Saux, V., Navrátil, L., Leclercq, S., and Olhagaray, J. (2018). Fast screening of the fatigue properties of thermoplastics reinforced with short carbon fibers based on thermal measurements. *Polymer Testing*, 68:19–26.

[Levieil et al., 2019] Levieil, B., Doudard, C., Thevenet, D., Bridier, F., Ezanno, A., and Calloch, S. (2019). An original simplified method based on the use of an adjustable localization operator for low-cycle fatigue life predictions in the case of confined plasticity. *Theoretical and Applied Fracture Mechanics*, 104:102383.

[Li et al., 2016] Li, H., Wen, D., Lu, Z., Wang, Y., and Deng, F. (2016). Identifying the probability distribution of fatigue life using the maximum entropy principle. *Entropy*, 18(4).

[Li et al., 2022] Li, X.-K., Zhu, S.-P., Liao, D., Correia, J. A., Berto, F., and Wang, Q. (2022). Probabilistic fatigue modelling of metallic materials under notch and size effect using the weakest link theory. *International Journal of Fatigue*, 159:106788.

[Liu et al., 2020] Liu, X., Wang, R., Hu, D., and Mao, J. (2020). A calibrated weakest-link model for probabilistic assessment of lcf life considering notch size effects. *International Journal of Fatigue*, 137:105631.

[Luong, 1995] Luong, M.-P. (1995). Infrared thermographic scanning of fatigue in metals. *Nuclear Engineering and Design*, 158(2-3):363–376.

[Makkonen, 2001] Makkonen, M. (2001). Statistical size effect in the fatigue limit of steel. *International Journal of Fatigue*, 23(5):395–402.

[Manson, 1953] Manson, S. S. (1953). Behavior of materials under conditions of thermal stress. Technical Note TN 2933, National Advisory Committee for Aeronautics (NACA).

[Matpadi Raghavendra et al., 2023] Matpadi Raghavendra, A. K., Lacourt, L., Marcin, L., Maurel, V., and Proudhon, H. (2023). Generation of synthetic microstructures containing casting defects: a machine learning approach. *Scientific Reports*, 13(1):11852.

[Matpadi Raghavendra et al., 2024] Matpadi Raghavendra, A. K., Maurel, V., Marcin, L., and Proudhon, H. (2024). Fatigue life prediction at mesoscopic scale of samples containing casting defects: A novel energy based non-local model. *International Journal of Fatigue*, 188:108485.

[Maurel et al., 2009] Maurel, V., Rémy, L., Dahmen, F., and Haddar, N. (2009). An engineering model for low cycle fatigue life based on a partition of energy and micro-crack growth. *International Journal of Fatigue*, 31(5):952–961.

[McDonald and Socie, 2011] McDonald, R. and Socie, D. (2011). A technique to estimate the local multiaxial elastic–plastic behavior from a purely elastic solution. *Engineering Fracture Mechanics*, 78(8):1696–1704. Multiaxial Fracture.

[Merot et al., 2024] Merot, P., Morel, F., Robert, C., Pessard, E., Gallegos Mayorga, L., and Buttin, P. (2024). Non local multiaxial fatigue modeling of defects : A unified approach to interpret size and shape effects. *Theoretical and Applied Fracture Mechanics*, 131:104378.

[Messager, 2020] Messager, A. (2020). *Étude de l'amorçage et de la propagation de fissures de fatigue internes courtes en régime gigacyclique dans un alliage d'aluminium de fonderie*. Theses, HESAM Université.

[Moftakhar et al., 1994] Moftakhar, A., Buczynski, A., and Glinka, G. (1994). Calculation of elasto-plastic strains and stresses in notches under multiaxial loading. *Int J Fract*, 70:357–373.

[Molski and Glinka, 1981] Molski, K. and Glinka, G. (1981). A method of elastic-plastic stress and strain calculation at a notch root. *Materials Science and Engineering*, 50:93–100.

[Morabito et al., 2007] Morabito, A., Chrysochoos, A., Dattoma, V., and Galietti, U. (2007). Analysis of heat sources accompanying the fatigue of 2024 t3 aluminium alloys. *International Journal of Fatigue*, 29(5):977–984.

[Morel et al., 2015] Morel, F., Guerchais, R., and Saintier, N. (2015). Competition between microstructure and defect in multiaxial high cycle fatigue. *FRATTURA ED INTEGRITA STRUCTTURALE*, 9(33):404–414.

[Morrow, 1968] Morrow, J. (1968). Fatigue properties of metals. *Fatigue Design Handbook, Soc. of Automotive Engineers*, Pub. No. AE-4(ch. Section 3.2.):1–132.

[Mukhopadhyay et al., 2018] Mukhopadhyay, S., Nixon-Pearson, O. J., and Hallett, S. R. (2018). An experimental and numerical study on fatigue damage development in laminates containing embedded wrinkle defects. *International Journal of Fatigue*, 107:1–12.

[Munier et al., 2014] Munier, R., Doudard, C., Calloch, S., and Weber, B. (2014). Determination of high cycle fatigue properties of a wide range of steel sheet grades from self-heating measurements. *International Journal of Fatigue*, 63:46–61.

[Muñiz-Calvente et al., 2015] Muñiz-Calvente, M., Fernández Canteli, A., Shlyannikov, V., and Castillo, E. (2015). Probabilistic weibull methodology for fracture prediction of brittle and ductile materials. In *Damage Mechanics: Theory, Computation and Practice*, volume 784 of *Applied Mechanics and Materials*, pages 443–451. Trans Tech Publications Ltd.

[Nadot, 2022] Nadot, Y. (2022). Fatigue from defect: Influence of size, type, position, morphology and loading. *International Journal of Fatigue*, 154:106531.

[Neuber, 1961] Neuber, H. (1961). Theory of Stress Concentration for Shear-Strained Prismatical Bodies With Arbitrary Nonlinear Stress-Strain Law. *Journal of Applied Mechanics*, 28(4):544–550.

[Ni and Mahadevan, 2004] Ni, K. and Mahadevan, S. (2004). Strain-based probabilistic fatigue life prediction of spot-welded joints. *International Journal of Fatigue*, 26(7):763–772.

[Nie et al., 2019] Nie, Z., Jiang, H., and Kara, L. B. (2019). Stress field prediction in cantilevered structures using convolutional neural networks. *Journal of Computing and Information Science in Engineering*, 20(1).

[Osmond et al., 2018] Osmond, P., LE, V.-D., MOREL, F., BELLETT, D., and SAINTIER, N. (2018). Effect of porosity on the fatigue strength of cast aluminium alloys: from the specimen to the structure. *Procedia Engineering*, 213:630–643. 7th International Conference on Fatigue Design, Fatigue Design 2017, 29-30 November 2017, Senlis, France.

[Palchoudhary et al., 2024a] Palchoudhary, A., Ovalle, C., Maurel, V., and Kerfriden, P. (2024a). A multi-scale probabilistic model for fatigue lifetime characterization of alloys in the presence of random process-induced pores.

[Palchoudhary et al., 2024b] Palchoudhary, A., Peter, S., Maurel, V., Ovalle, C., and Kerfriden, P. (2024b). A plastic correction algorithm for full-field elasto-plastic finite element simulations: critical assessment of predictive capabilities and improvement by machine learning. *Computational Mechanics*.

[Papadopoulos, 1993] Papadopoulos, I. (1993). *Fatigue limit of metals under multiaxial stress conditions: the microscopic approach*. Joint Research Centre, ISEI.

[Pegues et al., 2017] Pegues, J., Roach, M., Williamson, R., and Shamsaei, N. (2017). Effect of specimen surface area size on fatigue strength of additively manufactured ti-6al-4v parts. In *28th Annual International Solid Freeform Fabrication Symposium*.

[Pessard et al., 2011] Pessard, E., Morel, F., Morel, A., and Bellett, D. (2011). Modelling the role of non-metallic inclusions on the anisotropic fatigue behaviour of forged steel. *International Journal of Fatigue*, 33(4):568–577.

[Pollak and Palazotto, 2009] Pollak, R. D. and Palazotto, A. N. (2009). A comparison of maximum likelihood models for fatigue strength characterization in materials exhibiting a fatigue limit. *Probabilistic Engineering Mechanics*, 24(2):236–241.

[Qian et al., 2016] Qian, L., Cui, X., Liu, S., Chen, M., Ma, P., Xie, H., Zhang, F., and Meng, J. (2016). Image-based numerical simulation of the local cyclic deformation behavior around cast pore in steel. *Materials Science and Engineering: A*, 678:347–354.

[Qvale and Härkegård, 2017] Qvale, P. and Härkegård, G. (2017). A simplified method for weakest-link fatigue assessment based on finite element analysis. *International Journal of Fatigue*, 100:78–83.

[Raissi et al., 2019] Raissi, M., Perdikaris, P., and Karniadakis, G. (2019). Physics-informed neural networks: A deep learning framework for solving forward and inverse problems involving nonlinear partial differential equations. *Journal of Computational Physics*, 378:686–707.

[Rasmussen and Williams, 2006] Rasmussen, C. E. and Williams, C. K. (2006). *Gaussian Processes for Machine Learning*. MIT Press, Cambridge.

[Romano et al., 2019] Romano, S., Miccoli, S., and Beretta, S. (2019). A new fe post-processor for probabilistic fatigue assessment in the presence of defects and its application to am parts. *International Journal of Fatigue*, 125:324–341.

[Ryckelynck et al., 2015] Ryckelynck, D., Gallimard, L., and Jules, S. (2015). Estimation of the validity domain of hyper-reduction approximations in generalized standard elastoviscoplasticity. *Advances in Modeling and Simulation in Engineering Sciences*, 2(1):6.

[Sai, 1993] Sai, K. (1993). *Modèles à grand nombre de variables internes et méthodes numériques associées*. Theses, École Nationale Supérieure des Mines de Paris.

[Savalle and Culié, 1978] Savalle, S. and Culié, J. (1978). Méthodes de calcul associées aux lois de comportement cyclique et d'endommagement. *La Recherche Aérospatiale*, 5:263–278.

[Schijve, 2009] Schijve, J. (2009). *Fatigue of Structures and Materials*. Springer Dordrecht, 2 edition.

[Serrano-Munoz et al., 2018] Serrano-Munoz, I., Buffiere, J.-Y., and Verdu, C. (2018). Casting defects in structural components: Are they all dangerous? a 3d study. *International Journal of Fatigue*, 117:471–484.

[Shirani and Härkegård, 2012] Shirani, M. and Härkegård, G. (2012). Damage tolerant design of cast components based on defects detected by 3d x-ray computed tomography. *International Journal of Fatigue*, 41:188–198. Fatigue Design & Material Defects.

[Smith et al., 1970] Smith, K. N., Watson, P., and Topper, T. H. (1970). A stress-strain function for the fatigue of materials. *J. Mater.*, 5:767–778.

[Talemi, 2020] Talemi, R. (2020). A numerical study on effects of randomly distributed subsurface hydrogen pores on fretting fatigue behaviour of aluminium alsi10mg. *Tribology International*, 142:105997.

[Taud et al., 2005] Taud, H., Martinez-Angeles, R., Parrot, J., and Hernandez-Escobedo, L. (2005). Porosity estimation method by x-ray computed tomography. *Journal of Petroleum Science and Engineering*, 47(3-4):209–217.

[Taylor, 1999] Taylor, D. (1999). Geometrical effects in fatigue: a unifying theoretical model. *International Journal of Fatigue*, 21(5):413–420.

[Taylor, 2005] Taylor, D. (2005). Analysis of fatigue failures in components using the theory of critical distances. *Engineering Failure Analysis*, 12(6):906–914. Papers presented at the First International Conference on Engineering Failure Analysis (Lisbon, Portugal, 12–14 July 2004). Part II.

[Thumann et al., 2024] Thumann, P., Buchner, S., Marburg, S., and Wagner, M. (2024). A comparative study of glinka and neuber approaches for fatigue strength assessment on 42crmos4-qt specimens. *Strain*, 60(4):e12470.

[Tijani et al., 2013] Tijani, Y., Heinrietz, A., Bruder, T., and Hanselka, H. (2013). Quantitative evaluation of fatigue life of cast aluminum alloys by non-destructive testing and parameter model. *International Journal of Fatigue*, 57:73–78. Fatigue and Microstructure: A special issue on recent advances.

[Tkachuk et al., 2007] Tkachuk, A., Duewer, F., Cui, H., Feser, M., Wang, S., and Yun, W. (2007). X-ray computed tomography in zernike phase contrast mode at 8 kev with 50-nm resolution using cu rotating anode x-ray source. *Zeitschrift für Kristallographie - Crystalline Materials*, 222(11):650–655.

[Topper et al., 1967] Topper, T., Wetzel, R., and Morrow, J. (1967). Neuber's rule applied to fatigue of notched specimens. *J. Mater., ASTM*, 4:21.

[Van Paepegem et al., 2001] Van Paepegem, W., Degrieck, J., and De Baets, P. (2001). Finite element approach for modelling fatigue damage in fibre-reinforced composite materials. *Composites Part B: Engineering*, 32(7):575–588.

[Vásárhelyi et al., 2020] Vásárhelyi, L., Kónya, Z., Kukovecz, A., and Vajtai, R. (2020). Microcomputed tomography–based characterization of advanced materials: a review. *Materials Today Advances*, 8:100084.

[Wang et al., 2023] Wang, B., An, X., Xue, P., Liu, F., Ni, D., Xiao, B., Liu, Y., and Ma, Z. (2023). Grain size effects on high cycle fatigue behaviors of pure aluminum. *International Journal of Fatigue*, 170:107556.

[Wang et al., 2001] Wang, Q., Apelian, D., and Lados, D. (2001). Fatigue behavior of a356/357 aluminum cast alloys. part ii – effect of microstructural constituents. *Journal of Light Metals*, 1(1):85–97.

[Wei et al., 2024] Wei, W., He, L., Sun, Y., and Yang, X. (2024). A review of fatigue limit assessment using the thermography-based method. *Metals*, 14(6).

[Weibull, 1951] Weibull, W. (1951). A statistical distribution function of wide applicability. *Journal of applied mechanics*.

[Wicke et al., 2016] Wicke, M., Luetje, M., Bacaicoa, I., and Brueckner-Foit, A. (2016). Characterization of casting pores in fe-rich al-si-cu alloys by microtomography and finite element analysis. *Procedia Structural Integrity*, 2:2643–2649. 21st European Conference on Fracture, ECF21, 20-24 June 2016, Catania, Italy.

[Ye et al., 2008] Ye, D., Hertel, O., and Vormwald, M. (2008). A unified expression of elastic–plastic notch stress–strain calculation in bodies subjected to multiaxial cyclic loading. *International Journal of Solids and Structures*, 45(24):6177–6189.

[Yi et al., 2007] Yi, J., Zhu, X., Jones, J., et al. (2007). A probabilistic model of fatigue strength controlled by porosity population in a 319-type cast aluminum alloy: Part ii. monte-carlo simulation. *Metallurgical and Materials Transactions A*, 38:1123–1135.

[Zok, 2017] Zok, F. W. (2017). On weakest link theory and weibull statistics. *Journal of the American Ceramic Society*, 100(4):1265–1268.

RÉSUMÉ

Cette étude vise à établir une méthodologie permettant de prendre en compte la variabilité du comportement en fatigue à grand nombre de cycles (HCF) des alliages, en modélisant explicitement les pores à l'échelle méso (défauts géométriques) présents dans le matériau. Bien qu'il existe des stratégies numériques pour prédire la durée de vie en HCF à partir de simulations haute résolution des réseaux de pores, plusieurs défis subsistent. Premièrement, la prédiction de la durée de vie en fatigue devient difficile lorsque les réseaux de pores exacts présents dans le matériau sont inconnus. Deuxièmement, les coûts de calcul des simulations non-linéaires par éléments finis (EF) au niveau des défauts sont élevés, car un grand nombre de degrés de liberté est nécessaire pour représenter précisément le réseau de pores dans le matériau. Enfin, l'identification des modèles de fatigue exige de nombreuses données d'essais de fatigue, longues à obtenir.

Nous développons une méthodologie multi-échelle pour intégrer les effets des défauts sur la durée de vie en HCF. À l'échelle microscopique, la variabilité de la durée de vie est traitée via des modèles probabilistes, sans modélisation explicite des défauts. À l'échelle mésoscopique, des maillages EF haute résolution sont créés à partir d'images tomographiques, afin de rendre compte des effets conjugués de la morphologie, des interactions entre pores, ainsi que des effets de surface. Un échantillonneur statistique est utilisé pour générer différentes configurations et estimer la distribution de la durée de vie en fatigue en fonction des distributions de pores. Ainsi, une nouvelle méthode pour calibrer les modèles probabilistes tenant compte de cette incertitude liée aux pores est proposée. Cette approche permet de fournir des estimations de durée de vie en HCF fonction des deux échelles analysées, tout en réduisant le nombre de données nécessaires à l'identification robuste d'un tel modèle. De plus, afin de réduire les coûts de calcul de la méthode multi-échelle, nous développons un nouvel algorithme local de correction plastique de type Neuber pour approximer le comportement plastique à partir de calculs élastiques. Nous démontrons l'efficacité de notre méthode pour diverses structures poreuses, sous des conditions de plasticité confinée et de chargement proportionnel.

Dans la dernière partie de cette thèse, nous explorons l'usage des données d'auto-échauffement pour réduire les données de calibration, comme suggéré par Doudard et al., 2004. Une augmentation de température est observée autour des pores, liée à la conductivité thermique des alliages testés. Nous proposons une méthode d'identification qui renforce la robustesse du modèle face aux mesures thermiques bruitées. Le critère de ce modèle est ensuite étendu pour inclure la plasticité, permettant son application aux matériaux poreux.

MOTS CLÉS

Durée de vie en fatigue, Pores, Tomographie X, Elements Finis, Machine Learning

ABSTRACT

This thesis focuses on the development of methodology to account for variability in high-cycle fatigue (HCF) behaviour of alloys, by explicitly modelling the meso-scale pores (geometric defects) present in the material. Although numerical frameworks exist to predict the HCF lifetime using high-resolution simulations of pore networks, several challenges remain. Firstly, predicting fatigue lifetime becomes difficult when the exact pore networks present in the material are unknown. Secondly, the computational costs of non-linear finite element (FE) simulations at the pore level are high, as a large number of degrees of freedom are needed to accurately represent the pore networks within the material. Lastly, calibrating fatigue models requires a substantial amount of fatigue testing data, which is time-consuming to obtain.

We develop a multi-scale methodology to account for defect effects on HCF lifetime. At the micro-scale, variability in lifetime is treated by using probabilistic lifetime models, without explicit defect modelling. At the meso-scale, high-resolution FE meshes are generated based on tomographic images, accounting for the combined effects of pore morphology, inter-pore interactions, and pore-surface interactions. A statistical sampler is leveraged to generate different configurations to estimate the distribution of fatigue lifetime of the material as a function of pore distributions. Based on this, we propose a novel method to calibrate the probabilistic lifetime models in the event of uncertainty related to pore distribution. Thus, our proposed method provides HCF lifetime estimates integrating defect populations at two scales, and reduces the amount of data required to calibrate the models for alloys with different levels of porosity. Furthermore, in order to reduce the computational costs associated to the multi-scale method, we develop a new local Neuber-type plastic correction algorithm to approximate elasto-plastic behaviour from elastic computations. We demonstrate the effectiveness of our method for a range of porous materials, under conditions of confined plasticity and proportional loading.

In the last part of the thesis, we investigate the potential of using self-heating data to further reduce the data required to calibrate the fatigue model, as proposed by Doudard et al., 2004. A temperature rise from self-heating, driven by dissipative mechanisms due to defects, is observed. Temperature localisation around pores is governed by the thermal conductivity of alloys tested. We propose a new identification method for the aforementioned model, improving its robustness in the event of noisy temperature measurements. The criterion of this model is then extended to include plasticity, enabling its application to porous materials.

KEYWORDS

Fatigue Lifetime, Pores, X-Ray Tomography, Finite Elements, Machine Learning